Parallel Transmission MRI for Optimised Cardiac Imaging and Improved Safety

Beqiri, Arian

Awarding institution:
King's College London

Parallel Transmission MRI for Optimised Cardiac Imaging and Improved Safety

Arian Beqiri

A thesis submitted in partial fulfilment of the requirement for the degree of
Doctor of Philosophy of **King's College London**

August 2015

Department of Biomedical Engineering
King's College London

Abstract

The move towards higher static magnetic field strengths in MRI has allowed improved imaging quality from increased signal to noise ratio. However challenges have arisen from increased inhomogeneity in the radio frequency (RF) fields required to create MR signals and greater RF energy deposition – known as the specific absorption rate (SAR) – within imaging subjects. These factors have prompted the use of parallel transmission (PTx) MRI; in which multiple independent channels are used to control the RF electromagnetic fields.

In this thesis the aim was to develop methods for controlling SAR using PTx and to assess the impact of RF safety in various scenarios. The electromagnetic behaviour of an 8-channel PTx RF coil was fully simulated which enabled the examination of differences between full simulations and a commonly modelled idealised situation. It was found that large discrepancies could result in the idealised model in certain situations. The full RF coil model was for producing SAR simulations of various adult male voxel models.

These SAR models were used to perform RF shimming, in which a complex weighting is applied to each channel of a PTx system to yield improved RF conditions. This was done for two scenarios: to perform lower SAR cardiac MRI with greater RF field homogeneity in vivo for optimised imaging; and to explore methods for decoupling the transmit coil from a simulated prosthetic hip implant embedded within an adult male whilst still producing a uniform imaging field. In both scenarios, reduced SAR configurations could be found that enabled improved imaging with greater RF safety.

A separate model of a 2-channel birdcage RF coil was developed to assess SAR deposition in neonates during MRI examinations. It was found that under normal operation at 3 T, local SAR constraints produced by the scanner are conservative by a factor of four.

Acknowledgements

There are a number of people to whom I am indebted for enabling me to complete this PhD. Primarily I wish to thank my main supervisor, Shaihan Malik. Throughout the past three years, he has been wholly supportive, encouraging and incessantly enthusiastic; and his knowledge and advice were invaluable. I would also like to thank my second supervisor, Jo Hajnal, for his guidance and scientific insight. Without Shaihan and Jo as supervisors, my life would have been far, far more difficult and the PhD far less enjoyable so thank you both.

A further thanks goes to my friends across the Division of Imaging Sciences. I have been very lucky to have such a great group of people to discuss ideas with and to laugh with.

I also wish to thank who might possibly be the most patient person on the planet – Andia, I can't believe you've put up with me for so long! I would not have been able to start this PhD without you and I certainly could not have finished it.

And finally I wish to express my eternal gratitude to my family – Visar, Gini, Mum and Dad, I could not have made it this far without your support over the years. Thank you for everything.

Contents

List of Figures

List of Tables

List of Abbreviations

AFI	Actual flip angle imaging
BMI	Body mass index
bSSFP	Balanced steady state free precession
CAD	Computer aided design
CMR	Cardiac magnetic resonance imaging
CT	Computed tomography
DAM	Double angle method
DREAM	Dual refocusing echo acquisition mode
EM	Electromagnetic
EPI	Echo planar imaging
FCM	Full coil model
FCM:AD/f	Full coil model actively decoupled by fitting
FCMAD:puc	Full coil model actively decoupled by pickup coils
FDTD	Finite difference time domain
FHC	Fats heart-centred
FID	Free induction decay
FIT	Finite integration technique
FOV	Field of view
GPU	Graphics processing unit
ICM	Idealised coil model
LNHC	Enlarged NORMAN heart-centred
MBC	Multix body coil
mCGLS	Multi-shift conjugate gradient least-squares
MGE	Maxwell grid equations
MHD	Magneto-hydrodynamic
MIP	Maximum intensity projection
MLS	Magnitude least squares
MRI	Magnetic resonance imaging
MSE	Mean square error
NHC	NORMAN heart-centred
NHeC	NORMAN head-centred

NMR	Nuclear magnetic resonance
PML	Perfectly matched layer
PTx	Parallel transmission
RF	Radio-frequency
RMSE	Root mean square error
ROI	Region of interest
SAR	Specific absorption rate
SDAM	Saturated double angle method
SENSE	Sensitivity encoding
SNR	Signal to noise ratio
SOMA	Self-organising migrating algorithm
SPGR	Spoiled gradient echo
STE	Stimulated echo
STEAM	Stimulated echo acquisition mode
SVD	Singular value decomposition
T	Tesla
TEM	Transverse electromagnetic
TFE	Turbo field echo
TR	Repetition time
UHF	Ultra high field
VCG	Vector cardiogram
VOP	Virtual observation point

Chapter 1

Introduction

Generating more signal in magnetic resonance imaging (MRI) has been a key driver since its inception. The primary method for achieving this with every new generation of MRI scanners has been to increase the strength of the static magnetic field B_0, as this is directly proportional to the level of signal produced [1].

However as the strength of the B_0 field increases, so does the degree of inhomogeneity in the RF magnetic field B_1 [2]. Consequently despite the increased signal at higher field MRI, there can be far greater variation in contrast and areas with virtually no signal present.

One way of mitigating for this is to use parallel transmission (PTx) [3] in which an array of multiple RF coils are used to generate the RF transmit field B_1^+. Each of these has its own spatially localised field which can combine linearly with the fields from the other coils to produce different RF conditions. PTx can be used to correct for B_1^+ inhomogeneities found at high field by applying different weightings, or "shims", to the individual channels in what is known as RF shimming.

The field produced by the RF coils is not just a magnetic field but also has a concomitant electric field. This does not contribute to the MRI process but does facilitate energy deposition quantified using the specific absorption rate (SAR). Very high SAR conditions can potentially cause unsafe heating within subjects so SAR is subject to strict regulatory limits which then impose constraints on imaging. This is a greater problem with increasing B_0 as SAR is proportional to the square of the B_0 field amplitude [1].

In the same way that PTx is able to control the B_1^+ field, it will simultaneously affect the electric fields that cause SAR. Through careful optimisation both B_1^+ inhomogeneity and SAR deposition can be controlled with RF shimming using PTx MRI [4] thus making high field MRI more feasible.

The B_1^+ field can be measured during an MRI scan [5] and this data can be

used to correct for the inhomogeneities present. Unfortunately the electric fields that cause SAR cannot currently be measured in the same way. This issue is generally overcome through electromagnetic (EM) simulations from which the electric field in a subject can be modelled and SAR can be estimated. The resulting SAR model can be used along with the B_1^+ field data to optimise the driving conditions of the PTx array to produce a more homogenous B_1^+ field and lower SAR.

To be able to assess SAR for the RF shimming calculations in this thesis, an accurate EM model of the PTx coil being used had to initially be constructed. Once this was completed, a comparison into the way the different transmit elements are electrically decoupled from one another in simulation was performed. This comparison reinforced the correct decoupling regime to use for the SAR calculations which were then run for a range of different human models.

Once the SAR models were complete, two uses for RF shimming with regard to controlling SAR were explored. The first was for performing SAR optimised in vivo cardiac imaging at 3 T. For a given pulse sequence, a set of RF shims were found that were able to drastically improve B_1^+ inhomogeneity in a *localised* region encompassing the heart therefore improving imaging of the heart. The shims were also able to simultaneously reduce SAR, often to a substantial degree. This is highly beneficial for cardiac imaging as it is often a high SAR procedure.

RF shimming was also explored in a simulation study with regard to improving RF safety when scanning subjects with prosthetic hip implants. Very high SAR can occur at the ends of these implants when embedded in human tissue [6] and this could lead to potentially dangerous temperature rises within the body. Using the PTx array, it was possible to find a set of modes from sampling the B_1^+ or electric fields for the array that minimally coupled with the implant. These modes could be used as "virtual PTx channels" to perform RF shimming which would ensure minimal SAR and improved B_1^+ homogeneity.

The final component of the work for this thesis involved assessing SAR in a more typical RF coil used for clinical work known as a birdcage coil. A two channel variant of this was simulated and used to assess SAR in neonates at 1.5 and 3 T which was compared with SAR produced in adults at the same field strengths.

1.1 Thesis Outline

This thesis is laid out as follows:

Chapter 2 provides a description of the processes and physics underlying MRI.

Chapter 3 discusses the use of RF coils in MRI along with parallel transmission and how SAR can be calculated and controlled with PTx. This leads on to Chapter 4 which discusses the way EM simulations are run for characterising RF coils.

Chapter 5 presents a simulation study discussing how an 8-channel 3 T PTx body coil was modelled and then an analysis of how the modelling of decoupling between PTx channels affects SAR estimates.

Chapter 6 presents the major study for this thesis into how SAR can be controlled during high field in vivo cardiac imaging using RF shimming whilst also improving B_1^+ homogeneity and hence the quality of imaging.

Chapter 7 presents a simulation study into how SAR can be reduced when scanning subjects with prosthetic hip implants.

Chapter 8 presents another simulation study into the level of SAR deposition in neonates compared with adults during clinical scanning at 1.5 and 3 T

Chapter 9 summarises the thesis and discusses some possible avenues for future work.

Chapter 2

MRI Signal Formation & RF Fields

MRI is an invaluable clinical and research tool for performing in vivo imaging. It has numerous advantages over other medical imaging modalities in that it does not utilise ionising radiation and offers excellent soft tissue contrast.

The core physical principle that governs MRI is that of nuclear magnetic resonance (NMR) which provides the measured signals. NMR as a phenomenon was first measured by Rabi in 1938 [7], and its physical description was extended to apply more generally to liquids and solids by Bloch and Purcell in 1946 [8, 9]. However it wasn't until 1973 that the NMR process could be used to perform imaging. It was then that Lauterbur and Mansfield developed a method for spatially localising the NMR signal [10, 11] and hence MRI was made possible.

In this chapter the processes that govern NMR and enable MRI images to be acquired are discussed along with the radiofrequency electromagentic fields involved in MRI.

2.1 NMR

Nuclear magnetic resonance is fundamentally a quantum process; however a classical picture can be effectively used to describe it. In NMR, the intrinsic angular momentum (or spin) of atomic nuclei produces a magnetic moment on the nuclei. In the presence of a strong external magnetic field, the magnetic moment interacts with that field.

If the external field is of strength B_0 in units of Tesla, the magnetic moment will precess around the field with angular frequency ω_0 in units of rad s^{-1} [1] determined by the relation

$$\omega_0 = \gamma B_0 \tag{2.1}$$

where γ is a constant for a given nucleus with units rad s^{-1} T^{-1} known as the gyromagnetic ratio. A depiction of this precession can be seen in Figure 2.1. This is known as Larmor precession and the frequency ω_0 is the Larmor frequency.

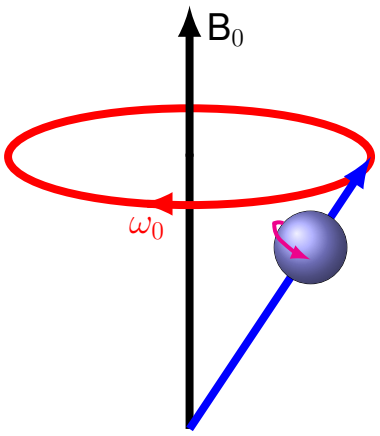

Figure 2.1: Precession of an atomic nucleus around external field B_0. The nucleus' rotation about B_0 at the Larmor frequency ω_0 is indicated with the red arrow and its rotation about its own axis is indicated with the magenta arrow.

For a given body of atomic nuclei in the presence of a magnetic field, some will have spins aligned with the B_0 field and some anti-aligned with it. If these nuclei are in total equilibrium (i.e. there are an exactly equal number of aligned and anti-aligned spins) there will be no net contribution from the sum of the magnetic moments as they will cancel each other out.

For a given system of nuclei, the equilibrium state of these is governed by thermodynamic principles. There is then an energy difference between the aligned and anti-aligned orientations and it can be shown that in a thermal equilibrium, the number of nuclei aligned with the magnetic field exceeds those anti-aligned with the field by a spin excess factor equal to

$$\text{spin excess} \simeq N\frac{\hbar\omega_0}{2kT} \tag{2.2}$$

where N is the total number of nuclei in the system, $\hbar$ is equal to Planck's constant divided by 2π, k is Boltzmann's constant and T is the temperature in units of Kelvin [1]. It is found that the spin excess is a very small number even for magnetic fields on the order of multiple Tesla. However the sheer numbers of atomic nuclei present in any given sample mean that it is still possible to produce a significant signal in NMR.

For a sample with a number of protons per unit volume ρ_0, the average magnetic dipole density – known as the longitudinal equilibrium magnetisation M_0 [1] – is given by

$$M_0 = \frac{\rho_0\gamma^2\hbar^2}{4kT}B_0. \tag{2.3}$$

It is this value which enables the production of measurable signals in NMR.

2.1.1 Excitation and Relaxation

When atomic nuclei are in their equilibrium state with respect to B_0, it is not possible to distinguish any signal from them. To be able to do so, the net equilibrium magnetisation M_0 must be perturbed away from its equilibrium such that a component of magnetisation lies in the plane orthogonal to the B_0 field. This is termed "excitation" and is achieved through the use of another magnetic field known as B_1 [12].

Whilst the B_0 field is a static magnetic field with magnitude generally on the order of Tesla (although technically any field strength can be used), the B_1 field is a radiofrequency (RF) electromagentic (EM) field with much smaller magnitude on the order of μT and frequency set to the Larmor frequency ω_0. By applying the B_1 field to the system for a short period of time τ, the angle through which the magnetisation in the system is rotated by the field [1] is given by

$$\theta = \gamma B_1 \tau. \tag{2.4}$$

This angle is generally known as the flip angle.

On the left side of Figure 2.2, the effect of a 90° flip angle is shown. The red line shows the perturbation of the magnetisation away from its equilibrium alignment with B_0 from the point of view of a reference frame rotating at the Larmor frequency. In this reference frame the rotation about B_0 is not seen. The perturbation viewed from the laboratory frame of reference is shown with the blue line.

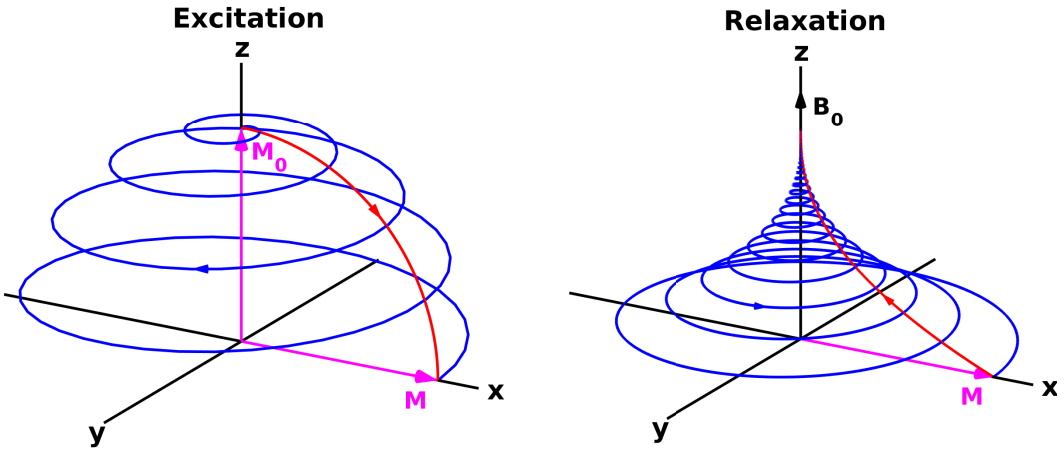

Figure 2.2: Excitation of a magnetisation vector (left) and its relaxation back back to equilibrium (right). In both cases the red line shows the traversal in the rotating frame of reference and the blue line shows the traversal in the laboratory frame of reference with the vector oscillating at the Larmor frequency ω_0.

After the magnetisation has been perturbed, the B_1 pulse is switched off and the magnetisation begins to relax back to equilibrium. This is depicted in the right side of Figure 2.2 where again the red line represents the relaxation in the rotating reference frame and the blue line in the laboratory frame. The vector that represents the magnetisation in the x-y plane – known as the transverse magnetisation M_{xy} – relaxes back to zero with time constant T_2, which is also known as the spin-spin relaxation time. The recovery of the magnetisation M_z in the longitudinal direction aligned with B_0 is governed by time constant T_1, also known as the spin-lattice relaxation time [12]. T_1 and T_2 vary for different substances or tissue types. It is these that determine the behaviour of the signal acquired during NMR for a given substance.

Magnetisation in the x-y plane M_{xy} is able to induce a voltage on an RF coil – this produces the NMR signal. By simply measuring the signal of the magnetisation as it relaxes back to equilibrium, an oscillating decaying signal known as the free induction decay (FID) can be measured. The decay of this signal is often faster than that dictated by T_2 and this is primarily due to inhomogeneities in the B_0 field. Measurements of a signal whose amplitude decays with time constant T_2 can be formed by forcing the phases of the set of magnetisation vectors that form the overall transverse magnetisation M_{xy} to realign thus forming an "echo". A series of these echoes will then decay with time constant proportional to T_2.

By manipulating the magnitudes and phases of the magnetisation vectors, different properties of substances can be deduced and it is this which make NMR such a useful and powerful technique.

2.2 Bloch Equations

The evolution of magnetisation as a result of external fields and relaxation processes is well described by a series of equations known as the Bloch equations [13]. If a situation with no relaxation is initially considered, the Bloch equations describe the Larmor precession of the magnetisation vector **M** due to an external magnetic field **B**:

$$\frac{d\mathbf{M}}{dt} = \gamma(\mathbf{M} \times \mathbf{B}) \tag{2.5}$$

where **M** is comprised of the magnetisation components in the x,y and z directions and **B** is comprised of any active external magnetic fields including B_0 and B_1 [12].

By incorporating relaxation terms governed by T_1 and T_2, the full Bloch equations are formulated as

$$\frac{d\mathbf{M}}{dt} = \gamma(\mathbf{M} \times \mathbf{B}) - \frac{M_{xy}}{T_2} - \frac{(M_z - M_0)}{T_1} \tag{2.6}$$

where M_{xy} is formally defined by $M_{xy} = M_x\hat{\mathbf{x}} + iM_y\hat{\mathbf{y}}$ where $\hat{\mathbf{x}}$ and $\hat{\mathbf{y}}$ represent unit vectors in the x and y directions respectively and $i = \sqrt{-1}$. This is complex notation which describes the transverse plane (i.e. the x-y plane) as a complex plane in which the x-axis is the real axis and the y-axis is the imaginary axis.

This set of equations can be used to calculate the behaviour of the magnetisation of a substance with a given T_1 and T_2 and can be used to predict the evolution of a measured signal when performing NMR.

Particular solutions to the Bloch equations for specific forms of **B** that describe the relaxation processes can be found [1]. For the case where **B**=0, i.e. assessed on resonance in the rotating frame with no active RF field, destruction of the transverse magnetisation M_{xy} is described by

$$M_{xy}(t) = M_{xy}(0)e^{-t/T_2} \tag{2.7}$$

where the expression gives the transverse magnetisation at a time t. The recovery of the longitudinal magnetisation M_z is described by

$$M_z(t) = M_0(1 - e^{-t/T_1}). \tag{2.8}$$

2.3 MRI

To perform imaging with NMR, the NMR signals must be spatially localised. This is achieved by using another set of magnetic fields to modify the spatial distribution of the main magnetic field B_0. These are configured such that a series of linear gradients are present in B_0 in each orthogonal direction.

With these gradients present, the angular frequency of precession at each spatial location is given by

$$\omega(\mathbf{r}, t) = \gamma(B_0 + \mathbf{G} \cdot \mathbf{r}) \tag{2.9}$$

where **r** is the position vector and **G** is a vector of the gradient strengths in the x,y and z directions. It is then possible to find the location of a signal from the angular frequency of the magnetisation that produces that signal thus making MRI possible. This is known as frequency encoding.

However frequency encoding only makes it possible to localise the signal in one direction which in MRI is known as the read direction. To localise the signal in the other two orthogonal directions in three dimensional space, the *phase* of the signal – i.e. its angular displacement relative to spins with the same frequency – must be varied in space in what is known as phase encoding. This is performed by applying gradients in the other spatial directions in the same way as for frequency

encoding. The signal with the gradients applied at a time t is found by

$$s(t) = \int \rho(\mathbf{r})\, e^{(i\gamma \int_0^t \mathbf{G}\cdot\mathbf{r}\, dt)} d\mathbf{r} \tag{2.10}$$

where $\rho(\mathbf{r})$ represents the spatial distribution of the proton density. The signal can be represented in terms of a vector **k** as

$$s(\mathbf{k}) = \int \rho(\mathbf{r})\, e^{(2\pi i\, \mathbf{k}\cdot\mathbf{r})} d\mathbf{r}. \tag{2.11}$$

This expression shows the way in which MRI signals are acquired in the frequency domain in what is known as “k-space”. Each point in k-space represents the integrated sum of signals over all the excited magnetisations in the imaging volume and the **k** vector is equal to the integral of the applied gradients through time:

$$\mathbf{k} = \frac{\gamma}{2\pi} \int_0^t \mathbf{G}(t)\, dt. \tag{2.12}$$

To generate the imaging data from the acquired k-space data, the k-space data is subjected to a Fourier transform.

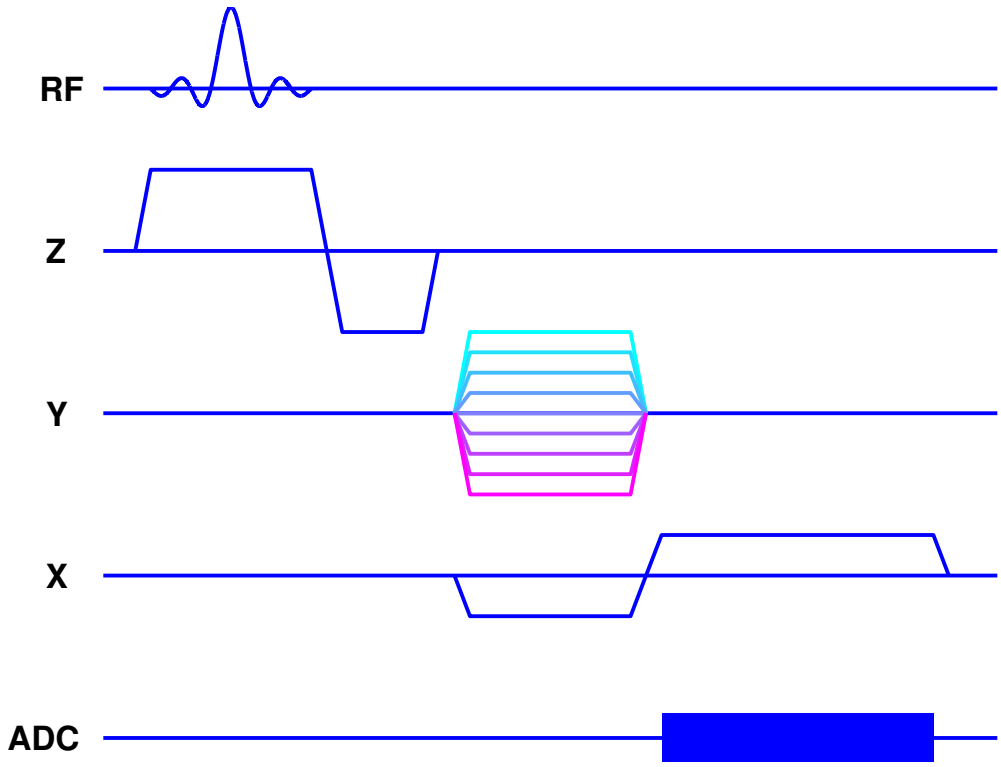

Figure 2.3: Pulse sequence diagram shown for an example slice selective gradient echo MRI pulse sequence. The slice is excited with the RF pulse applied to the transmit coil as shown on the top row. The next three rows show the amplitude of the gradient fields through the sequence. The resultant signal is received and sent to an analogue to digital converter (ADC) to be digitised.

The whole of the k-space data is acquired by applying a series of B_1 pulses and magnetic field gradients. The order and timing of these is known as a pulse sequence and pulse sequences are described by pulse sequence diagrams of which an example is shown in Figure 2.3.

There are a vast plethora of pulse sequences that have been designed for different purposes. Figure 2.3 shows an example of a basic gradient echo sequence [12] for the acquisition of a two dimensional slice. Each line shows the amplitude of pulses or gradients applied through time. The sequence is shown for one repetition of the sequence in a repetition time TR which is used to acquire a single line of data in k-space. To acquire the full data set, the sequence is applied multiple times to fill up the whole set of k-space data. An example schematic of a two-dimensional k-space sampling regime is shown in Figure 2.4 in which the frequency encoding corresponds to the k_x axis and phase encoding corresponds to the k_y axis.

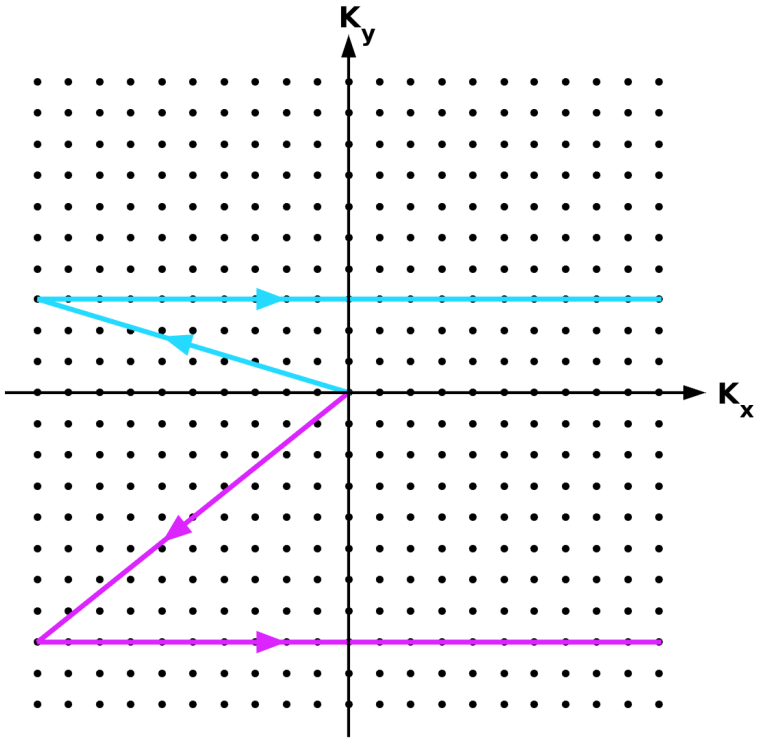

Figure 2.4: Sampling of a two dimensional k-space. The coloured lines indicate the traversal through k-space in two different repetition times whose colours correspond to the y-gradient in Figure 2.3.

The RF pulse in the sequence depicted excites a set of spins in a single slice in the z-direction. This is achieved by using a sinc shaped pulse as the Fourier transform of this means that a rect shaped region is excited in real space. The z-gradient is also necessary for the localisation of this excitation and its negative lobe after the RF pulse has ended is designed to rephase the spins that were

dephased by the application of the RF pulse.

The y-gradient then acts as the phase encoding gradient which effectively positions the sampling location in k-space along the k_y axis for a different line to be read in the frequency encoding direction towards the end of each TR. In the pulse sequence diagram, the different colours for the y-gradient represent the gradient amplitudes used for different TRs. As the y-gradient is being played out, an x-gradient is applied simultaneously to move the sampling location to the edge of the k-space to be sampled. This can be seen in Figure 2.4 for two different phase encodes where the coloured lines correspond to k-space traversals at different TRs within the same sequence. The diagonal component represents both the x and y-gradients being applied to move the sampling location to the correct part of k-space at which point the signal is sampled directly along a k_x line using a positive applied x-gradient.

During the application of this gradient, the signal is measured at discretised locations with an RF receiver coil and an echo is formed halfway through as the sampling passes through the centre of k-space and all the spins are rephased by the gradient at an echo time TE from the beginning of each TR.

In this way the full k-space can be acquired. Whilst this example was given for a two dimensional acquisition, it is straightforward to extend this to all three spatial dimensions by using the z-gradient to perform phase encoding in the z-direction as well.

As mentioned this has been described for a simple gradient echo imaging pulse sequence and there are many other pulse sequences available that are used for different purposes; not just imaging – these can include quantitative measurements of tissue properties, measurement of blood flow, magnetic field measurements, and so on [14]. Furthermore there is an entire zoo of different k-space trajectories that define the way k-space is traversed, such as spiral trajectories or radial trajectories [15]. Whilst a discussion of these is beyond the scope of this thesis, it is worth noting the sheer diversity of ways in which MRI can be utilised for different outcomes.

2.4 B_1 Field

The B_1 field in MRI is produced using an RF coil – these will be discussed in detail in the next chapter. However it is important to assess the behaviour of this field with regard to generation of an MRI signal.

As the B_1 field exists to couple with the NMR process, it is only active in the plane orthogonal to the direction of the B_0 field i.e. the x-y plane. By producing the overall $\mathbf{B}_1$ vector, its behaviour in a frame rotating with angular frequency ω

can be seen. If the laboratory and rotating frames are coincident at time $t = 0$, then at some later time t, the axes of the rotating frame (denoted by tildes above the variables) make an angle ωt with the laboratory frame.

This is depicted in Figure 2.5 where the laboratory frame is shown with black lines and the rotating frame is shown with blue lines. The frame rotating in a positive way makes an angle $+\omega t$ with the laboratory frame as shown on the left side of the figure and the negatively rotating frame makes an angle $-\omega t$ as shown on the right side of the figure.

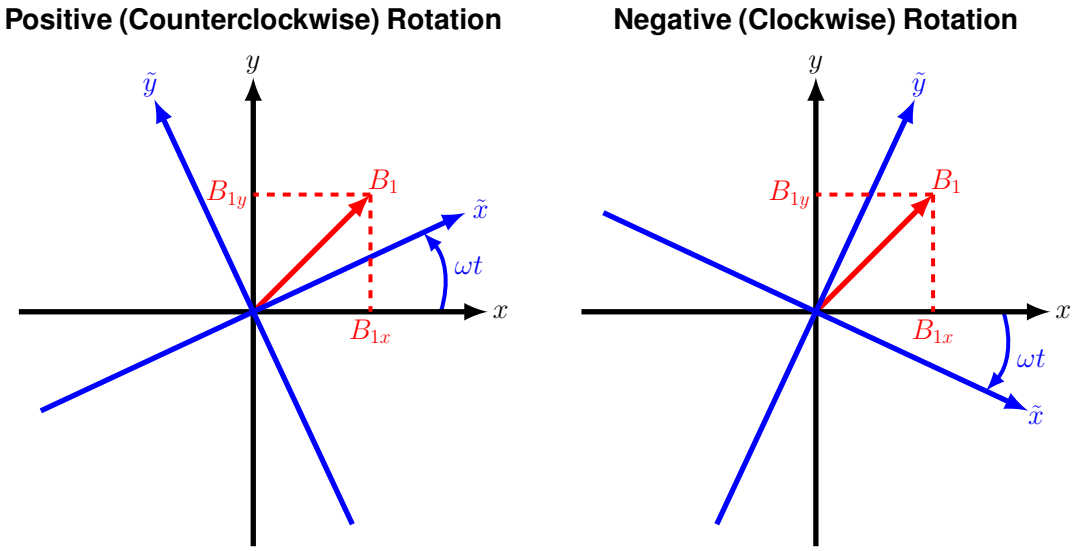

Figure 2.5: Coordinate systems for the positively (left) and negatively (right) rotating framed. The black axes show the laboratory reference frame and the blue axes show the rotating frames. The B_1 vector is shown in red.

By considering an Argand diagram representation [16] in which complex numbers lie on the $\tilde{y}$ axis and real numbers on the $\tilde{x}$ axis, the B_1 fields in the positively and negatively rotating frames produced by an RF coil can be expressed as

$$\tilde{B}_1^+ = \frac{(B_{1x} + iB_{1y})}{2} \tag{2.13}$$

$$\tilde{B}_1^- = \frac{(B_{1x} - iB_{1y})^*}{2} \tag{2.14}$$

These are extremely important expressions in MRI as depending on the relative orientation of the B_0 field, one of these will represent the transmit B_1 field and one will represent the receive field. Generally B_1^+ is the transmit field and B_1^- is the receive field.

From this expression, the efficiency of transmission and reception under different polarisations can be considered. If the B_1 field is linearly polarised where $\tilde{\mathbf{B}}_1 = B\hat{\mathbf{x}}$ or $\tilde{\mathbf{B}}_1 = B\hat{\mathbf{y}}$. This will yield overall $\tilde{B}_1^+$ and $\tilde{B}_1^-$ amplitudes of $B/2$ for each.

However if the fields are circularly polarised where $\tilde{\mathbf{B}}_1 = B\hat{\mathbf{x}} + iB\hat{\mathbf{y}}$, then $\tilde{B}_1^+$ will have an amplitude of B and $\tilde{B}_1^-$ will have an amplitude of 0. If the circular polarisation is instead expressed as $\tilde{\mathbf{B}}_1 = B\hat{\mathbf{x}} - iB\hat{\mathbf{y}}$ then $\tilde{B}_1^-$ will have an amplitude of B and $\tilde{B}_1^+$ will have an amplitude of 0. Hence it is clear that for the correct circular polarisation, it is possible to double the amplitude of the B_1 fields compared with linear polarisation, indicating that circular polarisation is maximally efficient.

It should now be noted that for the remainder of this thesis the transmit and receive B_1 fields will always be considered in the rotating frame of reference and will be referred to as B_1^+ and B_1^- respectively. The relevant x and y-components of the RF magnetic field in this frame will then be referred to simply as B_{1x} and B_{1y}.

2.4.1 Quadrature

The B_1 expressions can now be extended to assess a more common situation in MRI which is that of quadrature transmit and receive coils. This is a situation in which two (or more) separate coils are used simultaneously with a phase difference between them.

By considering a second RF coil to the one originally considered above, a rotation of this coil about the origin by angle $+\psi$ produces an additional phase term in the transmit and receive fields for the coil:

$$B'^{+}_{1} = \frac{(B'_{1x} + iB'_{1y})}{2} e^{i\psi} \tag{2.15}$$

$$B'^{-}_{1} = \frac{(B'_{1x} - iB'_{1y})^*}{2} e^{i\psi}. \tag{2.16}$$

By applying a correctional phase term on the second coil to undo the effects of this rotation, the potential reduction in signal from the phase term when adding the fields from the different coils is undone. This means that both coils are in phase with one another and a maximally efficient circularly polarised transmission or reception can be achieved. This combination of coils driven with a relative phase between them is what is known as quadrature [17]. It is commonly used in large body coils which have two input/outputs rotated about the origin by 90° in space and with a 90° phase between them.

When being driven to create a transmit B_1^+ field, the relative phase terms on the two drives must be zero on one and $e^{-i\psi}$ on the other coil that has been rotated. For receiving on the same coil, the phase term on the second coil must be $e^{+i\psi}$.

2.4.2 B_1^+ Mapping

As will be seen later in this thesis there are many cases in which is is useful to map out the spatial distribution of the RF transmit field, B_1^+. This can be achieved by using a B_1^+ mapping sequence. There are many different techniques for mapping these fields [5, 18–21] and they generally work by measuring the transmit flip angle θ_T and then relating this to the spatial dimensionless sensitivity of the B_1^+ map S by

$$S(\mathbf{r}) = \frac{\theta_T(\mathbf{r})}{\theta_{nom}} \tag{2.17}$$

where θ_{nom} is the nominal desired flip angle of the pulse sequence used for mapping – for a block pulse this is given by Equation 2.4. The sensitivity can be converted into a complex B_1^+ map in units of μT by multiplying by the amplitude of the RF pulse used in the mapping sequence for generating the nominal flip angle. Its complex phase would then be the transmit phase taken from the acquired images for the mapping sequence.

The gold standard B_1^+ mapping technique is considered to be the double angle method (DAM) [5, 22]. This works by acquiring two images, one with flip angle θ and a second with flip angle 2θ. The ratio of these two images will highlight variations in the B_1^+ field thereby producing a field map [5]. By analysing the relative behaviour of the signals produced by imaging with the different flip angles [23], it can be shown that the spatial distribution of the actual transmit flip angle $\theta_T(\mathbf{r})$ is found by

$$\theta_T(\mathbf{r}) = \arccos\left(\frac{I_2(\mathbf{r})}{2I_1(\mathbf{r})}\right) \tag{2.18}$$

where I_1 and I_2 represent the images acquired with some nominal flip angle θ and 2θ respectively.

A key issue with the double angle method is the requirement for a very long repetition time ($TR \geq 5T_1$) to allow for full longitudinal relaxation. This can lead to extremely long scan times (>1 hour) even for very low resolution images. This is clearly not a suitable mapping method for most purposes, particularly not for in vivo MRI.

Consequently Cunningham developed a modified version of the double angle pulse sequence named the saturated double angle method (SDAM) [20]. This takes the same approach as for the double angle method but incorporates a saturation pulse in between pulse repetitions in order to reset the longitudinal magnetisation so that the previous excitation does not affect the succeeding one. This means it is not necessary to wait for full relaxation to occur naturally. Using a spiral k-space trajectory or other similar scanner acceleration techniques produces a significantly faster B_1^+ mapping method with little increase in error [20].

There are challenges associated with the SDAM technique as the signal to noise ratio (SNR) can be lower with shorter acquisition time. Relatively faster B_1^+ mapping methods exist such as the actual flip angle imaging (AFI) method [18]. AFI is an accurate mapping technique that performs two acquisitions with different TRs and uses these to infer the flip angle. However AFI requires a steady state in the magnetisation to be formed which is not always possible, particularly for something like cardiac MRI where there is constant motion and blood flow. AFI is also limited in how fast it can go by the requirement that one of the TR periods must be a multiple – usually four or five – of the other. This means there is a lot of dead time and hence the sequence is not very efficient.

A very fast B_1^+ mapping method was developed by Nehrke named dual refocusing echo acquisition mode (DREAM) [19]. This is able to produce B_1^+ maps in under a second.

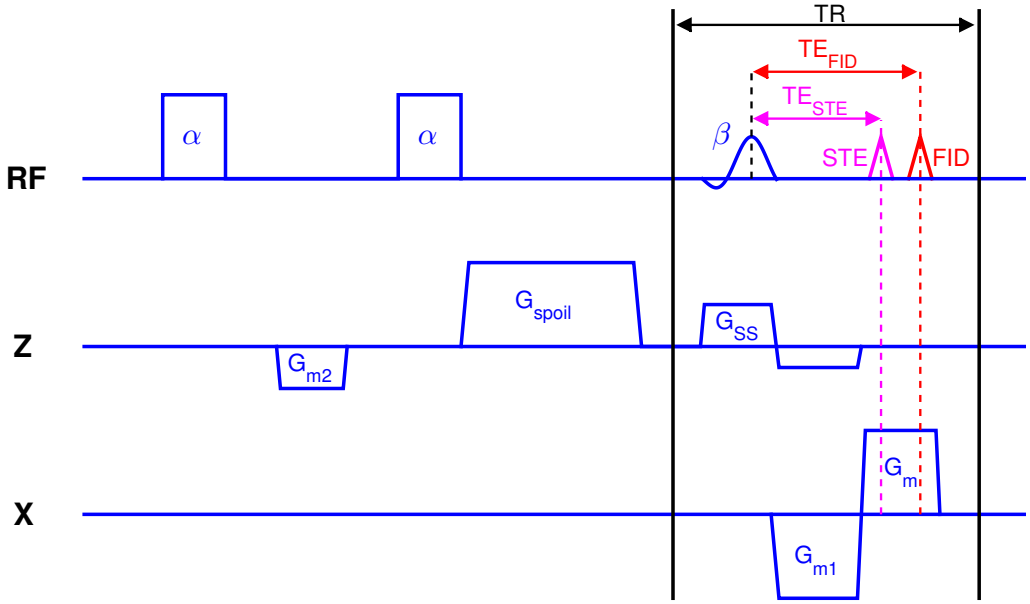

Figure 2.6: Pulse sequence for the DREAM B_1^+ mapping technique. The left side before the vertical black lines shows the STEAM preparation and the right side shows the acquisition of the two echoes: the stimulated echo and the FID.

DREAM works by separating the acquisition into two parts: one part producing a stimulated echo (STE) which is an echo formed from the application of three separate successive RF pulses and the other part producing a free induction decay (FID). The stimulated echo is set up by a magnetisation preparation sequence that encodes the B_1^+ field via a stimulated echo acquisition mode (STEAM) imaging sequence [24]. This is followed by a tailored single shot, low flip angle gradient echo train which encodes the spatial information and produces the FID.

A typical pulse sequence for DREAM is shown in Figure 2.6 where the left side of the sequence before the vertical black line represents the STEAM preparation

and the right side represents the echo acquisitions. The STEAM preparation consists of two non-selective RF pulses with flip angle α played out one after another and then a large z-gradient G_{spoil} to "spoil" any longitudinal magnetisation, effectively removing it from consideration. The imaging sequence on the right hand side then plays out another RF pulse with flip angle β – in Figure 2.6 this is shown as a slice selective pulse with its related gradient G_{SS} but this does not necessarily have to be the case [25]. The β pulse provides the final excitation needed to produce the stimulated echo and also produces the transverse magnetisation necessary for the FID to form.

The gradients G_{m1} and G_{m2} then rephase the magnetisation at the correct timings thus forming the two echoes for DREAM – the ratio of the echoes gives the flip angle of the STEAM sequence [19]. It should be noted that by changing the time between the STEAM preparation pulses and the relevant gradients, the relative timings of the FID and STE can be interchanged [19].

In order to extract the flip angle map, the STEAM prepared and unprepared magnetisation after the STEAM sequence $M_{z,\mathrm{STE}}$ and $M_{z,\mathrm{FID}}$ respectively for a particular spatial location are given by

$$M_{z,\mathrm{STE}} = \frac{1}{2}\sin^2(\alpha)\cdot M_0 \tag{2.19}$$

$$M_{z,\mathrm{FID}} = \cos^2(\alpha)\cdot M_0 \tag{2.20}$$

The gradient echo signals can then be described by:

$$I_{\mathrm{STE}} = \sin(\beta)\, M_{z,\mathrm{STE}} = \frac{1}{2}\sin(\beta)\sin^2(\alpha)\cdot M_0 \tag{2.21}$$

$$I_{\mathrm{FID}} = \sin(\beta)\, M_{z,\mathrm{FID}} = \sin(\beta)\cos^2(\alpha)\cdot M_0. \tag{2.22}$$

Taking the ratio of these two expressions and rearranging them gives the flip angle distribution [19] as a simple relation between the two gradient echo images:

$$\theta_T(\mathbf{r}) = \alpha(\mathbf{r}) = \arctan\sqrt{2\left|\frac{I_{STE}(\mathbf{r})}{I_{FID}(\mathbf{r})}\right|}. \tag{2.23}$$

It is necessary for the k-space encoding for DREAM to be performed starting at the centre of k-space and moving outwards. This is to ensure that the images acquired are not affected by T_1 effects [19].

The accuracy of the DREAM method has been shown to be only slightly diminished relative to other more accurate mapping techniques despite the very short acquisition times [19]. One downside to DREAM is that the stimulated echo produces very little signal in the presence of flow thus making the B_1^+ measurement

incorrect in regions that include flowing substances [26].

As mentioned, there are a large variety of different B_1^+ mapping techniques each with their different merits and shortcomings but SDAM, AFI and DREAM are the three used at various points in this thesis.

One challenge that arises with all B_1^+ mapping techniques is the measurement of the transmit field phase. As an RF coil transmits an EM field which produces the B_1^+ field, some spatially variable phase is imparted onto the magnetisations within the system. The B_1^+ field is then measured through a receiver coil which has a spatially varying sensitivity that also imparts a phase onto the measured signals. Hence it is currently not possible to disentangle the transmit and received phase in the B_1^+ field for anything but a highly idealised scenario [27] and any measured phase ϕ_M is a sum of the two:

$$\phi_M(\mathbf{r}) = \phi_T(\mathbf{r}) + \phi_R(\mathbf{r}) \tag{2.24}$$

where ϕ_T is the actual phase from the transmit field and ϕ_R is the phase from the receiver coil sensitivity.

If the transmit phase of a number of different transmit coils is measured using the same receiver coil for all the measurements, it is then possible to assess the phase of the channels relative to one channel. This will remove dependence on the receive phase although will still not provide full phase information.

Chapter 3

Parallel Transmission & SAR

In order to generate an appropriate B_1 field to be able to perform MRI, RF transmission coils are used, as was briefly mentioned in the previous chapter. At low field strengths, larger volume body coils are generally used which are usually powered by a single RF amplifier. Moving to higher field strengths in MRI (i.e. $B_0 > 1.5$T) has led to increasing need for more complex technologies to control the distribution of the B_1 field.

A large proportion of the the work used for this thesis is dependent upon what is known as parallel transmission (PTx) MRI. This is a technology which is becoming increasingly widely adopted for high field MRI. PTx involves using an array of RF transmitters each powered by an individual RF amplifier to generate the RF field. Each transmitter has a localised RF electromagnetic field thus enabling spatial control of these fields. This allows control over the imaging B_1 field and also the concomitant electric fields. These do not contribute to the imaging itself but do facilitate energy deposition into an imaging subject in what is known as the specific absorption rate (SAR).

This chapter will begin with an overview of transmission coils in general before moving on to PTx arrays and the ways in which they can be used to optimise MRI. Then SAR will be discussed both in general, and with regard to parallel transmission.

3.1 Transmission Coils

As mentioned in Section 2.4, the B_1^+ transmit field in an MRI system is generated by an RF coil, whose operating frequency is the Larmor frequency – the coil must be tuned to this frequency before being used.

To see how this is done, a simple electrical circuit can be considered as shown

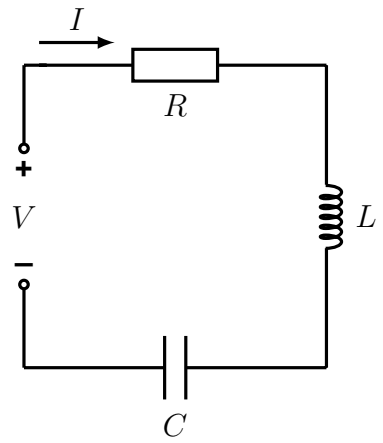

Figure 3.1: Circuit diagram for a basic, resonant electrical circuit. The circuit is driven by a voltage V which drives a current I through a circuit with resistance R, inductance L and capacitance C.

in Figure 3.1, which has some voltage V that produces a current I within a circuit with resistance R, inductance L and capacitance C. Through Kirchoff's voltage law [28] this will produce the following expression

$$V = RI + \frac{j}{\omega C} I - j\omega L I \tag{3.1}$$

where $j = \sqrt{-1}$ and ω is the angular frequency. In an idealised system, $R = 0$ and the current is given by

$$I = V \left(\frac{j}{\omega C} - j\omega L \right)^{-1} \tag{3.2a}$$

$$I = V \left[\frac{jL}{\omega} \left(\frac{1}{LC} - \omega^2 \right) \right]^{-1}. \tag{3.2b}$$

To maximise the current in the circuit for a given voltage, the situation when $I \to \infty$ is considered [29]. It is clear that this condition is achieved when

$$\omega = \omega_r = \frac{1}{\sqrt{LC}} \tag{3.3}$$

where ω_r is the resonant frequency – this is the frequency at which the circuit will resonate most strongly. By adjusting the capacitance and inductance of the circuit, it can be tuned to resonate at different frequencies and of course for MR purposes, this circuit would be analogous to an RF coil and its resonant frequency would be tuned to the Larmor frequency.

In reality, the resistance of a circuit will never be zero which means that the current will be maximal at the operating frequency but not infinite. The resistance also means that energy will be dissipated in the circuit [29] and the quality of its

resonance will be reduced. A measure of the quality can be defined with what is known as the “Q-factor”:

$$Q = 2\pi \frac{\text{Energy stored}}{\text{Energy dissipated per cycle}}. \tag{3.4}$$

For the circuit previously described this can be found from the circuit parameters:

$$Q = \frac{1}{R}\sqrt{\frac{L}{C}}. \tag{3.5}$$

The Q-factor can also be directly measured from the bandwidth $\Delta\omega$ of a resonant circuit’s frequency response as

$$Q = \frac{\omega_r}{\Delta\omega} \tag{3.6}$$

providing an easy way to quantify this in reality. For an RF coil the Q-factor is an important property as it determines how well the coil will perform with regard to signal transmission or reception [29].

An RF coil then is fundamentally a basic resonant circuit and can be described in terms of the circuit description mentioned above. This involves converting a physical coil description into an equivalent circuit based on lumped electrical elements and ideal wires. An example of this is shown in Figure 3.2 where a very basic coil in reality consisting of just a loop of conducting metal and a capacitor on the left side of the figure is described by a set of inductors and a capacitor with a current circulating around the loop in the equivalent circuit on the right.

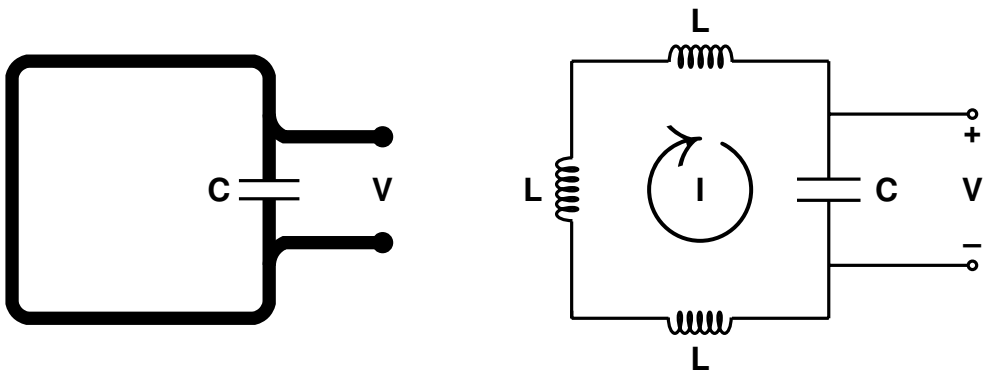

Figure 3.2: A schematic of a physical coil shown on the left which is comprised of a loop made of a conductive strip and a capacitor. Its equivalent circuit in terms of lumped electrical elements is shown on the right.

Practically it may be difficult to calculate or measure the inductances of the equivalent circuit as the RF coil structures become increasingly complex. However it is still useful to use these circuit descriptions to analyse complex structures such as RF coils and they can provide meaningful insights into coil behaviour.

3.1.1 Birdcage Coil

The most commonly used RF coil for MRI in the past few decades has been a volume coil known as a “birdcage coil”. This is usually comprised of two metallic circular rings connected by a series of parallel metallic rungs. An example of one type of birdcage coil is shown in the schematic in Figure 3.3.

Along with the metallic structures, birdcage coils include a set of capacitors placed periodically within the elements. The location of these depends on the type of birdcage coil of which there are primarily three types: lowpass, highpass and bandpass. A lowpass birdcage coil has its capacitors located in the centre of the rungs as depicted in Figure 3.3 which in this example has eight rungs connecting the end rings. A highpass coil has the capacitors located in both the end rings between each rung. A bandpass coil is basically a combination of a lowpass and highpass coil and has two sets of capacitors located both on the rungs and end rings. The main difference between these three types of coil in terms of their behaviour is the distribution of their respective resonances of which there are multiple for birdcage coils.

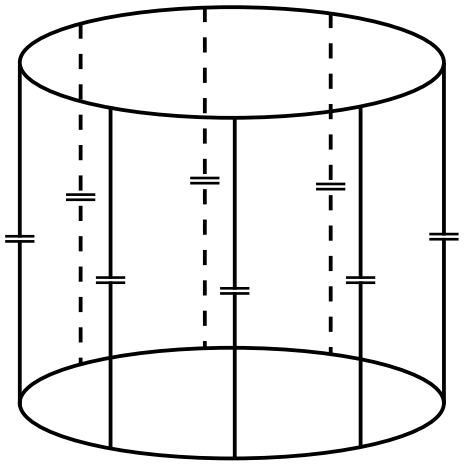

Figure 3.3: Schematic of a lowpass birdcage coil with eight rungs which have capacitors located halfway along them.

Although birdcage coils appear relatively complex in shape, they do form a unified resonant structure and can also be subjected to a lumped element circuit analysis. A section of the equivalent circuit for a bandpass birdcage coil is shown in Figure 3.4 [29] with the metallic components represented by inductors. In the figure the capacitors on the end-rings located between the j^{th} and $(j+1)^{th}$ rungs are represented by C_j. The self-inductance of the sections of end-ring used to connect the capacitors C_j are denoted by $L_{j,j}$. The capacitors located on the rungs are denoted by C'_j and $M_{j,j}$ represents the self-inductance of the j^{th} rung. I_j represents the current in the loop formed by each set of conductors and lumped

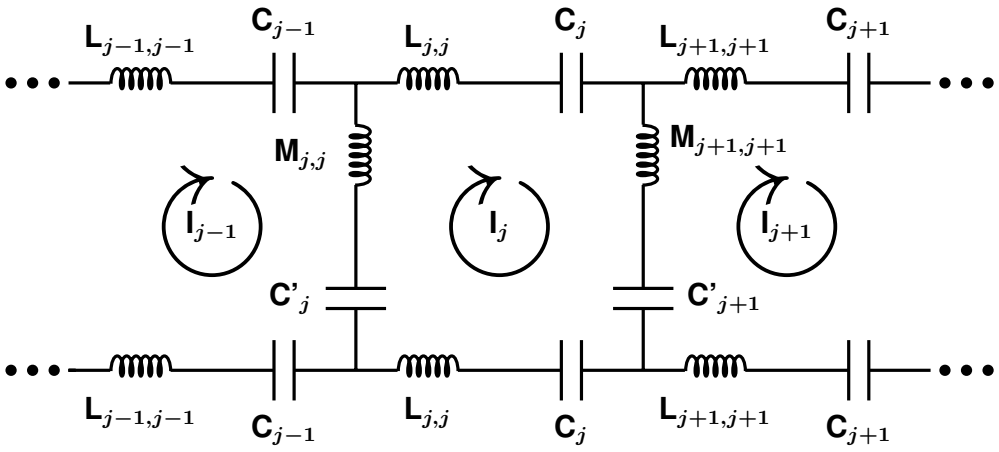

Figure 3.4: Equivalent circuit diagram shown for a section of a bandpass birdcage coil.

elements. All mutual inductances between sets of conductors are ignored in this analysis and it is assumed by symmetry that ($C_1 = C_2 = \cdots = C$), ($C'_1 = C'_2 = \cdots = C'$), ($L_{1,1} = L_{2,2} = \cdots = L$) and ($M_{1,1} = M_{2,2} = \cdots = M$) [29].

By using Kirchoff's voltage law the following expression for the circuit in the loop comprised of the j^{th} and $(j+1)^{th}$ rungs and the sections of end-rings connecting these can be expressed for a total of N loops as

$$(M - \frac{1}{\omega^2 C'})(I_{j+1} + I_{j-1}) + 2\left(\frac{1}{\omega^2 C} + \frac{1}{\omega^2 C'} - L - M\right) I_j = 0$$
$$j = 1, 2, \ldots, N. \tag{3.7}$$

By assuming that the birdcage coil has cylindrical symmetry, the current in the loops must fulfil the periodic boundary condition $I_{j+N} = I_j$ [29] thus Equation 3.7 must have N independent solutions of the form

$$I_{j,m} = \begin{cases} \cos\left(\dfrac{2\pi m j}{N}\right) & m = 0, 1, 2, \ldots, \dfrac{N}{2} \\ \sin\left(\dfrac{2\pi m j}{N}\right) & m = 1, 2, \ldots, \dfrac{N}{2} - 1 \end{cases} \tag{3.8}$$

where each solution for a given m produces a linearly independent mode of the birdcage. By substituting Equation 3.8 into 3.7 and doing some simple rearrangement, an expression for the resonant frequencies of the modes can be found:

$$\omega_m = \left(\frac{\dfrac{2}{C'}\sin^2\left(\dfrac{\pi m}{N}\right) + \dfrac{1}{C}}{2M\sin^2\left(\dfrac{\pi m}{N}\right) + L}\right)^{1/2} \qquad m = 0, 1, 2, \ldots, \frac{N}{2}. \tag{3.9}$$

In this expression it can be seen that a birdcage is able to produce multiple res-

onances. The resonance of the end-rings occurs for the mode $m = 0$ and for this bandpass coil, it can also be seen that the resonant frequency of that mode is $\omega_0 = \sqrt{LC}$. However the other modes which are more likely to be used as the dominant mode for MRI exhibit a more complicated relationship between the resonant frequency and the electrical properties.

It is also interesting to note for this expression that the equivalent expression for a lowpass and highpass coil can be found by taking the limits $C \to \infty$ and $C' \to \infty$ respectively.

Of course these equations represent highly idealised structures so when constructing or modelling a birdcage coil in reality it is necessary to experiment with the capacitor and inductor values to produce the desired behaviour.

When a birdcage coil is fed with a voltage at a single point, it will generate a linear excitation that produces an oscillating current as defined in Equation 3.8. However as discussed in Chapter 2, only part of this excitation that is circularly polarised in the correct orientation will couple with the NMR process. The other part will not contribute to signal generation.

A birdcage coil can be made very efficient with regard to B_1^+ field generation and signal reception by feeding it at two points, placed 90° apart on the coil and driven with a signal with a relative phase shift of 90° between the two. This will produce a highly efficient circularly polarised quadrature excitation from the two linear modes with the current circulating around the coil during transmission.

As the receive field (i.e. B_1^-) rotates in the opposite orientation relative to the transmit field, the phase shift applied between the two points must be flipped during signal reception. This then ensures a highly uniform B_1 field at all times within the birdcage coil when used in low field MRI.

3.2 High Field MRI

Over time each new generation of MRI scanners has gradually moved to higher B_0 field strengths. The primary motivation for doing so is the potentially quadratic increase in signal; as the signal is proportional to $(B_0)^2$ [1].

However in MRI it is the signal to noise ratio (SNR) that is truly important rather than just the overall signal. Unfortunately this has been shown to scale more linearly with increasing B_0 due to the increased noise from power dissipated in the coil and imaging subject [30]; but even a linear increase is potentially able to produce far better images at high and ultra-high field.

The move to greater field strengths does come with a number of challenges. One of these is the quadratic increase in energy deposition within imaging subjects from the electric fields generated by the RF coil. This deposition is known

as the specific absorption rate (SAR) in units of $\mathrm{W\,kg^{-1}}$. SAR is subject to strict regulatory limits as high levels of SAR can potentially cause high levels of heating within subjects.

Another challenge comes from the imaging itself. At low field MRI (i.e. $B_0 < 1.5\,\mathrm{T}$), the spatial distribution of the B_1^+ field is relatively uniform as the wavelength of the field within the human body is relatively large. However as the field strength is increased, the wavelengths of EM fields in the body decrease until they are on the order of the length of the body hence causing arbitrary regions of low and high B_1 to form.

It can be shown from the EM wave equation [28] that the wavelength of EM waves in dielectric materials is related to the relative permittivity ε_r (permittivity is discussed in more detail in Chapter 4) of that dielectric:

$$\lambda = \frac{c}{f\sqrt{\varepsilon_r(f)}} \tag{3.10}$$

where λ is the EM wavelength in metres, c is the speed of light in a vacuum in $\mathrm{m\,s^{-1}}$ and f is the frequency in Hz. The relative permittivity also varies with frequency. To show how the wavelength in human tissue changes with field strength, the relative permittivities of muscle and fat for frequencies representing B_0 up to 8 T were taken from the ITIS Foundation tissue properties database [31] and used to calculate the resulting EM wavelength. This is plotted in Figure 3.5.

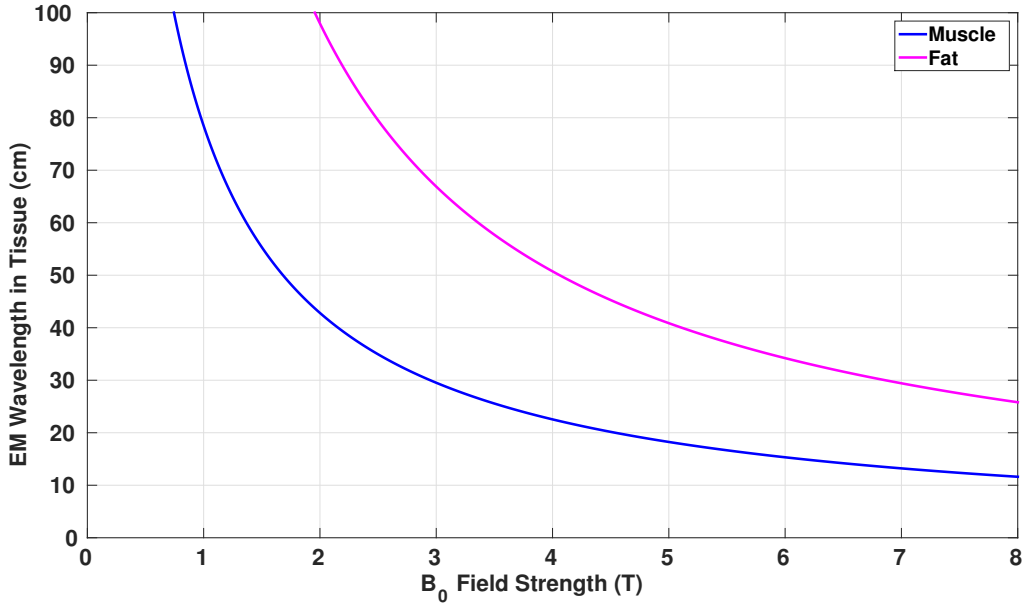

Figure 3.5: Plot showing the B_1 wavelength in human tissue at different B_0 field strengths for human muscle (blue) and fat (magenta).

At 1.5 T the wavelength in muscle is around 55 cm but at 3 T and 7 T this drops down to 30 and 13 cm respectively. These are smaller than the width of

most human bodies so greater inhomogeneity in the B_1^+ field will be seen as expected. This then affects the hardware required at high field. Whereas for low field, a volume birdcage coil driven with a single RF amplifier is able to generate a very uniform B_1^+ field, this is no longer the case for higher field. More novel and advanced coil technologies must be used.

3.3 Parallel Transmission MRI

With high field MRI, it is increasingly common to use parallel transmission (PTx) – for ultra high field, acquiring suitable images is extremely difficult without this. Parallel transmission involves using a series of multiple independent RF amplifiers connected to an array of transmit coils. By applying independent weightings – or even independent waveforms entirely – on each channel this enables a great level of control over the RF electromagnetic fields.

Parallel transmission then provides the tools to be able to mitigate for the challenges encountered in high and ultra high field MRI and enable imaging at these field strengths with improved SNR compared with lower field MRI.

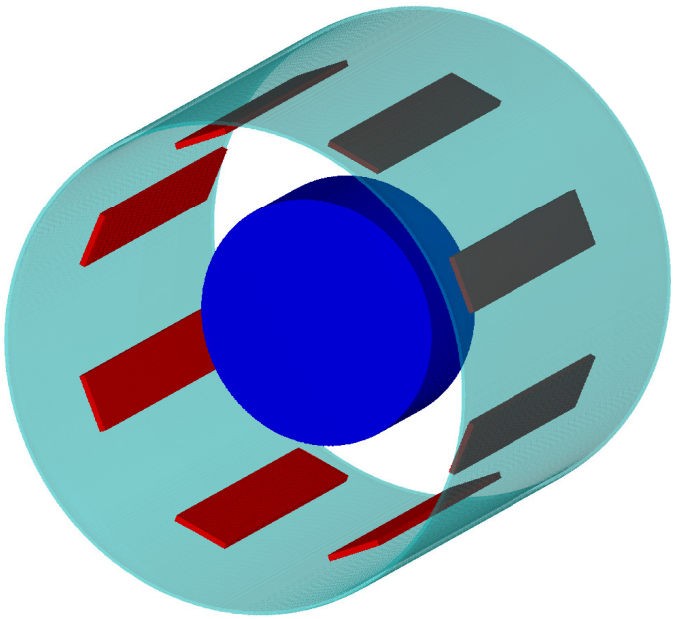

Figure 3.6: An example of an 8-channel PTx array with the array elements shown in red and the RF shield in cyan. A cylindrical oil phantom is also shown in blue located at the coil's isocentre.

3.3.1 Parallel Transmission Arrays

Parallel transmission arrays can be made up of any number of RF coils as their independent elements, and each coil may in theory be any type of transmit coil.

What is important is that each coil element is able to produce a spatially localised RF field when being driven.

Figure 3.6 shows an example schematic of an 8-channel volume PTx array. The eight transmit coil elements are shown in red and the RF shield which they are grounded to and protects the MRI system from RF EM waves is shown in transparent cyan. A cylindrical phantom (shown in blue) is placed at the coil's isocentre.

The B_1^+ measured in an axial slice in such a cylindrical oil phantom (oil is almost entirely non-conductive so will produce a measurable MRI signal but will minimally interact with the RF fields) in a similar physical 8-channel coil array can be seen in Figure 3.7. It is clear that each element of the array does indeed produce a highly localised B_1^+ field as desired.

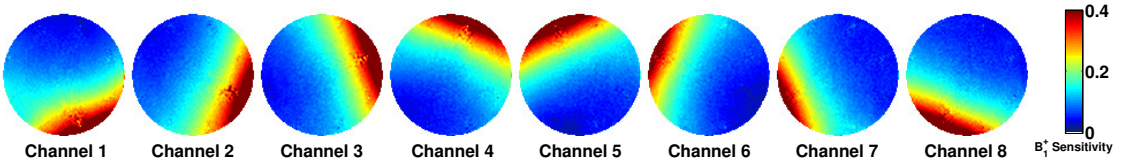

Figure 3.7: A set of B_1^+ maps acquired in an axial slice through a cylindrical oil phantom similar to that depicted in Figure 3.6. The maps are shown for each channel of the array in units relative to the mean amplitude of the total field.

It is also possible to drive a transmit array such that it produces a birdcage-like quadrature mode. To do so, the elements are driven in a phased combination such that a 2π phase evolution over the elements is achieved. This means that for a set of N_c coils, the weighting w_c applied to each coil c must be

$$w_c = e^{\frac{i2\pi(c-1)}{N_c}} \qquad c = 1, 2, \ldots, N_c. \tag{3.11}$$

In the example shown above, the coil elements are made from stripline coils [32]. These are coils made from a strip or sheet of metal through which a linear current is produced. The RF nature of the coil means that the currents run on the edges of the coil element and produce a transverse electromagnetic (TEM) mode [33]. This means that both the electric and magnetic fields are transverse to the direction of current propagation. So in the example shown in Figure 3.6, the current runs along the elements parallel to their long edge and the electromagnetic fields are directed perpendicular to this into the coil and the RF shield.

Stripline TEM coils do suffer from lesser efficiency in terms of field produced relative to input power particularly when compared with a birdcage coil driven in quadrature. This is because the largest EM fields in a stripline are produced between the coil and the RF shield rather than into the imaging region. This does not necessarily affect the overall performance of the coil, simply the power

required to drive them.

In any case, other novel types of PTx arrays with different types of coils are being developed particularly for ultra-high field where the even shorter RF wavelength means that often an array of *surface* coils is used which are directly in contact with the subject. Examples of these include an array of loops [34, 35], novel dipole antennas [36] and combinations of the two [37]. Dipoles themselves are becoming more of an interest at high field as they are able to produce a greater *radiative* component of the EM fields which can increase signal deeper within subjects compared with coils with a lesser radiative component [38].

The challenges with building RF transmit arrays with any type of coil can be substantial. Each element must be able to be driven independently without coupling to other coils. This can be a serious issue to solve as the coils must be highly resonant so are prone to electromagnetically coupling with the other elements. Carefully constructed decoupling networks are used to prevent this.

Furthermore each coil element must of course be tuned to the correct Larmor frequency which is also difficult to achieve in the presence of coupling from other elements.

Because of these challenges, it is generally not possible to analytically describe the EM behaviour of a whole physical RF PTx array with an equivalent circuit model. Therefore electromagnetic simulations are used to assist with the design and analysis of these types of coils.

3.3.2 RF chain

To be able to drive the PTx array with sufficient power and the correct RF signals required to acquire the MRI data, the propagation of power from the amplifiers to the coil elements must be configured correctly. This involves a set of hardware components arranged in what is known as the RF chain – an example of this for an eight-channel PTx system is shown in Figure 3.8 (for a single channel coil, this would be similar but with only one of the lines included).

Signal generation begins at the spectrometer which outputs a very low voltage RF waveform to the RF amplifiers. For modern PTx systems, these are generally digital solid state amplifiers. The amplifiers increase the signal amplitude power to the order of multiple kilowatts at which point this high voltage signal is sent through to the circulators in the RF chain.

The circulators are extremely important components in the RF chain. They are comprised of ferrite materials through which power can only flow one way. Hence they are used to direct power flow through the RF chain. When power is going through them down the RF chain to the coil, they act as passive elements

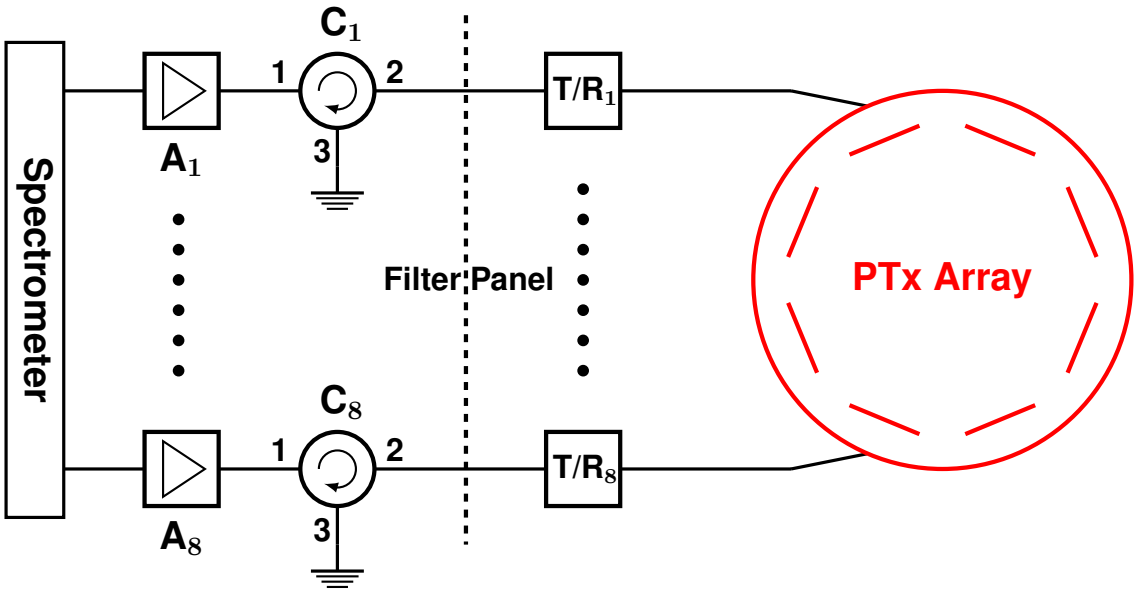

Figure 3.8: RF chain shown for a parallel transmission array. For an 8-channel system the first and last RF lines are shown.

and simply allow the power to pass through. However impedance mismatches between the coil when loaded by a subject and the rest of the transmission line will lead to power reflections (more on this in Chapter 4) travelling back down the RF chain. The circulator must not allow this high power to return to the amplifiers and spectrometer as these components will be damaged. Instead the circulator diverts this power into an RF load; which can essentially be though of as grounding the power. This means that circulators must be highly robust as they have to be able to handle the full high power voltage down the line and any high voltage reflections.

Challenges arise in PTx systems with regard to the relatively high power requirements for driving complex arrays. The fact that a series of high power RF amplifiers must be driven simultaneously means that producing sufficient drive to the channels is often problematic and PTx MRI at high field is often power limited.

The other key components in any RF chain are the transmit/receive (T/R) switches. These ensure that for a coil which is able to transmit RF fields and receive MRI signals, the signals are being directed to the correct pathway at any given time. This is critical for the receiver chain as if any of the electronics used to capture and process the signals on the receiver coil are exposed to the transmit power, they will be destroyed as this power is far greater than that from voltages induced by MRI signals.

3.4 RF Shimming

In a parallel transmission system, the individual channels have a spatially varying transmit sensitivity $S_c(\mathbf{r})$ for each channel c. The total B_1^+ field is produced by a superposition of these sensitivities. By applying a channel dependent complex weighting $w_c(t)$ the overall B_1^+ for a set of N_c channels can be modified over time as a function of the channel sensitivities and weightings:

$$B_1^+(\mathbf{r}, t) = \sum_{c=1}^{N_c} S_c(\mathbf{r}) \cdot w_c(t) \tag{3.12}$$

where $S_c(\mathbf{r})$ are in units of μT and w_c are dimensionless. This overall sensitivity determines the level of B_1 field that will be produced for a given input power and can be measured through B_1^+ mapping.

Once the individual channel sensitivities have been measured, the weightings applied to them can be defined over time such that independent waveforms are played out on each channel. This enables a great deal of control over the RF conditions. It is possible to design these waveforms to achieve the desired RF conditions in what is known as parallel transmission pulse design [39, 40].

A simpler way of utilising PTx is to instead apply a fixed weighting to the transmit channels through time. In this way the time variation is removed and the RF pulse being used does not need to be modified on a channel by channel basis but is simply scaled by the complex weightings. Doing this in an optimised way is known as RF shimming.

RF shimming is performed by setting up an optimisation in which a target homogenous overall sensitivity is aimed for and the different channel weightings, or "shims" as they are commonly known, are found which attempt to achieve the target. This can be generally formulated as

$$\arg\min_{\mathbf{w}}\{\|\mathbf{Sw} - \mathbf{m}_{targ}\|\} \tag{3.13}$$

where $\mathbf{S}$ represents the system matrix of all the coil B_1^+ sensitivities $\mathbf{S}_{B,c}$ of size number of voxels $N \times N_c$, $\mathbf{w}$ is a vector of length N_c comprised of the individual channel weightings and $\mathbf{m}_{targ}$ is a vector of length N of the target sensitivity over the region of interest to be optimised.

Solving this as described using any optimisation method should yield a solution with improved B_1^+ homogeneity provided there are a sufficient number of transmit channels relative to the original level of inhomogeneity. An example of this is shown in Figure 3.9 where the independent channel B_1^+ maps shown in Figure 3.7 are linearly combined giving the overall map on the left of the figure. The

total field with optimal RF shims applied is shown on the right and it is clear that the overall homogeneity has substantially improved and the relative B_1^+ amplitude has on average reached the desired value of 1.

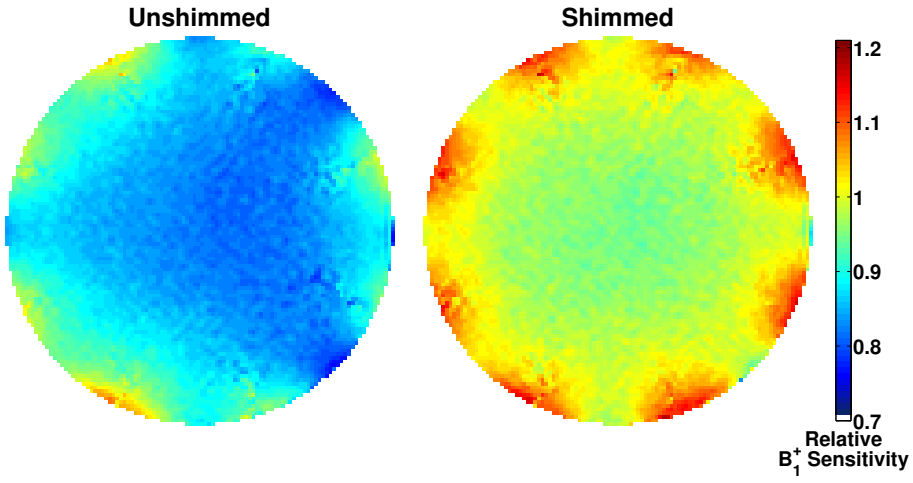

Figure 3.9: The combined unshimmed field produced by the B_1^+ maps shown in Figure 3.7 on the left and with optimised channel weightings applied on the right. The optimised weightings aimed to generate a uniform field.

Simply performing the basic optimisation as described above is likely to yield solutions for which the amplitudes of the RF shims are very high. This would mean very high power is demanded from the RF amplifiers and possibly high power deposition into the subject being imaged. This can be mitigated for by including a regularisation parameter λ that is able to regularise solutions against peak system power – given by $\|w\|^2$. This gives the regularised optimisation as

$$\arg\min_{\mathbf{w}}\{\|\mathbf{Sw} - \mathbf{m}_{targ}\| + \lambda\|\mathbf{w}\|\}. \tag{3.14}$$

This optimisation can then be evaluated for a range of λ which produces a set of solutions that lie on what is known as an "L-curve" [41] due to the shape of the plot when solution error is plotted against peak power. L-curves show the overall trend in the trade-offs in the possible solutions for a given optimisation and method of finding a solution.

3.4.1 Optimisation Methods

The regularised RF shimming optimisation can be solved in a number of ways but the simplest is to perform a least-squares matrix inversion [41] in which the regularisation term is incorporated along with the main minimisation into a single matrix inversion problem. Minimisation of Equation 3.14 is equivalent to the following expression

$$(\mathbf{S} + \lambda\mathbf{I})\mathbf{w} = \mathbf{m}_{targ} \tag{3.15}$$

where **I** represents the identity matrix of size $N_c \times N_c$. The two terms within the brackets in this expression can then be vertically concatenated into one matrix $\mathbf{S}_{reg}$ that incorporates both the coil B_1^+ sensitivities and the regularisation parameter which can be inverted to solve the optimisation problem:

$$\mathbf{S}_{reg}\mathbf{w} = \mathbf{m}_{targ} \tag{3.16a}$$

$$\mathbf{w} = \mathbf{S}_{reg}^{-1}\,\mathbf{m}_{targ}. \tag{3.16b}$$

As matrix $\mathbf{S}_{reg}$ is not usually a square matrix, this matrix inversion cannot be performed directly so either an iterative method must be used or a least-squares solution found as mentioned.

When performing RF shimming to improve B_1^+ homogeneity, it is generally not important for both the magnitude *and* phase of the B_1^+ distribution to be homogenous – only the magnitude is required provided the B_1^+ phase varies smoothly in space [42]. Consequently the RF shimming optimisation can be modified to relax the requirement for uniform phase and thus provide more freedom to find solutions that have better homogeneity in terms of their magnitude. A formulation for doing this was developed and is known as magnitude least-squares (MLS).

Mathematically MLS is a statement of the standard RF shimming formulation where only the magnitude of the first term within the minimisation function is included. One way of solving this is to add a background phase term **z** to the target vector:

$$\arg\min_{\mathbf{w},\mathbf{z}}\{\|\mathbf{S}\mathbf{w} - \mathbf{m}_{targ}\cdot\mathbf{z}\| + \lambda\|\mathbf{w}\|\}. \tag{3.17}$$

The optimisation can then be solved in the same way as for the linear problem only now multiple iterations must be run with the target phase varied until a solution is converged upon – this is known as the *variable exchange method* [43]. The target phase can be initialised with a set of random phases and then after each iteration it is set to the phase produced by the solution at that iteration. Each iteration is then solved as a linear least-squares matrix inversion and as these are convex problems [41], a globally optimal solution of **w** for that iteration is produced. However the overall problem becomes non-linear and is non-convex and is solved by finding the optimal non-uniform background phase **z**. Due to the non-convexity of the MLS formulation, it is possible to find better solutions by setting a different initialisation condition. Therefore a more effective way to operate is to run the optimisation for a set of different randomised starting phases and then select the best solution produced from the different optimisations.

Recently a more sophisticated formulation of the linear problem was outlined by Sbrizzi [44] in which a full set of solutions can be found for a range of regularisation parameters in a single iteration – known as multi-shift conjugate gradient

least-squares (mCGLS). mCGLS can be used for any linear inversion, finding all solutions in one step by decoupling the regularisation term. This is efficient when used inside an MLS type formulation [45] which again has been shown to produce better results than those from standard MLS.

Finally, a more principled way of performing these optimisations is to set up the problem such that optimal solutions are found that lie within predefined operating parameters. This can be achieved using a *constrained* optimisation in which solutions are found which always lie within the predefined constraints [41]. In contrast with regularised optimisations this can ensure that some of the trade-offs in the problem are known from the outset rather than producing a range of solutions and then assessing these trade-offs.

For RF shimming, an obvious constraint to set is the peak system power as is controlled in the regularised problem. It is possible to also incorporate constraints on SAR [46,47] thus potentially enabling control of SAR with parallel transmission as forms a large part of the work described later in this thesis.

An example of a constrained RF shimming problem could be formulated as

$$\begin{aligned} &\arg\min_{\mathbf{w}}\{\|\mathbf{Sw}-\mathbf{m}_{targ}\|\} \\ \text{such that} \quad &\|w\|^2 \leq P_{max} \\ &SAR \leq SAR_{max} \end{aligned} \tag{3.18}$$

where P_{max} and SAR_{max} represent the maximum allowed peak power and some maximum measure of allowed SAR respectively. This optimisation is then aiming for the lowest error in the B_1^+ field distribution subject to the maximum SAR and peak power limits.

It is theoretically possible to extend these constrained optimisations to include any number of constraints however each additional constraint will further reduce the number of possible solutions. Constrained optimisations are also more time intensive computationally compared with regularised optimisations [47] and for any given problem, each active constraint further exacerbates this issue.

3.5 Specific Absorption Rate

The specific absorption rate (SAR) is a measure of the rate of energy deposition per unit mass within a subject produced by the RF fields in units of $\mathrm{W\,kg^{-1}}$. This must be assessed in some way for RF interactions in MRI systems as SAR produced within a subject from RF coils can cause unnoticeable internal heat-

ing[1] [48] and therefore SAR is subject to stringent limits from regulatory bodies such as the FDA [49] and the IEC [50]. The ability to control SAR through constrained optimisations as described would enable safer and improved MRI.

SAR is produced by electric field interactions in the body induced by the RF coil. These electric fields cannot generally be measured directly hence making real time SAR quantification infeasible with current technology. A number of groups are working towards making this possible [51–54] by inferring electrical properties and electric fields from the measured B_1^+ transceive phase however this currently suffers from issues with large errors produced at boundaries between different tissue types [53]. Therefore to be able to quantify SAR, the current gold standard is to use electromagnetic simulations to model the EM interactions within a human subject and use the electric fields and material properties to calculate SAR [4]. These simulations will be discussed in detail in Chapter 4.

SAR can be calculated from the electric fields at any point in space at a given time t as:

$$SAR(\mathbf{r}, t) = \frac{\sigma(\mathbf{r})}{2\rho(\mathbf{r})}|\mathbf{E}(\mathbf{r}, t)|^2 \tag{3.19}$$

where σ is the electrical conductivity of the cell being evaluated in siemens per metre, ρ is the mass density (kg m^{-3}) and $\mathbf{E}$ is the total E-field vector at that location in Vm^{-1}. However this expression just gives the point SAR. In order to comply with regulatory guidelines, local SAR must be integrated over a volume V to give the mass averaged local SAR for a given location as

$$SAR(\mathbf{r}, t) = \frac{1}{V}\int_V \frac{\sigma(\mathbf{r})}{2\rho(\mathbf{r})}|\mathbf{E}(\mathbf{r}, t)|^2 \, dV. \tag{3.20}$$

The averaging is usually performed over 1g of mass for the FDA standard [49] and 10g for the IEC standard [50].

This integration is applied as a volume averaging by encompassing an increasingly larger volume until the required mass for the averaging is reached. As SAR is computed from EM field simulations, it is usually performed on a discretised grid of three dimensional cubes or cells. The averaging calculation is initialised at each cell and the volume for the averaging is grown cubically, encompassing another layer of cells each time. This algorithm is performed as defined by the IEEE [55].

An interpolation must be applied to ensure that the averaged mass does not encompass a volume that is much larger than required [56]. This is performed by

[1] It is technically possible to measure the level of heating using a technique known as MR thermometry however this is extremely time consuming and is prone to large errors if considerable care is not taken when running such experiments. Incorporating this technique into a standardised scanning pipeline would currently be infeasible.

taking the last averaged volume in for each cell that does not exceed the desired mass and considering this the *core* of the cell. The interpolation equation is then formulated as a cubic polynomial which must be solved to determine the fraction of the next layer to be added to the core to make the required mass [56]:

$$cf^3 + ef^2 + sf - k = 0 \tag{3.21}$$

where c is the mass of the corners of the volume, e is the mass of the edges, s is the mass of the sides/faces and k is the mass of the fraction of the layer to be added. For a cell of length Δx the fraction of the layer to be added is given by $f = dx/\Delta x$ where dx is the thickness of this layer [56].

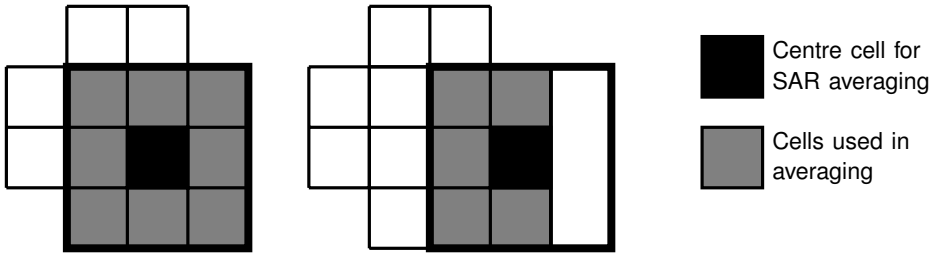

Figure 3.10: A grid of cells for SAR averaging shown. The current cell being assessed is shown in black and its initial averaging volume in grey. The left figure shows a valid cell to be averaged as its initial averaging volume does not extend into air whereas the right figure shows an invalid cell.

Equations 3.20 and 3.21 give the equations required to compute mass averaged SAR through the entirety of an EM simulation. However boundaries in the tissue with air must be treated carefully [55] because if any of the faces of the initial averaging volume extend into air, the cell must be either have a different SAR value applied to it or its volume grown outwards differently in a non-isotropic way. Figure 3.10 shows a two dimensional depiction of two different cells in a body of tissue with a valid initial averaging volume shown on the left and an invalid averaging volume shown on the right. The cell being considered for the SAR averaging is shown in black in the centre and the cells to be used for the mass averaging are shown in grey.

To deal with the invalid cells appropriately, they must be logged as such and any cells that use these invalid cells for averaging must have the highest value of the local SAR in their averaging volume assigned to them [55].

The invalid cells themselves that are not used in the mass averaging volumes of any other cells must then be centred on one face of a new averaging volume and that volume should be grown outwards until the required mass is reached regardless of air filled cells. This is repeated for each face of the invalid cell and the smallest averaging cube that contains the required mass is used for the local

SAR value. Figure 3.11 shows an example of an averaging cube from one face of an invalid cell that is not used in the SAR averaging of any other cells. In this way, it is ensured that local SAR values are not underestimated due to the presence of air.

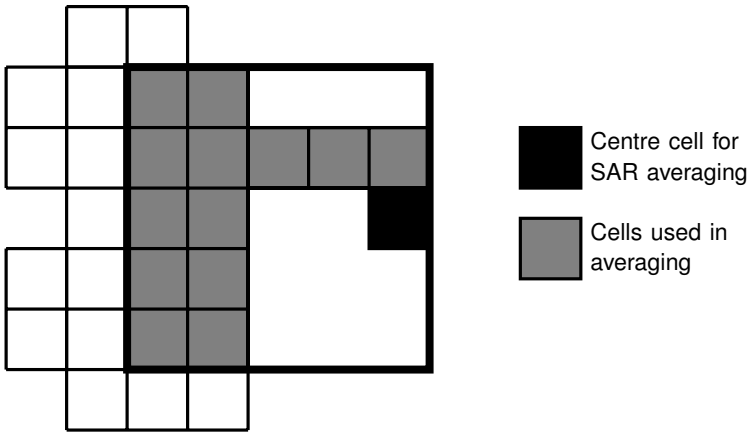

Figure 3.11: An isolated, invalid cell and its isotropically grown averaging volume is shown.

The final mass averaged local SAR values can also be used to assess the global properties of the SAR distribution by evaluating the global SAR – this corresponds to the total absorbed power by the subject. Global SAR can be calculated by multiplying the SAR value at each cell v in a volume of M cells by its cell mass m_v, summing these over the volume and then taking the total mass average over that volume [57]:

$$SAR_{global} = \frac{1}{m_{volume}} \sum_{v=1}^{M} SAR_v \cdot m_v. \tag{3.22}$$

All SAR values should be averaged through time to calculate the SAR over a particular period – either ten seconds or six minutes depending on regulatory guidelines. For an MRI exam using a pulse sequence that repeats every TR, the time average is equal to the average over one TR period. For a given sequence this time averaging is computed using various sequence parameters which are discussed at length in Chapter 6.

SAR in a single channel MRI system simply scales quadratically with the amplitude of the input power to the RF coil. However a parallel transmit system will introduce complex interactions between the RF coils due to the different channel dependent weightings leading to a less direct relationship with the input drives.

Therefore the local mass averaged SAR produced from a set of N_c transmit channels [58] each with dimensionless weighting w_c (as with the B_1^+ field) at a

time t is computed by

$$SAR(\mathbf{r},t) = \frac{1}{V}\int_V \frac{\sigma(\mathbf{r})}{2\rho(\mathbf{r})}\left|\sum_{c=1}^{N_c} E_c(\mathbf{r})\cdot w_c(t)\right|^2 dV \tag{3.23}$$

where E_c are the electric fields produced by each transmit coil.

3.5.1 Q-matrices

For a parallel transmission system, computing SAR over the whole body for different inputs to the channels would be very time consuming as the SAR averaging calculation takes some time and requires a significant amount of computer memory. Fortunately it is possible to formulate the calculation such that the SAR calculation and averaging is performed once and then PTx channel dependent weightings can be applied and the SAR computed for any weighting without having to fully recompute the SAR.

In an identical manner that a complex weighting can be applied to the transmit coils to affect their B_1^+ field, the electric fields of the coils may be treated with the same weighting **w** applied at a point in time t to their sensitivity profile $\mathbf{S}_E$ [59] in units of Vm^{-1}

$$\mathbf{E}(\mathbf{r},t) = \sum_{c=1}^{N_c} \mathbf{S}_{E,c}(\mathbf{r})\cdot w_c(t) = \mathbf{S}_E(\mathbf{r})\cdot\mathbf{w}(t). \tag{3.24}$$

This formulation enables the expression for the local SAR at each location **r** in a system to be described by a fixed inter-coil coupling matrix known as a "Q-matrix" [59] (named from the fact that this represents a *quadratic* form of the field sensitivites [59]) and the SAR values to be evaluated separately for any input **w** [58]. This description of the "SAR sensitivities" was first developed in the context of hyperthermia treatment [60]. The amalgamation of SAR values into a Q-matrix [59] is shown below for a particular location r_i

$$SAR(r_i,t) = \frac{1}{V}\int_V \frac{\sigma(r_i)}{2\rho(r_i)}|\mathbf{E}(r_i,t)|^2 dV \tag{3.25a}$$

$$= \mathbf{w}(t)^*\cdot\frac{1}{V}\int_V \frac{\sigma(r_i)}{2\rho(r_i)}|\mathbf{S}_E{}^*(r_i)\cdot\mathbf{S}_E(r_i)|^2 dV\cdot\mathbf{w}(t) \tag{3.25b}$$

$$= \mathbf{w}(t)^*\cdot\mathbf{Q}(r_i)\cdot\mathbf{w}(t) \tag{3.25c}$$

where * indicates Hermitian transpose. This produces an $N_c\times N_c$ matrix **Q** for each cell in a model which can then have any weighting applied to it through time and the SAR will be computed extremely quickly. It can be seen that the mass averaging is incorporated into the calculation through the volume integrals and

these are performed outside of the RF weightings hence the Q-matrix computation need only be performed once for each model and then stored in a database to be used when required. If the weightings are defined over a period of time as channel dependent pulse waveforms, the resultant SAR values must be averaged over the RF pulses used. Of course as stated before, this work will mainly focus on RF shimming so the time dependence of the weightings disappears and the resultant SAR values are simply averaged over the pulse sequence TR.

The system of Q-matrices can be used to assess global SAR in a similar way by creating a single global Q-matrix averaged over the whole model in the same way as for the local SAR:

$$SAR_{global} = \frac{1}{m_{volume}} \sum_{v=1}^{M} \mathbf{w}^* \cdot \mathbf{Q}_v \cdot \mathbf{w} \cdot m_v \tag{3.26a}$$

$$= \mathbf{w}^* \cdot \mathbf{Q}_{global} \cdot \mathbf{w}. \tag{3.26b}$$

The set of local Q-matrices and any global Q-matrices then enable the full assessment of SAR for a PTx system. The maximum possible SAR for any feasible input of complex channel drives can be calculated from the maximum eigenvalues of the Q-matrices [61]. As the Q-matrices are by construction positive semi-definite, all their eigenvalues are real, positive values and the maximum SAR will be produced when an input shim fully aligns with the eigenvector that yields the maximum eigenvalue.

3.5.2 Voxel Models

To evaluate SAR in simulations for human subjects, digital models of MRI subjects must be used. These are often produced from high resolution, whole body MRI or X-ray computed tomography (CT) scans which are manually segmented into different tissue types. Conventionally these are produced directly from the voxels acquired by the imaging data into voxel models and a number of these that represent different sexes, ages and body types [62,63] are available from different research groups or organisations.

The challenge with using these models for SAR quantification is that a given model will not necessarily match a particular subject. This is an open problem in the MRI community and a number of approaches to resolve this have been looked into such as individualised voxel models produced from a quick whole body scan and automatic segmentation [4]; or produced from non-rigid warping of voxel models to match a given subject [64]. Individualised models suffer from it not being possible to run a full EM SAR simulation during the examination period after having produced the model as these simulations can often take several days

to complete.

Voxel models are discretely segmented into around 30-100 different tissue types representing different organs or structures within the body. To create the individualised models in Reference [4] the imaging data was automatically segmented into just fat, water and muscle and this was shown to produce little difference compared with including all tissue types.

Instead of voxel models, computer aided design (CAD) human body models are also being used for EM simulations [48, 65]. Whilst these are far more challenging to produce, they offer the advantage over voxel models in that they are not initially wholly descretised as they are represented by a set of points and vectors. This enables them to be voxelised to any resolution when required.

3.5.3 Virtual Observation Points

For SAR values calculated in a voxel model a key issue is that there will be around 10^6–10^8 cells making up the body (depending on the model and its spatial resolution) which means there must exist an equal number of Q-matrices. For computing any global SAR, this is not a problem as these matrices are averaged into a single matrix before any computations must be done so evaluating this is fast. However for localised SAR it is necessary to evaluate the SAR values in *all* the cells for a given input and then compute the maximum value out of all of these. Assessing all Q-matrices in the body of a voxel model before producing a result makes this time consuming and computationally expensive; particularly if the maximum local SAR is required for an optimisation problem.

Consequently a method has been developed [57, 66] which effectively compresses the SAR model and substantially reduces the total number of Q-matrices. This converts the full set of Q-matrices into a smaller set of matrices known as virtual observation points (VOPs) [66]. Each VOP will then represent a large number of Q-matrices in any calculation of local SAR.

The fundamental principle behind VOPs lies in the fact that for any given input to the set of Q-matrices, a subset of cells will always 'dominate' the others implying that the SAR in those cells is always higher than a neighbouring subset. Hence it is sufficient to identify these dominant cells and use these to construct a matrix for which its SAR can be evaluated instead of all the matrices in the subset – this matrix is then a single VOP. As it is only the value of the maximum local SAR that is important, evaluating the highest SAR in a group for a given input is sufficient.

Provided any input $\mathbf{w}$ is normalised to $\|\mathbf{w}\| = 1$, the SAR values produced by the set of VOPs $\mathbf{V}$ will be constrained in their overestimation by a factor ϵ such

that:

$$(\max\{\mathbf{w}^*\mathbf{Q}_v\mathbf{w}\} + \epsilon) \geq \max\{\mathbf{w}^*\mathbf{V}_j\mathbf{w}\} \geq \max\{\mathbf{w}^*\mathbf{Q}_v\mathbf{w}\} \tag{3.27}$$

for $j = \{1, \ldots, L\}$ where there exists L VOPs representing M Q-matrices in a set Ω such that $v = \{1, \ldots, M\}$. The overestimation factor ϵ means that the maximum SAR predicted by the VOPs will usually be slightly larger than that calculated from all the Q-matrices subject to this overestimate constraint. However, the greatly reduced size of the set of VOPs compared with the set of Q-matrices means that the computation is much faster. Also, crucially the SAR estimate from the VOPs will never be *underestimated* which would present a concern from a safety perspective. The value of ϵ determines the number of VOPs for a given SAR model – a larger overestimation factor yields fewer VOPs and a smaller, more accurate overestimation factor yields a greater number of VOPs.

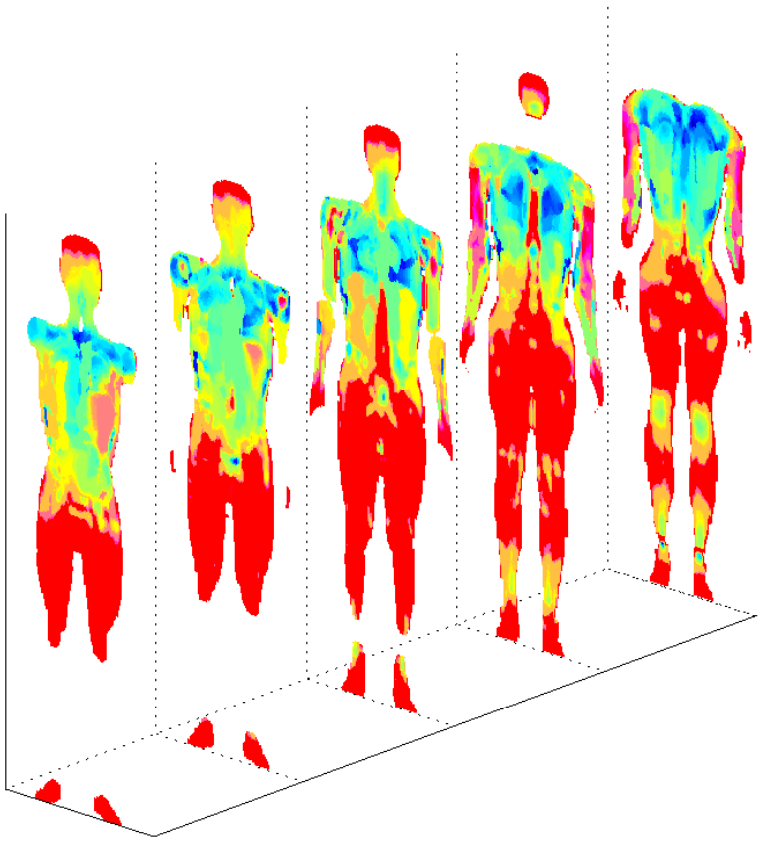

Figure 3.12: Location of clusters dominated by VOPs in voxel model shown for several coronal slices. Each colour represents a set of locations characterised by a single VOP.

To produce the VOPs, the set of Q-matrices in Ω must be clustered by iterating the following process:

1. Select a core matrix $\mathbf{A}^*$
2. Collect matrices mathematically similar to $\mathbf{A}^*$ in a cluster according to their eigenvalues

3. Determine a VOP for this cluster by finding a minimal solution to the overestimation

The algorithm to perform this clustering as described by Eichfelder and Gerbhardt is given in Appendix A, along with further details regarding the mathematical properties of VOPs.

An example of the spatial distribution of VOPs produced in a voxel model which was heart centred within an 8-channel PTx array is shown in Figure 3.12. The figure depicts a number of coronal slices through the voxel model and the regions dominated by each VOP (of which there were 3700 produced from 3.9×10^6 Q-matrices) are shown by a separate colour. It can be seen that a large region of the body located further away from the coil is dominated by a single VOP meaning that for an input to the system where the maximum local SAR would lie in the red region, the actual value of the SAR will be roughly computed by a single VOP matrix.

Chapter 4

RF Modelling

In order to assess the behaviour of the electromagnetic (EM) fields in an MRI system, it is necessary to perform simulations. In this chapter the mathematics behind these simulations and their methodology will be discussed. This will begin with a mathematical description of descretised equations required to simulate EM fields which will then move on to transmission line theory. The final sections of this chapter will discuss the way these simulations are run in practice and a technique that can be used to drastically speed up the characterisation of electrical properties within these EM simulations known as “circuit co-simulation”.

4.1 Maxwell’s Equations

Electromagnetic interactions are almost entirely described by Maxwell’s Equations [28]. These relate electric and magnetic fields within a calculation domain directly to one another. In Equations 4.1-4.4, the full set of Maxwell’s equations is shown with their differential form on the left column and integral form on the right:

$$\nabla \cdot \mathbf{E} = \frac{\rho}{\varepsilon} \qquad \oint_S \mathbf{E} \cdot d\mathbf{S} = \frac{1}{\varepsilon} \iiint \rho \, dV \tag{4.1}$$

$$\nabla \cdot \mathbf{B} = 0 \qquad \oint_S \mathbf{B} \cdot d\mathbf{S} = 0 \tag{4.2}$$

$$\nabla \times \mathbf{E} = -\frac{\partial \mathbf{B}}{\partial t} \qquad \oint_l \mathbf{E} \cdot d\boldsymbol{l} = -\frac{d}{dt} \iint \mathbf{B} \cdot d\mathbf{S} \tag{4.3}$$

$$\nabla \times \mathbf{B} = \mu \left(\mathbf{J} + \varepsilon \frac{\partial \mathbf{E}}{\partial t} \right) \qquad \oint_l \mathbf{B} \cdot d\boldsymbol{l} = \mu \left(\iint \mathbf{J} \cdot d\mathbf{S} + \varepsilon \frac{d}{dt} \iint \mathbf{E} \cdot d\mathbf{S} \right) \tag{4.4}$$

where $\mathbf{E}(\mathbf{r},t)$ (V m^{-1}) and $\mathbf{B}(\mathbf{r},t)$ (T) represent the electric and magnetic vector fields respectively and $\mathbf{J}(\mathbf{r})$ (A m^{-2}) is the electrical current density.

The material properties $\mu(\mathbf{r})$ (H m^{-1}) and $\varepsilon(\mathbf{r})$ (F m^{-1}) represent the permeability and permittivity of the medium under consideration. Permeability defines the ability of a material to support the production of a magnetic field within itself. Permittivity is then the analogous expression for the electric fields as it is a measure of how easily a material electrically polarises as an electric field is produced within it. $\rho(\mathbf{r})$ (C m^{-3}) represents the density of free charges within the medium.

The operator ∇ performs a spatial derivative over all spatial components as $\nabla = (\partial/\partial x, \partial/\partial y, \partial/\partial z)$. When this is applied as a dot product with a vector field, the resulting expression describes the divergence of the vector field i.e. the spatial directionality of the vector field relative to its sources and sinks. When ∇ is applied as a cross product with a vector field, the product yields the curl of that field i.e. a measure of the circulation of the vectors within it. The integral operator $\oint$ represents an integral over a closed geometric space – in this case this will either be over a loop l or a surface **S**.

Solving Maxwell's equations for a simple, symmetric, well defined problem is straightforward and full analytical solutions can even be found for some specific cases. However for more complex situations, the equations quickly become non-analytical and even intractable in their conventional form. It is then necessary to solve these using numerical techniques.

Doing so involves reformulating Maxwell's equations into a discrete set of equations in space and time that can be updated iteratively until the desired solution is realised. The spatial discretisation means that the problem to be solved must be performed on a two or three dimensional spatial grid which is created by taking into account the materials and objects to be included in the simulation.

There are a number of methods that can be used to numerically solve Maxwell's equations including the Finite Element Method [67] and the Method of Moments [68]. However the most commonly used method is Finite-Difference Time-Domain (FDTD) which was first formulated by Yee in 1966 [69]. This works by dividing the spatial domain into a pair of identical mesh grids with one offset from the other. One grid is used for calculating the electric fields, and the other is used for the magnetic fields. The grid is then iteratively updated in time using discretised versions of the differential form of Maxwell's equations until an appropriate solution is converged upon.

The use of FDTD inspired other methods of numerically solving Maxwell's equations and in the early 1980's, a method for solving EM problems using the *integral* form of Maxwell's equations was developed by Weiland [70]. This is now known as the Finite Integral Technique (FIT) and is the calculation that was used for all of the EM simulations present in this thesis – it will now be discussed in detail.

4.2 Finite Integration Technique

To formulate the Finite Integration Technique, the spatial calculation domain must first be defined. In this discussion this can be considered by creating a Cartesian grid **G** that discretises the spatial domain into a set of cubic cells [71]. On each cell it is possible to perform integral calculations in a straightforward manner on the edges of the cells, and over their surfaces as required by the integral form of Maxwell's equations.

This can begin by considering a single electric voltage potential e_i across a line l_i which is calculated from the electric field on l_i by

$$e_i = \int_{l_i} \mathbf{E} \cdot d\boldsymbol{l}. \tag{4.5}$$

Here l_i represents an unclosed line in space which is clearly analogous to the edges of a cube. By computing this integral over the four edges on one side of a cubic cell, the voltages will enclose the surface of that side thus forming a closed path which can be evaluated as a closed path integral.

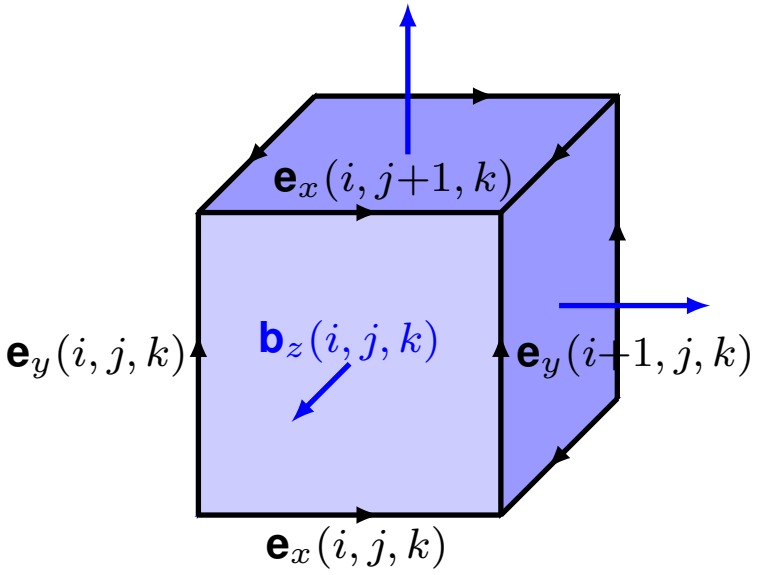

Figure 4.1: Single cell within grid **G**. The cell face at location (i,j,k) has its electrical edge voltages e_i indicated along with their corresponding magnetic fluxes b_i through the surfaces enclosed by the voltages.

Figure 4.1 shows a geometric representation of a single cell in the FIT grid **G** where the voltages expressed on the edges of the cell enclose the surfaces on the sides of the cell which produce a magnetic flux through that surface. A set of indices $\{i, j, k\}$ define the spatial location of the cell edges and surfaces within the overall calculation grid.

For the surface explicitly shown in Figure 4.1, the third Maxwell equation 4.3 (i.e. Faraday's Law) can be used to directly relate the electric voltages and the corresponding magnetic flux b from the magnetic field at location (i, j, k) as

$$e_x(i,j,k) + e_y(i+1,j,k) - e_x(i,j+1,k) - e_y(i,j,z) = -\frac{d}{dt} b_z(i,j,k) \tag{4.6}$$

where the individual components for each voltage and flux produced by the corresponding electric and magnetic fields are formally defined by

$$e_x(i,j,k) = \int_{(x_i,y_j,z_k)}^{(x_i+1,y_j,z_k)} \mathbf{E} \cdot d\boldsymbol{l} \quad \text{and} \quad b_z(i,j,k) = \iint_{S_z(i,j,k)} \mathbf{B} \cdot d\mathbf{S} \tag{4.7}$$

where S_z represents the cell surface on the indicated side of the cell.

Equation 4.6 must be generalised over the whole spatial domain in **G** for all of the cells contained within it. This is done by introducing a matrix **C** which only contains geometrical relations between the edges that lie on grid **G** [72] with regard to their orientation for each surface. Consequently the entries of **C** are solely comprised of $\{-1, 0, 1\}$ where any edges aligned with the path integral direction for the surface being evaluated in one row of the matrix are multiplied by 1, the edges in the opposite direction are multiplied by -1 and all other edges are multiplied by 0. Evidently the matrix **C** is sparse due to the predominance of zero values within it.

This matrix then allows Equation 4.6 to be formulated as a single matrix expression for the entirety of **G**:

$$\mathbf{Ce} = -\frac{d}{dt}\mathbf{b} \tag{4.8}$$

where **e** and **b** represent the electric voltages and magnetic fluxes respectively over the whole grid ordered as column vectors arranged with the x-direction components first, and then the y and z-directions.

In this regard **C** can be considered as a discrete curl operator that acts on **e** as $(\nabla \times \mathbf{e})$ which provides an interesting link back to the differential form of Faraday's Law from the integral form.

The rest of Maxwell's equations must also be incorporated into the FIT formulation. This is achieved by creating a second grid $\tilde{\mathbf{G}}$ within the same spatial domain that is offset from **G** in each orthogonal direction in the Cartesian space, as can be seen in Figure 4.2. The edges and surfaces of grid $\tilde{\mathbf{G}}$ are used to calculate analogous versions of the electric voltage for the magnetic fields, h_i, and electric fluxes d_i. For an arbitrary edge l_i, the magnetic "voltage" h_i is found by

$$h_i = \int_{l_i} \mathbf{H} \cdot d\boldsymbol{l} \tag{4.9}$$

where $\mathbf{H} = \mathbf{B}/\mu$. Then for an arbitrary surface S_i, d_i is found along with the current through that surface j_i by

$$d_i = \int_{S_i} \mathbf{D} \cdot d\mathbf{S} \quad \text{and} \quad j_i = \int_{S_i} \mathbf{J} \cdot d\mathbf{S} \tag{4.10}$$

where $\mathbf{D}$ represents the electric displacement field [28] and is defined as $\mathbf{D} = \varepsilon\mathbf{E}$. Expressions 4.9 and 4.10 can now be used along with the fourth Maxwell equation (i.e. the Maxwell-Ampere equation) under the same arguments used for Faraday's Law to produce its matrix form within $\tilde{\mathbf{G}}$ as

$$\tilde{\mathbf{C}}\mathbf{h} = \frac{d}{dt}\mathbf{d} + \mathbf{j} \tag{4.11}$$

where $\tilde{\mathbf{C}}$ operates in $\tilde{\mathbf{G}}$ in the same way that $\mathbf{C}$ does in $\mathbf{G}$.

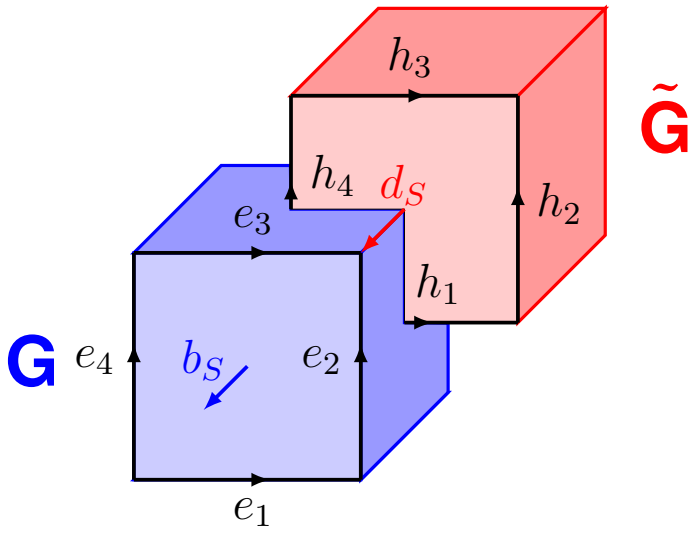

Figure 4.2: Dual grids $\mathbf{G}$ and $\tilde{\mathbf{G}}$ shown for a set of paired cells with the relevant magnetic and electric voltages and fluxes indicated on the edges and surfaces of the cells.

The two remaining Maxwell's equations (Equations 4.1 and 4.2) relate solely to the electric and magnetic fluxes through a surface. In order to incorporate these into the FIT formalism, a set of matrices $\mathbf{S}$ and $\tilde{\mathbf{S}}$ must be defined that operate in the grids $\mathbf{G}$ and $\tilde{\mathbf{G}}$ respectively. These matrices contain information regarding the directions of fluxes through a surface and their entries are made up by $\{-1, 1\}$. For a pair of parallel surfaces on a cube within the calculation grids, the fluxes through those surfaces will be given a value of -1 and 1 respectively depending on how they are directed relative to the coordinates of the calculation.

In a similar way to $\mathbf{C}$ and $\tilde{\mathbf{C}}$ representing discrete curl operators, $\mathbf{S}$ and $\tilde{\mathbf{S}}$ can be thought of as discrete divergence operators in Equations 4.13 acting as $\tilde{\nabla} \cdot \mathbf{d}$ and $\nabla \cdot \mathbf{b}$. This can further be shown in that for a given continuous vector

field **V**, the divergence of the curl of that vector field is always equal to zero as $\nabla \cdot (\nabla \times \mathbf{V}) = 0$ [16]; and the same is true for these discretised matrix operators:

$$\mathbf{SC} = 0 \qquad \tilde{\mathbf{S}}\tilde{\mathbf{C}} = 0. \tag{4.12}$$

The full set of discrete equations – known as the "Maxwell grid equations" [71] – can now be given as:

$$\tilde{\mathbf{S}}\mathbf{d} = \mathbf{q} \qquad \mathbf{Sb} = 0 \tag{4.13}$$

$$\mathbf{Ce} = -\frac{d}{dt}\mathbf{b} \qquad \tilde{\mathbf{C}}\mathbf{h} = \frac{d}{dt}\mathbf{d} + \mathbf{j} \tag{4.14}$$

where the elements in **q** are defined by

$$q_i = \iiint_{V_i} \rho \, dV. \tag{4.15}$$

The Maxwell grid equations represent discretised versions of Maxwell's equations with no approximations made in their formulation [71].

To complete the full set of FIT equations, the electric voltages that exist on the edges of cells must also be related to the electric fluxes through the cell surfaces; and the same must occur for the equivalent variables for the magnetic fields. Relations between the two will then link the grids **G** and $\tilde{\mathbf{G}}$. For a particular spatial location, the magnetic flux and magnetic voltage can be approximately related by

$$\frac{\int_{S_i} \mathbf{B} \cdot d\mathbf{S}}{\int_{l_i} \mathbf{H} \cdot d\boldsymbol{l}} \approx M_{\mu,i} \tag{4.16}$$

where $M_{\mu,1}$ represents the magnetic permeability at this spatial location – the approximation in the expression occurs as a result of the material relations as they vary through space over the two calculation grids. A material matrix representing the discrete permeability over the whole spatial domain can be defined as $\mathbf{M}_\mu$.

Using the same arguments for the permittivity and conductivity of the materials in the calculation grid yields matrices $\mathbf{M}_\varepsilon$ and $\mathbf{M}_\sigma$. These matrices then produce the matrix relations between the voltages and fluxes as desired:

$$\mathbf{d} = \mathbf{M}_\varepsilon \mathbf{e} \qquad \mathbf{b} = \mathbf{M}_\mu \mathbf{h} \qquad \mathbf{j} = \mathbf{M}_\sigma \mathbf{e}. \tag{4.17}$$

This final set of relations along with Equations 4.13 and 4.14 represent the full set of spatially discretised Maxwell's equations within the FIT formalism. They allow the computation of electromagnetic fields within a spatial domain for a set of materials located inside the domain whose electrical material properties are

known. However the FIT equations must also be discretised in *time* in order to calculate the full transient EM behaviour.

4.2.1 Time Domain

To be able to perform calculations through time using numerical expressions, update equations must be formed in which each time the equation is evaluated, the solution at the next time point is produced. This iteration can be continued until a suitable solution is converged upon.

For FIT, this is performed using a "leap-frog" regime in which **e** and **b** are computed at times separated by half a time step, Δt. The index m of the time points is defined by

$$t^m = t_0 + m\,\Delta t \qquad m = 0, 1, 2, \ldots \tag{4.18}$$

where t_0 represents the start time. To create the update equations for the two grids, Equations 4.14 are rearranged and central differences are used in place of the time derivatives giving

$$\mathbf{C}\mathbf{e}^{(m+\frac{1}{2})} = -\frac{d}{dt}\mathbf{b}^{(m+\frac{1}{2})} \approx -\frac{\mathbf{b}^{(m+1)} - \mathbf{b}^{(m)}}{\Delta t} \tag{4.19}$$

$$\tilde{\mathbf{C}}\mathbf{h}^{(m+1)} = \frac{d}{dt}\mathbf{d}^{(m+1)} + \mathbf{j}^{(m+1)} \approx \frac{\mathbf{d}^{(m+\frac{3}{2})} - \mathbf{d}^{(m+\frac{1}{2})}}{\Delta t} + \mathbf{j}^{(m+1)}. \tag{4.20}$$

The time step Δt can theoretically be of any duration. Ideally it would be simply the same as the duration of the simulated period. However to ensure accuracy and convergence of the calculation results, Δt must obey the Courant-Friedrichs-Lewy maximum time step condition [73]. This is a necessary condition and states that the simulation will yield incorrect results if the maximum time step is sufficiently long that an EM wave has time to traverse further than the distance across the smallest cell width. This is expressed mathematically as

$$\frac{c\Delta t}{\sqrt{\Delta x^2 \Delta y^2 \Delta z^2}} \leq C_{max} \tag{4.21}$$

where Δx, Δy and Δz are the minimum cell widths of all the cells within the calculation domain in each orthogonal direction. c represents the speed of light in a vacuum and C_{max} is a variable dependent upon the method used to solve the discretised equation – for FIT, this is equal to 1. Therefore the maximum allowed time step is given by

$$\Delta t \leq \frac{\sqrt{\Delta x^2 \Delta y^2 \Delta z^2}}{c}. \tag{4.22}$$

Equations 4.19 and 4.20 can be rearranged and the material matrices in Equations 4.17 used to convert the voltages to just **e** and the fluxes to **b** for convenience to give a form of the final update equations:

$$\mathbf{b}^{(m+1)} = \mathbf{b}^{(m)} - \Delta t\, \mathbf{C}\mathbf{e}^{(m+\frac{1}{2})} \tag{4.23}$$

$$\mathbf{e}^{(m+\frac{3}{2})} = \mathbf{e}^{(m+\frac{1}{2})} + \Delta t\, \mathbf{M}_{\varepsilon}^{-1}(\tilde{\mathbf{C}}\mathbf{M}_{\mu}^{-1}\mathbf{b}^{(m+1)} - j^{(m+1)}. \tag{4.24}$$

Equations 4.23 and 4.24 are the FIT update equations which can be used to calculate the full behaviour of EM fields in the time domain.

4.2.2 EM Boundary Conditions

Once a spatial calculation domain for FIT has been defined in terms of material properties, the FIT calculation is almost ready to be run. However one thing that must be considered is how the limits of the spatial grids **G** and $\tilde{\mathbf{G}}$ are terminated. An inappropriate boundary at these limits will result in reflections of any propagating EM waves back into the computation domain [74] leading to incorrect results from the calculation.

In light of this, it is important to ensure that the limits of the grid are located sufficiently far away from the objects being considered in the calculation. Then the behaviour of the boundary at the limits must be appropriately defined. This can be done in a number of ways but the most effective of these is to use a series of perfectly matched layers (PML) [75]. These define a boundary such that Maxwell's equations are conformed to and no reflections of EM waves at the boundary are produced.

However using PML is very computationally expensive and can greatly increase the overall calculation time so often other boundary conditions are defined which can be similarly effective provided care is taken in setting up the calculation.

As well as assessing the behaviour of the boundary conditions at the grid limits, the behaviour at boundaries within the domain must also be considered when looking at the results produced by an FIT calculation. This is particularly true when modelling RF interactions within human subjects from an RF coil as will be considered later in this thesis.

At a boundary between two dielectric materials, as might be found in a human body, on a point $\mathbf{r}_b$ on that boundary, the electric tangential fields (i.e. the component of the fields *parallel* to the boundary) must be continuous:

$$\mathbf{E}_{1t}(\mathbf{r}_b) = \mathbf{E}_{2t}(\mathbf{r}_b) \tag{4.25}$$

where the subscript 1 indicates the electric field in dielectric medium 1, and sub-

script 2 indicates the same for medium 2. The continuity across the boundary is also true for the normal component (i.e. the component *perpendicular* to the boundary) of the *displacement* fields at the same location:

$$\mathbf{D}_{1n}(\mathbf{r}_b) = \mathbf{D}_{2n}(\mathbf{r}_b). \tag{4.26}$$

Then the normal component of the electric field at the point $\mathbf{r}_b$ on the boundary can be expressed through the permittivities of the dielectric media as:

$$\varepsilon_1 \mathbf{E}_{1n}(\mathbf{r}_b) = \varepsilon_2 \mathbf{E}_{2n}(\mathbf{r}_b). \tag{4.27}$$

As permittivities of dielectrics can vary substantially between different materials, this expression means that the normal component of electric fields at dielectric boundaries can be fairly discontinuous.

Similar expressions can be found for the magnetic field boundary conditions:

$$\mathbf{B}_{1n}(\mathbf{r}_b) = \mathbf{B}_{2n}(\mathbf{r}_b) \tag{4.28a}$$

$$\mathbf{H}_{1t}(\mathbf{r}_b) = \mathbf{H}_{2t}(\mathbf{r}_b) \tag{4.28b}$$

$$\mu_2 \mathbf{B}_{1t}(\mathbf{r}_b) = \mu_1 \mathbf{B}_{2t}(\mathbf{r}_b) \tag{4.28c}$$

only here the normal component of the magnetic field is continuous at the boundary and the tangential component is defined across the boundary using the magnetic permeability of the dielectric media. Relative permeabilities μ/μ_0 for dielectrics are generally $\approx$1 so the tangential magnetic field is still relatively continuous across a boundary. This means that in an EM calculation involving a human model, the magnetic fields within the body of the model should vary smoothly through space whereas the electric fields may be highly discontinuous.

Whilst the discretised Maxwell equations in FIT can describe the electromagnetic behaviour within a simulation, the electrical behaviour of circuits and lumped electrical elements in the simulation cannot be wholly analysed by this. The next section presents a powerful tool for assessing such electrical behaviour know as transmission line theory.

4.3 Transmission Line Theory

Conventional circuit analysis can be used to assess electrical networks in general using equivalent circuits of lumped elements (such as capacitors, resistors, inductors, etc). However when considering high frequency electrical networks, the electrical behaviour of current carrying structures is more accurately described by

a formulation that accounts for the wave like nature of electrical transmission [76]. For structures such as RF coils such a formulation is needed to describe the coils and their behaviour, and link their basic electrical properties to the electromagnetic fields produced [67].

Transmission line theory offers the required framework for describing the wave-like behaviour of high frequency structures. A transmission line by definition is a structure that is capable of carrying alternating currents with frequencies of radio frequency or above. The size of network components in transmission line theory is generally on the order of a fraction of a wavelength to many wavelengths [33] which contrasts with the lumped element description of equivalent circuit descriptions in which components are treated as being point-like with instantaneous electrical connections between them. This means that at any given point in the structure, the voltage and current may have a different magnitude and associated phase compared with another location over the length of the same structure. For RF coils in MRI this is important as the wavelike nature of the electrical elements greatly affects the coils' behaviour and their interactions with loads.

To describe the relevant transmission line theory, a circuit theory based description can first be assessed. In this regard a transmission line can generally be represented by two parallel wires because transmission lines always have at least two conductors if they exhibit a transverse electromagnetic (TEM) behaviour [77]. The equivalent circuit for a transmission line is shown in Figure 4.3.

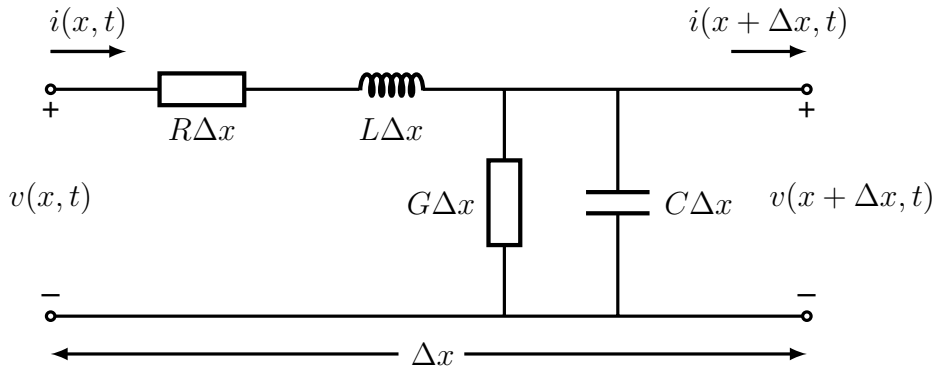

Figure 4.3: Equivalent circuit for a transmission line in which the line is represented by electrical properties per unit length.

The various components in the diagram represent electrical variables per unit length. R represents the series resistance for both conductors per unit length in Ω/m and L represents the series inductance for both conductors per unit length in H/m. G represents the conductance per unit length in S/m of the low resistance pathway – also known as a shunt [78] – produced by the dielectric loss within the medium between the two conductors [33]. The shunt capacitance per unit

length represented by C in units of F/m is produced from the close proximity of the conductors [33].

Kirchoff's voltage and current laws [28] can be used to give:

$$v(x+\Delta x,t)-v(x,t)=-R\,\Delta x\,i(z,t)-L\,\Delta x\,\frac{\partial i(x,t)}{\partial t} \tag{4.29}$$

$$i(x+\Delta x,t)-i(x,t)=-G\,\Delta x\,v(x+\Delta x,t)-C\,\Delta x\,\frac{\partial v(x+\Delta x,t)}{\partial t}. \tag{4.30}$$

Dividing by Δx and taking the limit $\Delta x \to 0$ will produce the time domain transmission line differential equations:

$$\frac{\partial v(x,t)}{\partial x}=-R\,i(x,t)-L\,\frac{\partial i(x,t)}{\partial t} \tag{4.31}$$

$$\frac{\partial i(x,t)}{\partial x}=-G\,v(x,t)-C\,\frac{\partial v(x,t)}{\partial t} \tag{4.32}$$

which are conventionally known as the "Telegrapher's Equations" [79]. If a sinusoidal steady state is assumed, the voltage and current can be represented as cosine based phasors, $V(x,t) = \mathrm{Re}\{V(x)\cdot e^{j\omega t}\}$ and $I(x,t) = \mathrm{Re}\{I(x)\cdot e^{j\omega t}\}$, meaning that the time-dependent behaviour can be represented outside of the differential equations and effectively ignored from this point onwards and the Telegrapher's Equations become

$$\frac{dV(x)}{dx}=-(R+j\omega L)I(x) \tag{4.33}$$

$$\frac{dI(x)}{dx}=-(G+j\omega C)V(x). \tag{4.34}$$

These now represent standard first order differential equations and can be solved simultaneously, producing wave equations for $V(x)$ and $I(x)$:

$$\frac{d^2V(x)}{dx^2}-\gamma^2V(x)=0 \tag{4.35}$$

$$\frac{d^2I(x)}{dx^2}-\gamma^2I(x)=0 \tag{4.36}$$

where the constant γ represents a frequency dependent complex propagation constant as

$$\gamma=\sqrt{(R+j\omega L)(G+j\omega C)}=\alpha+j\beta. \tag{4.37}$$

In expression 4.37, α represents the attenuation constant of the medium, and β represents the wavenumber of the propagating EM wave. A solution to Equations

4.35 and 4.36 can be found with travelling wave solutions given by

$$V(x) = V_0^+ e^{-\gamma x} + V_0^- e^{\gamma x} \tag{4.38}$$

$$I(x) = I_0^+ e^{-\gamma x} + I_0^- e^{\gamma x}. \tag{4.39}$$

In these expressions, propagation of waves in the $+x$ direction is represented by the $e^{-\gamma x}$ and wave propagation in the $-x$ direction is represented by the $e^{\gamma x}$ term. Then by differentiating Equation 4.38 by inserting it into Equation 4.33, the spatially varying amplitude of the current on the transmission line can be equated to the expression in Equation 4.39 and an expression for what is known as the *characteristic impedance*, Z_0 can be defined:

$$Z_0 = \frac{R + j\omega L}{\gamma} = \sqrt{\frac{R + j\omega L}{G + j\omega C}}. \tag{4.40}$$

This characteristic impedance is an important parameter when dealing with transmission lines as it gives the ratio between the voltage and current amplitudes of a single wave propagating along the line in one direction [33]:

$$Z_0 = \frac{V_0^+}{I_0^+} = -\frac{V_0^-}{I_0^-}. \tag{4.41}$$

Generally in practical use, transmission lines performing in high frequency conditions exhibit relatively little loss. This means that simplifications can be made to the expressions by setting the attenuation constant α to zero and therefore the propagation constant is represented by a purely imaginary term as $\gamma = j\beta$. The characteristic impedance Z_0 can then be expressed in terms of the inductance and capacitance per unit length of the transmission line as

$$Z_0 = \sqrt{\frac{L}{C}} \tag{4.42}$$

giving a direct way to measure the characteristic impedance of a given transmission line.

Under these assumptions, a new scenario can be considered when a transmission line is terminated with an arbitrary load of impedance Z_L. Figure 4.4 shows the lumped element equivalent circuit diagram of such a set-up with the load connected across the two conductors at the location $x = 0$.

An incident wave is assumed to assumed to be generated from a source located at $x < 0$ of the form $V_0^+ e^{-j\beta x}$. The impedance at the load ($Z_L \neq Z_0$) must be related to the ratio of the voltage and current at its location. By replacing γ in Equations 4.38 and 4.39 and rearraging those equations purely in terms of the

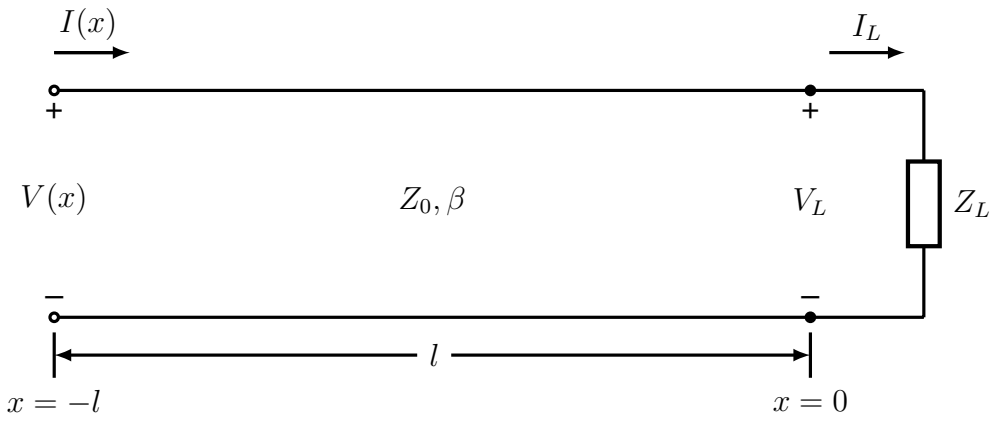

Figure 4.4: Equivalent circuit for a transmission line terminated with an arbitrary load of impedance Z_L.

voltage and characteristic impedance using Equation 4.41, the impedance of the load can be expressed as

$$Z_L = \frac{V(x=0)}{I(x=0)} = \frac{V_0^+ + V_0^-}{V_0^+ - V_0^-} Z_0. \tag{4.43}$$

Rearranging for the voltage waves gives the ratio

$$\frac{V_0^-}{V_0^+} = \frac{Z_L - Z_0}{Z_L + Z_0} = \Gamma \tag{4.44}$$

where Γ represents the voltage reflection coefficient produced by the load which expresses the amplitude of the reflected voltage wave relative to the incident voltage wave amplitude. This allows the total voltage and current waves on the loaded transmission line to be expressed as

$$V(x) = V_0^+(e^{-j\beta x} + \Gamma e^{j\beta x}) \tag{4.45}$$

$$I(x) = \frac{V_0^+}{Z_0}(e^{-j\beta x} - \Gamma e^{j\beta x}). \tag{4.46}$$

These expressions show that the current and voltage on the transmission line are formed of a superposition of an incident and reflected wave [33] as is the case for standing waves [28]. To prevent a reflected wave from forming, it is clear that Γ must be equal to zero. In order to obtain the necessary requirements for this condition to be fulfilled with the load located at $x = 0$, by assessing the impedance at the beginning of the transmission line $x = -l$, the ratio of $V(x = -l)$ and $I(x = -l)$ allows the reflection coefficient to be expressed as

$$\Gamma = \frac{Z_{in} - Z_0}{Z_{in} + Z_0} e^{2\beta l}. \tag{4.47}$$

From this it can be seen that if $Z_{in} = Z_L = Z_0$, the overall impedance is matched and both the input impedance and the load impedance are equal to the characteristic impedance meaning that there will be no reflected waves down the transmission line. The implications of this can be seen by looking at the time averaged power along the line at x [33] as

$$P_{avg} = \frac{1}{2}\mathrm{Re}\{V(x)I(x)^*\} = \frac{1}{2}\frac{|V_0^+|^2}{Z_0}\mathrm{Re}\{1 + \Gamma e^{2j\beta x} - \Gamma^* e^{-2j\beta x} - |\Gamma|^2\} \tag{4.48}$$

$$P_{avg} = \frac{1}{2}\frac{|V_0^+|^2}{Z_0}(1 - |\Gamma|^2). \tag{4.49}$$

It is clear from this expression that to maximise the average power on the transmission line from an incident wave, the reflection coefficient must be zero. So for a transmission line the impedance must be as well matched to its characteristic impedance as possible to ensure maximum power transfer into the system.

4.3.1 Two-port Network

When analysing high frequency electrical networks, it is beneficial to use an analysis based on energy and power [33]. To describe such an analysis, first a simple network is created that is analogous with an unterminated transmission line – this is known as a two-port network.

A two-port network consists of some electrical structure which has two locations through which electrical energy can enter and leave the system – these are the ports. Figure 4.5 depicts such a network.

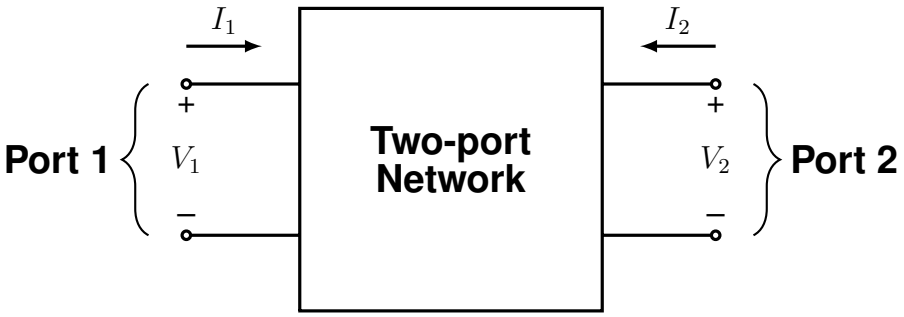

Figure 4.5: Basic schematic for a two-port network.

In a two-port network the structure within it may be basic or it may be complex but the high frequency behaviour of the network can be characterised by assessing the ways in which voltage waves are incident on and reflected from the network via the ports. However there must be no stored energy within the network before any power has been injected through the ports [33].

The relations between the ports can first be characterised by the voltages V_1

and V_2 as the voltages across port 1 and port 2 respectively; and their corresponding currents I_1 and I_2. A 2×2 matrix of the impedances can be constructed by considering the ratio of the voltages and currents at each port when one of the ports is made open circuit (i.e. the current on that port is zero):

$$\begin{bmatrix} V_1 \\ V_2 \end{bmatrix} = \begin{bmatrix} z_{11} & z_{12} \\ z_{21} & z_{22} \end{bmatrix} \begin{bmatrix} I_1 \\ I_2 \end{bmatrix} \tag{4.50}$$

where each entry in the impedance matrix is defined by

$$z_{11} = \left.\frac{V_1}{I_1}\right|_{I_2=0} \qquad z_{12} = \left.\frac{V_1}{I_2}\right|_{I_1=0} \tag{4.51a}$$

$$z_{21} = \left.\frac{V_2}{I_1}\right|_{I_2=0} \qquad z_{22} = \left.\frac{V_2}{I_2}\right|_{I_1=0}. \tag{4.51b}$$

Using similar logic, other parameters to describe this network can also be constructed such as admittance parameters and hybrid parameters [33]. More commonly used parameters to assess the behaviour of these networks – particularly at high frequencies – are scattering parameters.

4.3.2 Scattering Parameters

Scattering parameters (or S-parameters) relate the interactions of power waves at the ports and directly show the degree of waves being accepted into the system and waves being reflected. A single incident power wave a at a port with characteristic impedance Z_0 is expressed [76] as

$$a = \frac{1}{2}\frac{(V + Z_0 I)}{\sqrt{|R_0|}} \tag{4.52}$$

where V and I are the voltage and current on the port and R_0 is equal to the real part of the port's impedance. The reflected wave b from the same port is then

$$b = \frac{1}{2}\frac{(V - Z_0^* I)}{\sqrt{|R_0|}}. \tag{4.53}$$

In light of this, a two-port network can be considered as depicted in Figure 4.6. Here the ports into the network are single entry points characterised by their incident and reflected power waves. The incident and reflected waves at port 1 are given by a_1 and b_1 respectively and a_2 and b_2 for port 2. A 2×2 scattering matrix **S** can be constructed in a similar way as was done for the impedance

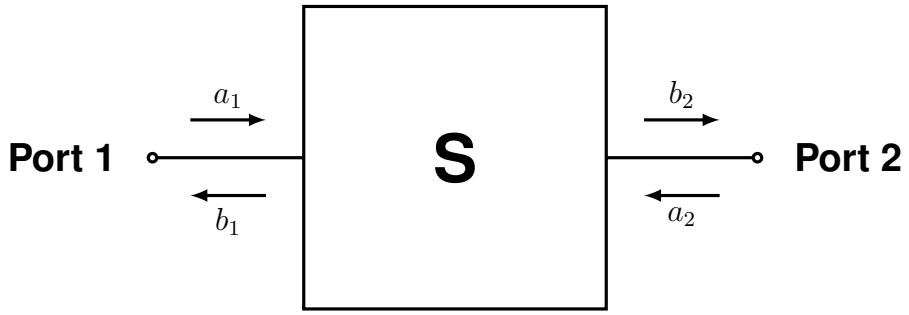

Figure 4.6: Basic schematic for a two-port network in terms of power waves and its S-parameters.

parameters:

$$\begin{bmatrix} b_1 \\ b_2 \end{bmatrix} = \begin{bmatrix} S_{11} & S_{12} \\ S_{21} & S_{22} \end{bmatrix} \begin{bmatrix} a_1 \\ a_2 \end{bmatrix} \tag{4.54}$$

where each entry in **S** is produced by terminating one of the ports with a load equal to the characteristic impedance of the ports. This means that for any incident wave on the open port, the reflected wave at the terminated port will be completely absorbed thus making the possible incident wave at the terminated port equal to zero. Doing this for both ports gives the entries in **S** as:

$$S_{11} = \frac{b_1}{a_1} = \left.\frac{V_1^-}{V_1^+}\right|_{a_2=0} \qquad S_{12} = \frac{b_1}{a_2} = \left.\frac{V_1^-}{V_2^+}\right|_{a_1=0} \tag{4.55a}$$

$$S_{21} = \frac{b_2}{a_1} = \left.\frac{V_2^-}{V_1^+}\right|_{a_2=0} \qquad S_{22} = \frac{b_2}{a_2} = \left.\frac{V_2^-}{V_2^+}\right|_{a_1=0}. \tag{4.55b}$$

These relations enable the behaviour of a two-port network to be evaluated at any frequency. Of course electrical networks are often more complex than this and can contain more than two ports. The S-parameter framework can straightforwardly be generalised for any N-port network giving an S-parameter matrix of size N$\times$N. This can be expressed for an incident wave vector **a** that acts across the N ports and a reflected wave **b** as

$$\mathbf{b} = \mathbf{S} \cdot \mathbf{a} \tag{4.56}$$

thus giving the general definition for an S-parameter matrix. In the S-parameter matrix, the diagonal elements express the degree of matching at each port – for perfectly matched ports these would be zero as there would be no self-reflectance at the port. The off-diagonal elements of the matrix indicate the level of coupling between the ports.

4.4 EM Simulations using FIT

Now that the theory behind the concepts involved in FIT EM simulations has been discussed, the practical aspects as to how they are run can be considered.

Initially the structures within the simulation must be set up. This includes all of the material elements to be included in the simulation. For an RF coil this would primarily mean the metallic components of the coil itself along with any other structures it is comprised from. Then either a phantom or human model could be placed within the coil to simulate RF interactions between the coil and load. It is important to allocate the correct material properties to all the materials within the simulation i.e. permittivity, permeability, conductivity and density.

The next step is to add the electrically active components to the simulation of which there are fundamentally two types. The first is electrical lumped elements which are components in the three dimensional simulation space that can have any capacitance, inductance and resistance applied to them in series or in parallel. This enables standard electrical components to be modelled in the simulation and the lumped elements are connected to other structures via perfect wires.

The other components needed in these simulations allow energy to enter and leave the system are the ports. The ports are modelled in a similar way to other lumped elements but these are where the simulation will be driven with a voltage in order to propagate EM energy into the simulation. They are configured with a certain internal impedance (generally $50\,\Omega$) which then needs to be matched by the structures in the simulation as described previously to maximise power into the system and minimise reflections. The ports are configured to monitor parameters such as voltages or S-parameters at the port in order to assess performance of the structures being simulated.

The calculation grid for the simulation or the *mesh* must then be created. This is one of the most important steps in terms of setting up EM simulations as the distribution of the mesh heavily impacts the accuracy and validity of the simulation. The finer the mesh, generally the more accurate the results. However a very fine mesh will result in long simulation run times and will require vast amounts of computer memory so a trade-off between accuracy and time has to be found. The electrical components within the simulation must be captured by at least a single cell within the mesh but preferably more to ensure accuracy. It is also necessary for the mesh to be small enough to capture the transient behaviour of EM fields so when the wavelength of the EM fields in simulation is decreased, the mesh size must also be reduced.

The simulation can begin once the material matrices and maximum time step have been calculated. At the start time within the simulation, the ports are excited

with some form of voltage signal. For FIT, the simulations are commonly run as broadband simulations [74] and these are excited at the port with a Gaussian excitation pulse which has a broad spectral profile. Two examples of these are shown in Figure 4.7. The top row of the figure shows the pulses as they are played out through time and the bottom row shows their spectral profile i.e. the power spectrum of their computed Fourier transform. Each pulse was defined with an effective bandwidth for the simulation of 150 MHz – the pulse on the left is active from from 0 Hz and the one on the right from 50 MHz. The bandwidth in this case is determined by having at least -40 dB of spectral power, as the signals at this level are still considered to be measurable well above noise from numerical precision errors – this becomes an issue at $<$ -140 dB [80].

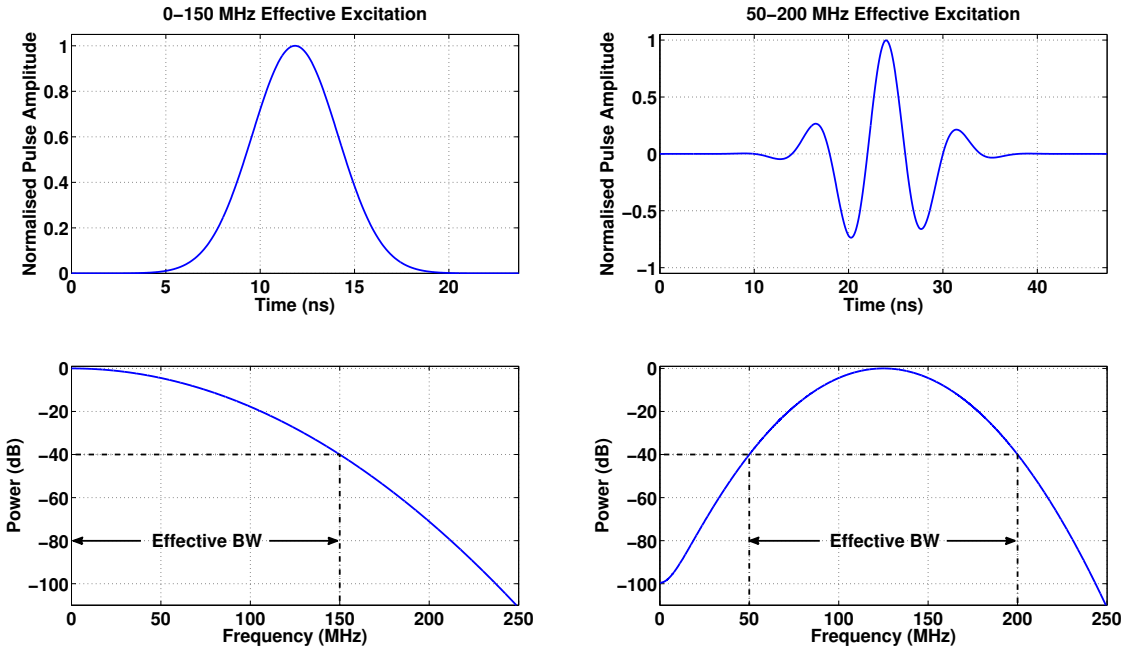

Figure 4.7: Broadband excitation pulses played through time (top row) and their spectral profile (bottom row) shown for a pulse with spectral range 0-150 MHz (left) and 50-200 MHz (right).

For a broadband FIT simulation, the simulation is still run in the time domain but the results are Fourier transformed at the end to produce the frequency dependent results. This presents an efficient way of operating as the spectral response of the system can be produced along with the EM fields for any predefined frequencies – this is achieved using "field monitors" at each frequency of interest.

The convergence condition for FIT broadband simulations must be carefully considered in light of this relationship between the time and frequency domain. The criteria is defined as the point at which the overall energy originally produced by the excitation pulse in the simulation has decayed or converged to a low value. This ensures that the spectral components of all the EM parameters in the simula-

tion have been fully captured. If the energy in the simulation has not fully decayed, information and spectral data will be lost and the results will be inaccurate.

It is also possible to run EM simulations as harmonic simulations in which they are excited at the driving ports with a continuous oscillating voltage at the frequency under consideration. The simulation is run until the current signals on the ports have converged to a steady state.

4.5 Circuit Co-Simulation

EM simulations are clearly an extremely powerful tool for modelling the EM behaviour of any kind of system. However even with the relentless increase of computational power over the past few decades, the simulations continue to take a considerable amount of time to run. As an example, simulating a birdcage coil with two ports loaded with a human voxel model at a resolution of around 3 mm^3 takes around 4-5 days on a modern, fairly powerful computer. This could be substantially sped up by using a graphics processing unit (GPU) to parallelise the calculations involved [81] but this is only likely to provide speed-up factors of up to ten meaning the simulation still requires some time to run and process.

The long run times can make tasks such as configuring RF coils within these simulations extremely problematic. Multiple runs of the full simulation are needed to iterate lumped element properties until their behaviour matches that of the physical device. This issue is then further exacerbated by more complex structures such as parallel transmit arrays – in these, each coil element of the array must be tuned and matched and then all elements must be electrically decoupled from one another. This is achieved by modifying the lumped element properties within the simulation of which there will be many that all have to be tuned to the correct behaviour. These properties are also sensitive to the load within the coil so each time the simulation is modified, it may need to be re-run and retuned. Clearly under this framework, tuning a parallel transmit array presents an almost impossible task.

Consequently another way of modelling such complex systems can be used. This involves a method known as “circuit co-simulation” [82]. Circuit co-simulation creates a tandem calculation in which the EM interactions between all electrical component locations in the simulation are first assessed globally and then these are used to define a computational domain in which any lumped element can be placed in the relevant locations with any electrical properties and the response of the system assessed. In this domain the behaviour of the system can be computed in times on the order of milliseconds thus enabling optimisations to be set up to automate the process of tuning the EM structures.

To perform circuit co-simulation, first a full 3D EM simulation of the structure being modelled must be run but here all of the lumped elements are replaced with driving ports. This simulation will produce fields and S-parameters for all ports in the model. To perform the circuit calculation these S-parameters, and eventually the measured fields, must be related to those expected for the ports that are actually driven when a set of defined impedances are placed across the ports corresponding to lumped elements.

Starting with the standard relation for S-parameters as given in Equation 4.56, this relationship may be subdivided into terms that correspond to the physical driving ports of the system and those that correspond to lumped elements [83]:

$$\begin{bmatrix} \mathbf{b}_{ports} \\ \mathbf{b}_{lumped} \end{bmatrix} = \begin{bmatrix} \mathbf{S}_{np\times np} & \mathbf{S}_{np\times nl} \\ \mathbf{S}_{nlxnp} & \mathbf{S}_{nlxnl} \end{bmatrix} \cdot \begin{bmatrix} \mathbf{a}_{ports} \\ \mathbf{a}_{lumped} \end{bmatrix} \tag{4.57}$$

where there are np driven ports and nl lumped element ports. The vectors are arbitrarily ordered such that the physical ports occupy indices 1 to np (compactly referred to via subscript "*ports*") and the lumped element ports occupy indices $(np + 1)$ to $(np + nl)$ (referred to via subscript "*lumped*"). A further relation for the lumped element ports is defined by considering the interactions of power waves at these ports:

$$\mathbf{a}_{lumped} = \Sigma \cdot \mathbf{b}_{lumped}. \tag{4.58}$$

Here Σ is another scattering matrix, but the definitions of incident and scattered waves are reversed because the reflected wave from each port becomes the incident wave on the lumped element with which the port is terminated [84]. A representation of this is shown in Figure 4.8 where the physical driving ports are denoted by D_i and the lumped elements by LE_i and these are connected to the relevant ports on the scattering matrix **S**.

Unlike **S**, Σ is not obtained from calculations made in the original EM simulation, but instead is produced by transformation of the impedance matrix **Z** [33] of the lumped elements that are to replace the relevant ports:

$$\Sigma = (\sqrt{y}\,\mathbf{Z}\sqrt{y} + \mathbf{I})^{-1}(\sqrt{y}\,\mathbf{Z}\sqrt{y} - \mathbf{I}) \tag{4.59}$$

where **I** is a size nl $\times$ nl identity matrix and y is the reciprocal of the characteristic admittance $1/Z_0$ of each port.

By assuming that the lumped elements are completely isolated from one another, **Z** is then a diagonal matrix. The entries of **Z** in a system in which all lumped elements to be tuned are capacitors (as is commonly the case for RF coils) are

defined as:

$$\mathbf{Z}_{n,n} = R - \frac{j}{\omega C_n} \tag{4.60}$$

where C_n is the value of the n^{th} capacitor with arbitrary numerical index n and R is a small series resistance added to modify the Q-factor of the capacitors in order reflect both losses within the capacitors themselves and losses in the conductors. This approach has been used previously [85, 86] in recognition of the

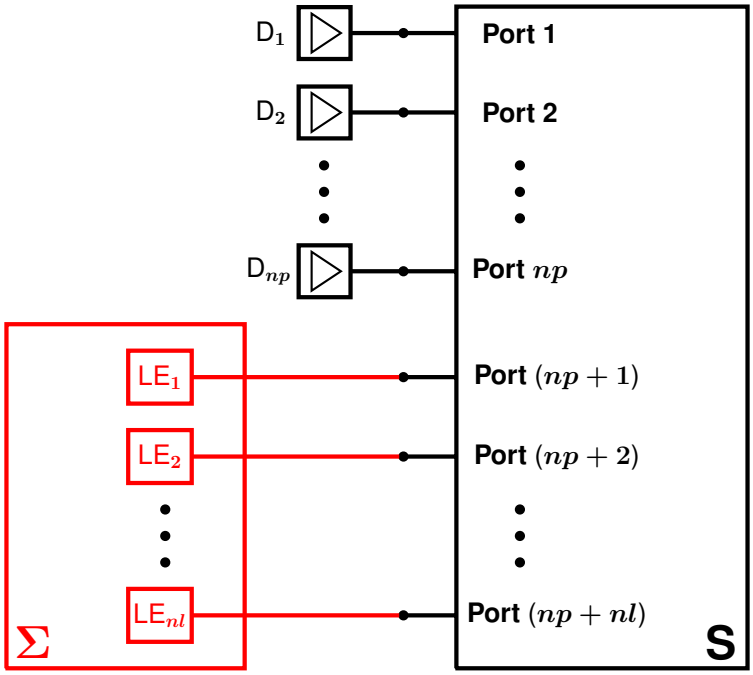

Figure 4.8: Diagram of S-matrix with $(nl + np)$ ports in which ports $(np + 1)$-$(nl + np)$ are terminated with a set of lumped elements in matrix $\mathbf{\Sigma}$.

fact that skin effects acting close to the surface of conductors and other losses are not accurately captured by discretised EM solvers. The value of R can be set empirically by comparing simulation with experimental measurements. For more complex systems or for systems where there are inductors or resistors present as lumped elements, $\mathbf{Z}$ can be reconfigured accordingly.

These relations can be combined to give the $np \times np$ physical S-matrix $\mathbf{S}^{phys}$ that would be measured in reality at the driven ports:

$$\mathbf{S}^{phys} = \mathbf{S}_{np\times np} + [\mathbf{S}_{np\times nl}] \cdot \mathbf{\Sigma} \cdot [\mathbf{I} - \mathbf{S}_{nl\times nl} \cdot \mathbf{\Sigma}]^{-1} \cdot [\mathbf{S}_{nl\times np}]. \tag{4.61}$$

Equations 4.56-4.61 are written for a single frequency; however if a broadband simulation is run, they can be applied to all frequencies in the original range to produce a full frequency response of the system.

The relevant electromagnetic fields can then be generated by first inferring the power waves present at each lumped element port when each driven port is

excited:

$$\mathbf{a}_{lumped} = \Sigma \cdot \left[\mathbf{I} - \mathbf{S}_{nl\times nl} \cdot \Sigma\right]^{-1} \cdot \left[\mathbf{S}_{nl\times np}\right] \cdot \mathbf{a}_{ports}. \tag{4.62}$$

Here $\mathbf{a}_{ports}$ is a vector of length np with unit amplitude for the driving port under consideration and zeros elsewhere. The units here depend on the units of the voltage waves used to excite the ports in the full EM simulation. Once the full vector **a** is constructed it can be used to calculate the combined magnetic and electric fields from the fields generated by every port excitation ($\mathbf{B}_k$ and $\mathbf{E}_k$ for port with index k):

$$\mathbf{B}_{combined} = \sum_{k=1}^{np+nl} \mathbf{B}_k \cdot \mathbf{a}_k \qquad \mathbf{E}_{combined} = \sum_{k=1}^{np+nl} \mathbf{E}_k \cdot \mathbf{a}_k \tag{4.63}$$

This means that all the desired outputs from an EM simulation can be evaluated for any set of lumped element properties within the system in the circuit co-simulation domain. If this is done using a standard programming environment, the results can be near instantaneous. This is also true for the combined EM fields provided enough memory is available or just a small region of the simulation grid is assessed.

Of course it may be thought that the penalty for performing this co-simulation is that the initial full simulation with a greater number of excitation ports takes much longer. However it is often the case that the simulation is in fact quicker to run. This is because the time for each port to be excited is roughly proportional to the Q-factor of the structure being modelled [87]. But when all lumped elements have been replaced with ports, the structure is no longer resonant so each port excitation is completed far more quickly.

One potential downside to circuit co-simulation is a possibility for less accuracy in the produced results. It is much more important in this regime to ensure that the energy in the simulation after each port excitation has sufficiently decayed before the simulation is terminated to ensure accuracy. As the structure is no longer resonant, energy is very quick to leave the system after having been excited into it, so the termination energy threshold should be set to be lower than for a conventional simulation to ensure all the spectral components of the decay are fully captured.

Chapter 5

Full Coil Modelling

Contributions

The findings in the following chapter have been partially discussed in the following publications:

> **A. Beqiri**, J.W. Hand, J.V. Hajnal, and S.J. Malik. Comparison between simulated decoupling regimes for specific absorption rate prediction in parallel transmit MRI. *Magnetic Resonance in Medicine*, November 2014
>
> **A. Beqiri**, J.W. Hand, F. Padormo, J.V. Hajnal, and S.J. Malik. SAR characterisation for parallel transmission MRI – comparison between modelling different decoupling regimes. *Proceedings of ISMRM 2014*

The code used to perform circuit co-simulation as discussed in Section 4.5 is available online at `https://github.com/mriphysics/circuit_cosimulation`.

5.1 Introduction

Computational modelling of RF coils is a challenging and time-intensive area of research. As discussed in Chapter 4, setting up RF electromagnetic simulations requires tuning of many variables including the calculation mesh, location of electrical components, values of electrical lumped elements and numerous other factors. This coupled with the length of time taken to simply run and process these simulations means that the overall simulation pipeline can easily become impractical for some modelling requirements. Therefore simulations are often simplified in various ways [74] to make the pipeline more practical.

Small inaccuracies in the simulation (particularly material properties) mean that if the coil model is constructed using lumped components whose impedance values are taken directly from those in the physical device that is being simulated, the simulated and physical behaviours generally do not match. As a result, lumped element impedances in the model must be altered, typically by adjusting them iteratively. This process is time consuming if full EM field simulations that take several days to run are required at each iteration.

This tuning of these models can be made much more efficient by using circuit co-simulation [82], as discussed in Chapter 4. This enables complex models to be tuned using numerical optimisation, with computation time per iteration on the order of milliseconds rather than days.

Previously parallel transmit coil arrays have been modelled in a simplified way by simulating each element independently in isolation [59,88,89]. By using circuit co-simulation, a complicated PTx array with multiple coil elements and electrical networks can be modelled in full, obviating the need for such simplifications.

In this chapter, the methodology utilised to model an 8-channel parallel transmission body array is discussed beginning with a more simple, symmetric model and moving on to the full coil model. The concept of decoupling PTx array elements using physical measurements of coupling is then discussed which finally leads onto the study of how different decoupling regimes affect the accuracy of SAR predictions.

5.2 Modelling of Parallel Transmit Arrays

Modelling of PTx arrays presents difficulties compared with conventional transmission coils in that there are multiple reactive elements present in the physical coils. These will then electromagnetically couple with one another if there is nothing in place to mitigate and reduce this effect. Consequently some form of electrical decoupling network [90] must be utilised to allow each element to perform independently – for a full model of a coil these decoupling networks must also be included in the simulation.

A practical solution as mentioned previously is to model individual transmit elements independently without including any decoupling networks, leading to a system model with “idealised decoupling” in which all elements but one are detuned and effectively deleted from the transmit array by removing their lumped capacitors.

As this is a simplified approach to the modelling it is important to ascertain if there are any implications for accuracy of the calculations when performing this type of modelling. So in this study, a full, non-idealised model of a PTx array was

created and compared to its corresponding idealised model with regard to SAR estimates produced from the different modelling methodologies.

5.2.1 Eight-Channel Transmit Array

The physical coil to be modelled in simulation was an 8-channel body transmit array as described in Reference [91]. This will be referred to as the Multix body coil (MBC) throughout the remainder of this thesis. In reality the MBC has been installed within a 3 T Philips Achieva MRI scanner in place of its standard birdcage body coil as can be seen in Figure 5.1.

The eight separate elements of the coil are comprised of transverse electromagnetic (TEM) resonators [33] that produce a localised electromagnetic field from a linear current mode on the element. In this case there are two parallel "rungs" that produce the current mode on each element in order to generate the desired response – the rungs are configured in this way because RF currents flow primarily on the edges of the elements.

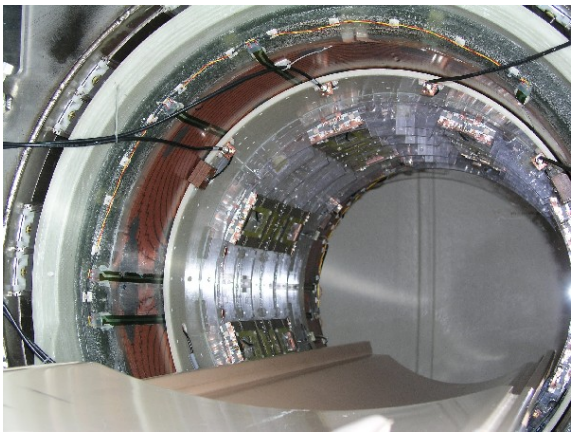

Figure 5.1: 8-channel PTx array installed within the Philips MRI system. The coils elements can be seen going around the inside of the bore.

The elements and RF shield are made of copper and a number of capacitors are located on each element. The elements are grounded to the RF shield and connected to one another by a copper decoupling ring which capacitively decouples the elements from one another.

The equivalent circuit diagram of a single TEM element *n* within the coil [91] is shown in Figure 5.2. The two rungs are represented by a set of inductors

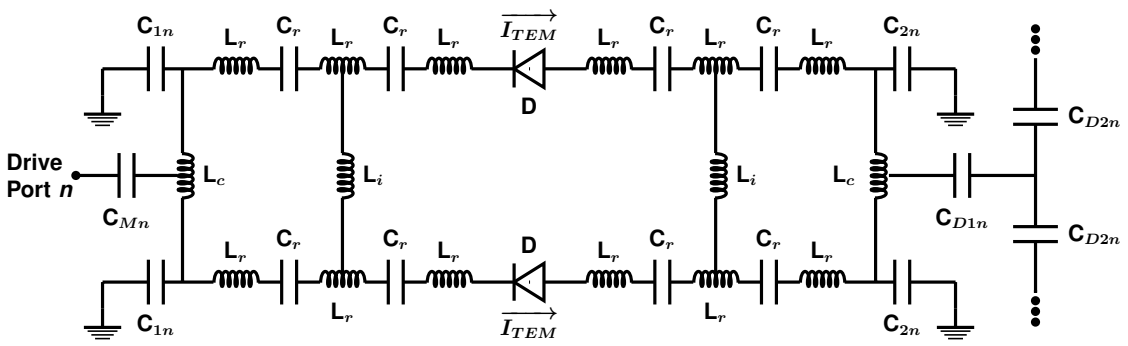

Figure 5.2: Circuit diagram of a single TEM element *n* within the transmit array.

for the pieces of copper, along with the capacitors in series all labelled with the index *r*. The capacitors C_r all have a fixed value of 33 pF in every element of the system. The rungs then grounded to the RF shield via a set of tuning capacitors C_{1n} and C_{2n} used to tune the coil elements to the Larmor frequency ($\sim$128 MHz at 3 T). Each transmit element is driven at one end with another capacitor C_{Mn} placed in series with the drive port to adapt the electrical matching of the element. Inductors L_c representing the copper pieces crossing the elements are used to connect the rungs together and L_i are used to control potential ring currents on the element [91]. The capacitive decoupling network is located on the opposite side of the elements to the side from which they are driven. The decoupling network is comprised of a set of capacitors and a conductive ring that is positioned between the coil elements and the RF shield. Each transmit element is connected to the ring via capacitors D_{1n} and there are a set of capacitors D_{2n} on the ring between elements. The diodes shown on the rungs are used to detune the TEM elements when other RF coils are being used – generally for signal reception.

5.2.2 Single Element Coil Model

Initially a simple model of a single TEM element tuned to the Larmor frequency placed on a large, flat copper ground plane was modelled to assess if the general behaviour of the EM field calculation – run using the time domain Finite Integration Technique of CST Microwave Studio (CST AG, Darmstadt, Germany) – was as expected. The CAD model from the simulation can be seen in Figure 5.3. All

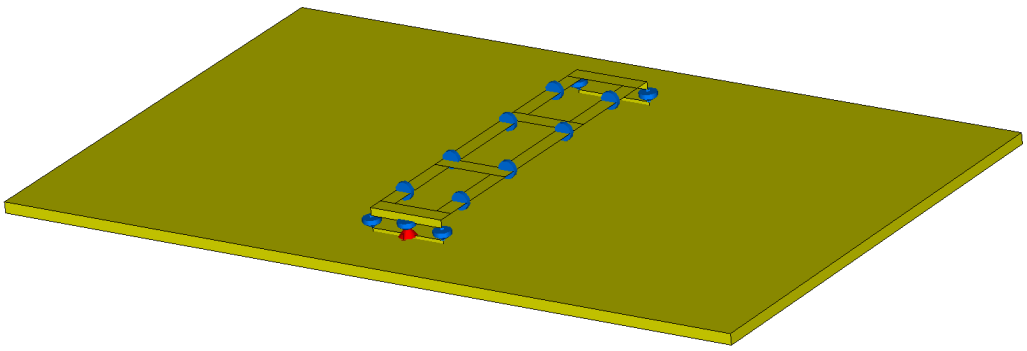

Figure 5.3: CAD model of a single TEM element on a large copper ground plane. Its driving port is shown in red and capacitors are shown in blue. All copper elements are in yellow.

conductive elements were modelled as lossy copper metal with a conductivity of 5.8×10^7 Sm^{-1}. The EM behaviour was assessed by looking at the polarisation ellipses of the transverse electromagnetic fields produced by the simulation. The ellipses were processed in MATLAB (MathWorks, Natick, MA) and they can be calculated for any spatial location in an x-y plane for an EM field **F** (this can be

either the electric or magnetic field **E** or **B** respectively) using the expression

$$x_{ellipse} = \frac{|F_x|}{|F_\perp|}\cos(t+\phi_x) \qquad y_{ellipse} = \frac{|F_y|}{|F_\perp|}\cos(t+\phi_y) \tag{5.1}$$

where $F_\perp$ is the absolute transverse EM field (i.e. $\sqrt{F_x^2 + F_y^2}$), t represents the phase which is calculated from 0 to 2π, and ϕ_x and ϕ_y represent the complex argument of F_x and F_y respectively.

In Figure 5.4 the polarisation ellipses for the electric and magnetic fields are shown for a single axial plane through the TEM element with the logarithm of the transverse fields shown in the heat map in the background. It can be seen that the fields do behave as would be expected with the electric fields diverging away from each rung of the element and the magnetic fields circulating around these rungs. It can also be seen from the ellipses that the polarisation is strongly linear

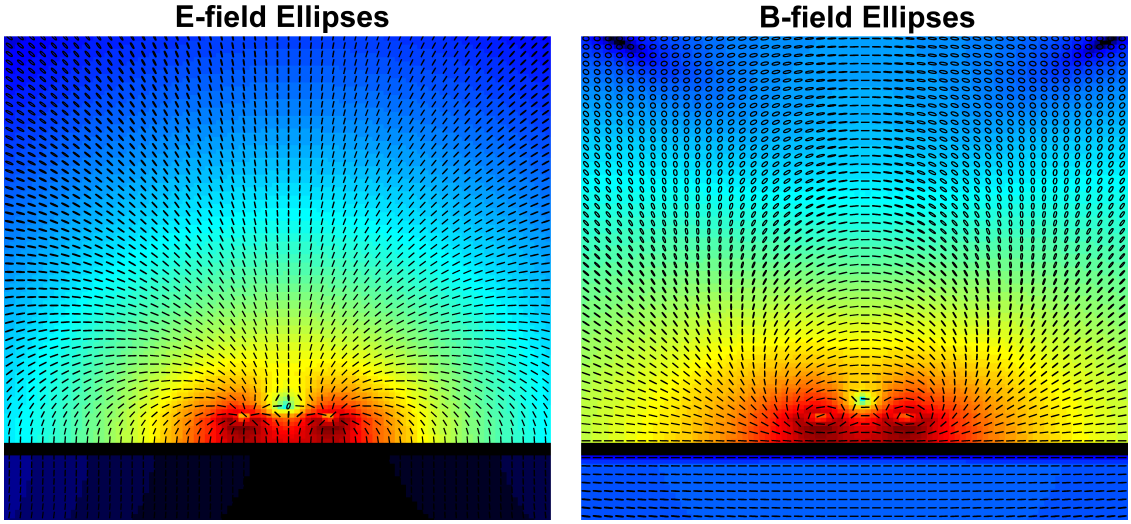

Figure 5.4: Polarisation ellipses are shown for the electric (left) and magnetic (right) fields in an axial plane through the centre of a single TEM element placed on a large ground plane. In the background the heat-map shows the logarithm of the absolute transverse field.

in the region near to the elements with it becoming more circular further way, particularly for the magnetic field. The ellipses representing linear polarisation can be thought of as being representative of field lines for the EM fields.

5.2.3 Building PTx Array Model

The full modelling of the entire transmit array began by placing all eight of the TEM elements on a cylindrical RF shield parallel to one another with a 45° angle between them such that they were equally spaced around the cylinder. A diagram of this is shown in Figure 5.5 which displays a transverse view of the array. To begin with, all eight elements were placed the same distance of 35 mm away

from the RF shield in a circular orientation as shown by the black lines in Figure 5.5 where the RF shield is shown in grey. This symmetric configuration was initially modelled as it was a more straightforward place to start from a simulation perspective; and this was the way in which a basic EM model of the coil was first built when the MBC was originally proposed in Reference [91].

By modelling the entire array with the lumped elements replaced with ports, it was simple to tune, match and decouple the circular array when unloaded using circuit co-simulation with a basic optimisation run the MATLAB `fminsearch` function. The complete symmetry of this configuration means that many of the capacitor values across the different elements are the same so only a small set of variables had to be supplied to the optimisation to find a satisfactory operating point. For an RF coil array it is important to ensure that all channels are well matched as this ensures low power loss – a figure of less than -15 dB is generally considered to be appropriate [32] which correspond to a percentage ratio of the input power of 3.2 %. Coupling between elements should also be less than this.

However the MBC is not arranged in such a symmetric manner in reality – four of the coil elements are displaced to produce a more elliptical arrangement of the elements which better suits the shape of an average human torso. As can be

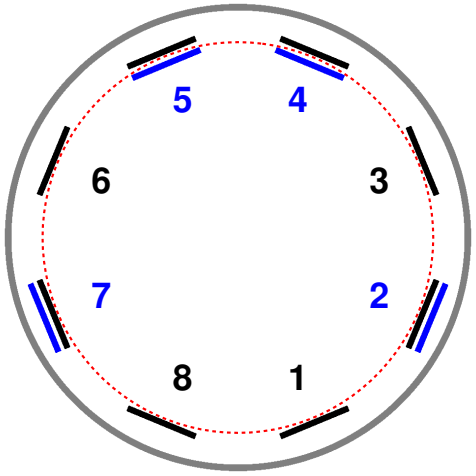

Figure 5.5: The location of the TEM elements and their identifying number within the RF shield (grey) are shown in black for the circular arrangement with the red dotted line indicating the circle they lie on. The coils displaced for the more elliptical arrangement and their new location are shown in blue.

seen in Figure 5.5, coil elements 2 and 7 – which would be located closest to a subjects arms during body imaging – are displaced by 5 mm outwards, closer to the RF shield. Elements 4 and 5 are displaced by 5 mm inwards, away from the RF shield. These positions are highlighted in blue in the figure and the original circle from which they were displaced is shown with a red dotted line. Whilst the displacements in element location are relatively minor, the complexity involved

with modelling the coil is greatly increased. This breaking of the geometric symmetry means that finding correct electrical component values to simulate the coil behaviour will involve many more variables as they will have to be independently tuned for each element. When loading the MBC, its RF interaction with the load will produce behaviour that further deviates from a simplistic situation.

Tuning of the non-symmetric model required a two step optimisation which is discussed in detail later in this chapter in Section 5.3.1. The complexity involved in performing this optimisation process, particularly if circuit co-simulation was not used, means that it is unsurprising that simplifications are often used; such as modelling with idealised decoupling.

5.2.4 Idealised and Active Decoupling

Modelling using idealised decoupling is relatively simple to implement. Each transmit element is modelled in a separate simulation in which all active lumped elements in all other coil elements are removed. An example of this can be seen on the right side of Figure 5.6 in which only the transmit coil element being modelled contains lumped elements.

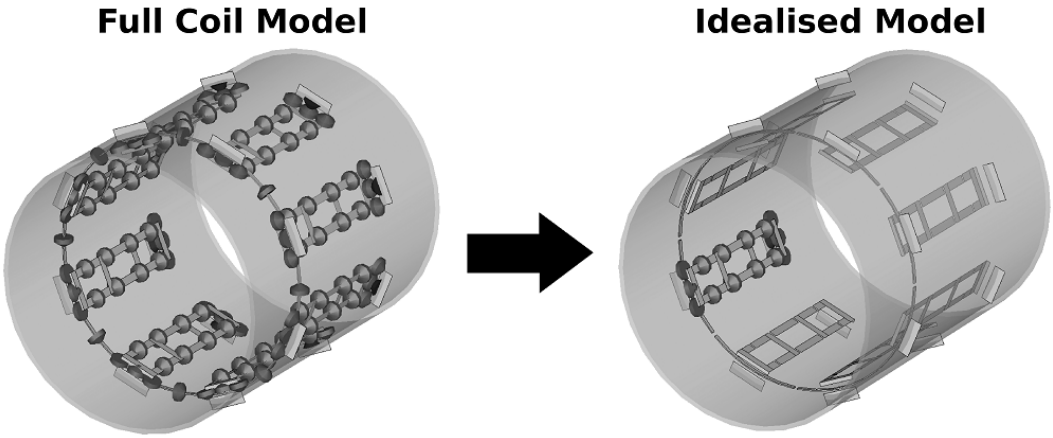

Figure 5.6: Schematic of the 8-channel TEM transmit coil. The ring structure at the closer end of the device is used for improving decoupling. The Full Coil Model (left) and Idealised Coil Model (right) differ in that the former includes all lumped capacitors and the latter excludes all those from channels other than the one under consideration. In practice these capacitors can be removed using circuit co-simulation by setting their associated ports in the Full Coil Model to be open circuit (i.e. by assigning a vanishingly small capacitance [92]).

The ease of modelling with idealised decoupling comes from the fact that each transmission element can be tuned and matched independently. This means that a full EM simulation will be quicker to run and as there are fewer electrical lumped elements present, the number of iterations required to tune the coil element will be small. However with an idealised model, the coupling present in the real sys-

tem is not represented. In order to use these simulations in practice, the model and real device should be reconciled. This can be achieved by estimating the coupling present and applying it to the idealised model, or by adapting the device itself to approximate the idealised situation as closely as possible. The latter is referred to as "active decoupling" [58, 91, 93] and can be done by measuring residual coupling, and then driving linear combinations of transmit channels so as to produce a response emulating the behaviour of the coil if no coupling was present between elements. Current pickup coils have been used for measurement of residual coupling [58], but the method is not limited to this exclusively.

In the 8-channel system discussed in this work, there are a set of current pickup coils present on the transmit elements [93] of the MBC (configured to produce one current measurement per element) that are designed to be used for active decoupling. Coupling is estimated by applying a low voltage RF signal

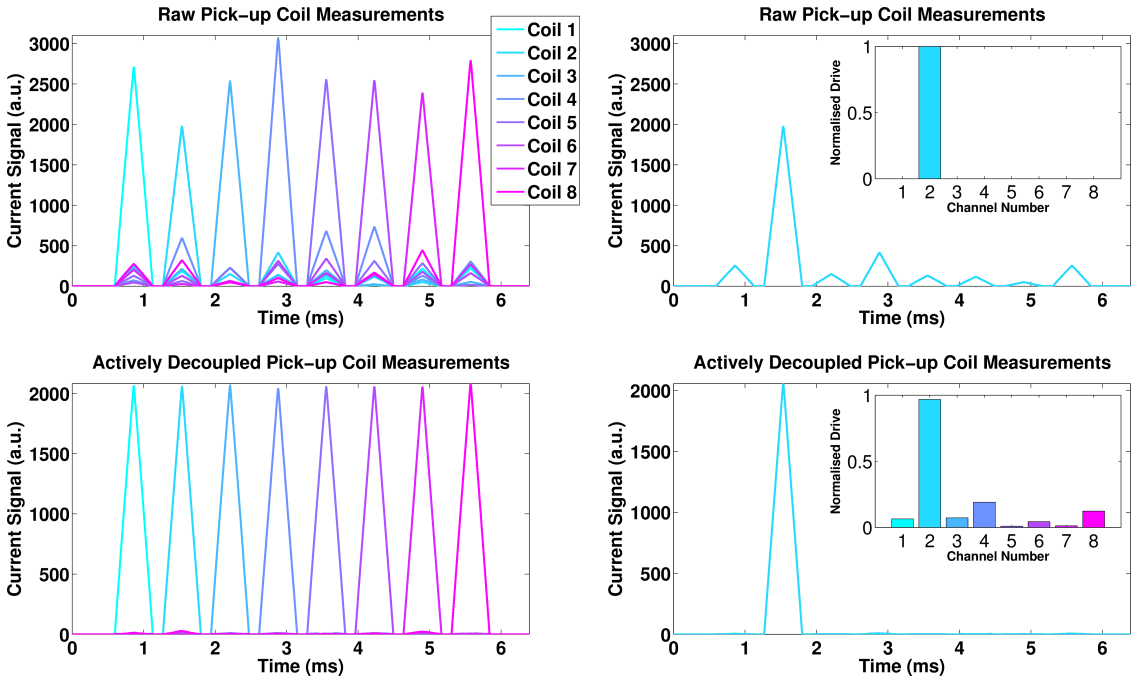

Figure 5.7: RF pulse waveforms measured on current pickup coils before (top) and after (bottom) active decoupling has been performed. The plots on the left show the pickup coil signals through time from all channels. The plots on the right show the same but only for channel 2. The bar graphs inset within these plots indicate the normalised drive amplitudes applied to the channels to produce these signals.

sequentially to the transmit elements in turn whilst simultaneously measuring the current signal induced on all pickup coils. This will produce a coupling matrix **C** of size $N_c \times N_c$ where N_c is the number of coil elements which in this case is eight and each entry C_{ij} gives the induced current signal measured on pickup coil j when transmitting on transmit channel i. The matrix **C** can then be inverted to find the set of linear coil combinations to be applied to the transmit channels to

remove any residual measured coupling.

To demonstrate this, a set of triangular waveforms were applied sequentially to the transmit elements whilst simultaneously measuring the signal on all pickup coil elements. The temporal signals are shown in the top left plot of Figure 5.7 and it can be seen that when the RF pulse is played on each channel, there is a dominant signal induced on the nearest pickup coil to that channel. However there is clearly still some signal on the other channels indicating residual coupling which can be more clearly seen for a single channel - this is shown for channel 2 on the top right of Figure 5.7.

The coupling matrix **C** can be constructed by taking the central measurement (i.e. the peak) for each waveform – doing this for the raw signals and taking the logarithm produces the matrix seen on the left side of Figure 5.8. When the in-

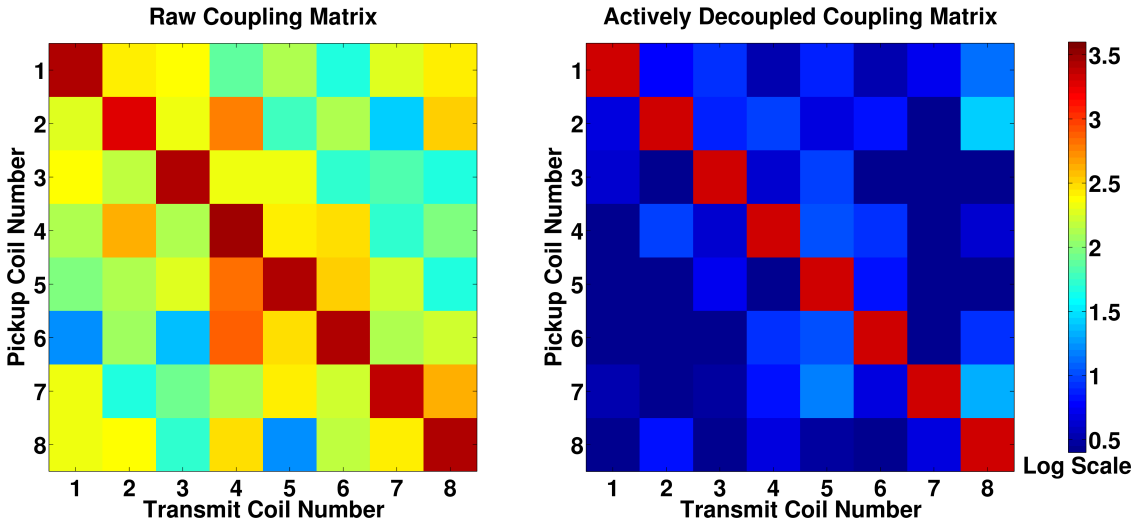

Figure 5.8: Coupling matrices created from peaks of the waveforms shown on the left side of Figure 5.7 on a logarithmic scale before (left) and after (right) active decoupling.

verse of this matrix $\mathbf{C}^{-1}$ is applied to the transmit channels, the residual coupling is effectively removed as shown by the heavily diagonal matrix on the right side of Figure 5.8. The full RF waveforms after the active decoupling has been performed are also shown in the lower left plot in Figure 5.7 again clearly displaying the suppression of any signals from alternate coils to the one being driven. On the bottom right is shown the same for just channel 2. For both the right hand plots of channel 2's pickup coil measurements, the normalised channel amplitudes applied to the RF waveforms for this channel are shown inset within the plots. Where initially only channel 2 being driven leads to coupling to the other channels, by driving all channels in a linear combination with the amplitudes shown in the inset bar graph, this coupling is suppressed.

Using this concept of active decoupling, in this study the specific example of the 8-channel MBC was studied and used to compare SAR predictions in several

different voxel models [59] from “Full Coil Model” simulations generated using circuit co-simulation with “Idealised Coil Model” simulations for the same models generated by excluding decoupling networks and treating each coil element in isolation. To make a direct comparison, the role of active decoupling was also simulated using two different approaches to model how this process may occur in the real world: directly fitting the B_1^+ fields in the isocentre of the models and simulating pickup coils near each transmit element.

5.3 Methods

All simulations for this study were performed using CST Microwave Studio with a 47 ns Gaussian pulse used for excitation and -50 dB energy decay used for the convergence criterion of the 3D EM simulation [74, 87, 94]. This convergence value was used as it was found to produce accurate results within a reasonable simulation run time. Simulations were run in a frequency range from 50 to 200 MHz. All other calculations and post-processing were performed in MATLAB.

The PTx array was modelled as a standalone entity driven directly on the coil elements. In reality the full RF chain means that the actual RF amplifiers driving the array are relatively far from the coil with a set of different components in between as discussed in Section 3.3.2. However it is not strictly necessary to model the entire RF chain to capture RF interactions within the coil, provided the EM fields are scaled such that they behave in the same way as the physical coil.

The simulation was run with all lumped elements modelled as 50 Ω ports as shown on the left side of Figure 5.6. By utilising circuit co-simulation (implemented in MATLAB) as discussed in Section 4.5, the results of this all ports simulation could be used to model the behaviour of the coil for any lumped element impedance values, including removing them by setting a very large impedance. The full coil model has 128 ports of which 120 represent lumped capacitors – 13 per channel and 16 in the decoupling ring structure (see Figure 5.6).

5.3.1 Tuning, Matching and Decoupling

Tuning, matching and decoupling of the full coil model was performed with the NORMAN male voxel model [63] placed inside the coil in a heart-centred configuration. The physical S-matrix $\mathbf{S}^{phys}$ of size 8×8 was constructed from the large 128×128 S-matrix taken from the full simulation using the relation detailed in Equation 4.61 and appropriate capacitor values were obtained by minimising

$$\arg\min\left\{\left\|\mathbf{S}_{i=j}^{phys,\omega_0}\right\| + \lambda(\max\left\{\left|\mathbf{S}_{i\neq j}^{phys,\omega_0}\right|\right\})\right\} \tag{5.2}$$

where superscript ω_0 indicates that the optimisation only considered the desired resonant frequency ω_0 (128 MHz at 3 T). The indices of the 8×8 matrix $\mathbf{S}^{phys}$, *i* and *j*, relate to the individual transmit channels. Parameter λ was used to adjust the relative weighting of coil matching $\mathbf{S}^{phys}_{i=j}$ and worst case coupling between transmission elements (max$\{\mathbf{S}^{phys}_{i\neq j}\}$). The cost function has many local minima; to adequately search the solution space the global optimisation algorithm SOMA [95] (Self-organising migrating algorithm) was used and run with bounds on the capacitor values based on those indicated in Reference [91]. Once a suitable local minimum was identified, results were refined using an unconstrained nonlinear optimisation (MATLAB's `fminsearch` function). λ was manually adjusted in both optimisation steps until a suitable solution was found – this was defined as having all elements tuned to 128 MHz, with matching and decoupling of all elements better than -15 dB. These can be compared to the measured S-parameters of the physical coil which can be found in Reference [91]. The final model with these optimised capacitor values is known as the "Full Coil Model" (FCM).

Once suitable capacitor values were determined, it was possible to generate the EM field distributions with Equations 4.62 and 4.63.

5.3.2 Comparison between Idealised and Full Modelling

Starting from the results of the same EM simulation, the fields produced by a single ideally decoupled transmit element were modelled by setting all capacitors in other transmit elements to values of $\sim 10^{-50}$ F [92] (effectively making them open circuit). Each transmit element was then tuned independently using a combined optimisation over several voxel models to find relevant capacitor values – this was done to ensure that the matching for any given model was not overly idealised and hence unrealistic. The results are equivalent to running a full simulation with those capacitors simply deleted from the model as in Reference [59] to produce the "Idealised Coil Model" (ICM) (Figure 5.6, right hand side).

Simulations using both decoupling regimes were run using an enlarged version of the NORMAN male voxel model [64], the virtual population Fats [62] male voxel model and the conventional NORMAN model as shown in Figure 5.9. All models were positioned heart-centred within the coil; an additional simulation was run with the NORMAN model in a head-centred configuration.

The fields were extracted from the simulation software on the calculation mesh (an irregular grid with ∼5 mm resolution on average – ranging between 0.5 and 5.2 mm with a very fine grid in regions including electrical components and coarser grid in regions with homogenous materials. The grid was calculated automatically by CST and manually tuned in some regions containing electrical compo-

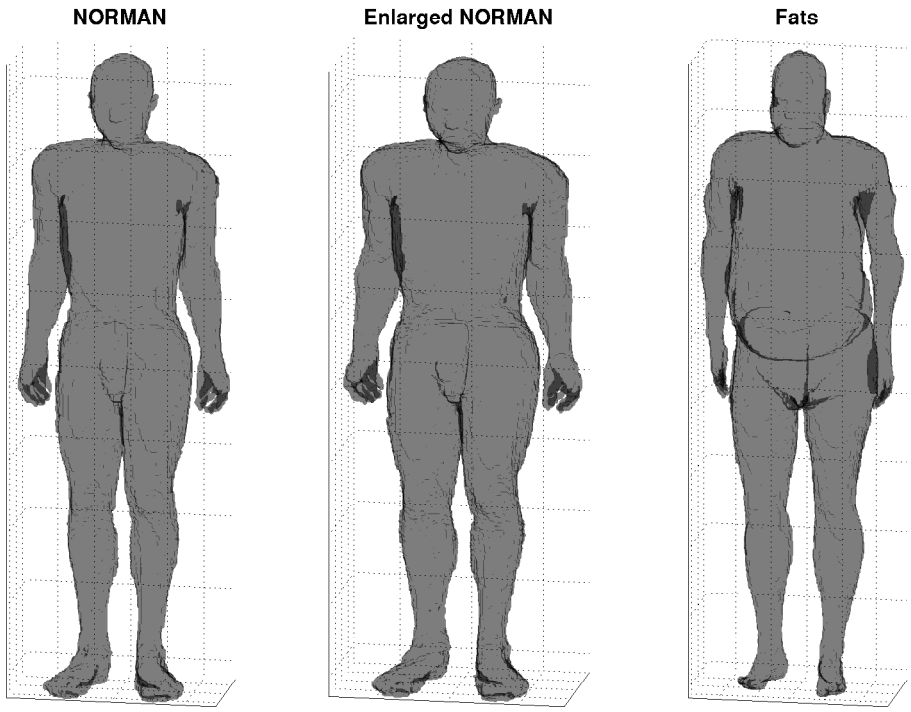

Figure 5.9: Voxel models used in simulation shown on same scale with BMI of 23.5 for NORMAN, 31.0 for Enlarged NORMAN and 36.1 for Fats.

nents) and the field distributions recovered using Equations 4.62 and 4.63. All SAR calculations were performed on the same grid with local 10g averaged Q-matrices [58] calculated for both sets of electric fields – the idealised and full coil model – for each voxel model. The 10g averaging was performed in MATLAB conforming to the IEEE C95.3 standard [96] as described in Section 3.5. The averaged Q-matrices were then condensed down into a much smaller set of Virtual Observation Points [66] (VOPs) with a 1 % overestimate bound for SAR comparison. An average compression factor of 2700 was achieved across all the simulations. Using these VOPs, maximum local 10g SAR estimates were calculated for a set of 10,000 random, complex drive settings all with a unit norm – this ensured that the overall power deposited by the drives was the same.

All simulations (both ICM and FCM; all voxel models) were first normalised such that the RF transmit field (B_1^+) when each transmit channel is driven independently had mean amplitude 1 μT and mean phase of 0° in a central region of interest (5 cm^2) in a slice at isocentre. This is referred to as "quadrature" normalisation since contributions from each coil were in-phase at the subject's centre.

As mentioned in Section 5.2.4, if an ideally decoupled simulation has been performed then one way of relating this to a real scenario is to employ "active decoupling" [58, 91] on the physical system, in which the physical channels are combined so as to further suppress the effects of the channels which are not being driven. In order to allow rigorous comparison of the modelling approaches,

the full coil model was subjected to active decoupling; in this way the FCM with active decoupling acts as a surrogate for a physical system with which the ICM can be compared. The efficacy of active decoupling depends on the decoupling matrix used, so in this work two methods were tested. The first was to fit the B_1^+ fields from the FCM in the central transverse slice of each voxel model (excluding regions outside the body) to their ICM counterparts using a least squares fit. This method allows a close as possible match for one set of simulation results to the other but is not feasible for a practical active decoupling implementation.

As discussed, for the MBC pickup coils are used to measure residual coupling [58, 91, 93]. The TEM elements of the MBC generate primarily azimuthally orientated magnetic fields between each element and the shield – this can be seen to some degree by the orientation of the ellipses in Figure 5.4. Local pickup coil measurements were simulated by sampling the azimuthal B-field, $B_\phi = -B_x \sin(\phi) + B_y \cos(\phi)$ in these regions, where ϕ is the angle defined in a polar coordinate system with its origin at isocentre. The simulated pickup coil measurements were collected into matrices of the form:

$$\mathbf{M}_{i,j} = \overline{\mathbf{B}_{\phi i}(R_j)} \tag{5.3}$$

containing the mean of $\mathbf{B}_{\phi i}$ produced by the i^{th} coil in a region of interest R_j near the j^{th} coil. Matrices $\mathbf{M_{ICM}}$ and $\mathbf{M_{FCM}}$ were produced for the idealised and full coil models respectively. The pickup coil actively decoupled FCM was created by applying decoupling matrix $\text{diag}\{\mathbf{M_{ICM}}\}\mathbf{M_{FCM}}^{-1}$ to the FCM. The term $\text{diag}\{\mathbf{M_{ICM}}\}$ renormalises the actively decoupled fields to give the same "pickup coil readings" as those from the ICM, making the closest possible match.

	Name	Abbreviation
Voxel Model	NORMAN Head-Centred	NHeC
	NORMAN Heart-Centred	NHC
	Enlarged NORMAN Heart-Centred	LNHC
	Fats Heart-Centred	FHC
Simulation Method	Idealised Coil Model	ICM
	Full Coil Model	FCM
	Full Coil Model actively decoupled by fitting	FCM:AD/f
	Full Coil Model actively decoupled by pickup coils	FCM:AD/puc

Table 5.1: Abbreviations used for different voxel models and different simulation methods

Table 5.1 displays a list of abbreviations used when referring to the different voxel models and normalisation methods in figures contained in this study.

5.4 Results

Decoupling of $<$-18 dB and matching of $<$-15 dB were achieved in the Full Coil Model, as can be seen in Figure 5.10 for the heart centred NORMAN model. The

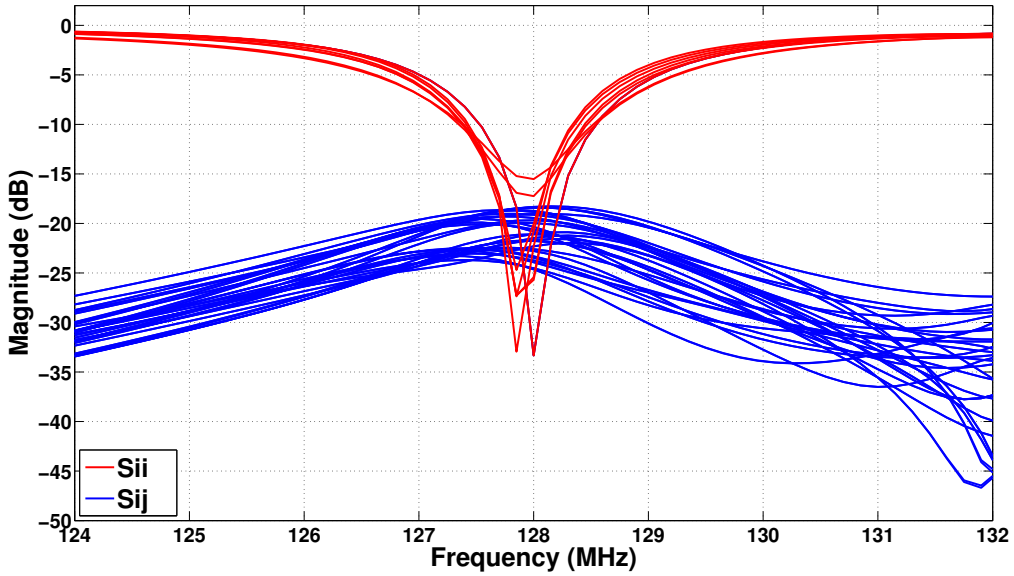

Figure 5.10: S-parameters for the Full Coil Model when loaded with the NORMAN voxel model, heart centred. Plot shows matching and decoupling equivalent to the physical coil ($\mathbf{S}_{ii}$ $<$-15 dB and $\mathbf{S}_{ij}$ $<$-18 dB at 128 MHz).

two coils with poorer matching are those closest to the arms of the voxel model leading to stronger loading. Better matching could be achieved but this does not reflect the behaviour of the true coil and would lead to an overly idealised situation in which the coil is perfectly tuned for one scenario but does not behave correctly with different loads. These S-parameters are similar to those measured in the physical coil when loaded (see Figure 5 in Reference [91]).

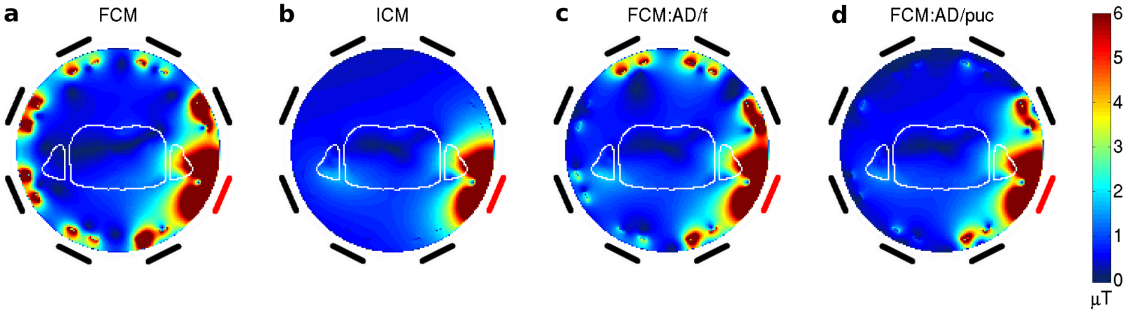

Figure 5.11: B_1^+ magnitudes over the entire coil region for the NORMAN heart centered model in an axial slice through the heart. Location of coil elements is shown outside region with active element highlighted in red; the voxel model outline is plotted in white. (**a**) Full Coil Model (FCM). (**b**) Idealised Coil Model (ICM). (**c**) Full Coil Model with active decoupling performed by directly fitting the B_1^+ from the FCM to the ICM (FCM:AD/f). (**d**) Full Coil Model with active decoupling performed by simulating pickup coils (FCM:AD/puc).

Figure 5.11 shows B_1^+ fields for the heart-centred NORMAN model when just one of the transmit coil elements (channel 2 – marked in red) is driven in the case of the full and idealised models, and with active decoupling to try to match the former to the latter. The full coil model without active decoupling has resid-

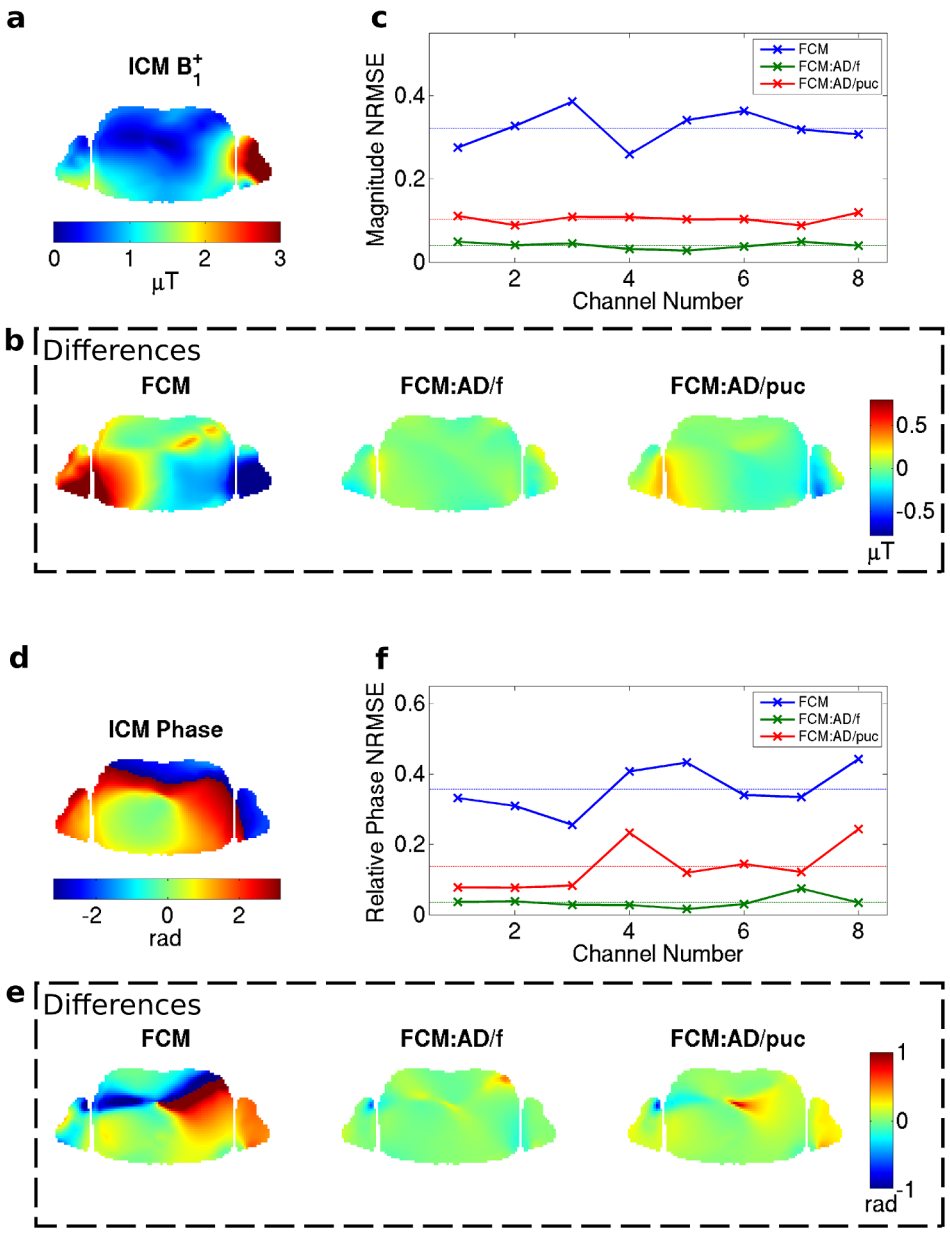

Figure 5.12: B_1^+ magnitude in axial slice through the cardiac region of the NORMAN heart centred model (channel 2 shown). (**a**) Idealised Coil Model. (**b**) Differences from ICM when using FCM with quadrature normalisation, active decoupling by fitting and active decoupling by pickup coils. (**c**) Normalised RMS difference in B_1^+ between FCM and ICM for the eight channels; the dashed lines correspond to averages over all channels. (**d-f**) As parts (a-c) for phase of B_1^+.

ual coupling between channels, particularly nearest neighbours (Figure 5.11 a), which is not present at all in the idealised coil model (Figure 5.11 b); as expected the other elements are not even visible in the simulated fields from the ICM. If

active decoupling is applied then agreement improves, particularly when using simulated pickup coils, in which case B_1^+ fields from all but the nearest neighbours of the active coil are suppressed (Figure 5.11 d). Fitting of B_1^+ within the voxel model results in some residual coupling to more distant elements (Figure 5.11 c).

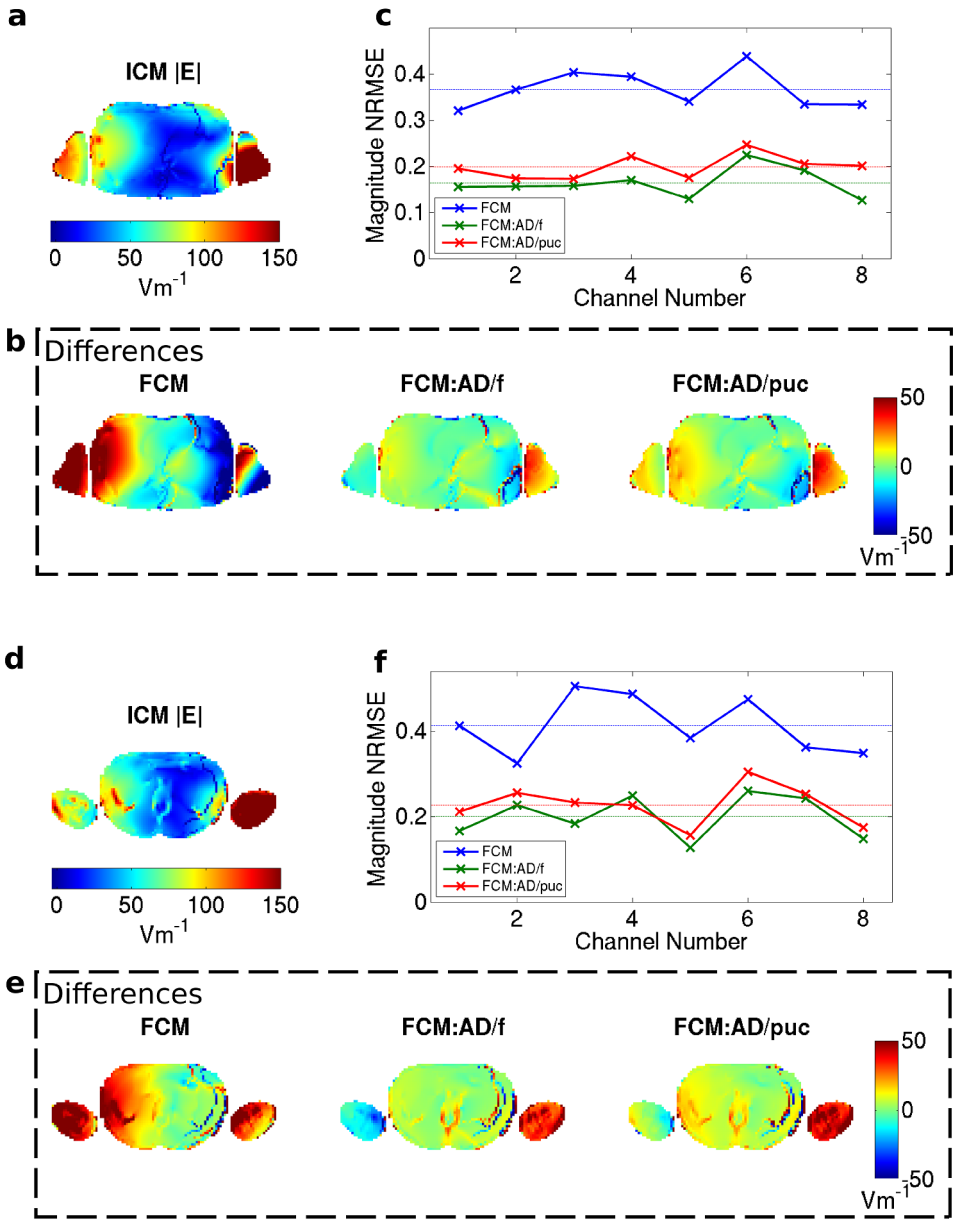

Figure 5.13: Magnitude of E-field in the body of the NORMAN heart centered model for channel 2 shown in an axial slice through the cardiac region for the Idealised Coil Model (**a**). (**b**) Differences from ICM when using FCM with quadrature normalisation, active decoupling by fitting and active decoupling by pickup coils. (**c**) Normalised RMS difference in |**E**| between FCM and ICM for the eight channels; the dashed lines correspond to averages over all channels. Stronger deviations are seen here compared with the B_1^+ fields for the same slice. (**d-f**) As parts (a-c) but for a different axial slice in the voxel model – a slice that was not used to calculate the normalisation matrices. Larger differences between the Idealised Coil Model and the Full Coil Model exist in this slice.

Figure 5.12 shows the B_1^+ field for the same coil element as shown in Figure 5.11, masked within the voxel model only, along with the differences between the ICM and various versions of the FCM for an axial slice through the cardiac region in the NORMAN heart-centred model. Significant differences in magnitude and phase are apparent when comparing the FCM with the ICM directly. Active decou-

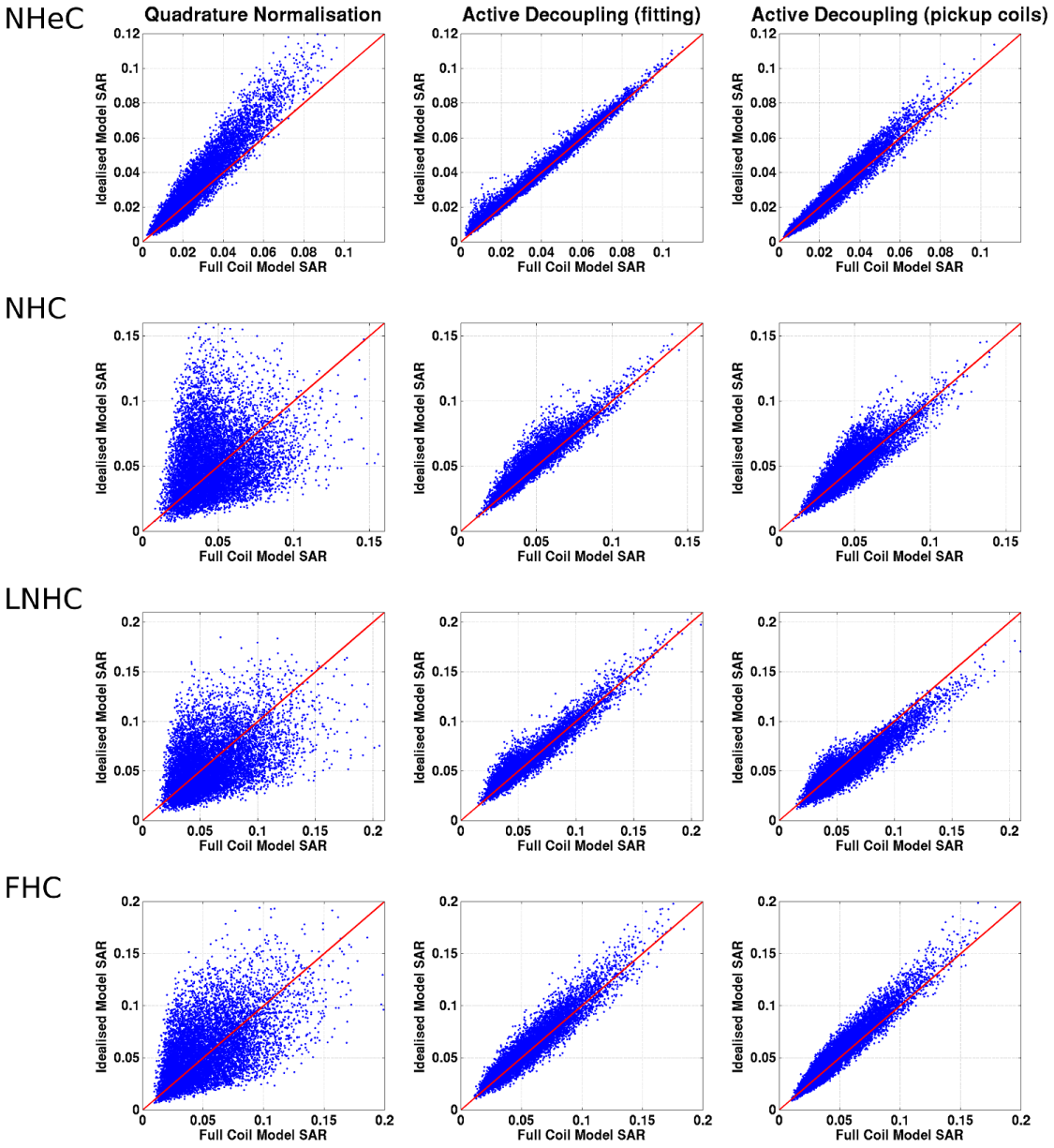

Figure 5.14: Maximum local 10g SAR predictions from the Idealised Coil Model plotted against the predictions from the Full Coil Model. Each blue dot corresponds to a single random RF shim; the red line indicates equality. The rows correspond to different voxel models, while the columns correspond to different decoupling settings applied to the FCM (abbreviations listed in Table 5.1).

pling leads to closer agreement with the idealised model; as expected, agreement within the subject is best when fitting B_1^+ directly in which case errors are $< 5\,\%$. Active decoupling with pickup coils shows better agreement than quadrature nor-

malisation but does not perform as well as active decoupling by fitting.

The corresponding comparisons for the electric fields show greater differences between the three FCM versions (Figure 5.13 a-c). Although most of the differences in fields from the fitted model are still relatively small, fairly strong variations can be seen in the voxel models' arms where the transmit elements are loaded more strongly, and this leads to greater errors in general. These deviations in the electric field will lead to differences in SAR estimates between the two simulation methods. Furthermore, the electric fields in a different slice show stronger differences (Figure 5.13 d-f). This is important since SAR must be evaluated throughout the body, not just in the imaging slice(s), in this case one slice at isocentre.

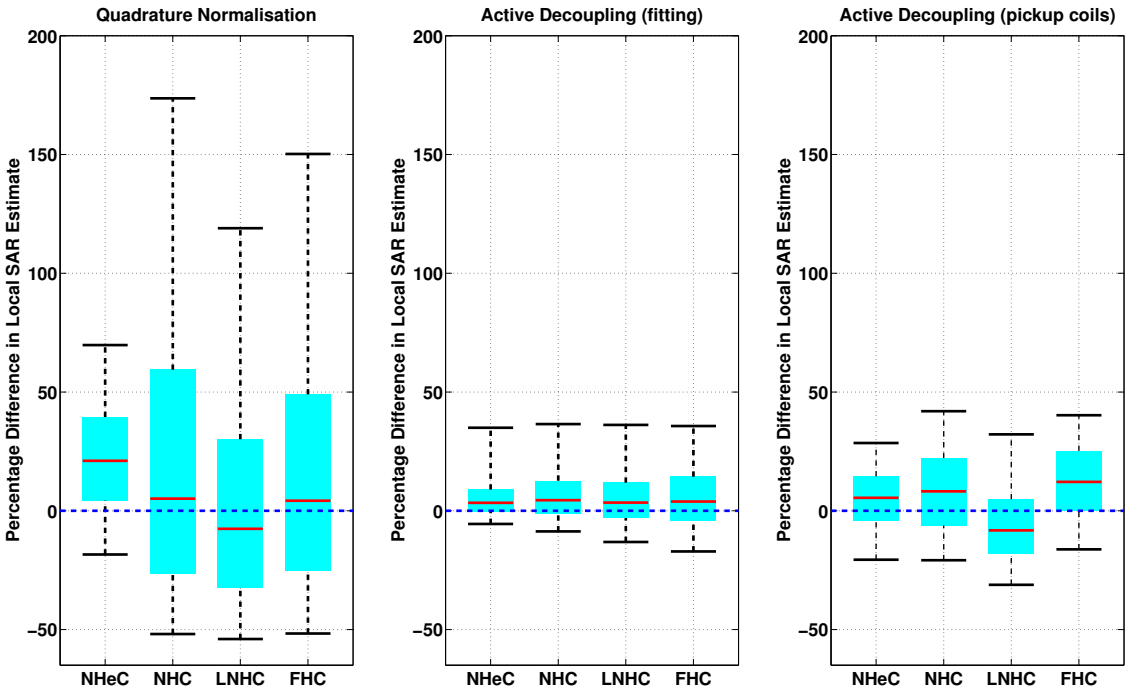

Figure 5.15: Boxplots of SAR estimate differences (ICM - FCM) for all three normalisation techniques indicating the 5^{th} and 95^{th} percentile as the upper and lower bounds and the interquartile range. Positive values indicate overestimation of SAR when using the ICM.

The local SAR estimates from the ICM and FCM (calculated from VOP compressed versions of the models) are plotted against each other in Figure 5.14; in this context the SAR values from the FCM are regarded as being true. The ICM leads to errors of varying degrees depending on the decoupling scheme applied. These differences are summarised by boxplots in Figure 5.15. It is clear that the plain "quadrature" normalised FCM leads to the largest discrepancies between the different simulations – this is to be expected because coupling is not at all present in the ICM. Active decoupling by fitting B_1^+ yields the lowest difference although there are still some significant variations, generally with an overestimate for the ICM. Using pickup coils for active decoupling performs in a similar way to

active decoupling by fitting. Again there is a tendency for the idealised coil model SAR estimates to be larger.

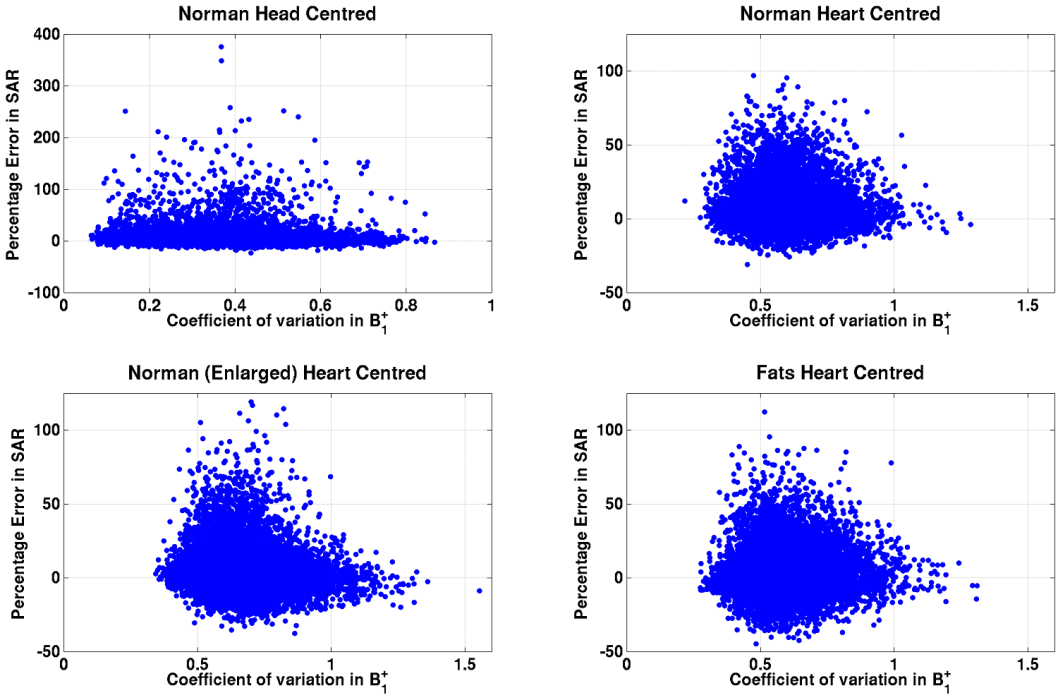

Figure 5.16: Coefficient of variation in B_1^+ (high coefficient = poor spatial homogeneity) in the idealised coil model plotted against error in SAR estimate for all voxel models. Each blue dot corresponds to a single random RF shim. There is no clear relation between the two variables.

In order to test whether shim settings resulting in large SAR errors are associated with particular B_1^+ patterns, Figure 5.16 shows B_1^+ inhomogeneity (coefficient of variation) in the idealised coil model plotted against percentage SAR error (ICM-FCM:AD/f). The two appear to be uncorrelated.

5.5 Discussion

This study compares EM simulations of a parallel transmit MRI body coil using a Full Coil Model consisting of all coil elements plus decoupling circuits with an Idealised Coil Model in which coil elements are treated in isolation. The work focused on a single RF coil model operating at 128 MHz but included three separate anatomical voxel models, one of which was simulated in two different positions. The B_1^+ fields predicted by the idealised and full coil models when both are treated with nominal “quadrature” normalisation agree qualitatively but there are large discrepancies in predicted SAR.

In practice an idealised coil model would only be used for comparison with a physical system if some extra step were taken to account for residual coupling

– one strategy is to adapt the physical system to emulate the ideally decoupled scenario – this is known as active decoupling [58, 91]. Active decoupling requires measured estimates of the residual coil coupling; this measurement was simulated by using either (simulated) pickup coils, or by directly fitting the B_1^+ fields. Figure 5.11 shows that the pickup coil method leads to better suppression of other coil elements than fitting of B_1^+ fields within the body, perhaps because in the latter case the EM fields produced very close to each individual coil element are ignored.

As might be expected, directly fitting B_1^+ leads to highly similar B_1^+ in the slice used for fitting (Figure 5.12) though errors are not precisely zero. Of course this good agreement is true by construction since B_1^+ was directly fitted; actually the fact that perfect agreement cannot be obtained demonstrates that the ICM and FCM are not simply linear combinations of one another.

Active decoupling by fitting also leads to lower median error in simulated SAR predictions (Figures 5.14 & 5.15) than the pickup coils method. This may seem counter-intuitive since the least-squares fitting is only considering the NMR active B_1^+ component of the magnetic field whereas pickup coils were simulated by considering the B-field produced by currents on the coil elements – as evidenced by the better performance of pickup coils in suppressing fields produced by alternate elements (Figure 5.11). Fitting was performed on the

Voxel Model	Quadrature Normalisation					Active Decoupling (fitting)					Active Decoupling (pickup coils)				
	1st Centile	5th Centile	Median	95th Centile	99th Centile	1st Centile	5th Centile	Median	95th Centile	99th Centile	1st Centile	5th Centile	Median	95th Centile	99th Centile
NHeC	-30.5%	-18.4%	21.1%	69.8%	96.2%	-9.7%	-5.5%	3.4%	35.0%	100.3%	-30.0%	-20.6%	5.5%	28.6%	42.6%
NHC	-63.1%	-51.9%	5.1%	173.7%	268.6%	-15.2%	-8.7%	4.5%	36.5%	57.0%	-27.9%	-20.8%	8.2%	41.9%	56.1%
LNHC	-64.5%	-54.0%	-7.6%	119.0%	202.8%	-20.5%	-13.1%	3.5%	36.2%	61.3%	-39.3%	-31.1%	-8.2%	32.2%	50.7%
FHC	-62.7%	-51.7%	4.2%	150.2%	248.0%	-27.4%	-17.1%	3.9%	35.7%	55.2%	-24.7%	-16.2%	12.2%	40.3%	53.6%

Table 5.2: 1^{st}, 5^{th}, 95^{th} and 99^{th} centile of differences along with the mean difference for all voxel models and normalisations.

fields within the body, which are relevant for SAR characterisation – this may explain the better performance. Another possibility is that ensuring similar current distributions on the elements for the two decoupling regimes doesnt necessarily guarantee similar fields within the subjects, hence direct fitting of fields yields better results. In practice both methods of active decoupling would be achievable – pickup coils already exist, while fitting could proceed by using in-vivo acquired B_1^+ maps. In reality fitting would be subject to a large degree of uncertainty because of spatial mismatch between the voxel model and acquired B_1^+ data, and so pickup coils will likely remain the preferred method for active decoupling. However it should be noted that for other types of transmit arrays, pickup coils may not be appropriate – for example, surface coils at 7 T and above in which the use of these pickup coils may complicate the design of the transmit coil elements.

Ultimately it is accuracy of SAR prediction that is the priority for these models. As indicated by the values in Table 5.2, the most common error if employing an ICM for SAR quantification in conjunction with active decoupling via fitting is to overestimate SAR, with the largest overestimate in the heart centred models (99^{th} centile of differences) being 61 %. The head centred model shows larger percentage differences but these are for SAR values which are very low relative to those seen in the other models, so are less of a concern. The data shows a general trend towards overestimation that is likely due to greater power dissipation in the subject in the ICM, since there are no other active coil elements for the power to dissipate into elsewhere. From the point of view of safety this makes the models more likely to be conservative, so less of a risk however they would lead to suboptimal operating conditions.

Underestimates are more cause for concern. The underestimates were generally of a smaller degree than the overestimates, however the extreme values were still quite large: the maximum underestimate from the ICMs compared with active decoupling by fitting (1^{st} centile of differences) was 27 %. Median errors in SAR estimation when considering decoupling by pickup coil were slightly larger than for active decoupling via fitting and the peak SAR underestimate in this case was 39 %, now for a different voxel model. The implication is that fitting would be a preferred method for active decoupling. However their performance is similar and as was mentioned earlier, though fitting is easy to do in a simulation study like this one, it would be much more error prone if used in reality, and this might introduce an additional source for uncertainty. In general the worst case underestimates and discrepancies between models are of the order of 20-40 %, and so margins for error when using such models for safety assessment must be made sufficiently large.

In Reference [97] power balance calculations were performed in simulations

of parallel transmission arrays and as part of this formulation it was theoretically proven that perfect decoupling between transmit elements made from coils exhibiting any resistive coupling is not physically realisable. This is because any decoupling networks that aim to eliminate mutual resistances must introduce additional losses to do so in order to meet the criteria of a fully power balanced system. In this regard this corroborates the findings shown in the study described here as the FCM is clearly unable to perfectly emulate the behaviour of the ICM.

Idealised modelling has been used as a simulation methodology in the past [59, 88] primarily due to simplicity of implementation – the models have fewer variables than a full modelling approach and optimisation of the model properties is more stable due to the lack of coupling. This simulation study has shown that such an approach when combined with active decoupling can lead to SAR predictions which are reasonably accurate, however there are a small number of cases in which larger errors do occur and it is not clear under which conditions these can be expected. In order to explore this, Figure 5.16 plots the relationship between B_1^+ inhomogeneity and error in SAR estimate, however there does not appear to be a correlation in any model.

The presented results are for one particular case study of an RF coil model – an 8-channel TEM device operating at 128 MHz – with findings relatively consistent across a number of anatomical voxel models. It is not immediately clear how these results would generalise to different coils or other frequencies, but a comparison similar to the one made in this work could be applied to different coil geometries and voxel models. Circuit co-simulation can be implemented to allow this comparison and its simplicity makes it straightforward to model complex devices, perhaps obviating the need for idealised models altogether.

To assist in this, another goal for this work was to be able to implement circuit co-simulation directly without using commercial software packages. This was not entirely straightforward as no existing publication was found that included all the relevant steps and theory. Consequently once this had been achieved, a paper detailing the relevant methodology along with the results presented here was published [98] and the relevant MATLAB code was made available online to assist others (as mentioned at the beginning of this chapter) which has now been used by a number of individuals.

Chapter 6

SAR Optimised Cardiac Imaging

Contributions

The findings in the following chapter have been partially discussed in the following publications:

> **A. Beqiri**, J.V. Hajnal, and S.J. Malik. SAR and peak power constrained excitation optimisation for 3T cardiac imaging. *Proceedings of ESMRMB 2015*
>
> **A. Beqiri**, F. Padormo, J.W. Hand, J.V. Hajnal, and S.J. Malik. SAR optimised local B_1^+ shimming for cardiac imaging at 3T – a multi-model study. *Proceedings of ISMRM 2014*
>
> **A. Beqiri**, J.W. Hand, J.V. Hajnal, and S.J. Malik. Local RF shimming for cardiac MRI at 3T with SAR considerations. *Proceedings of ESMRMB 2013*

The code used to perform the SAR constrained shimming optimisation with the CVX convex optimisation package [99, 100] as discussed in this chapter is available at `https://github.com/mriphysics/cardiac_RF_shimming`.

6.1 Introduction

Cardiac imaging using MRI is often limited by SAR constraints. These constraints mean that other imaging parameters must be compromised in some way in order to acquire suitable images. As SAR is proportional to the square of the static magnetic field, B_0, these constraints present greater limitations when imaging at

high and ultra high field. However, high field cardiac MRI (CMR) offers considerable gains in signal to noise ratio (SNR) and improved blood-tissue contrast [101], so high field imaging is thought to be worth the additional challenges.

As mentioned in Chapter 3, parallel transmission offers a way of controlling SAR and directly improving imaging by simultaneously reducing B_1^+ inhomogeneity. SAR reductions from using PTx potentially allow improved operating conditions in terms of pulse sequence parameters which will further benefit imaging.

Previous studies have shown imaging improvements for 3 T cardiac imaging with a commercial 2-channel system [101, 102]. In this chapter, the 8-channel parallel transmission coil – the MBC – simulated in the previous chapter is used for RF shimming. The increased degrees of freedom available with eight channels over two is likely to yield greater improvements in terms of SAR reduction and improved B_1^+ homogeneity. In Reference [103] it was shown that using more transmit channels does improve RF shimming efficacy when shimming is performed over a relatively large region. However in that study, only regularised shimming was performed which controlled peak input power as opposed to SAR. Local SAR has a far more dynamic behaviour not necessarily directly related to peak input power.

For this study two of the SAR models discussed in Chapter 5 were used to provide SAR estimates for subjects being scanned during a cardiac MRI exam. These SAR models formed part of the input to a constrained RF shimming optimisation along with in vivo measured B_1^+ maps of the subjects. The RF shimming was performed over a local region within the heart and the optimisation was run as a constrained optimisation with local and global SAR constraints, and peak power constraints incorporated. Furthermore within the optimisation the constraints are considered to be dynamic as the RF pulse properties for the sequence being optimised are modified. This produces a full framework for essentially shimming the excitation RF pulse in what can be considered as “excitation optimisation”.

This chapter begins by discussing cardiac MRI with and without PTx. Then the RF shimming excitation optimisation framework is outlined in full. This framework requires accurate cardiac B_1^+ maps – the optimisation of the B_1^+ mapping sequence and cardiac imaging is discussed next before moving on to the overall study.

6.2 Cardiac Imaging

As the heart is a very dynamic organ, it presents a challenge for MRI. The constant motion of the heart tissue, flowing blood, and respiration mean that cardiac imaging sequences must be fast so that they can essentially “freeze” the motion in a given imaging frame. Consequently a number of methods have to be used in

order to acquire cardiac images that are suitable for clinical use.

Standard ways of speeding up MRI acquisitions are often used in CMR such as partial Fourier in which up to half the k-space data is not acquired and the symmetry of the data is used to aid reconstruction [104]; or SENSE [105] in which multiple *receiver* coils are used in combination to allow undersampling of k-space.

The motion of the heart and its beating must be accounted for during CMR. This is generally done using a vector cardiogram (VCG) to track electrical activity in the heart and enable monitoring of the heart beat. This allows the overall image acquisition to be triggered to only acquire at certain points in the heart beat cycle, or gated such that data is acquired over the whole cycle and then binned into the correct phases of the cycle. VCGs are able to provide real time monitoring of the heart although at higher field strengths the VCG signal can become distorted when a patient is lying within the magnet due to the magneto-hydrodynamic (MHD) effect [106]. At 3 T this is usually still not an issue but at 7 T and above it becomes a considerable challenge to perform cardiac imaging as a result of this effect [107].

Respiratory motion can be mitigated for in a number of ways by using respiratory bellows or an image based navigator to track the breathing and gate the acquisition so images are only acquired at certain positions in the respiratory cycle. However this becomes inefficient in terms of the image acquisition. A simple way to account for breathing is to perform imaging with the subject under breath-hold. This will generally provide a very stable, more efficient acquisition although it limits the window in which images can be acquired as subjects can only hold their breath for a limited amount of time; particularly cardiac patients.

CMR acquisitions are performed using one or several of many radiological views [108]. These allow the desired features relevant for clinical diagnosis to be seen. Two commonly used ones are the short-axis view which shows the left and right ventricles, and the 4-chamber view which is a double oblique slice through the heart showing all four chambers.

A commonly used pulse sequence for cardiac imaging is the T_1 weighted turbo field echo (TFE). This is a gradient echo sequence performed with a relatively low flip angle and short TR. As a result full relaxation is never possible within each TR and hence the signal begins to approach a steady state. For the sake of acquisition speed, the steady state is never reached and image acquisition is performed in some transient state [12]. This means that the contrast changes throughout the acquisition so to ensure a T_1 weighting, the magnetisation is prepared at the beginning of the sequence with a single 180° inversion pulse. This then allows a very fast acquisition that can be used for cardiac imaging.

The sequence most often used for cardiac imaging is balanced steady state

free precession (bSSFP). This is also a gradient echo sequence but the imaging is performed only when a steady state has been achieved. It provides excellent contrast between blood and tissue and as the gradients are fully balanced within it, the sequence is highly insensitive to flow artefacts [1]. However its frequency response is very sensitive so images acquired with bSSFP are easily corrupted by inhomogeneities in B_0 causing dark bands to appear on images. The sequence also has high SAR [109].

6.3 PTx Cardiac Imaging

CMR is even more challenging at high field as the B_1^+ inhomogeneities present cause the achieved flip angle desired for imaging to be spatially variable over the subject [101]. This leads to suboptimal imaging.

Furthermore the fast pulse sequences being used mean that the RF duty cycle, i.e. the time the RF field is being applied relative to the repetition time of the sequence, can be very high and this will produce relatively high SAR, even at low field. In fact bSSFP is often run at the SAR limits allowed by the scanner software [101, 109].

An improvement in SAR efficiency (i.e. the ability to run current imaging protocols at a reduced SAR level) would lead to numerous benefits particularly for bSSFP imaging [109]. Flip angles could be increased leading to improved contrast and increased signal, and/or repetition times could be decreased which would lead to shorter overall scans times and would reduce banding artefacts [110] caused by off-resonance behaviour. Shorter scan times would be greatly beneficial as patient breath holds could be reduced accordingly. Current methods of reducing scan time as described above provide varying degrees of acceleration but they could be further enhanced by the intrinsic speed-up made possible by improving SAR efficiency.

SAR can be managed in a number of ways by trading off different pulse sequence parameters in order to reduce overall RF duty cycle or the amplitude of RF pulses. However local SAR distribution varies from subject to subject so a more tailored approach is required to effectively manage this. Parallel transmission offers a way to achieve a tailored approach by adapting the EM RF fields produced by a parallel transmit array using RF shimming in order to achieve more SAR efficient operating conditions [3] whilst simultaneously making the B_1^+ field which is actually used for imaging more homogenous [59]. This is achieved by performing a constrained optimisation such that the optimal field homogeneity is found that adheres to a strict set of SAR and system power constraints [46]. A number of groups have demonstrated the efficacy of this SAR constrained RF

shimming in simulation [57, 59, 111, 112] however there do not appear to be any prior studies showing imaging improvements possible with in vivo subjects; which comes with a number of challenges itself.

SAR constrained shimming is particularly effective if B_1^+ homogeneity is only being optimised for within a spatially limited region such as the heart, since there is greater freedom in available solutions with which to reduce SAR. To achieve this in practice the B_1^+ field distribution produced by each coil element and the SAR behaviour within the imaging subject must be known. It is possible to measure the B_1^+ field in vivo [22] as discussed in Chapter 3; however mapping this in the cardiac region is challenging due to motion and flow within the heart [113].

Unlike the B_1^+ fields required for measuring the achieved homogeneity, the SAR distribution must be estimated from simulations over the entire volume of the subject exposed to the RF fields. Estimates of global SAR and local SAR (in this case averaged over 10g of tissue [50]) are both required, though local SAR is generally the limiting factor in body imaging at 3 T.

Feasibility studies that are entirely simulation based can proceed using SAR and B_1^+ information extracted from the same numerical model in a straightforward manner [111, 112]. When attempting to apply similar methods to in vivo imaging, care must be taken to match the simulation to the real world. This is not a problem that is limited to parallel transmission MRI – it is common to use numerical model predictions of some type to assess local SAR. The result is a hybrid optimisation problem that uses in vivo measured B_1^+ maps along with a numerical model for SAR [47]. The EM model used to evaluate SAR also yields a simulated prediction for the B_1^+ field, and this extra information is used to match the model to the in vivo subject.

A further constraint that is commonly encountered at high field with complex transmit arrays is a peak forward power constraint from the RF amplifiers [46, 47, 111]. For the hardware used in this study (and in many reports in the literature [47, 114]) this limit is easily reached under standard operation during body imaging. RF shimming must therefore be performed under strict peak power constraints.

The aim of the work in this chapter is to move towards optimised cardiac imaging at high field by using all the degrees of freedom afforded by localised RF shimming with PTx in an “excitation optimisation”. Unlike most RF shimming approaches, which concentrate on the homogeneity of the achieved B_1^+ field, the problem is formulated in terms of the achieved flip angle and explores solutions in which the RF pulse amplitude and duration are changed. This approach allows more flexibility to operate within peak power constraints, and to still find solutions with reduced SAR and enhanced homogeneity under variable loading conditions. Where other studies have used RF shimming to improve homogeneity with SAR

as a constraint, here one aim was to push SAR values down by seeking the most conservative constraint that still gave good imaging performance. Example in vivo imaging experiments were performed to highlight the potential for improved imaging with this framework.

6.4 Constrained RF Shimming

The formulation of the constrained RF shimming optimisation was constructed in order to yield the best possible operating condition under all the active constraints. The following section discusses the mathematical relations required to formulate the constrained excitation optimisation, accounting for the dynamic variation of the constraints as RF pulse properties are varied. Some of the practical considerations regarding the in vivo aspect of this formulation are also discussed.

6.4.1 SAR Scaling

To obtain accurate SAR estimates for imaging subjects, a SAR model from a simulation that most closely represents that subject must be created. In such a simulation of a multi-channel system with N_c channels produces N_c B_1^+ fields; the total field produced depends on these and on a complex channel specific weighting w_j. Optimising this weighting amounts to RF shimming. The 8-channel scanner system used for this work is calibrated so that a nominally quadrature excitation is achieved when driven with equal amplitude and a 45° per-channel phase offset. The EM fields obtained from the simulation model therefore must also be normalised in this way, such that application of weighting $\mathbf{w}_{quad}$:

$$w_{quad,\,j} = e^{\frac{i\pi(j-1)}{4}} \qquad j = 1, 2, \ldots, 8 \tag{6.1}$$

results in a nominally quadrature excitation with mean B_1^+ = 1 μT over a central slice in the body of the voxel model. By scaling the model in this way, SAR for any arbitrary set of weights **w** can be obtained from the Q-matrices calculated from the model. The resulting value is appropriate for mean achieved B_1^+ = 1 μT and 100 % duty cycle, where the duty cycle represents the proportion of time during a pulse sequence for which the RF is being applied. For a sequence with fractional duty cycle Δ, this can be scaled using the relation

$$SAR = \mathbf{w}^*\mathbf{Q}\mathbf{w} \times \left(B_{1\,achieved}^+\right)^2 \times \Delta \tag{6.2}$$

where $B_{1\,achieved}^+$ is the achieved peak B_1^+ (i.e. the maximum amplitude of the RF pulse envelope) averaged over an isocentre slice when transmitting in quadrature

mode using the imaging sequence under evaluation. When scanning in vivo, this scaling value is produced from B_1^+ mapping and is used to match the scanner operating condition to that of the EM model, which is necessary since the models used could not predict subject specific loading effects.

As mentioned in Section 5.3, it is technically possible to create a more detailed model that includes the full RF chain and properly accounts for loading effects. In practice this would be difficult as the model would be highly sensitive to minor variations between simulation and reality.

6.4.2 Excitation Optimisation

The normalisation of the SAR models to in vivo measurements enables a constrained hybrid optimisation to be set up which includes SAR information from the EM models, and B_1^+ information from measured data. The next step is to incorporate peak power constraints but these are wholly dependent on the RF pulse waveform being demanded. To characterise the optimisation correctly, the pulse sequence parameters must also be considered.

In a typical MRI system architecture, production of an RF pulse begins with a low-level RF waveform $p(t)$ that is amplified by fixed gain RF amplifiers and fed to the coil, which produces a pulsed B_1^+ field of a certain amplitude (typically in the μT range) within the object to be imaged. The waveform $p(t)$ is defined in some units u and there exists a scaling factor, κ for conversion between u and μT produced within the subject. For some MRI scanner manufacturers units u are volts, whereas for others this scaling parameter is implicit, such that $p(t)$ is defined directly in μT – the latter is the case in the Philips MRI system used for this work. Additionally, due to RF inhomogeneity and subject-specific loading effects, a dimensionless scaling factor must also be introduced which here is the transmit sensitivity of the RF coil $S(\mathbf{r})$. The sensitivity quantifies the spatially dependent deviation from the ideal situation defined when the system is calibrated:

$$B_1^+(\mathbf{r}, t) = S(\mathbf{r})\, \kappa\, p(t). \tag{6.3}$$

$S(\mathbf{r})$ can deviate from the ideal value of 1 because of inhomogeneity effects at high RF frequencies, but also due to loading of the coil changing the efficiency of the coil in $\mu\mathrm{T}/u$. The flip angle, which is also generally spatially varying, is then defined by the integral:

$$\theta(\mathbf{r}) = \gamma \int_0^\tau B_1^+(\mathbf{r}, t)\, dt = \gamma\, \kappa\, S(\mathbf{r}) \int_0^\tau p(t)\, dt \tag{6.4}$$

where γ is the gyromagnetic ratio, here in units of rad $\mu\mathrm{T}^{-1}\,\mathrm{s}^{-1}$ and τ is the pulse

duration. Conventional MRI systems modify the duration and amplitude of $p(t)$ to achieve the appropriate flip angle.

A useful property of the given pulse shape is the fractional duration for a block pulse that generates the same flip angle as the pulse under consideration with the same peak amplitude $p_{max} \equiv \max\{|p(t)|\}$ given as:

$$\delta_1 = \frac{\int_0^\tau p(t)\,dt}{p_{max}\,\tau}. \tag{6.5}$$

For a given $p(t)$, the overall achieved flip angle is a linear sum over all transmit channels, which may be written as

$$\theta(\mathbf{r}) = \delta_1\, p_{max}\,\tau\,\gamma\,\kappa \sum_{j=1}^{N_c} S_j(\mathbf{r})\, w_j. \tag{6.6}$$

The sum may be expressed as a matrix-vector product

$$\boldsymbol{\theta}(\mathbf{r}) = \delta_1\, p_{max}\,\tau\,\gamma\,\kappa\,\mathbf{Sw} = \mathbf{S}_{\boldsymbol{\theta}}\mathbf{w} \tag{6.7}$$

where **S** is a matrix of the acquired transmit sensitivities for all channels of size number of voxels $\times\ N_c$, **w** is a column vector of complex channel-specific weighting factors and $\boldsymbol{\theta}$ is a vector of achieved flip angles (length is number of voxels). Here **S** was determined using B_1^+ mapping, normalised to account for the specific drive level at which it was acquired. To simplify the expressions, $\mathbf{S}_{\boldsymbol{\theta}} \equiv \theta_T\mathbf{S}$ is defined as the sensitivity of the system in units of flip angle, which directly relates the achieved flip angle to the input weighting factors **w** for a pulse $p(t)$. $\theta_T \equiv \delta_1\, p_{max}\,\tau\,\gamma\,\kappa$ is the flip angle that would be achieved by waveform $p(t)$ at unit sensitivity; this is then the target flip angle for which weighting factors **w** are determined by a constrained optimisation within peak power and SAR constraints.

The peak forward power limit on each channel can be translated into a limit on p_{max} (in units u) as $|w_j|\,p_{max} \leq A$ for all j, where A is a fixed constant for the RF amplifier – selecting a pulse with a larger peak amplitude will lead to a greater restriction on **w** than a pulse with a low peak amplitude. The pulse shape also affects the duty cycle, since reducing the amplitude necessitates increasing the duration to achieve the same flip angle. The fractional duration of a block pulse with equivalent integrated forward power to pulse $p(t)$ can be calculated as:

$$\delta_2 = \frac{\int_0^\tau p^2(t)\,dt}{p_{max}^2\,\tau}. \tag{6.8}$$

The duty cycle for a simple gradient echo sequence (i.e. no other RF pulses

present) is then defined as:

$$\Delta = \frac{\delta_2 \, \tau}{TR} \tag{6.9}$$

where TR is the repetition time of the sequence. Expressing τ in terms of θ_T gives

$$\Delta = \frac{\delta_2}{\delta_1} \cdot \frac{\theta_T}{\gamma \, \kappa \, p_{max} \, TR}. \tag{6.10}$$

Finally, in order to quantify the SAR of a given pulse sequence as per Equation 6.2, the required normalisation factor $B^+_{1\,achieved}$ may be written as

$$B^+_{1\,achieved} = \kappa \, p_{max} \, \overline{\mathbf{Sw_{quad}}} \tag{6.11}$$

where the over-bar indicates a spatial average over the imaging slice. The optimisation is then formulated and solved using a magnitude least squares (MLS) type approach [42, 43] within the region of interest (ROI) encompassing the cardiac tissue:

$$\arg\min_{\mathbf{w,z}} \|\mathbf{S}_{\boldsymbol{\theta}}\mathbf{w} - \boldsymbol{\theta}_\mathbf{T} \circ \mathbf{z}\|^2_{ROI}$$

$$\begin{aligned} \text{s.t.} \qquad \mathbf{w}^*\mathbf{V}_i\mathbf{w} \times (\overline{\mathbf{Sw_{quad}}} \, \kappa \, p_{max})^2 \times \Delta &\leq lSAR_{max} \quad \forall \, i \\ \mathbf{w}^*\mathbf{Q_G}\mathbf{w} \times (\overline{\mathbf{Sw_{quad}}} \, \kappa \, p_{max})^2 \times \Delta &\leq gSAR_{max} \\ p_{max}|w_j| &\leq A \quad \forall j \end{aligned} \tag{6.12}$$

where $\boldsymbol{\theta}_\mathbf{T}$ and $\mathbf{z}$ are both vectors and $\circ$ denotes element-wise multiplication. Equation 6.12 can be used to find optimal RF shims $\mathbf{w}$ and background spatial phase pattern $\mathbf{z}$ that minimise deviation of the magnitude of the flip angle from the target $\boldsymbol{\theta}_\mathbf{T}$ within the space defined by the ROI. Local SAR is evaluated using VOP matrices $\mathbf{V}_i$ and global SAR is evaluated from a single average matrix $\mathbf{Q_G}$. The maximum local and global SAR constraints are given by $lSAR_{max}$ and $gSAR_{max}$ respectively. By directly substituting the expression for Δ into the SAR constraints in Equation 6.12 the full relationship between the SAR constraints and pulse properties can be obtained:

$$\begin{aligned} \mathbf{w}^*\mathbf{V_i}\mathbf{w} \times (\overline{\mathbf{Sw_{quad}}})^2 \, \kappa \, p_{max} \times \frac{\delta_2}{\delta_1} \cdot \frac{\theta_T}{\gamma \, TR} &\leq lSAR_{max} \quad \forall \, i \\ \mathbf{w}^*\mathbf{Q_G}\mathbf{w} \times (\overline{\mathbf{Sw_{quad}}})^2 \, \kappa \, p_{max} \times \frac{\delta_2}{\delta_1} \cdot \frac{\theta_T}{\gamma \, TR} &\leq gSAR_{max} \; . \end{aligned} \tag{6.13}$$

In particular it can be seen that if the flexibility to change the duration of the pulse waveform is included, SAR is proportional to p_{max} (i.e. not the square of p_{max}) when the TR, flip angle and pulse shape are held constant.

As formulated, the optimisation is considered for a single set of constraints ($lSAR_{max}$, $gSAR_{max}$, A), a specific pulse waveform $p(t)$, and a specific amplitude p_{max}. In order to fully explore the available solutions for a given $p(t)$, the optimisation may be solved for different values of these constraints and for multiple values of p_{max}. In practice the global SAR constraint has little effect on the solution, and the peak power constraint is a function of hardware, which is fixed throughout ($A = 20u$ for the 8-channel system used in this work with peak forward power limit of 3 kW per channel at the amplifier outputs). The local SAR constraint and pulse amplitude may both be varied, depending on the desired operating conditions – for example minimum SAR, minimum pulse duration, fixed echo time, etc. In each case the solution to the optimisation yields a particular **w** whose efficacy is evaluated by considering the resulting flip angle distribution $\boldsymbol{\theta}$ within the heart.

Doing so then theoretically enables the selection of an optimal operating point over the entire solution space essentially giving the best possible excitation conditions for imaging.

6.4.3 Operating Point Error

The cost function (Equation 6.12) is set up to minimise the total squared deviation (i.e. the mean squared error (MSE)) between the achieved and target flip angles in space. This term can further be decomposed into a term related to variance and a term related to bias (squared error in the mean) [115]:

$$MSE(\theta, \theta_T) = Var(\theta) + (Bias(\theta, \theta_T))^2 \tag{6.14}$$

with bias and MSE defined as follows:

$$MSE(\theta, \theta_T) = \frac{1}{n}\sum_{i=1}^{n}(\theta_i - \theta_T)^2 \tag{6.15a}$$

$$Bias(\theta, \theta_T) = \theta_T - \overline{\theta} \tag{6.15b}$$

where the sums run over the n voxels included within the optimisation ROI. In practice it is desirable to minimise both variance and bias in achieved flip angle.

The RF power optimisation step employed by standard single-channel transmit MRI effectively plays the same role as the minimisation in Equation 6.12, and is subject to the same constraints, except that $\mathbf{w} = d\,\mathbf{w_{quad}}$ – i.e. now only the single parameter d can be varied. As such it is not possible to alter the variance of the flip angle distribution, instead the bias is minimised via appropriate scaling. On the other hand, the more complex RF shimming optimisation may reduce the variance at the expense of non-zero bias. Selection of a suitable solution in part

relies on selecting which of these two terms is more important.

For this study, solutions were selected with maximum bias 5 %. For fair comparison, quadrature mode acquisitions were run using solutions with the same 5 % bias, subject to the peak power constraint (if exceeded, the quadrature solution with maximum allowable peak power was selected). This amounts to performing the scanner's conventional power optimisation manually. Doing so is necessary as the conventional process was found to yield suboptimal operating conditions. The reason for this is because the conventional power optimisation depends on assessing whether an integrated signal quantity achieves the correct flip angle [116]. However as this signal is integrated through a slice over the whole field of view, this is prone to error – particularly for body imaging – and has generally been found to yield biases of up to 40 % within the cardiac region, meaning that the achieved flip angle within the heart is far lower than desired.

6.4.4 Cardiac B_1^+ Mapping

To perform the desired constrained optimisation, it was necessary to be able to measure the B_1^+ field within the heart produced by each independent channel of the transmit array. There are a number of methods available to do this as previously discussed in Section 2.4.2. However, measuring B_1^+ within the heart is more challenging because of cardiac and respiratory motion, and blood flow.

Previously the saturated double angle method (SDAM) has been used by other groups for absolute B_1^+ mapping at 3 T and was shown to give accurate maps over the whole heart [101, 113]. To do so requires the use of a fast readout k-space trajectory such as echo planar imaging (EPI) or a spiral trajectory. However even with a fast readout, SDAM is still relatively slow requiring around 5 s to obtain a two dimensional B_1^+ map. For cardiac imaging the entire map should be acquired in a breath-hold so acquiring absolute maps of all eight PTx channels would require an unacceptably long breath-hold of > 40 s.

This issue can be circumvented to some degree by acquiring one B_1^+ map in quadrature mode with all PTx channels active, and then performing linear combinations of the eight channels in a separate acquisition acquiring a series of low flip angle spoiled gradient echo (SPGR) images. These can then be used as relative measures against the absolute quadrature B_1^+ map using the linearity of the PTx system to produce the independent channel maps [117].

The other candidate for a suitable B_1^+ mapping technique was DREAM [19] which, as mentioned in Chapter 2, enables extremely fast acquisition of B_1^+ maps. This allows the acquisition of eight maps in under 11 s which should be a manageable breath-hold even for most cardiac patients. However DREAM is sensitive

to flow so the B_1^+ within the blood pool of the heart is not captured correctly.

To assess which B_1^+ mapping sequence would be most appropriate to use in this study, some preliminary experiments were performed with B_1^+ maps acquired on all transmit channels using SDAM and DREAM. In each case a quadrature B_1^+ map in an axial slice through the body was acquired and then a set of low flip angle SPGRs were used to infer the individual channel maps.

The B_1^+ mapping experiments were performed in vivo on a healthy, male volunteer. All acquisitions were performed in a single breath-hold and triggered at mid-diastole using a four lead vector-cardiogram (VCG). At the time of these experiments a cardiac receive coil was not available so the experiments were performed whilst receiving on the MBC.

SDAM maps were acquired using a segmented EPI readout with target flip angle = 90°, nominal slice thickness = 10 mm, EPI speed-up factor = 3, number of signal averages (NSA) = 4, and a 700 ms saturation delay with the VCG trigger set to include this. The total scan time was 20 s for a quadrature excitation map with the four averages. DREAM maps were acquired with a target STEAM flip angle = 60°, imaging flip angle = 15° and slice thickness = 10 mm. This produced a total scan time of 0.8 s. A series of nine (quadrature plus eight linear combinations) low flip angle, gradient echo scans were used to acquire the linear combination maps. These scans were gated with a 250 ms gating period and 500 ms acquisition time for a repetition time TR = 3.6 ms, echo time TE = 2.3 ms, NSA = 32 and flip angle = 10°.

Post acquisition, the linear combinations of the SPGRs were undone through a matrix inversion and a pixel-wise division by the quadrature SPGR and these images were registered to the same space as the quadrature B_1^+ maps using the Image Registration Toolkit [118].

The SDAM maps are also susceptible to errors from slice profile effects so these were corrected for in a similar way to that shown in Reference [119]. Bloch simulations were run for the RF pulses used in the experiments and a lookup table was produced for different values of a simulated constant B_1^+ sensitivity map. Values from the lookup table were referred back to values in measured data assuming no variation in the applied excitation pulse through the acquisition slice.

The resultant individual channel maps are shown in Figure 6.1. All of the maps have low SNR due to the MBC being used for data acquisition. In later experiments for this study using online RF shimming a cardiac receive coil was used thus circumventing this issue. Despite this, it can be seen that there is good correspondence between the two datasets from the different mapping techniques.

DREAM is seen to have considerably better SNR compared with SDAM especially when considering that under the same hardware conditions SDAM also

had four signal averages whereas DREAM only had one. The reason for lower SNR in the SDAM maps is primarily due to the saturation pulse being used – this does not necessarily enable full longitudinal recovery so the amount of signal being produced is generally much lower after the initial RF pulse. This provides a

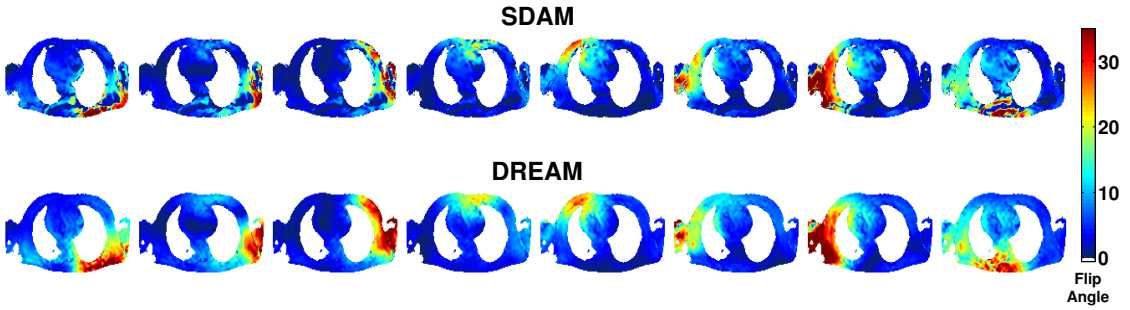

Figure 6.1: Flip angle maps in an axial slice through the heart of all eight transmit channels shown for SDAM (top) and DREAM (bottom). The channels are shown from 1 to 8 going left to right. N.B. these maps were acquired with the subject laying feet first in the scanner which does not correspond with the SAR maps or any later experiment hence the different orientation of the heart compared with other figures in this chapter.

key reason to use DREAM and crucially the speed of the DREAM sequence also means that linear combinations of the B_1^+ maps themselves could be acquired directly so only one acquisition would be needed to capture the channel maps. Whereas SDAM would always require a second acquisition for the SPGRs; plus more time would be needed for the post processing steps of slice profile correction and registering the SPGRs to the same space.

For these reasons it was decided to use DREAM for the experiments in this study. The downside to using DREAM is that the B_1^+ is incorrectly shown to be very low in the blood pool within the heart. However this low signal means it is relatively easy to manually mask out and not include in a shimming optimisation.

6.4.5 Receiver Phase Shim

When beginning in vivo cardiac imaging experiments, it was found that there was a region of low signal within the heart when using SENSE for the acquisition. This was due to the per-channel receiver phase configuration on the MBC – the SENSE reference scan uses image profiles received from the body coil to calculate receiver coil sensitivities for the SENSE reconstruction. The relative phases between receive channels had been optimised for head imaging hence this configuration was not optimal for cardiac imaging.

The left column of Figure 6.2 shows the region of low signal produced by using this nominal configuration for the SENSE reference scan in a TFE acquisition for two different cardiac views. Although the receiver coil used to acquire this

data was a 6-channel cardiac coil, the act of using SENSE (factor 1.5) for the acquisition has produced a region of very low signal.

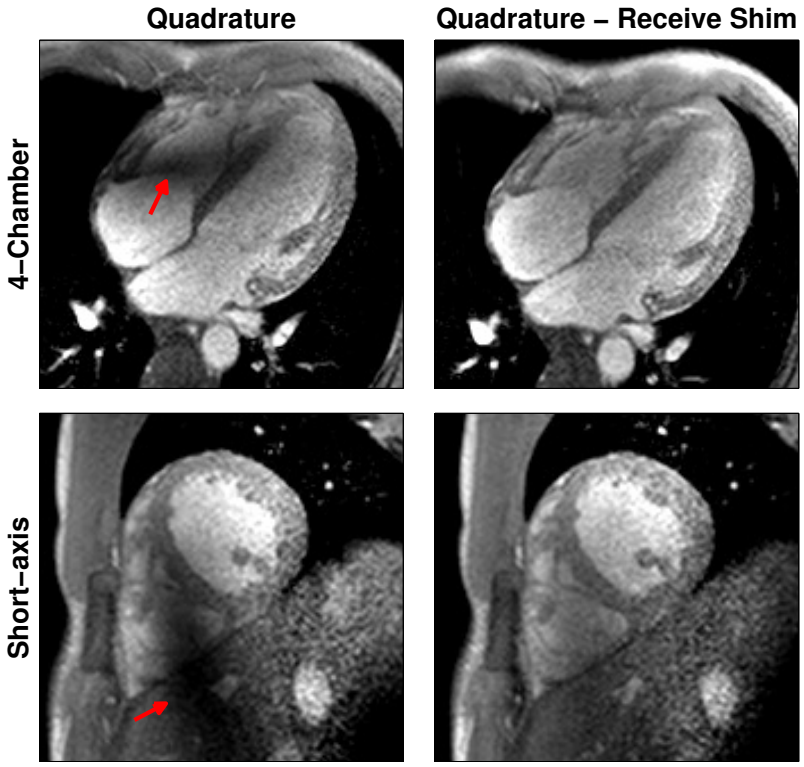

Figure 6.2: The left column shows the region of low signal caused by the low receive sensitivity on the MBC. The region is indicated with a red arrow for a four-chamber (top) and short-axis (bottom) cardiac view when transmitting in quadrature mode for a larger subject. The right column shows the same views after the receive phases on the body coil channels have been adjusted to account for the low sensitivity region.

To remove this artefact, a series of gradient echo images were acquired individually on each channel of the MBC. A basic constrained optimisation was set up (using MATLAB's `fmincon` function) to find a set of relative phases between receive channels that minimised the coefficient of variation of the signal in the region encompassing the heart. The receiver phase configuration was found for the short-axis view in a single smaller subject. In Figure 6.3 the overall image amplitude measured on the MBC using the standard receive phase configuration is shown on the left as a heat map and the amplitude with the optimised phases is shown on the right. It is clear that the optimised phases dramatically improve the overall signal homogeneity as desired.

This optimisation was performed once in a separate exam for a single subject but the same configuration was found to be equally effective for any cardiac view and for all subjects imaged with this phase configuration. This can be seen on the right side of Figure 6.2 where the cardiac images in both views for a larger subject are shown with the optimal receiver phase configuration applied and it is

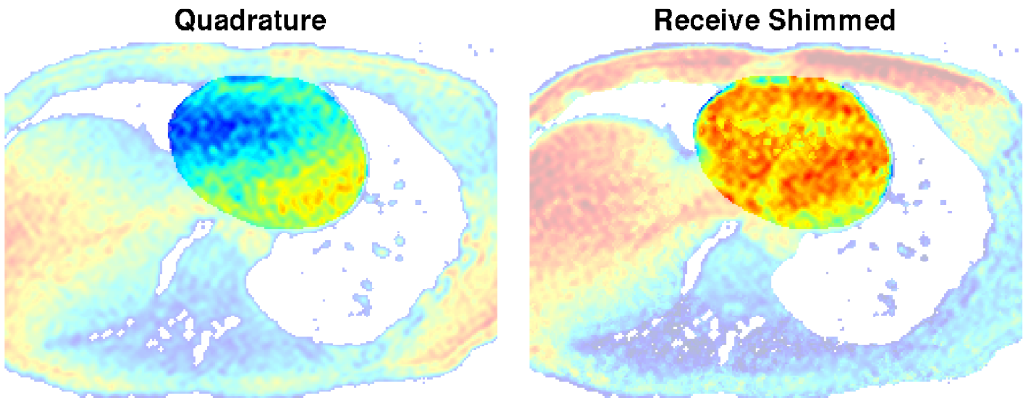

Figure 6.3: Overall image signal amplitude shown in arbitrary units from all channels when receiving on the MBC. Images are shown for the standard receive phase configuration (left) and with the optimised receive phases (right). The region used for optimisation has been highlighted to distinguish it from the rest of the image.

clear that the region of low signal caused by the SENSE reconstruction has been removed completely.

6.4.6 Integration with Scanner Software

The shimming optimisation and SAR calculations were all performed independently using MATLAB. However the Phillips scanner software (a modified version of the Achieva software version R2.5.3) for the 8-channel MRI system does include a framework for loading Q-matrices directly into it and then calculating the SAR for any RF shim being applied to the system. A compute unified device architecture (CUDA, Nvidia Corporation) framework has also been implemented by the Phillips Hamburg group [58] which parallelises the act of running through all Q-matrices for a given RF shim to produce SAR values meaning that VOPs are not strictly required, although they can be used for further speed-up.

In light of this, the heart-centred NORMAN model (described in the previous chapter) was loaded onto the scanner in order to allow online calculation of SAR values for any pulse sequence. However this was not used for the experimental work described here as the current implementation of this SAR framework utilises a normalisation which has been found to be unreliable. In future the implementation will be altered in light of the methods detailed in this study.

6.5 Methods

Simulations and experiments were performed to test the framework outlined above. All experiments were performed on a Philips Achieva 3 T system fitted with the MBC [91], and a 6-channel cardiac receive coil was used for signal reception.

Research ethics committee approval was obtained for the study; all participants gave written informed consent prior to enrolment.

6.5.1 EM Simulations

The EM simulations used to generate SAR estimates for this work were two of those created in Chapter 5 – one using the standard NORMAN voxel model, and the other using the enlarged NORMAN model with both models shown previously in Figure 5.9. These represent adult males of body mass index (BMI) 23.5 and 31 respectively. The simulations were run exactly as described in the previous chapter with the two voxel models positioned heart centred in the MBC and the EM fields calculated using CST Microwave Studio.

EM fields were extracted from the simulations with the electric fields used to produce Q-matrices which were then compressed down into two sets of VOPs – one set with a 3 % overestimate (419 and 314 VOPs for the smaller and larger model respectively) which were used to speed up optimisation calculation times, and another set with a 1 % overestimate (3658 and 2673 VOPs for the smaller and larger model respectively) used for more accurate SAR estimates for selected solutions from the optimisation.

These were then normalised such that the B_1^+ fields from the simulation produced a quadrature mode when driven with unit amplitude on each channel as described earlier in this chapter.

A generic 2-channel birdcage coil – as are now commonly used in 3 T MRI systems – was also simulated. Specifically this was a circular, band-pass coil of diameter 0.6 m composed of 16 rungs which was tuned to 128 MHz. SAR calculations were performed using the standard NORMAN voxel model. There are more details on this simulation in Chapter 8. This model was used to assess SAR constrained RF shimming performance with a 2-channel birdcage system against an 8-channel TEM array system; in the case of the birdcage system all of the outlined terminology still applies, except $\mathbf{w}$ becomes a two element vector and $\mathbf{w}_{quad} = [1 \; e^{-i\pi/2}]$. The birdcage model was used for simulated comparisons only – all physical experiments used the 8-channel MBC.

6.5.2 Optimisation

The minimisation outlined in Equation 6.12 was performed using the variable exchange method [43] which iteratively updates $\mathbf{z}$ while optimising $\mathbf{w}$ in an inner loop. This inner step was performed using the CVX convex programming interface [99, 100] with the SeDuMi [120] solver. Constrained optimisations for these types of problems are inherently time intensive as all the constraints must be

evaluated at each optimisation step [41]. As mentioned above, in order to speed up the optimisation run time, the 3 % overestimate bound set of VOPs was used within the optimisation; the reported local SAR values for the solution were then calculated with the 1 % overestimate set.

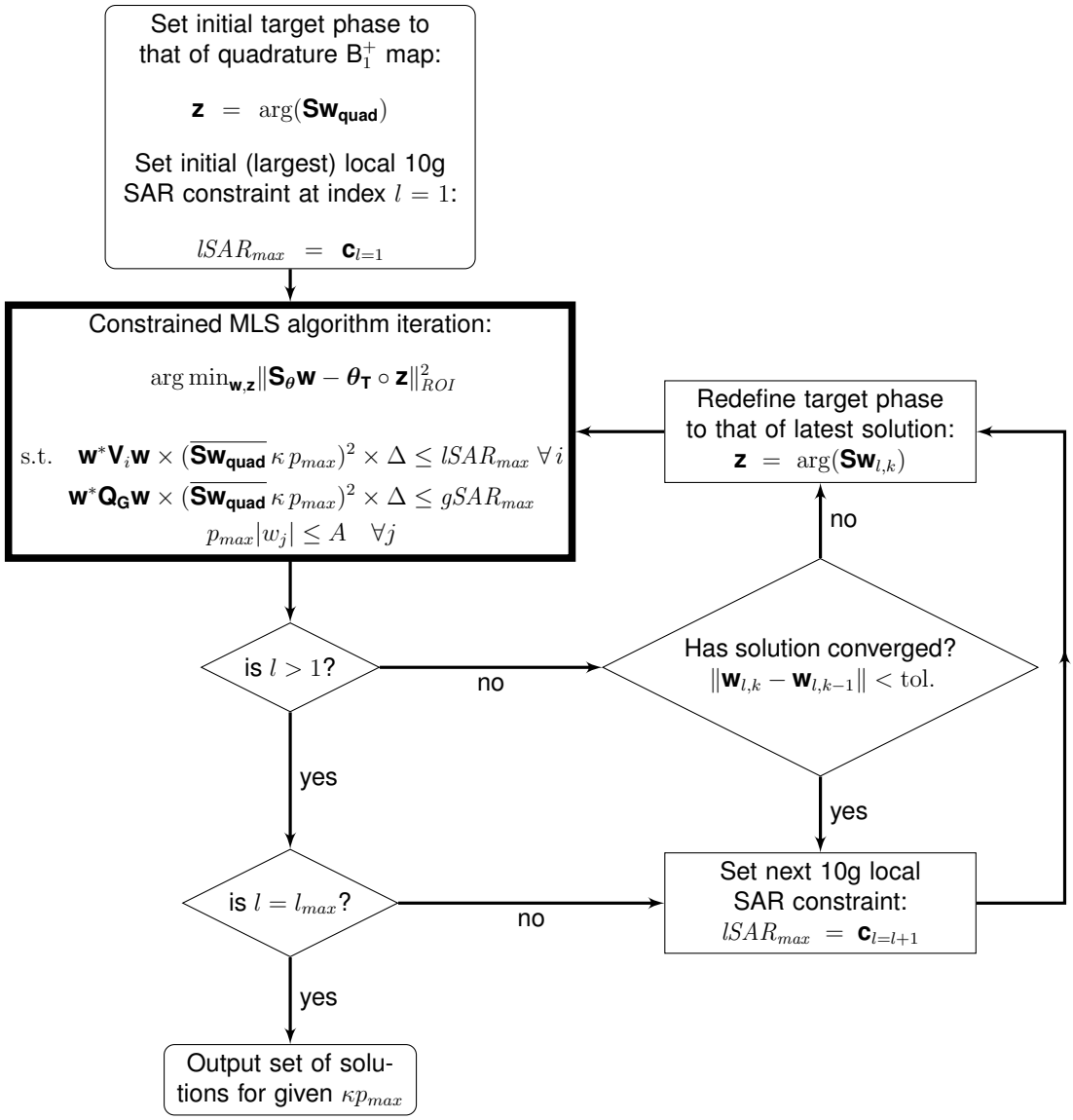

Figure 6.4: Constrained MLS optimisation flowchart for a single κp_{max} value. The algorithm iterates through decreasing local 10g SAR constraints defined in a vector **c** beforehand. After the first local SAR constraint solution has been found, no further phase iterations are run through and the algorithm proceeds to the next constraint and sets the target phase to that of the previous solution. The final output is a set of solutions that form an L-curve. This full sequence could then be iterated for a set of κp_{max} values to generate a full solution space.

Optimisations were performed offline for a large range of pulse amplitude and local SAR constraints. This could not be completed within a feasible duration for online scanning in vivo. Instead during imaging experiments the optimisations were performed for fixed pulse amplitude κp_{max} = 4.6 µT; selected as it gave

generally good performance across multiple subjects under different loading conditions in test experiments. The optimisation was performed for multiple different $lSAR_{max}$; the solution with the lowest $lSAR_{max}$ with bias less than or equal to 5 % was selected for imaging.

Optimisation for multiple $lSAR_{max}$ values, for a given κp_{max}, was accelerated by performing the stated MLS variable exchange optimisation only for the highest value of $lSAR_{max}$ (10 W kg^{-1}). The optimal phase pattern obtained was then propagated as the target phase for subsequent optimisations with lower $lSAR_{max}$ – the flow chart outlining this procedure can be seen in Figure 6.4. In this way constrained solutions for six different local SAR constraints for a single κp_{max} value could be obtained in under two minutes thus producing an L-curve of local SAR against B_1^+ error for the given RF pulse parameters.

6.5.3 Imaging Experiments

Cardiac imaging experiments were performed on seven male subjects in total and they were matched to the corresponding SAR model according to their body mass index. Five subjects (mean BMI 22 ± 2.2) were matched to the smaller model. The other two subjects had BMI values of 30 and 31 and were matched to the larger model, with the latter of these scanned twice.

B_1^+ maps were acquired for all subjects using DREAM. Single channel maps were obtained by mapping eight linear combinations of channels in order to increase SNR [121, 122] – the combinations were acquired with all channels active but one channel set to negative amplitude in an “all but one” manner. Each acquisition of linear combinations was performed in a single shot such that all channels were mapped within a single breath hold of duration < 11 s. DREAM imaging parameters were: imaging flip angle = 15 °, stimulated echo flip angle = 60 °, resolution = 7×7 mm, slice thickness = 8 mm. Mapping was triggered at mid-diastole using a four lead vector-cardiograph (VCG) with a 0.5 s additional delay added between each individual B_1^+ map to allow some longitudinal recovery and ensure one acquisition per heartbeat. Slices were acquired in the 4-chamber standard radiological view.

Imaging was performed in the same 4-chamber view using a T_1 weighted turbo field echo CINE sequence with parameters: TFE factor = 7, flip angle = 15 °, TE = 2.4 ms, TR = 6 ms, SENSE factor = 1.5, resolution = 1.8×1.8 mm, and slice thickness = 8 mm. The selected pulse had parameters $\delta_1 = 0.35$, $\delta_2 = 0.29$, giving duty cycle = 2.94×10^{-2} for this sequence. Scans were performed within single breath-holds with duration 15-20 s depending on FOV and subjects’ heart rates, and were retrospectively gated using 30 heart phases.

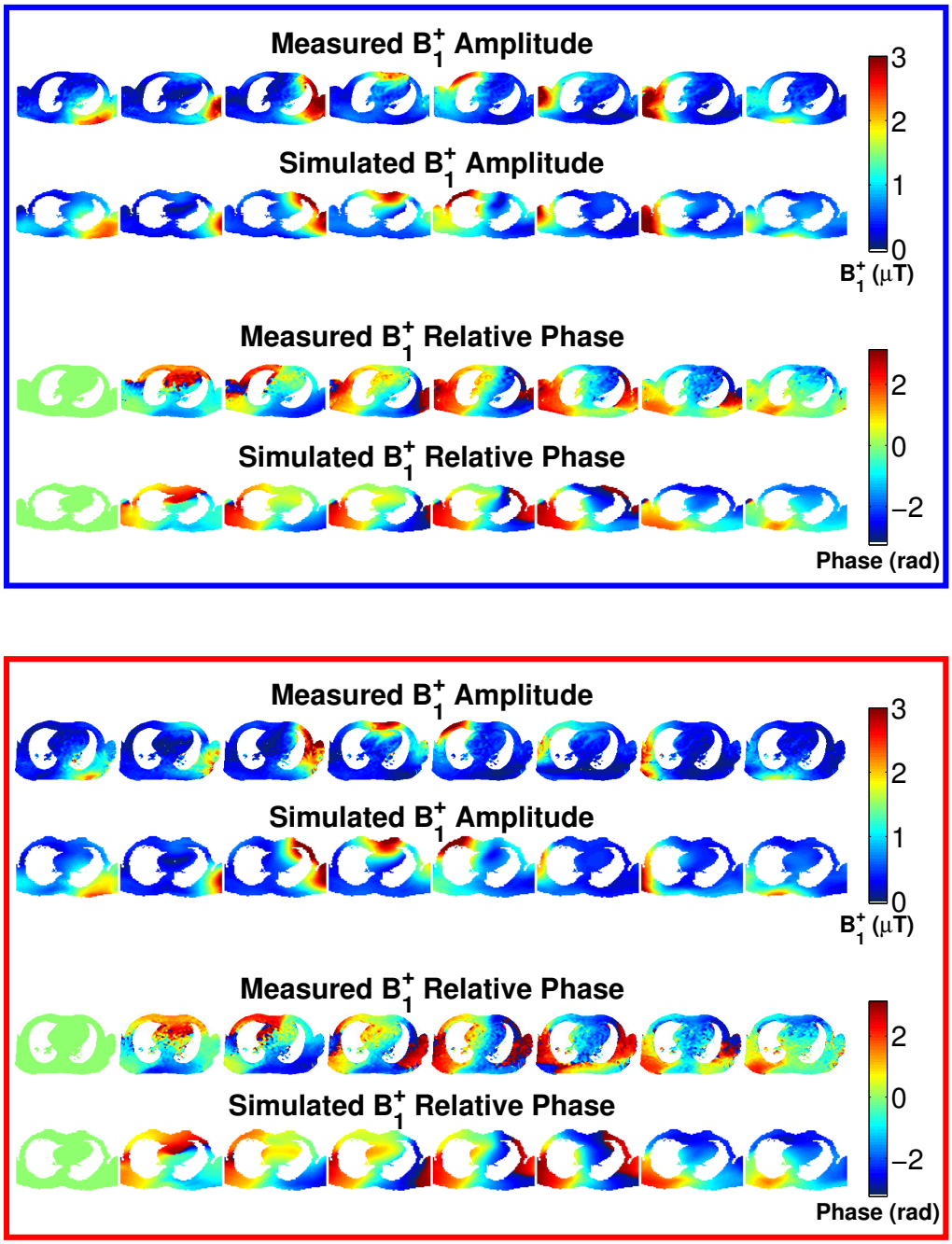

Figure 6.5: B_1^+ magnitude and relative phase (relative to channel 1) shown in 4-chamber view for the small subject/model (top, blue box) and large subject/model (bottom, red box). In each box the in vivo maps measured in a subject are shown above the simulated maps from the corresponding EM model.

6.6 Results

Figure 6.5 compares simulated per-channel B_1^+ fields in a 4-chamber view of the heart from both voxel models with those measured in a smaller and larger subject in vivo. It can be seen that there is good qualitative agreement between the in vivo measured fields and their corresponding simulated fields.

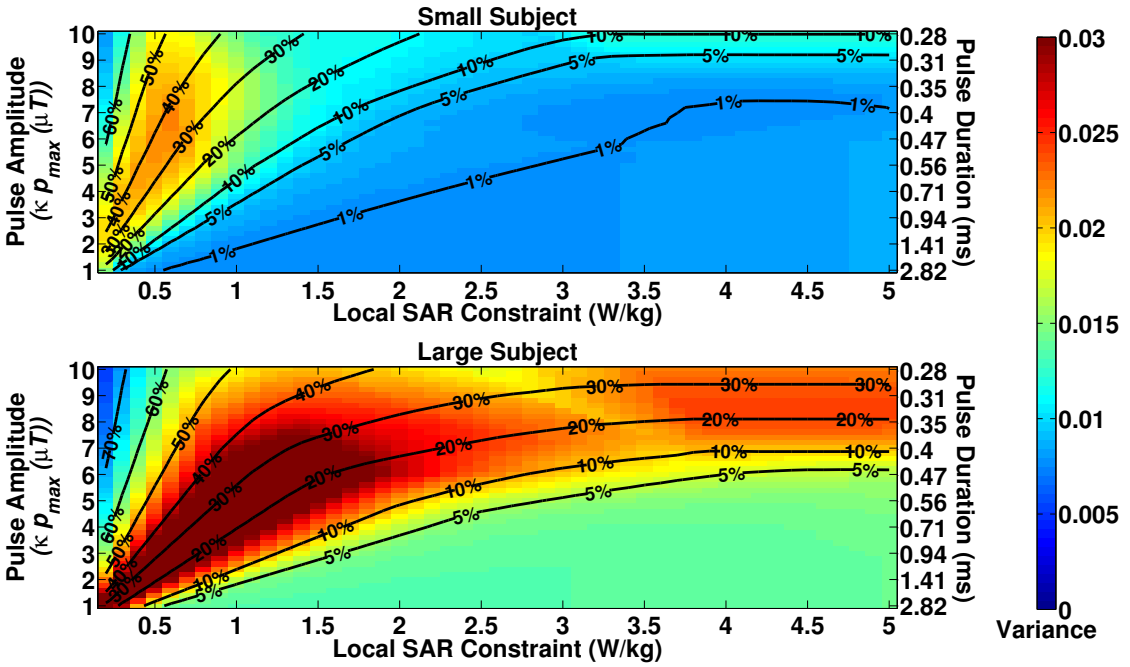

Figure 6.6: Two dimensional solution space shown for a small subject/model (top) and a large subject/model (bottom). The optimisation solution properties are shown for each local 10g SAR constraint on the x-axis and for each pulse amplitude on the y-axis along with the corresponding pulse duration on the alternate y-axis. The heat map on the plots shows the variance for the solutions with the ROI and the contours show the percentage mean bias in the ROI relative to the desired pulse amplitude.

To fully characterise the performance of the optimisation, it was run for one small and one large subject for a range of pulse amplitudes and local SAR constraints. Figure 6.6 presents the results for these calculations. Each point on these two dimensional plots corresponds to a separate local SAR constraint (horizontal axis) and pulse amplitude κp_{max} (vertical axis, given in units of μT). The heat map indicates the variance and the contours indicate the bias of the obtained flip angle within the ROI (bias is quoted as percentage of θ_T). It can be seen that as the desired pulse amplitude is increased, it becomes more difficult to achieve good solutions when considering both variance and bias together. The higher SAR and greater power required to achieve the correct flip angle within the larger subject means that it is more difficult to find good solutions compared with the smaller subject.

The plots shown in Figure 6.7 display the corresponding values that would be obtained in quadrature mode (i.e. without performing the RF shimming optimisation). The SAR values increase linearly as the pulse amplitude is increased until the RF amplifier limits are hit, and then the SAR begins to decrease as $1/p_{max}$ as it is governed by the reciprocal relationship with the maximum RF amplifier output A. The bias stays fixed at the target 5 % level until the amplifier limits no longer allow this. As the larger subject requires more power to achieve the desired level,

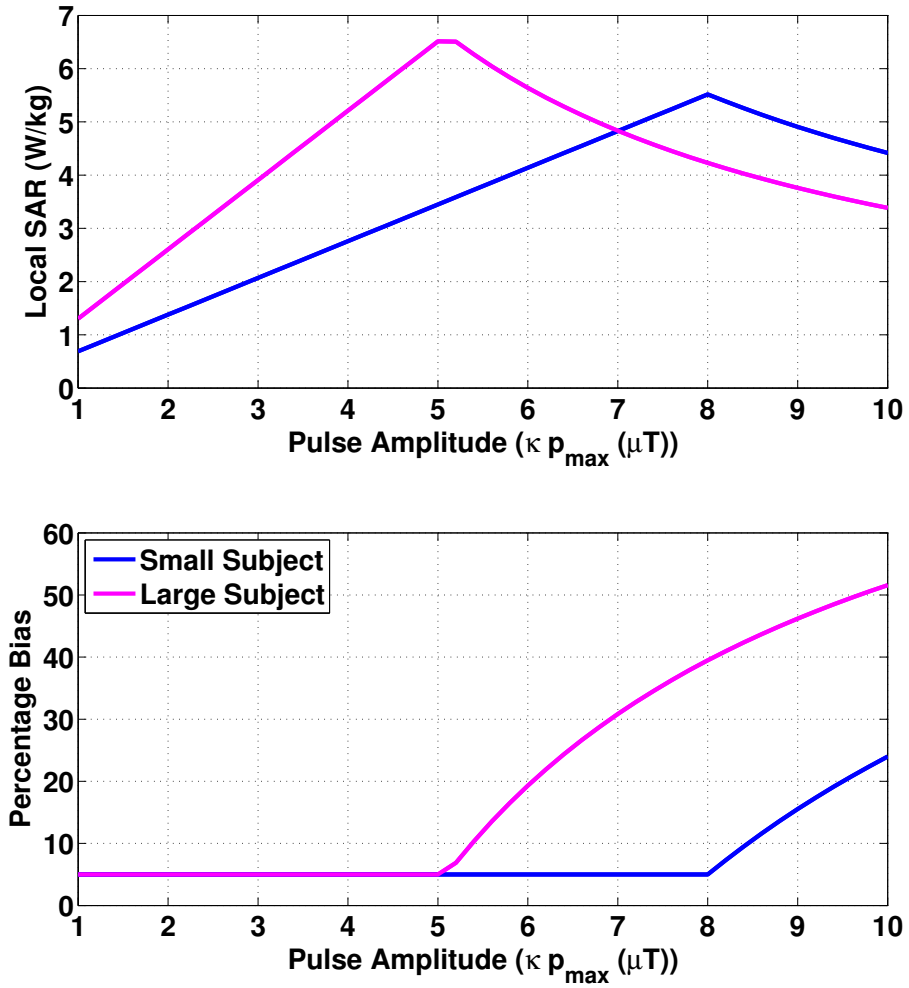

Figure 6.7: Plots of the quadrature mode local SAR (top) and percentage bias in ROI (bottom) as the desired pulse amplitude is increased. The blues lines correspond to the small subject and the magenta lines correspond to the large subject.

their variance deviates from the desired value at a lower pulse amplitude than for the smaller subject.

Figures 6.8 and 6.9 show L-curves for all subjects in two scenarios – a lower pulse amplitude sequence of 4.6 μT (Figure 6.8) and a higher amplitude sequence of 9 μT (Figure 6.9). The former was used for in vivo imaging. The plots show different measures of error on the x-axes against local 10g SAR on the y-axis. For the lower amplitude sequence, solutions that both reduce SAR and improve homogeneity (i.e. reduce variance) relative to the quadrature mode of the scanner can be found for every subject. The L-curves from the smaller and larger subjects naturally separate into two groups.

For the larger amplitude pulse (Figure 6.9), it was more difficult for the required B_1^+ to be achieved within the peak forward power constraint. For this pulse amplitude, standard power scaling of the quadrature mode was unable to achieve the target maximum 5 % bias. The displayed quadrature mode solutions are operat-

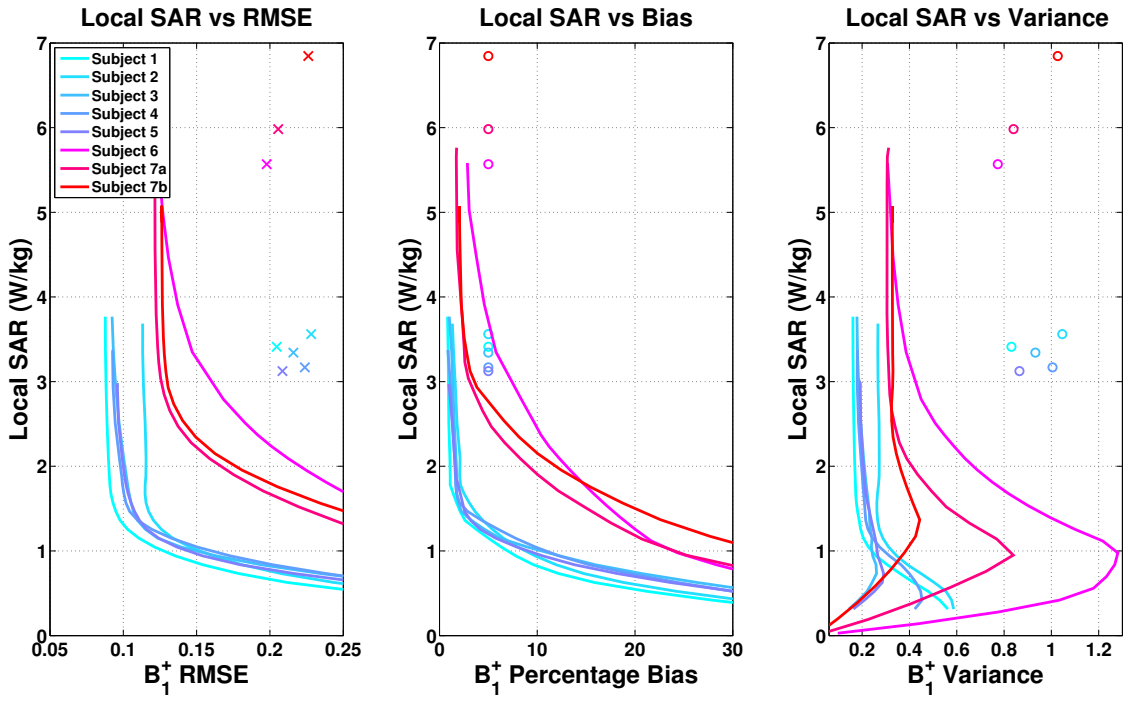

Figure 6.8: L-curves produced from measured B_1^+ data in the 4-chamber cardiac view from 7 different subjects (Subjects 1-5 are small, 6 and 7 are large; with Subject 7 scanned twice) showing the quadrature value (single points) for each subject and their L-curve (lines) for local SAR produced for a large range of local SAR constraints against RMSE (left), proportion of achieved flip angle as bias (centre) and variance (right). The results are shown for the lower amplitude 4.6 μT sequence – the quadrature points indicate those after power scaling has been performed.

ing at the peak forward power limit, but have larger bias (shown in the central plot). Somewhat counter-intuitively the larger subjects have lower SAR on average in quadrature mode, because strong loading meant that high amplitudes could not be achieved within the subjects while respecting the forward power constraint (i.e. low bias could not be achieved). After RF shimming, improvements were possible for all of the small subjects to achieve the target of 5 % bias within the peak power constraints. For the large subjects this was not possible, however RF shimming still yielded substantial improvements over quadrature mode.

Solutions yielding 5 % bias (or the minimum achievable bias if larger) are plotted on a polar plot in Figure 6.10. The maximum allowed drive corresponds to equally spaced points around a circle (black solid line). For both pulse amplitudes it is evident that there is some similarity between optimal solutions within each subject group. There is also a clear difference between the small and large subjects' sets of solutions for the lower pulse amplitude sequence. Optimal shims were able to improve MSE error in all cases with a mean improvement of 48 ± 2.6 % for the small subjects and 36 ± 5.8 % for the large subjects. They also reduced the maximum local 10g SAR by 61 ± 2.5 % and 48 ± 15.3 % for the

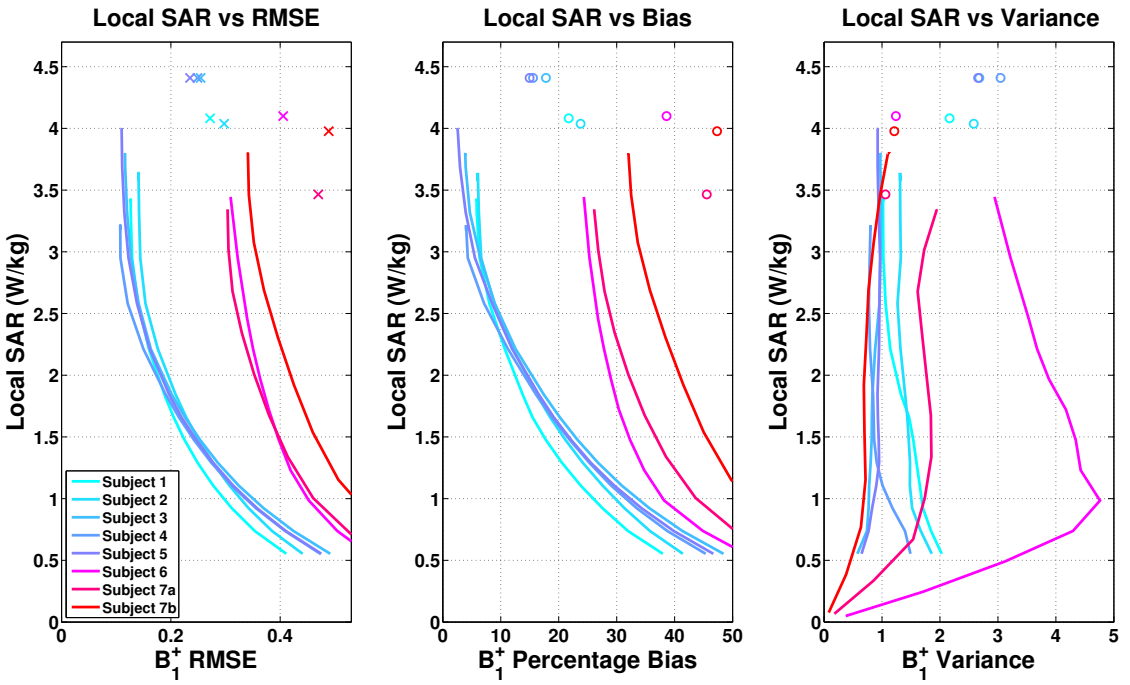

Figure 6.9: The same as for Figure 6.8 but for a pulse of 9 μT amplitude (note the different axes) – the quadrature points are shown for the maximum available drive as standard power optimisation could not be run within the amplifier limits.

small and large subjects respectively on average and global SAR was reduced by 49 ± 2.8 % and 41 ± 10.4 % on average despite not being specifically optimised for. For the 9 μT version, there is again agreement between each subject group but now the solutions are much more heavily power limited with almost all the channels running at their maximum allowed amplitudes. Nevertheless improved homogeneity for the smaller subjects was achieved – specifically the B_1^+ error was reduced by 53 ± 2.1 % and the local SAR was reduced by 22 ± 8.6 % relative to the quadrature mode. For the larger subjects, as it was not possible to achieve the required B_1^+ amplitude, the reduction in B_1^+ error was less at 30 ± 5.8 % and the local SAR reduction was 13.5 %. Across all the subjects again the global SAR was also reduced by 18 ± 5.0 %.

Figure 6.11 shows results of in vivo imaging studies for both a small (blue box) and large (red box) subject. The bottom row of Figure 6.11 shows matching B_1^+ maps for the peak pulse amplitude in each case. Clear improvements in homogeneity are apparent after RF shimming, both in the B_1^+ maps and the images themselves. Image contrast is substantially improved after shimming particularly at the apex of the heart in both examples, highlighted by red arrows; the B_1^+ maps show this was significantly lower in quadrature mode. The larger subject data shows lower SNR due to greater loading of the receive coil by the subject.

Figure 6.12 shows local 10g SAR maximum intensity projections for both small and large models using the values produced from the in vivo data shown in Figure

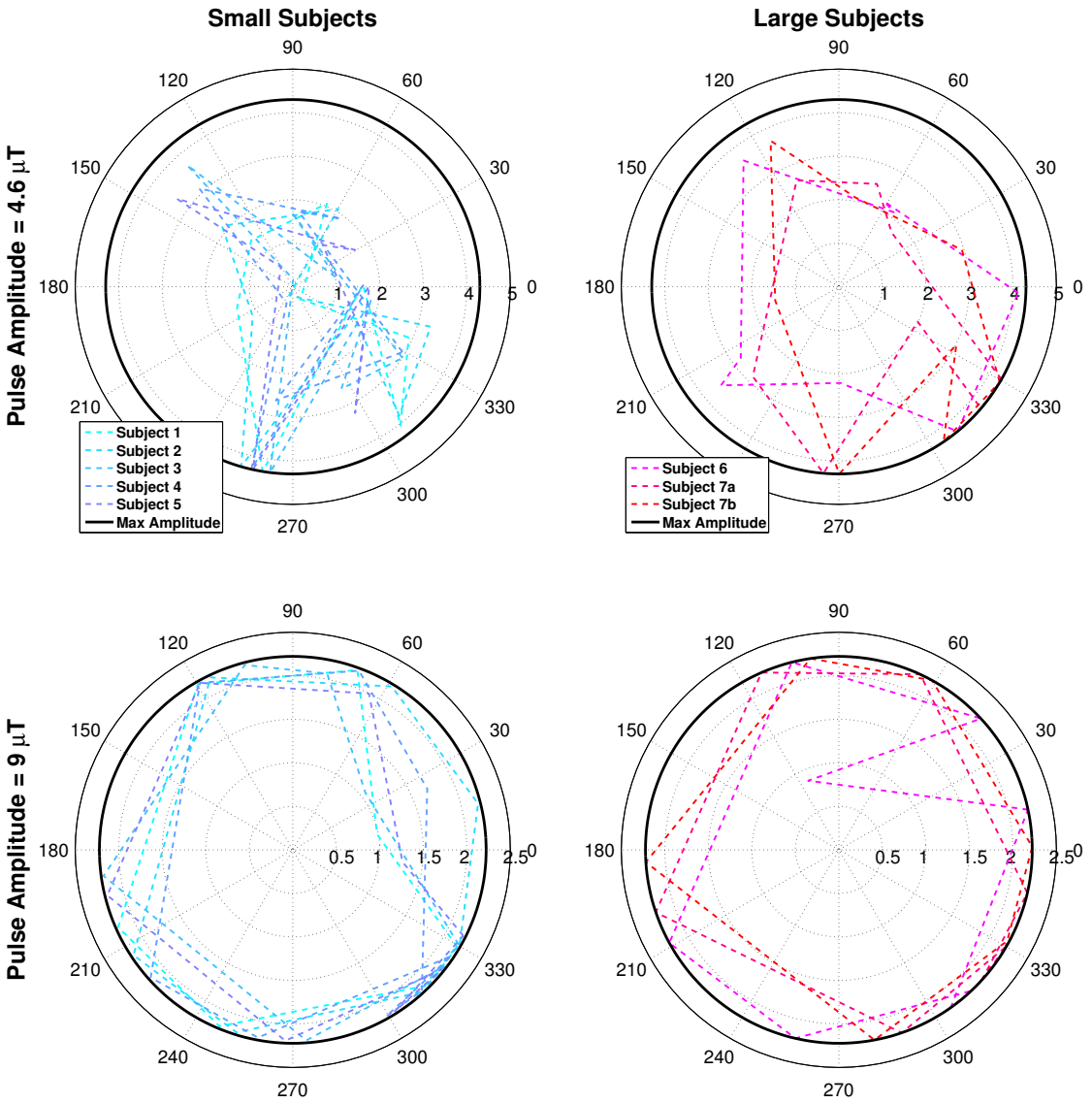

Figure 6.10: Polar plot of complex shims from the optimisation for the smaller subjects (left) and larger subjects (right) – minimum local SAR solutions achieving maximum 5% bias in flip angle (or smallest possible if larger than 5%). Top row solutions are for pulse amplitude 4.6 μT, bottom row for 9 μT.

6.11. The quadrature SAR maps are scaled to achieve the desired 5 % bias and the shimmed maps use the shimming solutions found. The large decrease in SAR is clearly evident.

This study has focused primarily on a prototype 8-channel TEM transmit coil, however similar methods could be applied to 2-channel birdcage devices that are currently available for use clinically. Figure 6.13 shows a simulated comparison between the two types of device, for the optimisation with pulse amplitude 4.6 μT. Since loading effects and peak power constraints would differ between these two types of device, the results in Figure 6.13 were computed with no peak power constraint. The results indicate that local SAR in quadrature mode is similar for

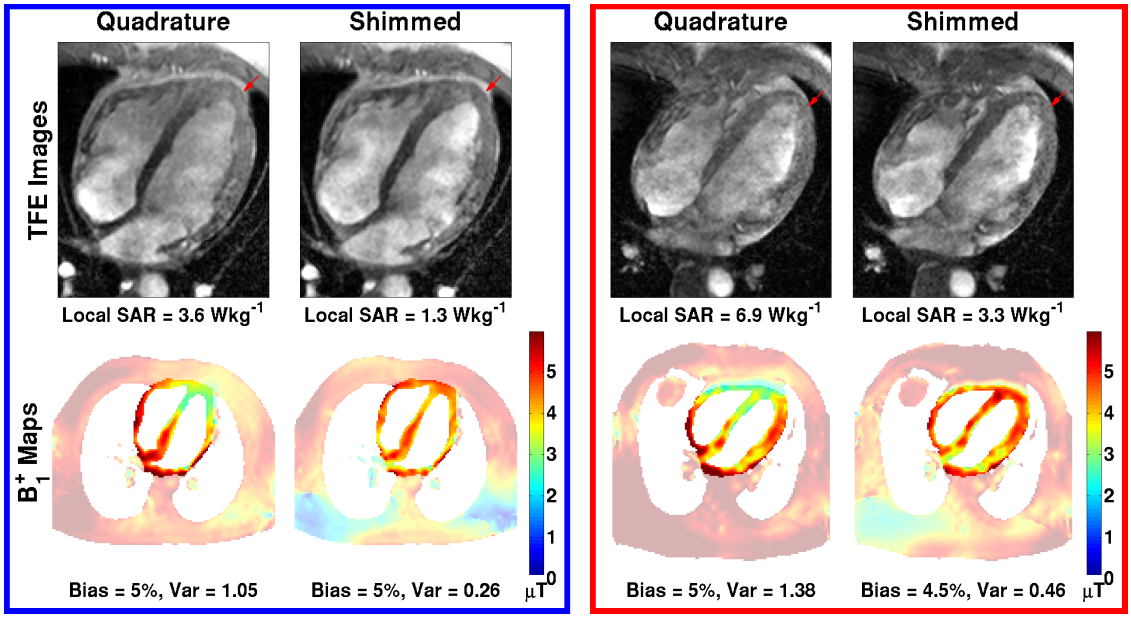

Figure 6.11: TFE imaging data (top row) and B_1^+ maps (bottom row) for a small (blue box) and large (red box) subject. Data are shown for quadrature mode with the amplifier drives scaled to achieve the desired 5 % bias and with the optimal RF shims applied. Greater contrast is seen in the TFE images after shimming, particularly in the apex of the heart (indicated with red arrows).

the two devices, with the 8-channel device being 8 % higher. The 8-channel coil produces better solutions with regard to both SAR reduction and improvement in B_1^+ homogeneity compared with the 2-channel coil. However the 2-channel system is able to achieve marked improvements for this localised shimming.

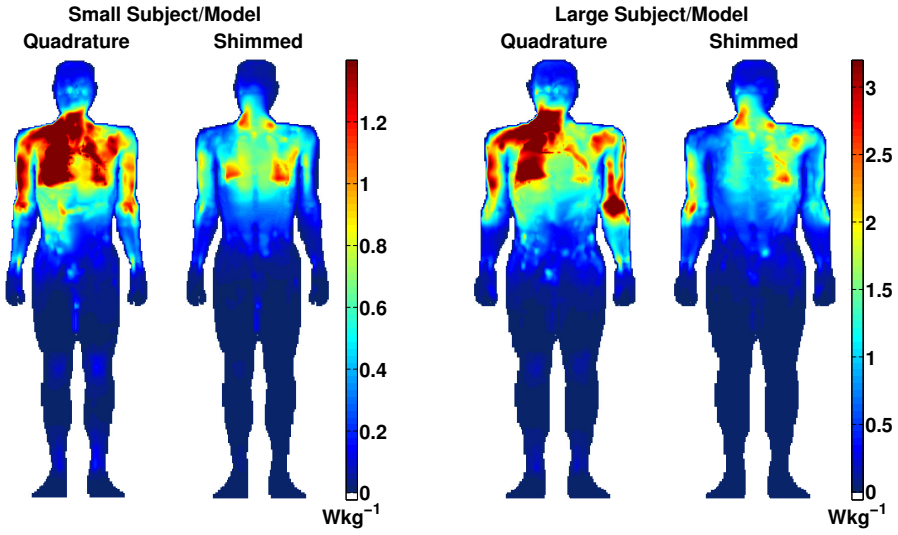

Figure 6.12: Maximum intensity projections for the small (left) and large (right) subjects' solutions from the in vivo imaging studies along with the quadrature mode scaled to the same values as for the acquisitions shown in Figure 6.11. Note the different colour scales for the two models.

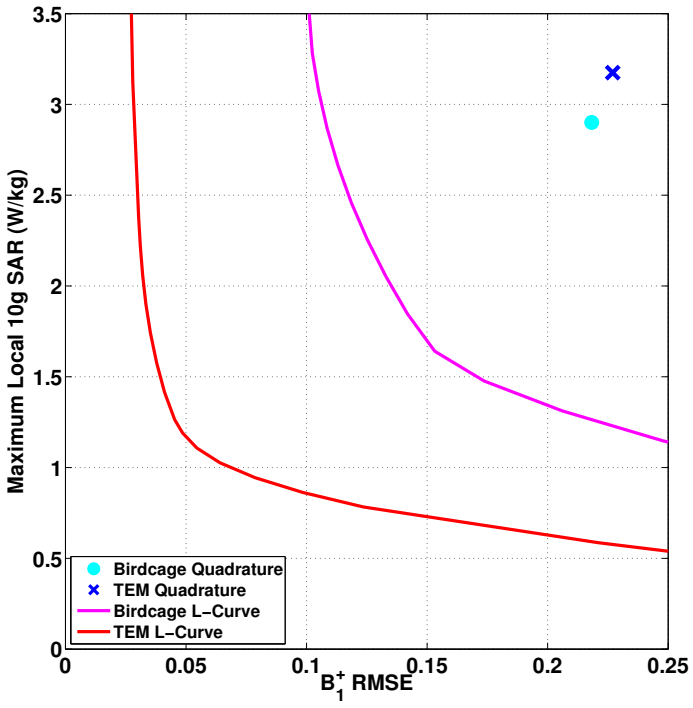

Figure 6.13: Simulated shimming L-curves and quadrature mode points shown for the 8-channel TEM coil (red line and blue cross respectively) and a 2-channel birdcage (magenta line and cyan point respectively) for the standard NORMAN model with the B_1^+ error within the heart plotted against the maximum local 10g SAR. The SAR values are calculated for the 4.6 μT amplitude TFE sequence.

6.7 Discussion

This study demonstrated the ability to substantially reduce SAR whilst simultaneously improving excitation homogeneity within strict peak power constraints for optimised cardiac imaging at 3 T. Large reductions in SAR were achieved by using 8-channel parallel transmission and by optimising flip angle distribution in a local region encompassing the heart. The imaging study with seven volunteers achieved a mean reduction in local SAR of 56 ± 10.9 % while simultaneously improving flip angle error by 43 ± 6.9 % across all subjects. Some of these results are consistent with previous work showing the benefits of in vivo 8-channel shimming at 3 T when a full field of view is to be made more homogeneous [103], but the gains in both homogeneity and SAR are greater for the presented local solutions. The problem was formulated as an "excitation optimisation" by including the ability to trade pulse amplitude/duration to lower SAR while staying within explicit hardware constraints. This is a more unified approach to RF shimming than considering only B_1^+ fields, and it enabled scans that would generally not be possible during conventional operation to proceed. This is essential for in vivo experiments with hardware constraints.

The optimisation as written can be performed for any given local SAR con-

straint and pulse waveform, which as Figure 6.6 shows, represents a two dimensional solution space. In principle the entire space could be explored by an optimisation that also takes into account additional constraints from the pulse sequence – for example the requirement for a specific echo time or pulse duration, or the trade-off between staying within the SAR limit and adding more slices, to give just two examples.

The pipeline outlined in this work could in future be added to supplement online sequence optimisation that is already performed by commercial scanner console software. Selection of the desired solution is also subject to some debate – each solution has a different bias and variance in the achieved flip angle within the target region. In order to have a more prescribed optimisation to apply online (and also in order to keep computation times manageable) the approach taken for imaging experiments was to fix the pulse amplitude, and to search for the lowest local SAR while achieving 5 % or lower bias in the achieved mean flip angle.

The optimisation was seen to be robust in terms of its inter-subject performance. It was always able to produce substantially improved flip angle distribution in the ROI within the given constraints when using an optimal solution. In this work, solutions were computed for two specific RF pulse amplitudes. Simultaneous reductions in SAR and flip angle variance were achieved for the lower amplitude pulse. The higher amplitude pulse produced less even performance, and in many cases solutions resulted in larger than ideal bias – i.e. the desired 5 % level could not be reached, particularly for the large subjects. However the solutions still always achieved improved operating conditions compared with quadrature excitation, with a mean reduction in flip angle error over all subjects of 45 ± 12.7 %, a mean local SAR reduction of 19 ± 9.4 %, and a mean global SAR reduction of 18 ± 5.0 %.

From Figure 6.6 it is clear that as the pulse amplitude increases, the optimisation struggles to achieve solutions with the required mean flip angle (i.e. low bias). As well as having generally higher SAR, the higher loading effect of the large subject on the RF coil means that there is much less “headroom” to form solutions that obey the peak power limits. Figure 6.9 shows that for the peak pulse amplitude of 9 μT the solutions are heavily influenced by this constraint. The variations in SAR performance for the different models show a need to match subject with as similar a voxel model as possible to ensure optimal performance. In Reference [64], it was shown that by warping models to their exact shape and location within the MRI scanner coil, there can be significant variations in SAR distribution thus further expressing a need for appropriate subject models. In Reference [59], it was shown that using a SAR model from a larger subject in a constrained optimisation always ensured a shim with reduced SAR. However this is clearly restrictive as

the same study showed that larger improvements were sometimes possible when using the appropriate, matching model for a given subject.

It is interesting to note that the large subject who was scanned twice – Subject 7 – produced different behaviour in terms of the optimisation for both scans (the examinations were performed several months apart). This was because the flip angle achieved within the heart in the B_1^+ maps in the second scan was considerably lower on average (i.e. there was a higher bias) than the first scan. This is likely due to different loading of the transmit coil from minor variations in the set-up and perhaps the subject's muscle/fat distribution – in the time between the two scans, this subject's appearance had changed somewhat. For the lower amplitude sequence, the L-curve was almost the same but the quadrature mode generated higher SAR as a greater drive was required to achieve the correct flip angle. For the higher amplitude sequence, the behaviour of the two datasets then diverges as the amplifier limits constrain the solutions for the high bias scan more heavily compared with the other scan. The B_1^+ maps from the other large subject (Subject 6) showed more noise leading to greater errors from increased variance in the data. Generally it can be said that the variability in the data from the large subjects is far greater than for the smaller subjects which show much better agreement in performance of the optimisation.

For the imaging experiments, improvements in flip angle homogeneity directly led to improved imaging with increased tissue signal and greater contrast clearly seen. Specifically, contrast improvements were seen at the apex of the heart in the smaller subjects. This can be seen in Figure 6.11 where the quadrature excitation shows very little delineation between blood pool and myocardium in this region; whereas the shimmed image shows clear contrast between the two. It is also interesting to note from the B_1^+ maps in Figure 6.11 that the B_1^+ magnitude is reduced substantially in some regions outside the heart – the local shim uses the available flexibility to reduce B_1^+ in areas where it is not needed so that it can be enhanced where it is needed. As these reduced regions are often close to the subjects' arms, this may correlate with solutions decreasing the drive on channels close to the arms to reduce the frequently high local SAR within the arms.

The imaging was performed with a TFE sequence in preference over bSSFP imaging as it provided a stable operating point across all subjects for comparison – it was well below the SAR limit so the scan could always be run unmodified. This would not be true for an SSFP examination as these are often run at the local SAR limit. However one of the aims of this work was to act as a proof of concept for reducing SAR in high SAR SSFP cardiac scans. Whilst the TFE sequence used to demonstrate this cannot be improved by increasing flip angle or decreasing TR after SAR reduction due to saturation effects, the methodology

outlined in this study would lead to direct improvements in SSFP scans.

Another observation from Figure 6.6 is that achieved bias is always positive – i.e. the mean achieved flip angle is always less than the desired value. The optimisation minimises RMSE, which is a composite of both bias and variance. In this framework it is not possible to force zero bias solutions, and so an arbitrary acceptable level of 5 % was used in this work. An alternative method could be to directly minimise the variance subject to the constraint of zero bias, but this would result in a non-convex optimisation which may not be possible to implement in an efficient manner.

A limitation of the online optimisation, which must be performed during the examination, is the calculation time; currently this is under two minutes for a set of six solutions with different local SAR constraints. These solutions are also just for one value of p_{max} which ideally would also be optimised for when imaging but this is not feasible under the current framework as the calculation takes much longer. The online calculation time could be reduced by more efficient implementation (the current work used the CVX software package in Matlab, which is not optimised for speed) as has shown to be possible to some degree in Reference [47]. Alternatively the process could be sped up by selecting just one local SAR constraint for which to optimise for – i.e. 50 % reduction in local SAR compared with quadrature mode. Figure 6.10 shows that the general nature of the optimal solutions found for the different groups of subjects is similar. This suggests that a generic solution could be used depending on subject size. This would mean that no optimisation would have to be run at all and furthermore, B_1^+ mapping would not need to be performed thus reducing the overall exam time. A similar result was found by Van den Berg et al. [112] using purely simulated data over multiple models and shimming over the whole slice and not just locally. A potential drawback would be that loading effects on the coil would not be reflected by the generic solution, and so the system would not always be driven effectively within peak power constraints (which are subject independent). Furthermore, all results presented were optimised for a single slice in a 4-chamber view through the heart. To find a truly optimal general configuration for cardiac imaging of any subject, optimisations including the whole heart volume would have to be explored otherwise they may not be as effective in different views; or indeed, may worsen the image quality in other cardiac views.

Whilst this study was performed at 3 T, ultra high field (UHF) MRI scanners (>7 T) are becoming more widely adopted, and these are commonly built with eight or more transmit channels. Clearly the framework outlined in this work would be even more pertinent for UHF due to the higher SAR and greater B_1^+ inhomogeneities that are seen. A simulation only study performed by another

group at 7 T with 12-channel PTx using localised SAR constrained shimming for body imaging [123] was able to produce similar SAR reductions to those seen in this study were found. Furthermore RF amplifier amplitude constraints present serious limitations on UHF imaging in general [47, 114] hence the optimisation and treatment of power limits described in this work would improve feasibility of UHF body imaging.

The RF amplifier limitations at UHF are generally due to an available power limit on what is able to be supplied by the amplifiers. This is how the peak power limitation has been represented and addressed in this work. However there is also a maximum voltage that can be applied to the RF coil itself which would produce a more dynamic constraint as it would be even more load dependent – as the coil was loaded to a greater degree, the impedance of the coil would increase and hence the applied voltage would also have to increase, meaning that voltage limits on the coil may be more easily reached with a larger load. A change in load is likely to cause issues as well: with an applied voltage, going from a loaded to unloaded situation means that the voltage on the coil components would dramatically increase and these components may be destroyed. Incorporating this constraint would be much less straightforward as an accurate measure of the coil loading would be required, so this is left for future work.

Staying at 3 T, it is also possible to compare performance of the prototype 8-channel device with more standard 2-channel birdcage systems – a scenario simulated in this work (Figure 6.13). The results showed that the two devices perform similarly when in quadrature mode, however the 8-channel device achieves 55 % greater reduction in local SAR for the same homogeneity and 73 % greater improvement in flip angle error for the same SAR when used for RF shimming. This increased performance reflects others' findings [103] but unlike Reference [103], compares physically realistic devices. The 8-channel TEM coil produces much more spatially localised RF fields than the birdcage coil, and so is better suited for the localised shimming used in this work. Still, the improvements possible with two channels are not negligible and the framework described here could also be used in standard 2-channel birdcages for conventional clinical use.

These results produced by this study indicate the potential to produce improvements in high field cardiac MRI across the board as the SAR reductions and B_1^+ improvements achieved will directly lead to imaging improvements by reducing limitations caused by these.

Chapter 7

Safe MRI with Metallic Implants

Contributions

The findings in the following chapter have been partially discussed in the following publication:

> **A. Beqiri**, J.W. Hand, J.V. Hajnal, and S.J. Malik. SAR reduction for metallic implants using volume PTx array. *Proceedings of ESMRMB 2015*

7.1 Introduction

Provided MRI scans are performed within conventional safety limits, it is unlikely that a dangerously high SAR situation will arise. However one area in which there is a great deal for concern with regard to SAR is when imaging patients with medically implanted devices such as pacemakers, catheters, guide-wires and prosthetic limbs.

Previous studies, both simulation based and experimental, have shown that at the boundary where human tissue comes into contact with electrically conductive implants, very high electric fields can be produced which will lead to significant heating within the subject [124–126].

A method was recently developed to decouple guide-wires within a patient from an RF coil using a 4-channel PTx array [127] by making measurements of the coupling to each channel of the array and then driving combinations of the channels to cancel out this coupling. This proved to be an effective way to suppress currents induced on the guide-wires by an RF coil and therefore ensure there is no significant heating at the wire tip.

In this chapter, the specific case of safe imaging of the increasing number of people with prosthetic hip implants [128] will be assessed. A simulation study was previously performed that showed high SAR can be produced within a prosthetic hip implant [6] if the implant is located in certain positions within the transmit coil – this would as mentioned lead to substantial heating.

The aim here was to generalise the PTx decoupling method described in [127] to reduce heating from larger implants which will have more complex current distributions and may not behave in such a straightforward manner. This was performed using the MBC EM model described in Chapter 5 to simulate the EM interactions with a hip prosthesis embedded within a male voxel model. The 8-channel MBC was used with its associated degrees of freedom to attempt to null the simulated electric fields around the region encompassing a hip prosthesis to ensure low SAR whilst still producing a suitable B_1^+ field for imaging.

This chapter begins with the theory behind how operating modes that do not couple to the implant can be calculated from EM field measurements. The use of these modes for shimming is then discussed before moving onto the simulation study which utilised these methods.

7.2 Decoupling with PTx Array

High electric fields around an implant induced from an RF coil will lead to greater energy deposition and hence temperature increases within a subject. Over the course of an MRI exam these temperature increases could potentially be harmful. If the electric fields around the implant could be nulled by electrically decoupling the prosthesis from the coil, this would diminish the risk of significant heating.

With a PTx coil, it is possible to assess the measure of coupling between each transmit element to the implant. Then a series of safe “null modes” [127] can be found with no measurable coupling to the implant. These modes can be used to shim the B_1^+ field whilst having very low E-field coupling and therefore low SAR.

To find these modes, first a measure of the coupling to the implant from the RF coil must be made. One practically realisable method that was recently proposed uses the local perturbation to the B_1^+ field by the implant to infer the level of coupling to the implant by the RF transmit coil [127]. This will now be described in the context of an implanted wire as in the original study and then generalised for a hip prosthesis.

The total B_1^+ field near a wire will experience a measurable perturbation provided the wire is positioned largely parallel with the B_0 field [129]. This is because the magnetic fields circulating around the wire will be primarily orientated perpendicular to the wire. Consequently this magnetic field produces only a true B_x and

B_y component if the wire is parallel to B_0. Otherwise only the projection of these components onto the plane perpendicular to B_0 can be measured.

To do this it is considered that the total field local to a wire aligned with the B_0 field within a transmit coil can be expressed from a solution to the Biot-Savart law [130] as

$$B_1^+ = -j\frac{\mu\, I_w\, e^{j\phi}}{4\pi r} e^{-j\theta} + B_1^{+\,coil} \tag{7.1}$$

where $j = \sqrt{-1}$, I_w represents the current magnitude induced on a wire and ϕ represents its temporal phase, μ is the magnetic permeability of the external medium, θ is the azimuthal polar coordinate and $B_1^{+\,coil}$ is the B_1^+ background field produced by the coil. This expression shows that for a given B_1^+ field produced by a transmit coil, there is a local, radial perturbation produced by induced currents on a wire.

As can be seen in on the left side of figure 7.1, the shaft end of the prosthesis is relatively narrow and provided the patient is lying in an MRI system in a conventional manner, the prosthesis will generally be aligned with the B_0 field. Given

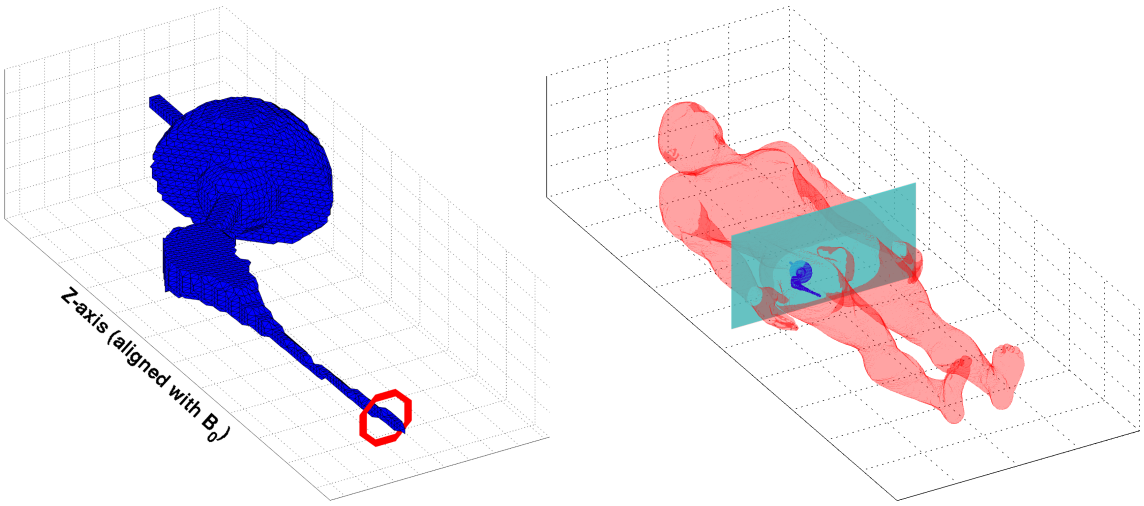

Figure 7.1: On the left is the 3D model of the prosthetic implant with the annulus region that was used to sample the B_1^+ shown in red. The location of the prosthesis within the voxel model is shown on the right along with the imaging plane used for B_1^+ shimming highlighted in light blue.

this, it is possible that the EM behaviour of the prosthesis shaft may be similar to a wire and therefore may produce a similar perturbation to the B_1^+.

Equation 7.1 can be expressed as an approximation where the B_1^+ field from the coil is estimated as a background field spatial varying as a polynomial function. If the assumption is made that the prosthesis shaft does indeed behave as a wire then the total B_1^+ field can approximately be expressed as

$$B_1^+ \approx \frac{\mu_0 I_p}{4\pi r} e^{j\phi} + f(x,y) \tag{7.2}$$

where the inferred current amplitude on the prosthesis is given by I_p and, as most dielectrics have a relative magnetic permeability of $\sim$1, μ can be substituted for the permeability of free space μ_0. The polar coordinate term may also be ignored as variations in the azimuthal angle over a discretised annulus region around the prosthesis will lead to numerical cancellations.

A least-squares fit can be used to approximate the polynomial and radial term for the full expression [127]. The various terms for this approximation are shown below:

$$B_1^+ \approx \frac{\alpha_0}{r} + \alpha_1 + \alpha_2 x + \alpha_3 y + \alpha_4 xy + \alpha_5 x^2 + \alpha_6 y^2. \tag{7.3}$$

The α_0 term produced by the fit can then be directly equated to the current on the prosthesis at this spatial location by a factor of 1×10^7. By performing the fit on a per transmit channel basis, the electrical current coupling to the prosthesis by each transmit element can be inferred therefore giving a vector of this coupling measure $\mathbf{m}_B$.

Once the coupling has been calculated, the singular modes of the system can be found. This is achieved by taking taking the singular value decomposition (SVD) of some measure of the coupling **m**. Conventionally the SVD decomposes a matrix of size $M \times N$ into three matrices that represent a rotation, a scaling and another rotation. For the coupling measure **m**, by definition this will yield the relation

$$\mathbf{m} = \mathbf{U}\boldsymbol{\Sigma}\mathbf{V}^* \tag{7.4}$$

where **U** is a unitary matrix of size $M \times M$, $\boldsymbol{\Sigma}$ is an $M \times N$ diagonal matrix of singular values of the system and **V** is a unitary matrix of size $N \times N$. For a full decomposition, the singular values defined in the diagonal of $\boldsymbol{\Sigma}$ will be comprised of M non-zero values and the remainder of zeros. In the case of a PTx array with N_c coils, **m** is a vector of size $1\times N_c$; this means there will be one non-zero singular value and N_c-1 zero valued singular values.

Each column of the matrix **V** corresponds to the complex weightings to be applied to the transmit channels of the system in order to produce each one of the N SVD modes of the system where in this case $N = N_c$. The first of these modes will correspond to the non-zero singular value and hence represents the mode with maximum measured coupling to the implant. The remaining modes correspond to the zero valued singular values. These span the nullspace of the measured coupling vector **m** and represent the modes that produce zero measured coupling to the prosthetic implant – these are referred to as the "null modes" of the system [127].

The reason why the SVD produces N_c-1 null modes from a single coupling measurement is because the measurement has rank 1, so the other N_c-1 modes

are null by definition. If the device acts in a common mode (i.e. one coupling measure is sufficient to characterise it) then the N_c-1 null modes are applicable to the whole device. However for more complex devices this may not be the case and the the N_c-1 modes may not truly act as null modes.

7.2.1 Shimming with Null Modes

Once the null modes have been calculated, complex weightings can be found to apply to them to achieve more optimal RF conditions. Essentially this can be considered as RF shimming with a set of "virtual transmit coils" in which each virtual coil is one of the N_c-1 null modes. The matrix **V** represents the transformation between the null mode virtual drives and the physical transmit coil drives.

The B_1^+ distributions from the transmit channels are configured into a matrix **A** of size $N_{ROI} \times N_c$ where N_{ROI} is the number of voxels in the region of interest for which the B_1^+ field is to be made more homogenous. $\mathbf{A}_m = \mathbf{AV}$ represents a matrix of the null modes in terms of the B_1^+ field in the region to be optimised – the high coupling mode (i.e. $\mathbf{A}_1$) is discarded for the purposes of the optimisation. The optimisation can then be formulated as shown below:

$$\mathrm{argmin}_{\mathbf{w}_m}\{\||\mathbf{A}_m\mathbf{w}_m| - \mathbf{t}\| + \lambda\|\mathbf{w}_m\|\} \tag{7.5}$$

where **t** represents a vector of length N_{ROI} of the target B_1^+ value and λ is the regularisation parameter used to tune the optimisation between favouring high power, low error solutions and low power, high error solutions. It should be noted that as this optimisation is being performed in the null mode space, the power expressed in this optimisation by $\|\mathbf{w}_m\|^2$ is not directly applicable to the total power deposition by the transmit coil, as would conventionally be the case.

After an optimal weighting $\mathbf{w}_m$ has been found, $\mathbf{w}_s = \mathbf{V}\mathbf{w}_m$ recovers the RF shims to apply to the different channels in order to use the solution provided by weighting the modes with $\mathbf{w}_m$. Then by applying $\mathbf{w}_s$ to the transmit array, this should yield a uniform B_1^+ in the region being optimised along with very low E-fields around the prosthetic implant.

7.3 Methods

To generate the EM fields required to perform the calculations described above, a full 3D EM simulation was performed using the same methodology as described in Chapter 5 for the same 8-channel parallel transmit array – the MBC. The Duke adult male voxel model [62] was simulated pelvis centred in the PTx coil with a generic hip prosthesis implanted within the model's right hand side. The three

dimensional prosthesis model can be seen on the left side of Figure 7.1 and its location within the body can be seen on the right side of the figure. The prosthesis was modelled as being made primarily of a non-ferrous Cobalt-Chromium alloy with conductivity of $1.16\times10^6\,\mathrm{Sm}^{-1}$ and density of $8425\,\mathrm{kg\,m}^{-3}$. It also has a thin polyethylene liner within it with no conductivity and density of $940\,\mathrm{kg\,m}^{-3}$.

RF shimming was optimised over the entirety of a central axial slice (highlighted in cyan on the right side of Figure 7.1) to assess how good general shimming performance was with only the null modes. The shimming optimisation shown in Equation 7.5 was performed using the multi-shift conjugate gradient least-squares method (mCGLS) [44] within an MLS-type framework [45].

7.3.1 Coupling Measurement

For the coupling measure **m**, along with the B_1^+ based measurement $\mathbf{m}_B$ another coupling measure $\mathbf{m}_E$ was produced from the electric fields. This represents an idealised measure that is most closely related to SAR deposition. However the electric fields around the implant embedded within the imaging subject cannot currently be measured in this way in reality so this is purely to assess some form of gold standard measure.

A small region of the electric fields from the EM simulation around the prosthesis was considered by assessing a set of N_v voxels. To emulate a single hypothetical measurement made of the electric field around the prosthesis for each channel, the z-component of the field produced by each individual transmit coil was numerically integrated over all voxels in the reduced region

$$m_{E,c} = \sum_{i=1}^{N_v} E_{z\,i,c} \quad c = 1, \ldots, N_c. \tag{7.6}$$

This gave a complex measure of the coupling between the implant and each channel of the transmit array from the electric fields as the vector $\mathbf{m}_E$. The region used for this was produced by taking the volume up to 1 cm away from the surface of the prosthesis – this then defined the N_v voxels.

The sampling region for the B_1^+ based measurement and least-squares fit was performed within an annulus around the shaft end of the prosthesis in a single slice of the B_1^+ data. The location of the sampled region is shown on the left side of Figure 7.1 in red.

As the radial component of the B-field is to be used for inferring the current on the implant, it is important to see how well this is captured by the fit in the region near to the annulus. This can be done by taking the terms for the polynomial found from the least-squares fit α_n and applying these directly to the co-ordinate

components in Equation 7.3. The true B_1^+ field magnitudes in the slice in the region around the annulus are shown in Figure 7.2 along with the field produced from the fitting terms; and the difference between the two. It can be seen that

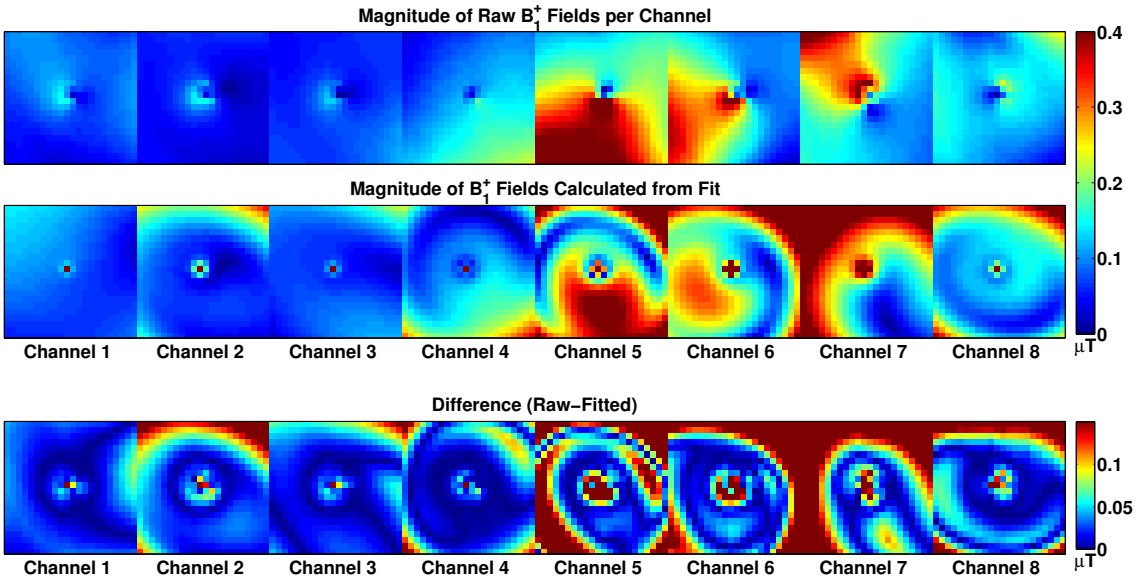

Figure 7.2: Raw B_1^+ fields (top row) and fields from produced from applying terms from least squares fit (middle row), along with the difference (raw fields minus fitted fields) between the two (bottom row). A 10 cm$\times$10 cm region around the shaft of the prosthesis is shown in each image.

the fit captures the data relatively well in the region around the prosthesis shaft (located in the centre of each channel image), but performs progressively ineffectively when moving away from the implant.

Looking at the summed total fields within the annulus only (Figure 7.3) shows that the fit performs well at capturing the data directly in the region used for the fitting. The difference between the true field and the field from the fit is also seen to be low.

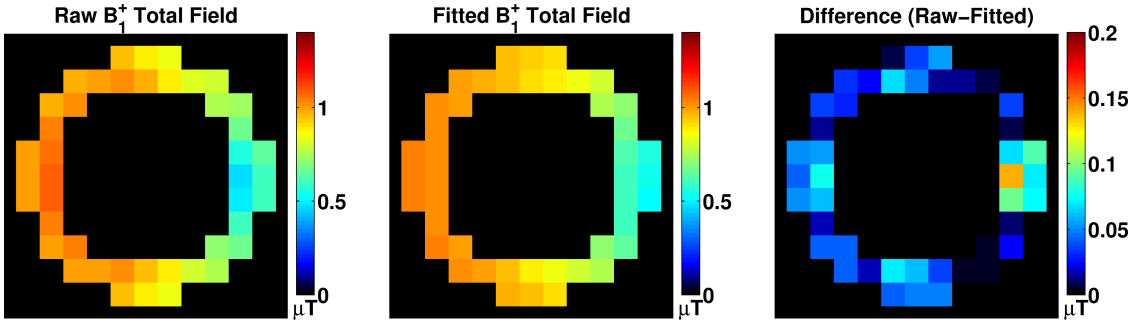

Figure 7.3: The total B_1^+ field within the annulus used for fitting for the raw B_1^+ fields (left), the fitted fields (centre) and the difference (raw minus fitted) between the two (right).

7.4 Results

The results are presented for the calculations performed for both measures of coupling. These consist of the null coupling modes and their effects on the behaviour of the B_1^+ fields as well as the total E-fields and hence SAR, and the results from using the null modes to shim the B_1^+ field.

7.4.1 Null Modes

The singular values from both coupling measures represented in the diagonal of Σ by definition yield one non-zero value corresponding to the high coupling mode for the MBC for which N_c=8 and seven null modes with singular values of zero. These are plotted in Figure 7.4 with the amplitudes normalised to the maximum in each case. Whilst these values indicate that the null coupling modes will have

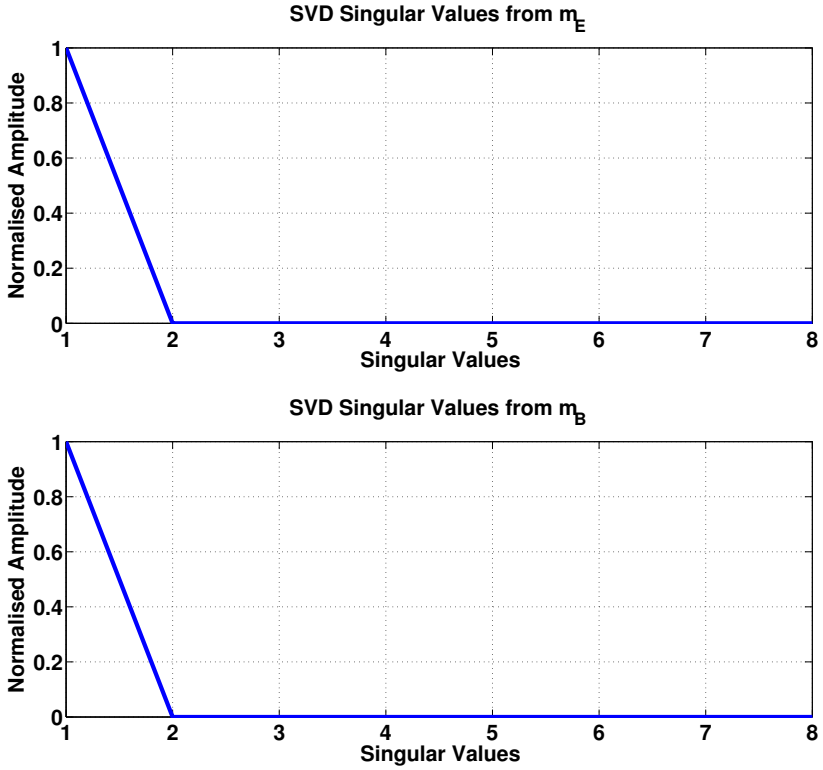

Figure 7.4: Singular values normalised to the maximum are shown for both the electric field based measurement technique (top) and theB_1^+ based measurement technique (bottom). It can be seen that the null modes yield zero amplitude with regard to the measurement itself.

absolutely zero coupling to the implant, in practice this is unlikely to be the case as the measures are single values that aim to capture complicated interactions over an object with a non-ideal structure. Therefore to directly see the level of coupling produced by each mode, the absolute magnitude of the E-fields in a maximum

intensity projection (MIP) within a cuboid region immediately around the implant for all the modes produced by both coupling measures is shown on the left side of Figure 7.5.

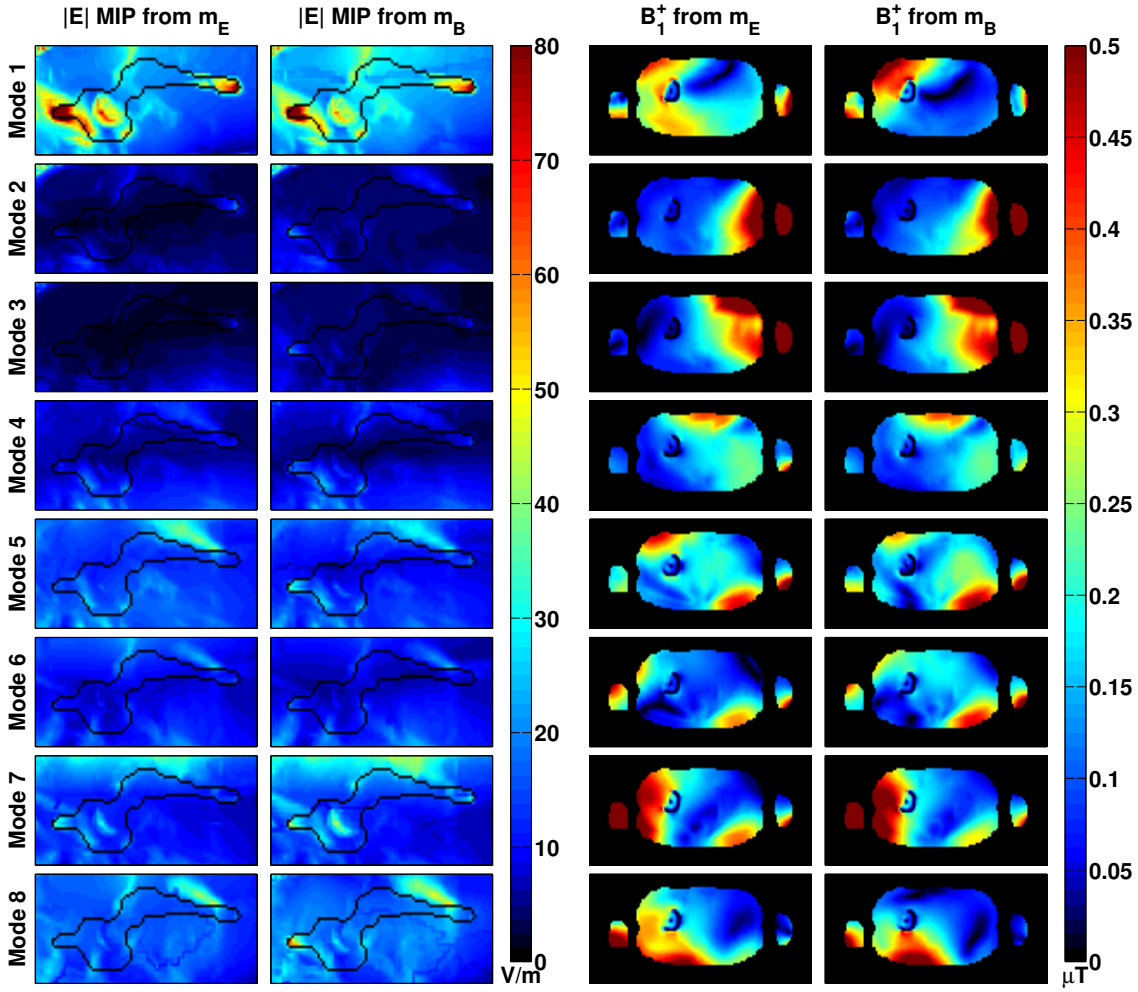

Figure 7.5: The electric fields (left) and the B_1^+ fields (right) are shown for all the SVD modes from both the electric field based measurement (left side of each column) and for the B_1^+ field based measurement (right side of each column). The null modes (i.e. modes 2-8) show electric fields with substantially reduced amplitude around the implant.

It is clear that the the first mode shows a high level of coupling with the implant as predicted by the singular values. The electric fields around the implant from the remaining modes (i.e. modes 2-8) are far lower although the null modes from the direct E-field measurement of coupling show lower amplitude of electric field around the implant than for the modes produced by the B_1^+ field based method. The B_1^+ fields from the null modes produced from both coupling measures show strong spatial localisation to the transmit coils and collectively give good coverage over the field of view thus indicating their shimming potential.

Whilst the behaviour of the E-fields shows that the null modes are effective at decoupling the coil interactions with the implant, it is not immediately clear how

this translates to SAR deposition. This is assessed in Figure 7.6 by looking at the MIP of the maximum eigenvalues of the local 10g SAR Q-matrices in the region around the implant. This shows the maximum possible level of SAR that can be produced in any situation [61]. The maximum eigenvalues are shown using all

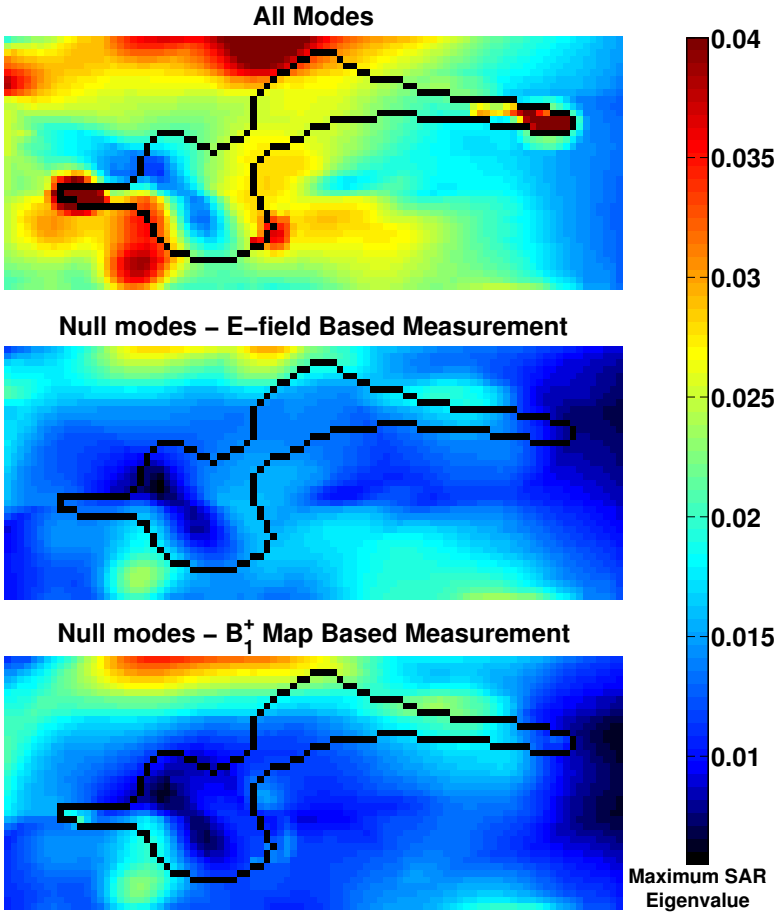

Figure 7.6: Maximum intensity projection of maximum SAR values in the region around the prosthesis with all coupling modes (top), with just the null modes from the E-field based measurement (centre) and with the null modes from the B_1^+ map based measurement (bottom). The extreme edge of the prosthesis is highlighted with a black line.

the coupling modes; and with just the null modes produced from both measures of the coupling. It is clear that the null modes have a substantial effect in terms of SAR reduction around the implant. By discarding the high coupling mode, there exists no situation in which the highest SAR generated with all the modes can be produced thus indicating that imaging using just these modes should be safe with regard to RF interactions with the implant. However one degree of freedom is lost in discarding this mode.

7.4.2 B_1^+ Shimming with Null Modes

The efficacy of RF shimming with the "safe" null modes was assessed by generating a set of 10,000 random, complex weightings to apply to the modes themselves – these were all of size 8×1. These weightings were applied to the SVD modes by multiplying with the matrix of the modes **V**. This then produced the RF shims to be applied to the actual transmit channels.

The SVD weightings were applied to all the SVD modes in two ways: with all the modes used; and with the first index set to zero in order to remove the high coupling mode. This was performed for the modes calculated from both coupling measures.

The resulting local 10g SAR in the region around the implant and the coefficient of variation of the B_1^+ field over the imaging slice were assessed for the shims with all modes used and with just the null modes. In Figure 7.7, maxi-

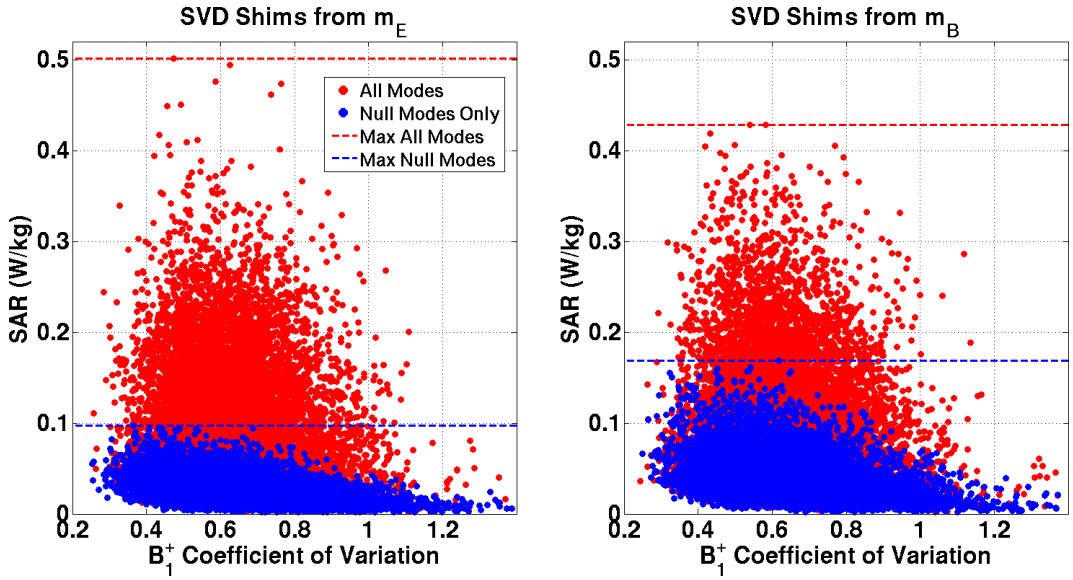

Figure 7.7: Coefficient of variation in B_1^+ plotted against maximum local 10g SAR in the region around the prosthesis for a set of 10,000 random RF shims applied to the system with all eight SVD modes (red), and with just the seven null modes (blue). The maximum SAR point of each group is indicated with a dotted line. The plot on the left is produced from the electric field based measurement and the right hand plot uses the B_1^+ field based measurement to estimate coupling.

mum local 10g SAR and coefficient of variation of the B_1^+ field are plotted against each other for both sets of modes. It is clear that by just using the null modes the maximum SAR around the implant is substantially reduced, as would be expected. The highest SAR values from the set of results with just the null modes and with all the modes differ by $>60\,\%$ for the B_1^+ based coupling measure and by 80 % for the E-field based coupling measure. Furthermore despite the loss of one degree of freedom, only using the null modes gives equal possibility of

generating solutions with low coefficient of variation in B_1^+ in both cases – just using these modes will still allow sufficient degrees of freedom to produce good imaging performance.

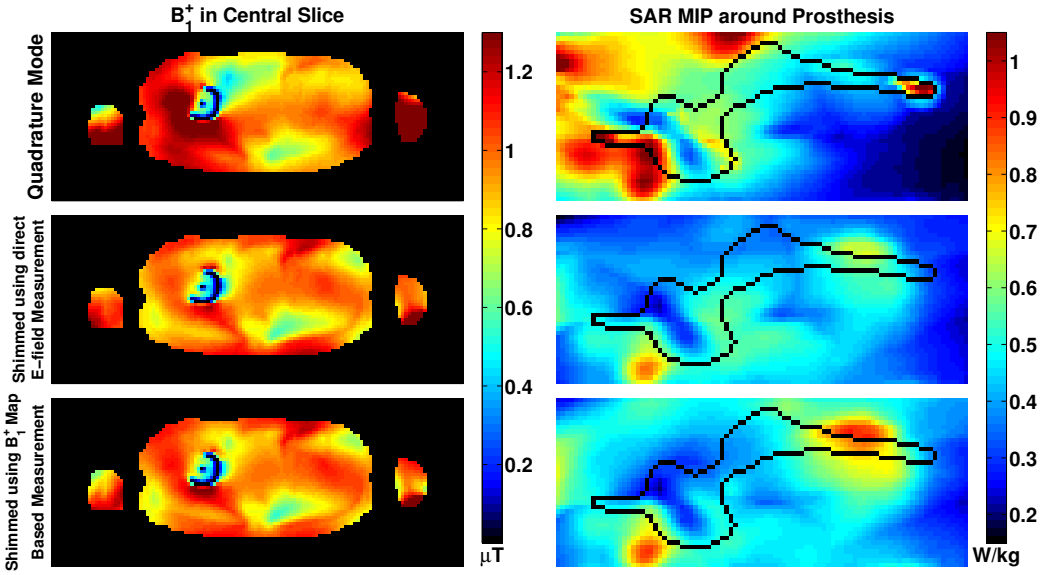

Figure 7.8: B_1^+ distribution in an axial slice including the prosthesis is shown on the left column and local 10g SAR maximum intensity projection in a cuboid around the prosthesis is shown on the right with the extreme edge of the prosthesis highlighted with a black line. Results are shown for quadrature mode (top), and RF shimming with E-field (middle) and B_1^+ map based coupling measurements (bottom).

To assess an example of this, the optimisation shown in Equation 7.5 was run for a range of regularisation parameters, and relatively high-power solutions were selected with the same transmit coil power (i.e. $\|\mathbf{w}_s\|^2$) for both the B_1^+ based coupling modes and the E-field based modes. The B_1^+ distribution in the selected slice and the local SAR maximum intensity projection in the region around the implant are shown in Figure 7.8 for the two shimmed solutions and the quadrature mode of the scanner. After shimming, improved B_1^+ field homogeneity is achieved over the slice along with substantially reduced SAR around the implant.

	Quadrature	E-field Coupling Measure	B_1^+ Map Coupling Measure
B_1^+ inhomogeneity measure (RMSE)	0.32	0.19	0.19
Maximum local 10g SAR in prosthesis region (W/kg)	1.31	0.45	0.51

Table 7.1: Quantitative results after RF shimming showing the reduction in B_1^+ inhomogeneity over the imaging slice and reduction in maximum local 10g SAR in the region within 1 cm of the prosthesis surface.

In Table 7.1, quantitative results for the RF shimming are presented showing

that with both measures of coupling, the improvement in B_1^+ homogeneity over the imaging slice is greater than 40 %. The SAR in the region within 1 cm of the implant surface is seen to be reduced by more than 60 % with both coupling measures but as expected, the E-field based coupling measure yields marginally more effective performance.

7.5 Discussion

In this study the potential to control RF interactions with a prosthetic hip implant using a PTx array was explored. The 8-channel MBC was able to produce a set of seven null modes that could be used for RF shimming. By just using these modes, it was possible to categorically ensure high levels of SAR caused by RF coupling to the implant could not be produced in the region around the implant.

If shimming with the null modes is considered to be analogous to shimming with a set of "virtual" transmit coils, then moving to the seven null modes from the full set of eight coils removes one degree of freedom. However in Figure 7.7 it is clearly shown that the effect of this on shimming performance is negligible. Using the full set of modes produced by the SVD has a similar distribution of coefficient of variation in B_1^+ as only using the set of null modes, showing they have the same potential to yield suitable solutions with RF shimming. Just using these modes also ensures that the maximum possible SAR is reduced by more than 60 % when using the modes produced by the B_1^+ field based measurement of the implant coupling. Using the direct E-field measurement is considerably more effective with the maximum SAR from the null modes being 80 % less than the SAR from all the modes.

It is intuitive that the direct E-field measure performs more effectively in terms of producing null modes with less coupling to the implant as SAR is proportional to the square of the electric field. However in reality it is currently not possible to measure these electric fields using MRI. One possible way of acquiring a direct measure of these fields would be to place an active, MRI-safe device [127] on the implant that would monitor some measure of the implant's EM interactions; although this may not be a very practical option in reality due to the high financial cost and considerable engineering challenges. Another possibility of assessing the degree of coupling is to measure the variation in electrical properties of the transmit coil in the presence of an implanted device e.g. scattering or impedance parameters. Strong coupling to a device will cause a split in resonance peaks of scattering parameters [33] as was shown in Reference [131] provided there is relatively strong localised coupling – this may not be the case with a hip prosthesis located within a subject. A similar method that instead uses

current pickup coils [124] potentially suffers from sensitivity issues also although the results shown in that study indicate high sensitivity for embedded catheters and unsafe pacemakers.

In Reference [130] it was shown that setting the receiver coil to reverse polarisation (i.e. B_1^+ instead of B_1^-) makes the receive signal sensitive to currents on implanted devices and have minimal sensitivity to the NMR signal. Reversing both transmit and receive polarisations is shown to suppress the NMR signal and highlight the signal from RF eddy currents on the wire. This may be a good way of assessing the coupling to the implant but it suffers from decreasing the efficiency of the total MRI examination as doing this would involve a separate calibration scan without a usable B_1^+ map that could be further utilised for RF shimming.

Using the B_1^+ field distribution around the shaft of the prosthesis, as was done in this work, to assess the coupling is wholly realisable in reality. On the left side of Figure 7.5 it can be seen that the null modes from the B_1^+ based measure truly do represent minimal interaction with the implant. It is only the eighth mode that shows any noticeable E-field on one end of the implant which is where a long screw which bolts the implant into the pelvis is located. This is on the opposite end of the implant to the shaft where the B_1^+ field was sampled to obtain the coupling measure. Therefore it may be possible to reduce the coupling on the eighth mode by including a measurement from this end of the implant. This would be easily incorporated into the SVD as it would simply increase the size of one dimension of the coupling measure matrices **m** from M=1 to M=2. It should be noted however that as the screw is relatively short very near to the "cup" of the prosthesis where the lower part of the implant sits in, it is less likely to behave as a wire in terms of its electrical properties than the implant shaft.

In Reference [132], a simplified analytical expression of the EM field behaviour within a metal cylinder embedded in a dielectric was used to remove the effect of image shading due to a hip prosthesis. Therefore it may be possible to extend the expression for the inferred current on the prosthesis shaft in Equation 7.2 to incorporate more complicated interactions over the whole prosthesis by perhaps using an expression for a sphere connected to a cylinder. This may improve the characterisation of the null modes by the SVD of the coupling measure.

In any case, Figure 7.6 comprehensively shows that the B_1^+ based measure sufficiently captures the null modes to ensure that very high levels of SAR cannot be achieved when just using the null modes. The maximum possible SAR with all the modes shows high peaks at the ends of the implant and these are almost completely diminished with the null modes from either measure. When using the null modes for RF shimming as shown in Figure 7.8, shimming with the B_1^+ based modes does appear to show a region of moderately increased possible SAR in

the centre of the implant shaft. However this region lies in the tissue away from the implant and is simply projected through. In any case the SAR in this region is still considerably lower than the SAR values seen for the quadrature mode.

Unlike the constrained RF shimming performed in Chapter 6, here a regularised shimming approach was used. The aim of this work was to present a practical approach to controlling potential heating around the implant without depending on SAR models which will struggle to capture local variations in EM fields around an implant when it is located in different places within the transmit coil. If a SAR model could be included that was sufficiently able to capture this variability, it would be pertinent to adapt the shimming calculation to include SAR constraints. RF amplifier constraints could also be incorporated within the optimisation to ensure that none of the drives actually applied to the the transmit channels exceeds hardware limits as in the cardiac study in Chapter 6. However the act of regularising against peak power keeps this under control to some degree.

As in Chapter 6, the efficacy of the RF shimming with null modes with regard to improving B_1^+ homogeneity will be improved if optimising over a smaller, localised region; particularly if the optimisation region does not include the implant itself, as this produces a very non-uniform local B_1^+ field. Of course the degree of localisation depends on which region within a subject is being imaged.

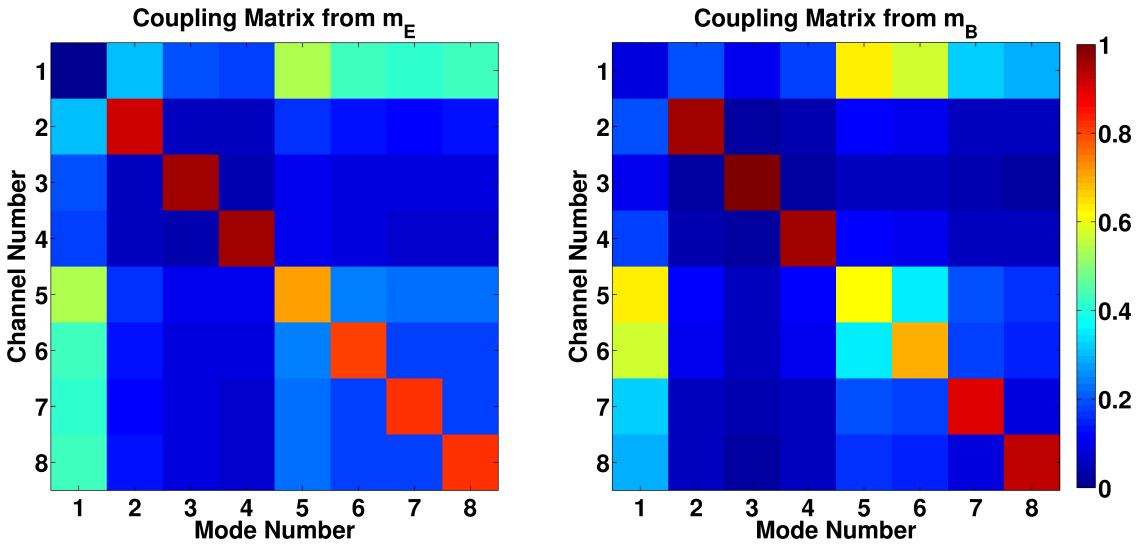

Figure 7.9: Coupling matrices **V** produced by both measures of coupling are shown. On the left is the matrix from the E-field based measurement and on the right is the matrix from the B_1^+ map based coupling measurements.

The coupling matrix produced by the SVD is seen to be highly diagonal as shown in Figure 7.9 where the matrix **V** produced by both coupling measures is displayed. The only mode in each case that does not conform to this diagonality is the first, high-coupling mode. The effect of this is that the null modes generally correspond to the behaviour of the transmit coils that produced that particular

coupling measure i.e. the second mode corresponds to the coil that gave the second coupling measure. Therefore whichever coil measure is ordered first in the vector **m** provided to the SVD will be lost as a local coil in the SVD modes and replaced with a combination of all the coils that produces the high coupling mode. If performing localised shimming, some care could be taken to provide the SVD with the coupling measures such that the first measure is a transmit channel whose local B_1^+ field does not primarily lie in the region to be optimised.

It is also interesting to note in Figure 7.9 that the first column of the matrix from the B_1^+ based measurement which represents the high coupling mode is dominated by channels 5 and 6 which represent the two transmit elements located physically closest to the implant. However the E-field based measurement more accurately captures the fact that the implant is relatively equally close to channels 5-8. Evidently the location in which the annulus in the B_1^+ field was sampled around the implant shaft experienced greater coupling to coils 5 and 6 thus causing this moderate distortion in the coupling measure.

In Reference [6] a similar prosthetic hip implant was simulated within a quadrature birdcage coil. It was found that when the hip prosthesis was positioned in certain locations within the RF coil, large local SAR hotspots were produced at the ends of the implant that in some specific instances included the overall maximum local 10g SAR over the whole body. In the simulation performed for this work, the coupling to the transmit array was substantial but the maximum 10g local SAR over the whole voxel model was not necessarily located in the region around the implant. However relatively high SAR was seen at the ends of the prosthesis in the coil's quadrature mode as shown in Figure 7.8 and there exists the possibility of higher SAR for particular driving conditions as indicated by the map of eigenvalues with all the modes in Figure 7.6. It should also be noted that after RF shimming with the null modes, the maximum local 10g SAR over the whole body was always reduced to some degree – it was never seen to increase.

Whilst this study showed the ability to control RF interactions on the implant, other safety concerns from MRI may also need to be considered [133]. In Reference [134] it was shown that low frequency EM interactions with the imaging gradient coils can also causing heating around the implant of several degrees centigrade. This finding is purely based on simulation data so it remains to be seen how much heating is caused in a real life scenario.

In conclusion, the framework described here presents a feasible way of minimising any coupling to prosthetic hip implants although further work would be required to fully assess if this is sufficient to ensure safe imaging in all cases. In particular, physical experiments must be performed to see how effective the null mode shimming is in reality.

Chapter 8

Neonatal SAR Evaluation

Contributions

The findings in the following chapter form part of a group study and have been discussed in the following publications:

> S.J. Malik, **A. Beqiri**, A.N. Price, J.N. Teixeira, J.W. Hand, and J.V. Hajnal. Specific absorption rate in neonates undergoing magnetic resonance procedures at 1.5T and 3T. *NMR in Biomedicine*, January 2015
>
> S.J. Malik, **A. Beqiri**, A.N. Price, J.W. Hand, and J.V. Hajnal. RF safety evaluation for neonatal MRI at 3T. *Proceedings of ISMRM 2014*

The project was overseen by Dr Shaihan Malik who performed the analysis of simulation results. The key contributions from the author of this thesis were to configure the birdcage coil EM model to run correctly; to run the 1.5 T SAR simulations for both the adult and neonatal model; and to jointly run the adult 3 T SAR simulation. All other 3 T SAR simulations were run by Professor Jeff Hand, and calorimetry experiments were performed by Dr Shaihan Malik and Dr Anthony Price – for information regarding these, please refer to the above publications.

8.1 Introduction

As MRI of neonates is becoming increasingly common in clinical practice [135], it is necessary to assess the safety concerns for this demographic directly. This is particularly true with regard to RF safety and SAR. Currently SAR estimates for neonates in the MRI systems used for this work (Philips Achieva systems) are

the same as for adults with perhaps some accounting for the difference in weight, which clearly will not accurately estimate SAR for this population group.

In this chapter, SAR produced by a generic RF birdcage coil being driven in a quadrature mode – as is generally the case for clinical systems – at low and high field (1.5 T and 3 T respectively) is assessed for neonates and compared with SAR levels for adult males. The chapter begins with a broad overview of clinical neonatal MRI. Then the modelling of the birdcage coil used for this study is discussed. The voxel models used and the SAR analysis performed are outlined before leading onto the study itself.

8.2 Neonatal MRI

When imaging neonates in an MRI system, numerous modifications are made to the scanning setup and pipeline [136]. In terms of practical considerations these modifications account for the the fact that neonates are much smaller than most imaging subjects. The modifications generally include hardware adaptations such as bespoke receiver coils. It is also important to adjust imaging pulse sequence parameters to account for the differences in tissue properties within the neonates when compared with adult subjects – such as longer relaxation times [137]. Not doing so will result in suboptimal imaging quality and incorrect tissue contrast.

However the issue of RF safety in neonates has not been effectively addressed despite the ongoing use of MRI for imaging neonates. In a standard MRI exam, SAR in general is not estimated on a neonate specific basis, and this is particularly the case for the Philips scanners used by the research group at King's College London. Given the group's interest in scanning neonates, this study was undertaken to assess whether the known safety process used by the Philips system was actually safe for neonates, and to establish bounds for safe use in an ongoing clinical research programme.

In any case SAR estimates made by an MRI system will not give a completely accurate value even for a conventional adult subject. In particular the local distribution of SAR can vary substantially between subjects and this is unlikely to be captured by these models.

The move to high field MRI may also be a cause for concern as SAR is proportional to the square of the B_0 field so going from 1.5 T to 3 T may produce a fourfold increase in SAR. Of course MRI at 1.5 and 3 T under normal operation with a birdcage coil has been shown to be safe for adult subjects [2, 138–140]. Therefore it is probable that whole body SAR in neonates will also be safe and reduced compared with adults. Neonates load the coil far less thus allowing increased efficiency, and they have a much smaller mass for power to deposit into.

If SAR is indeed much less in neonates then provided care is taken, it may be possible to make the SAR constraints on operation less conservative and hence allow more optimised imaging without any hardware modifications. This may not necessarily be true for local SAR however. The distribution of this can vary greatly between different subjects and it may be possible that hotspots occur in neonates which exceed regulatory limits.

Therefore it was important to attempt to quantify the level of SAR deposited during a conventional exam in a neonate; especially at 1.5 T and 3 T as these field strengths are the current clinical standard. This was achieved by running a full 3D EM model with a generic birdcage RF coil. In order to do this, a voxelised model of a neonate had to be utilised. One was obtained on licence from the Research Unit Medical Radiation Physics and Diagnostics at the Helmholtz Zentrum München, German Research Centre for Environmental Health [141, 142].

8.3 Birdcage Coil Modelling

As discussed in Chapter 3, clinical MRI systems generally use a volume birdcage coil to generate the RF B_1^+ field. These coils are fed with high voltage at two points and driven with a single RF amplifier with a phase shift of 90° between the feed points which are located 90° apart on the coil to generate a uniform quadrature mode excitation.

A number of these birdcage coils that are used for high field imaging now also have parallel transmission facilities with two or more channels with independent amplifiers being used to drive the birdcage coil in order to allow the B_1^+ field homogeneity to be improved. However even with the PTx features available, in a clinical setting these systems are generally still driven with the birdcage coil in a

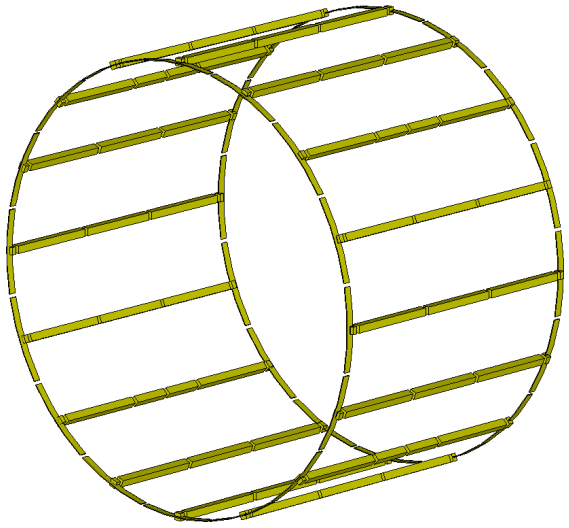

Figure 8.1: CAD model of metallic elements of birdcage coil.

quadrature mode single channel configuration.

The coil used for this study was generic but it was partially based on the birdcage coil present in the Philips Achieva TX 3T MRI systems. Specifically this was a circular band-pass birdcage coil comprised of 16 rungs. The diameter of the coil was 0.6 m and its length from one end-ring to the other was 0.4 m. The entire coil was positioned within a 1 m long cylindrical metal RF shield with inner diameter 0.678 m and thickness 1 mm.

8.3.1 Birdcage Driving Conditions

The coil model was originally provided directly by Philips as a CAD model of just the metallic components i.e. the rungs and the two end rings; with no electrical lumped components included. This can be seen in Figure 8.1.

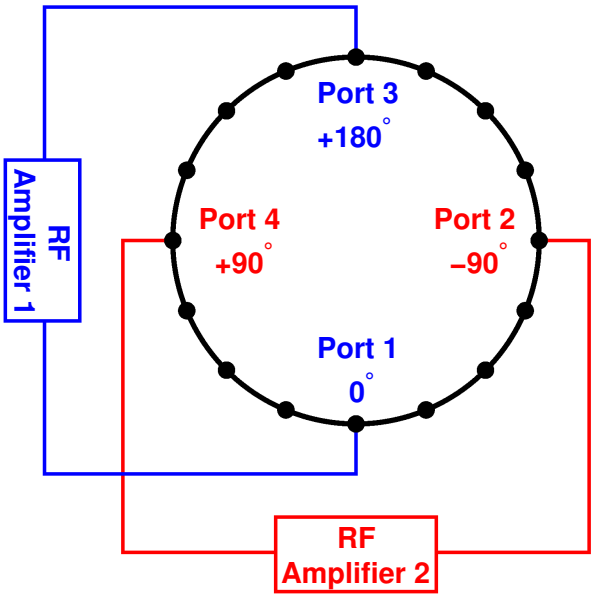

Figure 8.2: Diagram showing axial view of theoretical four-port birdcage coil. The 16 rungs are shown as small black circles located at equal displacements around the birdcage ring. The driving ports are all labelled and their phase offset shown. The coupled pairs are indicated with red and blue colours and their independent amplifiers are shown.

The first step was to investigate how to drive the birdcage coil such that it behaved correctly. By simply driving the coil in the centre of two rungs 90° apart (it was known that the Achieva TX birdcage coil was driven centrally in some way), it was not possible to tune the coil in order to achieve a quadrature mode. It was hypothesised that the symmetry of the driving conditions was causing this issue. Therefore driving the coil with four ports placed symmetrically around the coil [143] was experimented with.

In such a configuration to achieve a quadrature mode excitation, this would mean placing the driving ports in the centre of every fourth rung such that they

were all situated 90° apart from one another. Then the ports facing one another must be coupled together with a fixed 180° phase shift between them to ensure that the overall drive was fully balanced, with the pairs of ports phase shifted by 90° relative to the alternate pair for quadrature mode – this gives phase shifts of 0°, -90°, +180° and +90° for ports numbered 1-4 respectively. A diagram of this configuration is shown in Figure 8.2 with the two pairs of coupled ports indicated in separate colours.

To explore this, all of the lumped element locations in the birdcage CAD model had S-parameter ports inserted and an EM simulation was run using CST Microwave Studio. The S-parameters from all the ports were placed into a basic optimisation using MATLAB's `fminsearch` optimisation function (as was done for the 8-channel MBC) to tune the coil to 64 MHz with circuit co-simulation. The resulting combined S-parameters after optimisation can be seen in Figure 8.3.

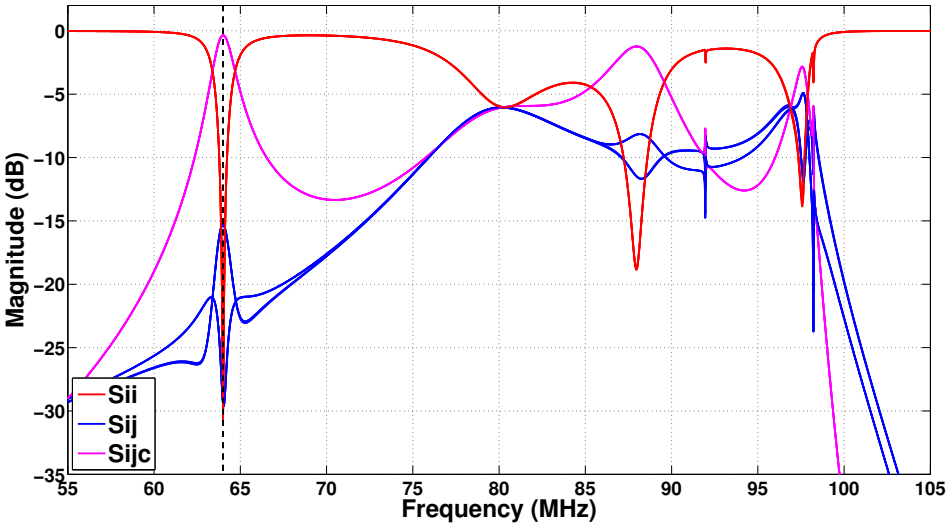

Figure 8.3: S-parameters for the four-port birdcage coil after tuning to 64 MHz. It is clear that good matching (S_{ii}) and decoupling (S_{ij}) have been achieved at the resonant frequency (indicated with a dotted black line). The S_{ijc} line indicates coupling between the cross-coupled ports which show very strong coupling so they can act as a pair.

As would be expected for a birdcage coil, multiple resonances can be seen across the frequency range although the strongest is at 64 MHz – good matching and decoupling can be seen at this frequency with S_{ii} and S_{ij} both below -15 dB. This is of course by design as the optimisation tuned the coil to maximise matching at this frequency. Despite no prior information being supplied to the optimisation, the drive ports that are opposite each other – with their coupling terms denoted as S_{ijc} (shown in magenta in the plot) – are fully coupled as desired.

By driving the four ports with the relative phases stated earlier, it was found that a quadrature mode was indeed produced on the coil. Whilst this four-port configuration does present a feasible way of driving the coil, it is somewhat in-

elegant as to then be driven by two independent amplifiers in order to perform parallel transmission, the two pairs of ports would have to maintain a fixed relationship between them in terms of the amplitude and fixed 180° phase shift.

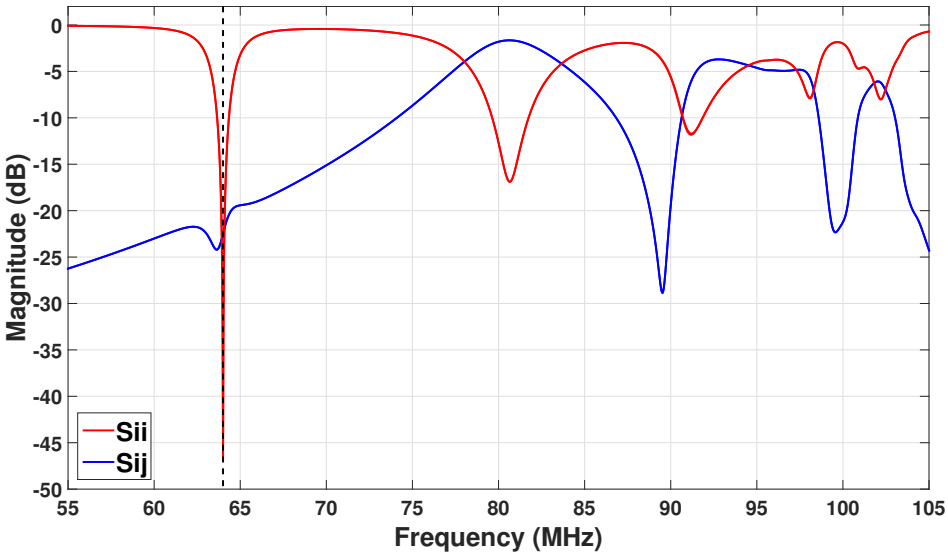

Figure 8.4: S-parameters for the two-port birdcage coil after tuning to 64 MHz. It is clear that excellent matching (S_{ii}) and decoupling (S_{ij}) have been achieved at the resonant frequency (indicated with a dotted black line).

It was then realised that driving the coil with four ports in a paired combination may be equivalent to adding a pair of tuning capacitors opposite two main driving ports and hence only having a two port drive. A two-port birdcage model configured as such was set up and tuned using circuit co-simulation and the resulting S-parameters are shown in Figure 8.4. In this case, matching was substantially improved compared with the four-port model although the EM fields produced within the voxel models were similar when scaled appropriately. The two ports could of course be driven independently, or simply used in quadrature mode with the standard 90° phase relation between the ports which was found to produce the desired quadrature mode as expected. This two port configuration driven in quadrature was then used for the simulations discussed in this chapter.

It was later discovered that the physical coil in the Philips MRI system was actually driven at the centre of the rungs in just two places with capacitors indeed placed in the centre of all the rungs in order to balance the drives thus corroborating the model configuration.

8.4 Methods

Initially the birdcage coil in the simulation had to be tuned to the desired frequency. Once this was done it was possible to investigate the SAR deposition in neonates as desired. SAR was also evaluated in an adult male voxel model within the coil model for comparison. The methods required for accomplishing these are discussed below.

8.4.1 Tuning of Coil

For the study, birdcage coil models were desired at both 64 MHz and 128 MHz, corresponding to 1.5 T and 3 T respectively. The simulations used for the final SAR results were all run as full simulations – i.e. *not* using circuit co-simulation – but circuit co-simulation was used to find the correct capacitor values in order to tune the birdcage coils appropriately for the different frequencies. This was achieved using the optimisation described in Equation 5.2 in Section 5.3.1. In some cases it was possible to do this in an unconstrained way but in others doing so yielded unreasonable capacitor values so a constrained optimisation was required which was performed with the optimisation algorithm SOMA [95].

To account for losses and non-ideal capacitors in the system, a fixed small resistance R_c was added in series to all the capacitors in the system; as was done for the 8-channel MBC. To produce roughly the same capacitor Q-factor at the different operating frequencies and ensure reasonable behaviour, it was necessary to adjust this resistance appropriately. When increasing frequency of operation, the resistance of the capacitors must be decreased and vice versa as can be seen in the equation below:

$$Q_c = \frac{X_c}{R_c} = \frac{1}{\omega C R_c} \tag{8.1}$$

where Q_c is the Q-factor of the capacitor of capacitance C; X_c is its reactance, and ω is the operating frequency.

After the correct capacitor values were found, full EM simulations with all electrical components modelled as lumped elements were constructed and it was possible to place voxel models inside the RF coil models for evaluating SAR.

8.4.2 Voxel Models

The original voxel model of the neonate was created from a CT scan of a deceased eight week old female baby which was imaged 24 hours post-mortem – the baby was of height 57 cm and mass 4.2 kg. The CT data was segmented

into 31 different tissue types from the data of resolution $0.85 \times 0.85 \times 4\,\text{mm}^3$. The model can be seen in Figure 8.5 with various major organs highlighted within it.

It was found that the baby from which the voxel model was derived was exceptionally large for its demographic – its mass lay in the 97^{th} percentile for term aged females and 95^{th} percentile for males, and its length exceeded the median by more than three standard deviations for both sexes [144]. Consequently the voxel model was isotropically scaled down in all three dimensions to a voxel size of $0.76 \times 0.76 \times 3.6\,\text{mm}^3$ to create a model that was better representative of the standard demographic. This meant that the model was then 3.02 kg in mass and 51.3 cm in height – these correspond to the 32^{nd} percentile for females and 25^{th} percentile for males at term equivalent age for mass; and 88^{th} percentile for females and 77^{th} percentile for males for height.

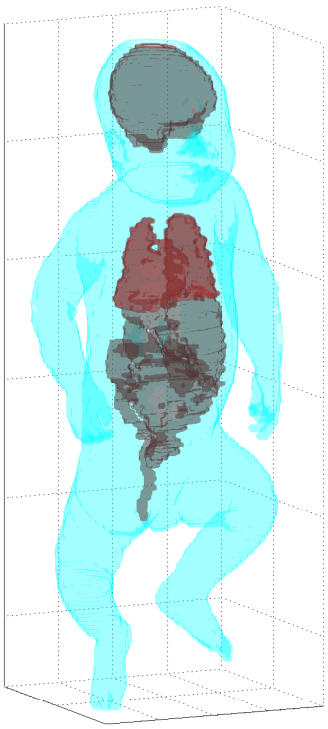

Figure 8.5: Voxel model of neonate shown. Major organs are highlighted in brown and the heart and lungs in red.

The voxel model needed to have the correct dielectric properties applied to the tissues represented within it. It is important to distinguish these from adult tissue properties as their make up is considerably different – for example the neonatal brain has 10 % higher proportion of water compared with adults [137] which would mean its electrical conductivity will be greatly increased.

Whilst adult tissue properties have been extensively studied and a number of databases are available online [31, 145], this is not the case for neonatal tissue properties. The properties must somehow be inferred – this was done using the methodology outlined in Reference [146] which involves taking the measured dielectric properties of adult and newborn rats and using the ratio of these as the scaling factor to infer the human neonate tissue dielectric properties from those of the human adult properties. The tissue properties for the newborn and adult rats were taken from Reference [147] and the ratios were calculated from the measured tissue properties given for 130 MHz as this was the lowest frequency studied in that work. The adult human tissue properties were taken from the database in Reference [145]. The neonatal tissue densities were provided directly by the Helmholtz Zentrum München. All of the neonatal tissue properties and the ratios used to infer them are given in Table B.1 in Appendix B.

The EM simulations were also run with an adult male voxel model which was the standard NORMAN voxel model [63] – this has a height of 1.76 m and mass of 73 kg. Both the neonatal and adult simulations at both field strengths were run with the voxel models placed heart centred within the birdcage coil.

8.4.3 SAR Evaluation

All SAR values were initially calculated directly in CST with 10g averaging performed according to the IEC standards [50]. However for volume RF coils, there is no official local 10g SAR limit, but there is a limit on partial body SAR. This is calculated by averaging the SAR over the region within the effective volume of the RF coil. As there is no option to calculate this directly in CST, this was done by numerically integrating over the relevant volumes in MATLAB. The relevant exposure levels for the models were 100 % for the heart centred baby model and 43 % for the heart centred adult (exposed mass = 31 kg).

To directly compare SAR values from all simulations, they were scaled in two ways. One was to set them to 100 % duty cycle with a mean B_1^+ field amplitude in a central region of interest (ROI) of 1 μT. The region of interest was defined as a 5 mm thick disc of 50 mm diameter in the centre of all the voxel models in the slice that was located at the isocentre of the birdcage coil.

The other method for scaling the SAR values was to use realistic operational values obtained from Phillips Achieva MRI scanners at both field strengths. The pulse sequences from which the duty cycle and B_1^+ amplitude were taken were selected to reflect maximum allowed SAR levels at both assessed field strengths.

At 3 T, the maximum SAR limit was constrained in the Philips scanner software (version R3.2.1) in two different ways: one for body scanning, and the other for head scanning. The body scanning limit is constrained by the maximum local 10g SAR within the scanner SAR model exceeding a value of 10 W kg^{-1}. The head scanning limit is a little less strict and is constrained by the head averaged SAR exceeding 3.2 W kg^{-1}. This SAR model assumes that the majority of the body of an adult lies outside the RF coil therefore there is far less RF deposition in general. The head scanning SAR model and its corresponding limits are automatically selected when a head receiver coil is used for signal reception. As neonates are often scanned using adult head receiver coils, these SAR limits must also be evaluated. At 1.5 T the same scanner software version has a single SAR constraint for all scanning scenarios: the global whole body averaged SAR must not exceed 4 W kg^{-1}.

Details for a subject of mass 73 kg were entered into the scanner software and the conditions that yield the highest SAR sequences were obtained: for 1.5 T,

B_1^+ = 23.0 μT, duty cycle = 3.9 %; for 3 T body limited scanning, B_1^+ = 13.5 μT, duty cycle = 1.4 %; for 3 T head limited scanning, B_1^+ = 13.5 μT, duty cycle = 3.0 %. The operational SAR values were then obtained from the 100 %, 1 μT values by scaling according to

$$SAR = \left(\frac{B_1^+}{1\mu T}\right)^2 \times \left(\frac{\text{duty cycle}}{100}\right). \tag{8.2}$$

8.5 Results

Once the simulations were completed, SAR calculations were run as a post processing step in CST and the SAR values were extracted along with B_1^+ maps at the isocentre of the birdcage coils to generate the relevant results.

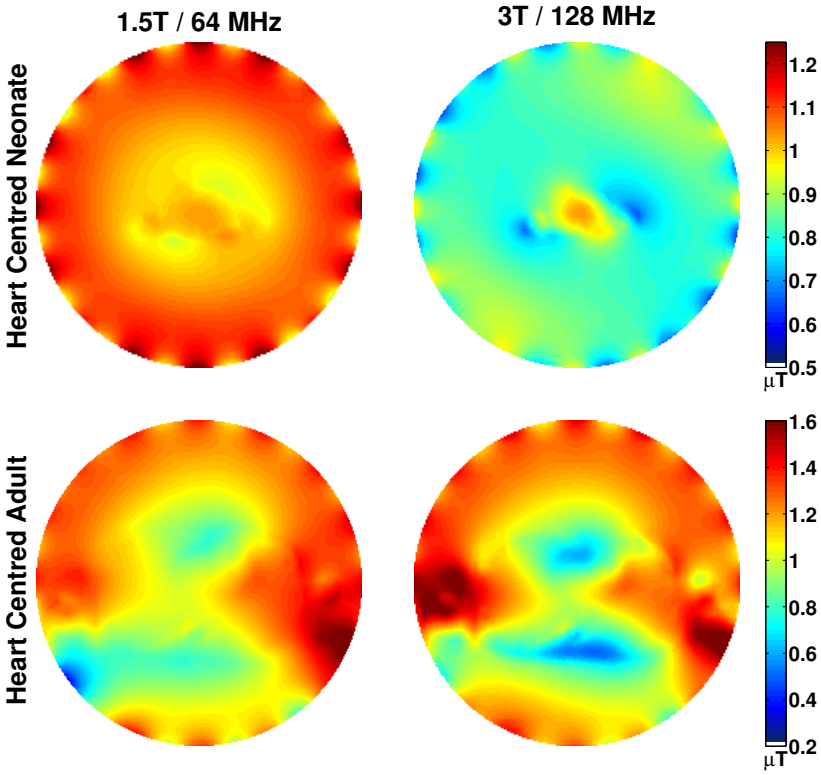

Figure 8.6: Quadrature B_1^+ maps for a central axial slice through the heart centred neonate model (top row) and the heart centred adult model (bottom row). These are shown for 1.5 T (left column) and 3 T (right column). All the maps have been scaled to a mean B_1^+ amplitude of 1 μT within the central ROI. Please note the different colour scales for the neonatal and adult maps.

8.5.1 Quadrature B_1^+ Maps

Initially the behaviour of the simulated B_1^+ field within the birdcage coil at the two field strengths and for the different loading conditions of the heart centred neonate and the adult models was assessed and can be seen in Figure 8.6. All the maps

have been scaled to a mean B_1^+ amplitude of 1 μT within the central ROI. As would be expected when moving from 1.5 to 3 T, the decreasing wavelength produces greater spatial variation in the B_1^+ field – the 1.5 T fields are much more homogenous particularly those for the neonate which has loaded the RF coil to a lesser degree. The greater load on the coil by the adult model causes greater interaction with the EM fields and exacerbates the increased level of inhomogeneity in the B_1^+ field. The size of the adult being larger relative to the RF wavelength also contributes to this effect.

8.5.2 SAR

The SAR values from all the simulations were scaled for 100 % duty cycle and a mean B_1^+ amplitude in the ROI of 1 μT. Figure 8.7 shows maximum intensity projections of local 10g SAR through the heart centred voxel models for the neonate and adult at both field strengths. It is clear that for this basic scaling, SAR deposi-

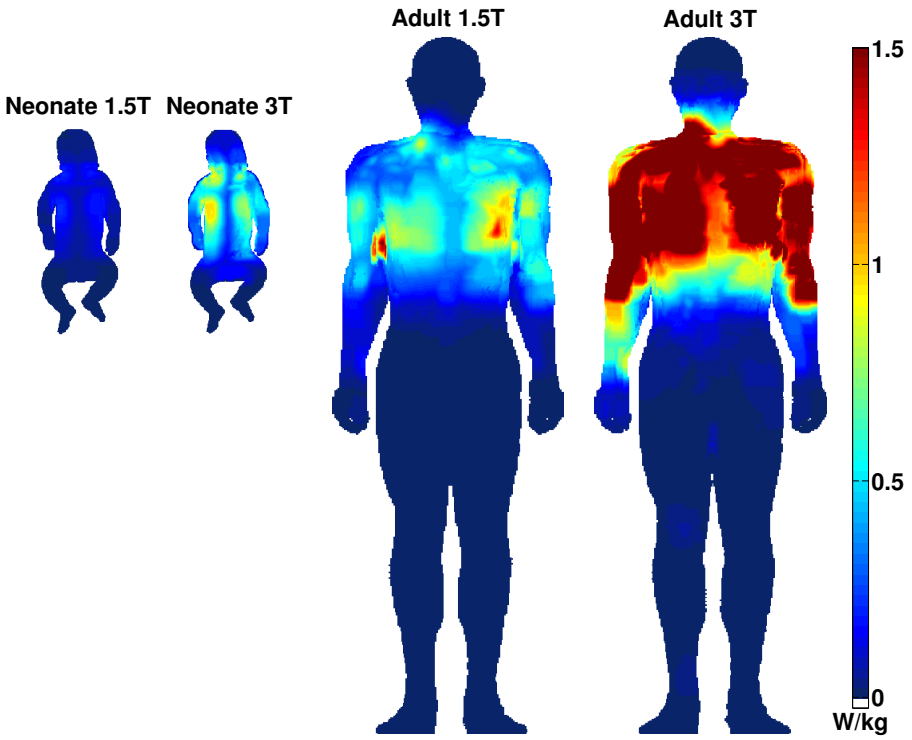

Figure 8.7: Maximum intensity projections of SAR for the neonate and the adult heart centred models at 1.5 T and 3 T. The results are scaled to achieve a mean B_1^+ amplitude of 1 μT in the central ROI and for 100 % duty cycle.

tion at 3 T is much greater than for 1.5 T as would be expected given the quadratic relationship between SAR and B_0 field strength. The neonate experiences much lower SAR as less power is required to achieve the desired B_1^+ field. This would not necessarily be the case for local SAR hotspots but in Figure 8.7 there do not

appear to be any that are of the same order as the local SAR values in the adult model.

Table 8.1 summarises all of the SAR values for the 100 % duty cycle scaling showing quantitatively that the SAR values at 1.5 T and 3 T for the voxel models differ by around a factor of four as would be expected, particularly for the whole body averaged SAR.

Model	Total Accepted Power (W)	Whole Body Averaged SAR	Head Averaged SAR	Partial Body SAR	Max Local 10g SAR Trunk	Max Local 10g SAR Head
128 MHz						
Baby	0.95	0.20	0.14	0.20	0.96	0.92
Adult	28.4	0.33	0.07	0.74	3.83	2.06
64 MHz						
Baby	0.54	0.05	0.03	0.05	0.21	0.21
Adult	16.0	0.08	0.01	0.18	1.32	0.34

Table 8.1: SAR values from all simulations scaled to a mean B_1^+ amplitude in the ROI of 1 μT at 100 % duty cycle. All SAR values given in W kg^{-1}.

The SAR results scaled to realistic operational conditions are shown in Table 8.2. For the 3 T adult model, the local 10g SAR value was calculated to be 10.1 W kg^{-1}. The MRI scanner software estimates a value of 10 W kg^{-1} so although the details of the scanner SAR model are not known, there is clearly strong correspondence between the SAR estimates.

The same scan parameters for the neonate model show much lower SAR values with the maximum local 10g SAR around a factor of four less that of the adult. The whole body SAR in the neonate is around 30 % lower than that for the adult which was already low.

Of course for the 3 T neonatal model, it is more pertinent to look at SAR values when scaled to the head scanning limits. These are increased by just over twofold compared with the body scanning limit SAR. Despite this, all the values are well below the 10 W kg^{-1} local 10g SAR limit for local array coils with a maximum value of 5.3 W kg^{-1}. The relevant limit for volume coils, the partial body SAR, is also well within the IEC limit of 2 W kg^{-1} for the fully exposed heart centred neonate.

8.6 Discussion

In this work, the SAR levels produced in neonates undergoing standard clinical MRI procedures was assessed. As SAR estimates from commercial MRI systems do not accurately reflect this population demographic, it was necessary to perform EM simulations to obtain correct SAR behaviour. SAR in neonates was found to

be substantially lower in all of the cases assessed with all simulations being run using a generic birdcage RF coil. The birdcage coil model was carefully tuned to the desired frequencies and its resulting behaviour in terms of resonant properties and EM fields produced was seen to be as would be expected.

When SAR values were scaled simply to a mean B_1^+ amplitude of 1 μT in the central ROI and 100 % duty cycle, the neonate experienced approximately a quarter of the local 10g SAR within the body compared with the adult and around 30 % less whole body SAR at 3 T. At 1.5 T, the whole body SAR difference was similar but the local 10g SAR in the neonate was only 16 % of that of the adult. When going from 1.5 to 3 T, the increase in whole body SAR was almost exactly a factor of four for both the adult and neonate which directly agrees with theoretical expectations – all of the other SAR measures also follow a similar trend.

While these results are very encouraging in terms of neonatal MRI safety, they do mean that the SAR estimates from the scanner are fundamentally incorrect for neonates. When the SAR values are then scaled to realistic operational values, these large discrepancies are of course unchanged for the body scanning parameters. However as neonates are usually scanned with a head receiver coil which in a Philips system activates the less conservative head scanning limits, these limits allow a greater than twofold increase in SAR.

Model	Scanner set at 100% body scanning limit					Scanner set at 100% head scanning limit				
	Whole Body Avg	Head Avg	Partial Body	Max Local Trunk	Max Local Head	Whole Body Avg	Head Avg	Partial Body	Max Local Trunk	Max Local Head
128 MHz										
Baby	0.52	0.37	0.52	2.53	2.43	1.09	0.77	1.09	5.29	5.07
Adult	0.87	0.19	1.95	10.10	5.44	–	–	–	–	–
64 MHz										
Baby	0.98	0.65	0.98	4.38	4.35	–	–	–	–	–
Adult	1.63	0.11	3.74	27.19	6.88	–	–	–	–	–

Table 8.2: SAR values given for all the models scaled to the scanner operational limits at both field strengths and for the 3 T head scanning limits.

The SAR values for the head scanning limits are still well within the maximum allowed SAR levels but the resulting SAR increase would not be apparent to any scanner operator so should be considered during imaging. The SAR values for the adult model at 1.5 T when scaled to realistic operational values were found to be higher than for 3 T as a result of the far less stringent constraints on operation for the Philips Achieva scanners at 1.5 T.

In any case, the findings clearly indicate that neonatal MRI is safe in terms of RF interactions. This could be predicted for the whole body SAR by using geometrical simplifications to consider the imaging subjects as spherical objects. Doing so gives the losses within the spherical object as being proportional to the radius to the fifth power [148]. Therefore if a neonate represents a sphere with half the radius of the adult, this would indicate a factor of 32 reduction in power lost into the subject. The total accepted power shown in Table 8.1 shows a factor of $\sim$30 at both field strengths which supports the predictions given by this simplification.

As well as alleviating RF safety concerns, the findings in this work indicate that SAR estimates were highly conservative in all cases which suggests the possibility of relaxing these constraints when scanning neonates. This would require careful experiments to fully characterise safe levels of energy deposition in this population group. However in the end SAR is a surrogate for the real safety concern – temperature rises within the subject due to RF exposure. In adults, local 10g SAR values have been shown to not corroborate with localised temperature increases particularly well [149] and in neonates, temperature control mechanisms within the body behave differently that those in adults [136] – for example, body surface heat loss in neonates is greater as their surface area to bodyweight ratio is up to three times higher than for adults [150]. Therefore an accurate thermal simulation model that comprehensively investigates these factors should be considered before any SAR constraints are relaxed when scanning neonates.

Given the increasing prevalence of two channel MRI systems for 3 T imaging, RF shimming could also be used to control SAR in neonatal subjects in a similar manner to that described in Chapter 6. As was shown in Figure 6.13, it is possible to substantially reduce SAR relative to quadrature mode with localised shimming using just two transmit channels. As neonates are small, they represent a localised region which should allow similar possible improvements for imaging and SAR reduction as those seen for adult cardiac imaging.

In conclusion, neonatal MRI for current clinical examinations has been shown to be safe with regard to RF energy deposition and in future it may be possible to use the freedom available with lower SAR levels to improve imaging.

Chapter 9

Conclusions

In this chapter, the achievements from this thesis are presented along with their relevant conclusions and potential avenues for further research.

This thesis generally focused on the modelling of SAR in MRI and using this modelling to enable control of SAR for improved imaging. After creating an accurate model for an 8-channel PTx array, it was possible to use the model to assess SAR effectively in a number of different scenarios.

9.1 Summary of Findings

The initial goal was to simulate the EM behaviour of an 8-channel RF PTx array. This is challenging due to coupling between PTx elements, so previously simulations were run in a simplified manner with each element simulated in isolation. By using circuit co-simulation it was possible to model the PTx array in full including decoupling networks. Circuit co-simulation was self-implemented and the code made available online; a number of individuals have used it for their own research and it has formed the basis of circuit co-simulation scripts being incorporated into the Sim4Life (Speag and ZMT, Zurich, Switzerland) FDTD software package.

This full coil model made using circuit co-simulation generated field simulations and SAR predictions that were much more appropriate to the behaviour of the real physical scanner. The full model was also compared with an idealised model. It was found that even after active decoupling (used to ensure the fully modelled simulation behaved as closely as possible to the idealised one), the models differed in terms of SAR behaviour. The differences were generally $< 5\%$ but sometimes the models' SAR predictions varied to a substantial degree. There was also a tendency for the idealised model to *over*estimate SAR values.

The full coil model was used as part of a study into performing SAR con-

strained RF shimming for in vivo cardiac imaging. The RF shimming optimisation was formulated as an "excitation optimisation" in which the properties of the RF pulse being used in the sequence and the overall sequence timing were also considered. This provides a more sophisticated way of utilising the full degrees of freedom of PTx RF shimming thus enabling a range of optimal solutions to be found for a given RF waveform which can trade-off B_1^+ homogeneity within the heart with reductions in maximum local 10g SAR over the whole body. As the B_1^+ optimisation was performed over a small region, the range of possible solutions was greater leading to improved performance of the optimisation. Some MRI scanners already perform an optimisation process in order to select an appropriate RF pulse for the imaging sequence being used. Therefore this framework presents a practically realisable way of extending this optimisation step and dramatically improving clinical MRI by incorporating PTx.

By using in vivo B_1^+ data in the optimisation along with the SAR models produced from EM simulations, it was seen that the optimisation was always able to produce improved operating conditions compared with the scanner's nominal quadrature mode. For a specific cardiac sequence, local SAR was reduced by 56 % across several subjects whilst improving the error in the achieved flip angle by 44 % all within the physical peak RF power constraints of the amplifiers. Images acquired under these improved conditions yielded greater image contrast between blood pool and myocardium and increased signal in general.

The implementation of this capability on a physical MRI system is a key result from this work. The full coil model was found to produce appropriate predictions that matched the performance of the physical system well. This led to consistent and expected benefits from the RF shimming framework which directly translated into improvements in vivo.

The 8-channel RF coil model was then used to assess the possibility of ensuring RF safety in imaging subjects with prosthetic hip implants. It was possible to ascertain a set of null modes with no measured coupling to the implant. By only operating using these modes, it could be ensured that high SAR conditions in the proximity of the implant were no longer produced. Furthermore the set of seven null modes was still as effective at improving the B_1^+ field homogeneity as with using all eight channels of the PTx array. This study is highly promising from a safety perspective as the ability to infer the coupling between coil and implant from B_1^+ maps means these measurements could be made in reality and there would be no need to depend on simulations for SAR estimates which would be difficult to configure such that they correctly characterised the behaviour of the many different types of implants. Furthermore, as increasingly large numbers of the general population have metallic implants within them, this study provides the

possibility of imaging more of these subjects safely.

The final study in this thesis was undertaken with the aim of assessing SAR behaviour in neonates under routine clinical examinations. It was found that if safety is governed by an adult-appropriate model (as in the Philips systems used for this work), for sequences running at the maximum SAR levels, SAR in neonates is always considerably less than for adults. These results confirm intuitive arguments based on load size but do not necessarily reflect the behaviour of local SAR. Maximum local 10g SAR was found to be around a quarter of that seen in adults at 3 T and only 16 % of the adult value at 1.5 T. Of course these findings also mean there is potential for optimising imaging by relaxing the SAR constraints to a degree when using these adult model based SAR numbers, or by using a more appropriate SAR model.

9.2 Future Work

For each section of work presented in this thesis there are multiple potential avenues of research in which the findings could be further explored.

The study on decoupling regimes was performed for one type of PTx array and the methodology used was found to be effective at exploring the performance of the two modelling techniques. This provides confidence that the methods can be used for modelling other coils and the framework developed can be applied to important scenarios such as local PTx at 3 T, UHF volume and surface arrays, and perhaps novel scenarios such as niche systems for specialist applications – for example, extremity scanners, interventional systems, etc.

The PTx excitation optimisation study offers great potential for further exploration. The outlined framework has been found to be effective and robust and can now be expanded upon to provide clinical capability; it also provides an appropriate way to incorporate PTx in a natural way. An obvious initial extension would be to apply the optimisation to the SAR intensive bSSFP sequence which is often used for clinical cardiac imaging. As mentioned in Chapter 6, this sequence would benefit far more from the SAR reductions achieved and could yield real clinical benefit in terms of improved imaging or reduced breath holds for subjects.

A more involved extension to the study would be the incorporation of full PTx pulse design. Instead of simply weighting the same RF pulse differently on each channel as with RF shimming, a unique waveform is played out on each channel leading to more degrees of freedom in controlling RF fields. This would enable the B_1^+ distribution to be controlled to a greater degree and the potential for SAR reduction would also be substantially increased. The possibility for optimising different parts of imaging sequences independently could also be explored in the

context of trading off SAR reduction and B_1^+ improvement in different ways for each part of a sequence – for example, spin echo sequences which include fat saturation pre-pulses [151] could have the pre-pulse, excitation pulse and refocussing pulses optimised with different objectives in mind.

A key open question in the field of RF safety is that of matching subjects to SAR models. If a model closely matches that of a subject, it has been shown that the predicted fields are accurate [59]. However it is still unclear how closely the model should match the subject. In this regard, studies of the appropriateness of SAR models for a population would be useful. One way of approaching this would be to combine a group of multiple SAR models into one set of Q-matrices and then compress this set into one global set of VOPs. These VOPs could then be used to find solutions to the excitation optimisation that optimised MRI for the worst case over a representative SAR value for the population.

This ties into the fact that the hip prosthesis used for the study in Chapter 7 is only a single example of the broad range of metallic implants potentially present in MRI subjects; such as catheters, heart pacemakers, deep brain stimulation leads, etc. It is necessary to investigate through modelling how coupling to each different type of implant could be measured and whether it is possible to ensure RF safety for any given implant configuration.

The prosthesis study would also benefit greatly from extending the current simulation work into physical experiments. It would then be possible to see temperature rises produced from high SAR at the ends of the phantom which should diminish when using the null coupling modes. This experiment would act as a proof of concept towards utilising this methodology in vivo and potentially making MRI with implanted devices much safer in clinical settings.

9.3 Concluding Remarks

In this thesis, the ability to create SAR models and use these models to reduce SAR through RF shimming whilst simultaneously optimising imaging was shown to be a powerful and versatile technique. The increasing use of PTx clinically means that the methods outlined will potentially be extremely useful in the very near future.

In general it has been shown that whilst SAR is often thought of as an inherent limit on scanning, understanding and then controlling it provides substantial opportunities for improving MRI.

Publications and Software

Journal articles:

F. Padormo, **A. Beqiri**, S.J. Malik, and J.V. Hajnal. Parallel transmission for ultrahigh-field imaging. *Magnetic Resonance in Medicine*, May 2015

S.J. Malik, **A. Beqiri**, A.N. Price, J.N. Teixeira, J.W. Hand, and J.V. Hajnal. Specific absorption rate in neonates undergoing magnetic resonance procedures at 1.5T and 3T. *NMR in Biomedicine*, January 2015

A. Beqiri, J.W. Hand, J.V. Hajnal, and S.J. Malik. Comparison between simulated decoupling regimes for specific absorption rate prediction in parallel transmit MRI. *Magnetic Resonance in Medicine*, November 2014

F. Padormo, **A. Beqiri**, S.J. Malik, and J.V. Hajnal. PRIMO: Precise radiofrequency inference from multiple observations. *Magnetic Resonance in Medicine*, August 2014

S.J. Malik, **A. Beqiri**, F. Padormo, and J.V. Hajnal. Direct signal control of the steady-state response of 3D-FSE sequences. *Magnetic Resonance in Medicine*, January 2014

Conference presentations:

A. Beqiri, J.V. Hajnal, and S.J. Malik. SAR and peak power constrained excitation optimisation for 3T cardiac imaging. *Proceedings of ESMRMB 2015*

A. Beqiri, J.W. hand, J.V. Hajnal, and S.J. Malik. SAR reduction for metallic implants using volume PTx array. *Proceedings of ESMRMB 2015*

A. Beqiri, F. Padormo, J.W. Hand, J.V. Hajnal, and S.J. Malik. SAR optimised local B_1^+ shimming for cardiac imaging at 3T – a multi-model study. *Proceedings of ISMRM 2014*

A. Beqiri, J.W. Hand, F. Padormo, J.V. Hajnal, and S.J. Malik. SAR characterisation for parallel transmission MRI – comparison between modelling different decoupling regimes. *Proceedings of ISMRM 2014*

S.J. Malik, **A. Beqiri**, A.N. Price, J.W. Hand, and J.V. Hajnal. RF safety evaluation for neonatal MRI at 3T. *Proceedings of ISMRM 2014*

F. Padormo, **A. Beqiri**, S.J. Malik, and J.V. Hajnal. On the correction of cable losses for in-situ subject-specific global Q matrix calibration. *Proceedings of ISMRM 2014*

A. Beqiri, J.W. Hand, J.V. Hajnal, and S.J. Malik. Local RF shimming for cardiac MRI at 3T with SAR considerations. *Proceedings of ESMRMB 2013*

Software

The code used to perform Circuit Co-simulation as discussed in Chapters 4 and 5 is available online at `https://github.com/mriphysics/circuit_cosimulation`.

The code used to perform the SAR constrained shimming optimisation with the CVX convex optimisation package [99,100] as discussed in Chapter 6 is available at `https://github.com/mriphysics/cardiac_RF_shimming`.

Bibliography

[1] M. E. Haacke, R. W. Brown, M. R. Thompson, and R. Venkatesen, *Magnetic Resonance Imaging: Physical Principles and Sequence Design*. John Wiley & Sons, 1999.

[2] C. M. Collins, S. Li, and M. B. Smith, "SAR and B_1 field distributions in a heterogeneous human head model within a birdcage coil. Specific energy absorption rate," *Magnetic Resonance in Medicine*, vol. 40, no. 6, pp. 847–856, 1998.

[3] Y. Zhu, "Parallel excitation with an array of transmit coils," *Magnetic Resonance in Medicine*, vol. 51, pp. 775–84, Apr. 2004.

[4] H. Homann, P. Börnert, H. Eggers, K. Nehrke, O. Dössel, and I. Graesslin, "Toward individualized SAR models and in vivo validation," *Magnetic Resonance in Medicine*, vol. 66, pp. 1767–76, Dec. 2011.

[5] R. Stollberger, P. Wach, G. McKinnon, E. Justich, and F. Ebner, "RF-field mapping in vivo," in *Proceedings of SMRM, 7th Annual Meeting*, p. 106, 1988.

[6] J. Powell, A. Papadaki, J. Hand, A. Hart, and D. McRobbie, "Numerical simulation of SAR induced around Co-Cr-Mo hip prostheses in situ exposed to RF fields associated with 1.5 and 3 T MRI body coils," *Magnetic Resonance in Medicine*, vol. 68, pp. 960–968, 2012.

[7] I. I. Rabi, J. R. Zacharias, S. Millman, and P. Kusch, "A new method of measuring nuclear magnetic moment," *Physical Review*, vol. 53, pp. 318–318, Feb 1938.

[8] F. Bloch, W. W. Hansen, and M. Packard, "The nuclear induction experiment," *Physical Review*, vol. 70, pp. 474–485, Oct 1946.

[9] E. M. Purcell, H. C. Torrey, and R. V. Pound, "Resonance absorption by nuclear magnetic moments in a solid," *Physical Review*, vol. 69, pp. 37–38, Jan 1946.

[10] P. C. Lauterbur, "Image formation by induced local interactions: examples employing nuclear magnetic resonance," *Nature*, vol. 242, no. 5394, pp. 190–191, 1973.

[11] P. Mansfield and P. K. Grannell, "NMR 'diffraction' in solids?," *Journal of Physics C: Solid State Physics*, vol. 6, no. 22, p. L422, 1973.

[12] M. Vlaardingerbroek and J. Boer, *Magnetic Resonance Imaging: Theory and Practice*. Springer, 2003.

[13] F. Bloch, "Nuclear Induction," *Physical Review*, vol. 70, pp. 460–474, Oct 1946.

[14] M. A. Bernstein, K. F. King, and X. J. Zhou, *Handbook of MRI Pulse Sequences*. Elsevier, 2004.

[15] R. Mezrich, "A perspective on K-space," *Radiology*, vol. 195, no. 2, pp. 297–315, 1995.

[16] M. Boas, *Mathematical Methods in the Physical Sciences*. Wiley, 2005.

[17] G. Glover, C. Hayes, N. Pelc, W. Edelstein, O. Mueller, H. Hart, C. Hardy, M. O'Donnell, and W. Barber, "Comparison of linear and circular polarization for magnetic resonance imaging," *Journal of Magnetic Resonance (1969)*, vol. 64, no. 2, pp. 255–270, 1985.

[18] V. L. Yarnykh, "Actual flip-angle imaging in the pulsed steady state: a method for rapid three-dimensional mapping of the transmitted radiofrequency field," *Magnetic Resonance in Medicine*, vol. 57, pp. 192–200, Jan. 2007.

[19] K. Nehrke and P. Börnert, "DREAM – A novel approach for robust, ultrafast, multislice B_1 mapping," *Magnetic Resonance in Medicine*, vol. 68, pp. 1517–1526, Jan. 2012.

[20] C. H. Cunningham, J. M. Pauly, and K. S. Nayak, "Saturated double-angle method for rapid B_1^+ mapping," *Magnetic Resonance in Medicine*, vol. 55, pp. 1326–33, June 2006.

[21] L. I. Sacolick, F. Wiesinger, I. Hancu, and M. W. Vogel, "B_1 mapping by Bloch-Siegert shift," *Magnetic Resonance in Medicine*, vol. 63, pp. 1315–22, May 2010.

[22] E. K. Insko and L. Bolinger, "Mapping of the radiofrequency field," *Journal of Magnetic Resonance*, vol. 103, no. 1, pp. 82–85, 1993.

[23] R. Stollberger and P. Wach, "Imaging of the Active B_1 Field in Vivo," *Magnetic Resonance in Medicine*, vol. 35, no. 2, pp. 246–251, 1996.

[24] J. Frahm, K. D. Merboldt, W. Hänicke, and A. Haase, "Stimulated echo imaging," *Journal of Magnetic Resonance*, vol. 93, pp. 81–93, 1985.

[25] K. Nehrke, M. J. Versluis, A. Webb, and P. Börnert, "Volumetric B_1^+ Mapping of the Brain at 7T using DREAM," *Magnetic Resonance in Medicine*, vol. 000, pp. 1–11, Feb. 2013.

[26] K. Nehrke, A. M. Sprinkart, H. H. Schild, and P. Börnert, "Fast B_1^+ Mapping for Cardiac MR using a Black Blood DREAM Sequence," in *Proceedings of ISMRM*, p. 4271, 2013.

[27] A. L. van Lier, D. O. Brunner, K. P. Pruessmann, D. W. Klomp, P. R. Luijten, J. J. Lagendijk, and C. A. van den Berg, "B_1^+ Phase mapping at 7 T and its application for in vivo electrical conductivity mapping," *Magnetic Resonance in Medicine*, vol. 67, no. 2, pp. 552–561, 2012.

[28] H. Young, R. Freedman, and A. Ford, *Sears and Zemansky's University Physics: With Modern Physics*. Pearson Addison Wesley, 12^{th} ed., 2008.

[29] J. Jin, *Electromagnetic Analysis and Design in Magnetic Resonance Imaging*. Biomedical Engineering, Taylor & Francis, 1998.

[30] J. T. Vaughan, M. Garwood, C. M. Collins, W. Liu, L. Delabarre, G. Adriany, P. Andersen, H. Merkle, R. Goebel, M. B. Smith, and K. Ugurbil, "7T vs. 4T: RF power, homogeneity, and signal-to-noise comparison in head images," *Magnetic Resonance in Medicine*, vol. 46, no. 1, pp. 24–30, 2001.

[31] P. Hasgall, F. Di Gennaro, C. Baumgartner, E. Neufeld, M. Gosselin, D. Payne, A. Klingenböck, and N. Kuster, "ITIS Database for thermal and electromagnetic parameters of biological tissues." `http://www.itis.ethz.ch/virtual-population/tissue-properties/`, Jan. 2015.

[32] J. Vaughan and J. Griffiths, *RF Coils for MRI*. eMagRes Books, Wiley, 2012.

[33] D. Pozar, *Microwave Engineering*. John Wiley & Sons, 4th ed., 1998.

[34] G. Shajan, M. Kozlov, J. Hoffmann, R. Turner, K. Scheffler, and R. Pohmann, "A 16-channel dual-row transmit array in combination with a 31-element receive array for human brain imaging at 9.4 T," *Magnetic Resonance in Medicine*, vol. 879, pp. 870–879, Mar. 2013.

[35] A. Graessl, A. Ruehle, H. Waiczies, A. Resetar, S. H. Hoffmann, J. Rieger, F. Wetterling, L. Winter, A. M. Nagel, and T. Niendorf, "Sodium MRI of the human heart at 7.0T: preliminary results," *NMR in Biomedicine*, January 2015.

[36] A. J. Raaijmakers, M. Italiaander, I. J. Voogt, P. R. Luijten, J. M. Hoogduin, D. W. Klomp, and C. A.T. van den Berg, "The fractionated dipole antenna: A new antenna for body imaging at 7 Tesla," *Magnetic Resonance in Medicine*, May 2015.

[37] K. Lakshmanan, M. Cloos, R. Lattanzi, D. Sodickson, and G. Wig, "The Loopole Antenna : Capturing Magnetic and Electric Dipole Fields with a Single Structure to Improve Transmit and Receive Performance," in *Proceedings of ISMRM*, vol. 25, p. 2737, 2014.

[38] A. J. Raaijmakers, O. Ipek, D. W. Klomp, C. Possanzini, P. R. Harvey, J. J. Lagendijk, and C. A. T. Van Den Berg, "Design of a radiative surface coil array element at 7 T: The single-side adapted dipole antenna," *Magnetic Resonance in Medicine*, vol. 66, no. 5, pp. 1488–1497, 2011.

[39] U. Katscher, P. Börnert, C. Leussler, and J. S. Van Den Brink, "Transmit SENSE," *Magnetic Resonance in Medicine*, vol. 49, pp. 144–50, Jan. 2003.

[40] W. Grissom, C.-y. Yip, Z. Zhang, V. A. Stenger, J. a. Fessler, and D. C. Noll, "Spatial domain method for the design of RF pulses in multicoil parallel excitation," *Magnetic Resonance in Medicine*, vol. 56, pp. 620–9, Sept. 2006.

[41] S. Boyd and L. Vandenberghe, *Convex Optimization*. Cambridge: Cambridge University Press, 2004.

[42] K. Setsompop, L. L. Wald, V. Alagappan, B. A. Gagoski, and E. Adalsteinsson, "Magnitude least squares optimization for parallel radio frequency excitation design demonstrated at 7 Tesla with eight channels," *Magnetic Resonance in Medicine*, vol. 59, pp. 908–15, Apr. 2008.

[43] P. W. Kassakian, "Convex Approximation and Optimization with Applications in Magnitude Filter Design and Radiation Pattern Synthesis," *University of California Berkeley*, 2006.

[44] A. Sbrizzi, H. Hoogduin, J. J. Lagendijk, P. Luijten, G. L. G. Sleijpen, and C. A. T. Van Den Berg, "Time efficient design of multi dimensional RF pulses: Application of a multi shift CGLS algorithm," *Magnetic Resonance in Medicine*, vol. 66, no. 3, pp. 879–885, 2011.

[45] A. Sbrizzi, S. Malik, C. A. T. Van Den Berg, P. R. Luijten, and H. Hoogduin, "Joint multi-shift and magnitude least squares (MSMLS) algorithm for time efficient low SAR and low peak RF pulse design," in *Proceedings of ISMRM*, vol. 22, p. 4334, 2014.

[46] D. O. Brunner and K. P. Pruessmann, "Optimal design of multiple-channel RF pulses under strict power and SAR constraints," *Magnetic Resonance in Medicine*, vol. 63, pp. 1280–91, May 2010.

[47] A. Hoyos-Idrobo, P. Weiss, A. Massire, A. Amadon, and N. Boulant, "On variant strategies to solve the magnitude least squares optimization problem in parallel transmission pulse design and under strict SAR and power constraints," *IEEE Transactions on Medical Imaging*, vol. 33, no. 3, pp. 739–748, 2014.

[48] M. Murbach, E. Neufeld, M. Capstick, W. Kainz, D. O. Brunner, T. Samaras, K. P. Pruessmann, and N. Kuster, "Thermal tissue damage model analyzed for different whole-body SAR and scan durations for standard MR body coils," *Magnetic Resonance in Medicine*, vol. 71, pp. 421–31, Jan. 2014.

[49] US Food and Drug Administration (FDA), "Criteria for Significant Risk Investigations of Magnetic Resonance Diagnostic Devices," tech. rep., U.S. Department of Health and Human Services, 2014.

[50] IEC, "International standard, Medical equipment Part 2-33: Particular requirements for the safety of Magnetic resonance equipment," tech. rep., International Electrotechnical Commission, 2002.

[51] U. Katscher, T. Voigt, C. Findeklee, P. Vernickel, K. Nehrke, and O. Dössel, "Determination of electric conductivity and local SAR via B_1 mapping," *IEEE Transactions on Medical Imaging*, vol. 28, pp. 1365–74, Sept. 2009.

[52] T. Voigt, H. Homann, U. Katscher, and O. Doessel, "Patient-individual local SAR determination: In vivo measurements and numerical validation," *Magnetic Resonance in Medicine*, vol. 1126, pp. 1117–1126, Dec. 2011.

[53] U. Katscher, C. Findeklee, and T. Voigt, "B_1-based specific energy absorption rate determination for nonquadrature radiofrequency excitation," *Magnetic Resonance in Medicine*, vol. 000, Feb. 2012.

[54] D. K. Sodickson, L. Alon, C. M. Deniz, R. Brown, B. Zhang, G. C. Wiggins, G. Y. Cho, N. B. Eliezer, D. S. Novikov, R. Lattanzi, Q. Duan, L. a. Sodickson, and Y. Zhu, "Local Maxwell Tomography Using Transmit-Receive Coil

Arrays for Contact-Free Mapping of Tissue Electrical Properties and Determination of Absolute RF Phase," in *Proceedings of ISMRM*, vol. 20, p. 387, 2012.

[55] IEEE Standards Coordinating Committee, "IEEE Recommended Practice for Measurements and Computations of Radio Frequency Electromagnetic Fields with Respect to Human Exposure to Such Fields," *IEEE Standards*, vol. 2002, 2003.

[56] K. Caputa, M. Okoniewski, and M. A. Stuchly, "An algorithm for computations of the power deposition in human tissue," *IEEE Antennas and Propagation Magazine*, vol. 41, no. 4, pp. 102–107, 1999.

[57] J. Lee, M. Gebhardt, L. L. Wald, and E. Adalsteinsson, "Local SAR in parallel transmission pulse design," *Magnetic Resonance in Medicine*, vol. 67, pp. 1566–78, June 2012.

[58] I. Graesslin, H. Homann, S. Biederer, P. Börnert, K. Nehrke, P. Vernickel, G. Mens, P. Harvey, and U. Katscher, "A specific absorption rate prediction concept for parallel transmission MR," *Magnetic Resonance in Medicine*, vol. 68, pp. 1664–1674, Jan. 2012.

[59] H. Homann, I. Graesslin, H. Eggers, K. Nehrke, P. Vernickel, U. Katscher, O. Dössel, and P. Börnert, "Local SAR management by RF Shimming: A simulation study with multiple human body models," *Magnetic Resonance Materials in Physics, Biology and Medicine*, vol. 25, pp. 193–204, June 2012.

[60] F. Bardati, A. Borrani, A. Gerardino, and G. A. Lovisolo, "SAR optimization in a phased array radiofrequency hyperthermia system," *IEEE Transactions on Biomedical Engineering*, vol. 42, no. 12, pp. 1201–1207, 1995.

[61] H. Homann, *SAR Prediction and SAR Management for Parallel Transmit MRI*. Karlsruhe Transactions on Biomedical Engineering, KIT Scientific Publ, 2012.

[62] A. Christ, W. Kainz, E. G. Hahn, K. Honegger, M. Zefferer, E. Neufeld, W. Rascher, R. Janka, W. Bautz, J. Chen, B. Kiefer, P. Schmitt, H.-P. Hollenbach, J. Shen, M. Oberle, D. Szczerba, A. Kam, J. W. Guag, and N. Kuster, "The Virtual Family–development of surface-based anatomical models of two adults and two children for dosimetric simulations," *Physics in Medicine and Biology*, vol. 55, pp. N23–38, Jan. 2010.

[63] P. J. Dimbylow, “FDTD calculations of the whole-body averaged SAR in an anatomically realistic voxel model of the human body from 1 MHz to 1 GHz,” *Physics in Medicine and Biology*, vol. 42, no. 3, pp. 479–490, 1997.

[64] J. Jin, F. Liu, E. Weber, and S. Crozier, “Improving SAR estimations in MRI using subject-specific models,” *Physics in Medicine and Biology*, vol. 57, pp. 8153–8171, Dec. 2012.

[65] S. Benkler, N. Chavannes, and N. Kuster, “Mastering conformal meshing for complex CAD-Based C-FDTD simulations,” *IEEE Antennas and Propagation Magazine*, vol. 50, no. 2, pp. 45–57, 2008.

[66] G. Eichfelder and M. Gebhardt, “Local specific absorption rate control for parallel transmission by virtual observation points,” *Magnetic Resonance in Medicine*, vol. 66, pp. 1468–76, Nov. 2011.

[67] M. N. O. Sadiku, “A simple introduction to finite element analysis of electromagnetic problems,” *IEEE Transactions on Education*, vol. 32, no. 2, pp. 85–93, 1989.

[68] M. Ney, “Method of Moments Electromagnetic,” *IEEE Transactions on Microwave Theory and Techniques*, vol. 33, no. 10, pp. 972–980, 1985.

[69] K. S. Yee, “Numerical Solution of Initial Boundary Value Problems Involving Maxwells Equations in Isotropic Media,” *IEEE Transactions on Antennas and Propagation*, vol. AP-14, pp. 302–307, 1966.

[70] T. Weiland, *On the unique numerical solution of Maxwellian eigenvalue problems in three dimensions*. DESY: Deutsches Elektronen-Synchrotron, DESY, 1984.

[71] T. Weiland, “Time Domain Electromagnetic Field Computation With Finite Difference Methods,” *International Journal of Numerical Modelling Electronic Networks Devices and Fields*, vol. 9, no. 4, pp. 295–319, 1996.

[72] M. Clemens and T. Weil, “Discrete Electromagnetism with the Finite Integration Technique,” *Progress In Electromagnetics Research*, vol. 32, pp. 65–87, 2001.

[73] R. Courant, K. Friedrichs, and H. Lewy, “Über die partiellen Differenzengleichungen der mathematischen Physik,” *Mathematische Annalen*, vol. 100, no. 1, pp. 32–74, 1928.

[74] T. Weiland, M. Timm, and I. Munteanu, “A Practical Guide to 3-D Simulation,” *IEEE Microwave Magazine*, pp. 62–75, December 2008.

[75] J. P. Berenger, “A perfectly matched layer for the absorption of electromagnetic waves,” *Journal of Computational Physics*, vol. 114, no. 2, pp. 185–200, 1994.

[76] K. Kurokawa, “Power Waves and the Scattering Matrix,” *IEEE Transactions on Microwave Theory and Techniques*, vol. 13, no. 1, pp. 194–202, 1964.

[77] S. Orfanidis, *Electromagnetic Waves and Antennas*. 2014.

[78] G. Matthaei, L. Young, and E. Jones, *Microwave Filters, Impedance-Matching Networks, and Coupling Structures*. Artech House Microwave Library, McGraw-Hill, 1964.

[79] G. Metzger and J. Vabre, *Transmission Lines With Pulse Excitation*. Academic Press, New York and London, 1969.

[80] C. S. Shin and R. Nevels, “Optimizing the Gaussian excitation function in the finite difference time domain method,” *IEEE Transactions on Education*, vol. 45, no. 1, pp. 15–18, 2002.

[81] G. Stantchev, W. Dorland, and N. Gumerov, “Fast parallel Particle-To-Grid interpolation for plasma PIC simulations on the GPU,” *Journal of Parallel and Distributed Computing*, vol. 68, no. 10, pp. 1339–1349, 2008.

[82] M. Kozlov and R. Turner, “Fast MRI coil analysis based on 3-D electromagnetic and RF circuit co-simulation,” *Journal of Magnetic Resonance*, vol. 200, pp. 147–152, Sept. 2009.

[83] R. Zhang, Y. Xing, J. Nistler, and J. Wang, “Field and S-Parameter Simulation of Arbitrary Antenna Structure with Variable Lumped Elements,” in *Proceedings of ISMRM*, vol. 17, p. 3040, 2009.

[84] R. A. Lemdiasov, A. O. Obi, and R. Ludwig, “A numerical postprocessing procedure for analyzing radio frequency MRI coils,” *Concepts in Magnetic Resonance Part A*, vol. 38A, no. 4, pp. 133–137, 2011.

[85] J. H. Beggs, S. S. Member, R. J. Luebbers, S. S. Member, K. S. Yee, and K. S. Kunz, “Implementation of Surface Conditions,” *IEEE Transactions on Antennas and Propagation*, vol. 40, no. 1, pp. 49–56, 1992.

[86] A. Kuehne, H. Waiczies, E. Moser, and E. Laistler, “Skin effect estimation accuracy in FDTD coil simulations,” in *Proceedings of ISMRM*, p. 1363, 2014.

[87] M. Kozlov and R. Turner, “A Comparison of Ansoft HFSS and CST Microwave Studio Simulation Software for Multi-channel Coil Design and SAR Estimation at 7T MRI,” *PIERS Online*, vol. 6, no. 4, pp. 395–399, 2010.

[88] W. Mao, Z. Wang, M. B. Smith, and C. M. Collins, “Calculation of SAR for Transmit Coil Arrays,” *Concepts in Magnetic Resonance, Part B, Magnetic Resonance Engineering*, vol. 31B, no. 2, pp. 127–131, 2007.

[89] A. Graessl, W. Renz, F. Hezel, M. A. Dieringer, L. Winter, C. Oezerdem, J. Rieger, P. Kellman, D. Santoro, T. D. Lindel, T. Frauenrath, H. Pfeiffer, and T. Niendorf, “Modular 32-channel transceiver coil array for cardiac MRI at 7.0T,” *Magnetic Resonance in Medicine*, vol. 72, pp. 276–290, July 2014.

[90] N. I. Avdievich, J. W. Pan, and H. P. Hetherington, “Resonant inductive decoupling (RID) for transceiver arrays to compensate for both reactive and resistive components of the mutual impedance,” *NMR in Biomedicine*, vol. 26, pp. 1547–54, Nov. 2013.

[91] P. Vernickel, P. Röschmann, C. Findeklee, K. M. Lüdeke, C. Leussler, J. Overweg, U. Katscher, I. Grässlin, and K. Schünemann, “Eight-channel transmit/receive body MRI coil at 3T,” *Magnetic Resonance in Medicine*, vol. 58, pp. 381–9, Aug. 2007.

[92] B. Guérin, M. Gebhardt, P. Serano, E. Adalsteinsson, M. Hamm, J. Pfeuffer, J. Nistler, and L. L. Wald, “Comparison of simulated parallel transmit body arrays at 3 T using excitation uniformity, global SAR, local SAR, and power efficiency metrics,” *Magnetic Resonance in Medicine*, vol. 00, pp. 1–14, 2014.

[93] P. Vernickel and C. Findeklee, “Active digital decoupling for multi-channel transmit MRI Systems,” *Proceedings of ISMRM*, vol. 19, no. 436, p. 170, 2007.

[94] M. Kozlov and R. Turner, “Effects of Tuning Condition, Head Size and Position on the SAR of a 9.4T Dual Row Array,” in *PIERS Proceedings, Taipei*, pp. 422–426, 2013.

[95] I. Zelinka, “SOMA – self-organizing migrating algorithm,” in *New optimization techniques in engineering*, vol. 141 of *Studies in Fuzziness and Soft Computing*, pp. 167–217, Springer Berlin Heidelberg, 2004.

[96] IEEE, “C95.3-2002 - IEEE Recommended Practice for Measurements and Computations of Radio Frequency Electromagnetic Fields With Respect to Human Exposure to Such Fields, 100 kHz-300 GHz.” 2002.

[97] A. Kuehne, S. Goluch, P. Waxmann, F. Seifert, B. Ittermann, E. Moser, and E. Laistler, "On power balance calculation in multi-channel transmit coil arrays," *Magnetic Resonance in Medicine*, December 2014.

[98] A. Beqiri, J. W. Hand, J. V. Hajnal, and S. J. Malik, "Comparison between simulated decoupling regimes for specific absorption rate prediction in parallel transmit MRI," *Magnetic Resonance in Medicine*, November 2014.

[99] M. Grant and S. Boyd, "CVX: Matlab software for disciplined convex programming, version 2.1." `http://cvxr.com/cvx`, Mar. 2014.

[100] M. Grant and S. Boyd, "Graph implementations for nonsmooth convex programs," in *Recent Advances in Learning and Control* (V. Blondel, S. Boyd, and H. Kimura, eds.), Lecture Notes in Control and Information Sciences, pp. 95–110, Springer-Verlag Limited, 2008. `http://stanford.edu/~boyd/graph_dcp.html`.

[101] A. Mueller, M. Kouwenhoven, C. P. Naehle, J. Gieseke, K. Strach, W. A. Willinek, H. H. Schild, and D. Thomas, "Dual-Source Radiofrequency Transmission with Patient-Adaptive Local Radiofrequency Shimming for 3.0-T Cardiac MR Imaging: Initial Experience," *Radiology*, vol. 263, no. 1, pp. 77–85, 2012.

[102] R. Krishnamurthy, A. Pednekar, M. Kouwenhoven, B. Cheong, and R. Muthupillai, "Evaluation of a subject specific dual-transmit approach for improving B_1 field homogeneity in cardiovascular magnetic resonance at 3 T," *Journal of Cardiovascular Magnetic Resonance*, vol. 15, p. 68, Jan. 2013.

[103] A. S. Childs, S. J. Malik, D. P. O'Regan, and J. V. Hajnal, "Impact of number of channels on RF shimming at 3T," *Magnetic Resonance Materials in Physics, Biology and Medicine*, vol. 26, pp. 401–410, Jan. 2013.

[104] D. A. Feinberg, J. D. Hale, J. C. Watts, L. Kaufman, and A. Mark, "Halving MR imaging time by conjugation: demonstration at 3.5 kG," *Radiology*, vol. 161, no. 2, pp. 527–531, 1986.

[105] K. P. Pruessmann, M. Weiger, M. B. Scheidegger, and P. Boesiger, "SENSE: Sensitivity Encoding for Fast MRI," *Magnetic Resonance in Medicine*, vol. 962, pp. 952–962, Nov. 1999.

[106] T. Togawa, O. Okai, and M. Oshima, "Observation of blood flow EMF in externally applied strong magnetic field by surface electrodes," *Medical and Biological Engineering*, vol. 5, no. 2, pp. 169–170, 1967.

[107] J. J. Suttie, L. Delabarre, A. Pitcher, P. F. van de Moortele, S. Dass, C. J. Snyder, J. M. Francis, G. J. Metzger, P. Weale, K. Ugurbil, S. Neubauer, M. Robson, and T. Vaughan, "7 Tesla (T) human cardiovascular magnetic resonance imaging using FLASH and SSFP to assess cardiac function: validation against 1.5 T and 3 T," *NMR in Biomedicine*, vol. 25, pp. 27–34, Jan. 2012.

[108] D. T. Ginat, M. W. Fong, D. J. Tuttle, S. K. Hobbs, and R. C. Vyas, "Cardiac imaging: Part 1, MR pulse sequences, imaging planes, and basic anatomy," *American Journal of Roentgenology*, vol. 197, pp. 808–815, October 2011.

[109] M. Schär, S. Kozerke, S. E. Fischer, and P. Boesiger, "Cardiac SSFP Imaging at 3 Tesla," *Magnetic Resonance in Medicine*, vol. 51, pp. 799–806, 2004.

[110] O. Bieri and K. Scheffler, "Fundamentals of balanced steady state free precession MRI," *Journal of Magnetic Resonance Imaging*, vol. 38, pp. 2–11, 2013.

[111] B. Guérin, M. Gebhardt, S. Cauley, E. Adalsteinsson, and L. L. Wald, "Local specific absorption rate (SAR), global SAR, transmitter power, and excitation accuracy trade-offs in low flip-angle parallel transmit pulse design," *Magnetic Resonance in Medicine*, vol. 71, pp. 1446–1457, June 2014.

[112] C. A. T. Van Den Berg, B. Van Den Bergen, J. B. Van De Kamer, B. W. Raaymakers, H. Kroeze, L. W. Bartels, and J. J. W. Lagendijk, "Simultaneous B_1^+ homogenization and specific absorption rate hotspot suppression using a magnetic resonance phased array transmit coil," *Magnetic Resonance in Medicine*, vol. 57, pp. 577–586, 2007.

[113] K. Sung and K. S. Nayak, "Measurement and characterization of RF nonuniformity over the heart at 3T using body coil transmission," *Journal of Magnetic Resonance Imaging*, vol. 27, pp. 643–8, Mar. 2008.

[114] C. J. Snyder, L. Delabarre, S. Moeller, J. Tian, C. Akgun, P. F. Van De Moortele, P. J. Bolan, K. Ugurbil, J. T. Vaughan, and G. J. Metzger, "Comparison between eight- and sixteen-channel TEM transceive arrays for body imaging at 7 T," *Magnetic Resonance in Medicine*, vol. 67, pp. 954–964, 2012.

[115] D. D. Wackerly, W. Mendenhall, and R. L. Scheaffer, *Mathematical Statistics with Applications*. Thomson Brooks/Cole, 7th ed., 2008.

[116] J. W. Carlson and D. M. Kramer, “Rapid radiofrequency calibration in MRI,” *Magnetic Resonance in Medicine*, vol. 15, no. 3, pp. 438–445, 1990.

[117] P. F. Van de Moortele and K. Ugurbil, “Very Fast Multi Channel B_1 Calibration at High Field in the Small Flip Angle Regime,” *Proceedings of ISMRM*, p. 367, 2009.

[118] C. Studholme, D. Hill, and D. Hawkes, “An overlap invariant entropy measure of 3D medical image alignment,” *Pattern Recognition*, vol. 32, no. 1, pp. 71 – 86, 1999.

[119] S. J. Malik, G. D. Kenny, and J. V. Hajnal, “Slice profile correction for transmit sensitivity mapping using actual flip angle imaging,” *Magnetic Resonance in Medicine*, vol. 65, pp. 1393–9, May 2011.

[120] J. F. Sturm, “SeDuMi - Software for Optimization over Symmetric Cones,” 2003.

[121] D. Brunner and K. Pruessmann, “A matrix approach for mapping array transmit fields in under a minute,” *Proceedings of ISMRM*, p. 354, 2008.

[122] S. J. Malik, D. J. Larkman, and J. V. Hajnal, “Optimal linear combinations of array elements for B1 mapping,” *Magnetic Resonance in Medicine*, vol. 62, pp. 902–9, Oct. 2009.

[123] B. Van Den Bergen, C. A. T. Van Den Berg, L. W. Bartels, and J. J. W. Lagendijk, “7 T body MRI: B1 shimming with simultaneous SAR reduction,” *Physics in Medicine and Biology*, vol. 52, pp. 5429–5441, 2007.

[124] I. Graesslin, S. Krueger, P. Vernickel, J. Achtzehn, K. Nehrke, and S. Weiss, “Detection of RF unsafe devices using a parallel transmission MR system,” *Magnetic Resonance in Medicine*, vol. 70, pp. 1440–9, Nov. 2013.

[125] M. K. Konings, L. W. Bartels, H. F. M. Smits, and C. J. G. Bakker, “Heating around intravascular guidewires by resonating RF waves,” *Journal of Magnetic Resonance Imaging*, vol. 12, no. 1, pp. 79–85, 2000.

[126] Y. Eryaman, B. Akin, and E. Atalar, “Reduction of implant RF heating through modification of transmit coil electric field,” *Magnetic Resonance in Medicine*, vol. 65, pp. 1305–13, May 2011.

[127] M. Etezadi-Amoli, P. Stang, M. G. Zanchi, J. M. Pauly, G. C. Scott, and A. B. Kerr, “Controlling Induced Currents in Guidewires Using Parallel Transmit,” *Magnetic Resonance in Medicine*, 2014.

[128] J. M. Drew, J. K. Lange, V. Briggs, P. Franklin, and D. C. Ayers, "Trends in Total Hip Arthroplasty in the United States: The Shift to a Younger Demographic," in *American Academy of Orthopaedic Surgeons 2014*, p. 542, 2014.

[129] M. R. Van Den Bosch, M. A. Moerland, J. J. W. Lagendijk, L. W. Bartels, and C. A. T. van den Berg, "New method to monitor RF safety in MRI-guided interventions based on RF induced image artefacts," *Medical Physics*, vol. 37, no. 2, pp. 814–821, 2010.

[130] W. R. Overall, J. M. Pauly, P. P. Stang, and G. C. Scott, "Ensuring safety of implanted devices under MRI using reversed RF polarization," *Magnetic Resonance in Medicine*, vol. 64, no. 3, pp. 823–833, 2010.

[131] C. W. Ellenor, P. P. Stang, M. Etezadi-Amoli, J. M. Pauly, and G. C. Scott, "Offline impedance measurements for detection and mitigation of dangerous implant interactions: An RF safety prescreen," *Magnetic Resonance in Medicine*, vol. 1339, pp. 1328–1339, 2014.

[132] T. J. Bachschmidt, M. Köhler, J. Nistler, C. Geppert, P. M. Jakob, and M. Nittka, "Polarized multichannel transmit MRI to reduce shading near metal implants," *Magnetic Resonance in Medicine*, November 2014.

[133] P. T. Hardy and K. M. Weil, "A review of thermal MR injuries," *Radiologic Technology*, vol. 81, no. 6, pp. 606–609, 2010.

[134] L. Zilberti, O. Bottauscio, M. Chiampi, J. Hand, H. S. Lopez, R. Brühl, and S. Crozier, "Numerical prediction of temperature elevation induced around metallic hip prostheses by traditional, split, and uniplanar gradient coils," *Magnetic Resonance in Medicine*, 2015.

[135] C. D. Smyser, H. Kidokoro, and T. E. Inder, "Magnetic resonance imaging of the brain at term equivalent age in extremely premature neonates: To scan or not to scan?," *Journal of Paediatrics and Child Health*, vol. 48, no. 9, pp. 794–800, 2012.

[136] M. Rutherford, *MRI of the Neonatal Brain*. W.B. Saunders, 2002.

[137] M. A. Johnson, J. M. Pennock, G. M. Bydder, R. E. Steiner, D. J. Thomas, R. Hayward, D. R. Bryant, J. A. Payne, M. I. Levene, A. Whitelaw, and al. Et, "Clinical NMR imaging of the brain in children: normal and neurologic disease," *American Journal of Roentgenology*, vol. 141, pp. 1005–1018, Nov. 1983.

[138] J. Jin and J. Chen, "On the SAR and field inhomogeneity of birdcage coils loaded with the human head," *Magnetic Resonance in Medicine*, vol. 38, no. 6, pp. 953–963, 1997.

[139] J. Chen, Z. Feng, and J. M. Jin, "Numerical simulation of SAR and B_1-field inhomogeneity of shielded rf coils loaded with the human head," *IEEE Transactions on Biomedical Engineering*, vol. 45, no. 5, pp. 642–649, 1998.

[140] T. S. Ibrahim, R. Lee, B. A. Baertlein, and P. M. Robitaille, "B_1 field homogeneity and SAR calculations for the birdcage coil," *Physics in Medicine and Biology*, vol. 46, no. 2, pp. 609–619, 2001.

[141] M. Zankl, R. Veit, G. Williams, K. Schneider, H. Fendel, N. Petoussi, and G. Drexler, "The construction of computer tomographic phantoms and their application in radiology and radiation protection," *Radiation and Environmental Biophysics*, vol. 27, no. 2, pp. 153–164, 1988.

[142] R. Veit, G. Williams, G. Drexler, E. Mannweiler, N. Petoussi, and M. Zankl, "Tomographic Anthropomorphic Models, Part I: Construction Techniqueand Description of Models of an 8 Week Old Baby and a 7 Year Old Child," *Gesellschaft für Strahlen und Umweltforschung: Munich, Germany*, p. 58, 1989.

[143] T. Chmielewski, J. Flock, and T. Eagan, "Degenerate birdcage coil and transmit/receive apparatus and method for same," Feb. 20 2007. US Patent 7, 180, 291.

[144] World Health Organisation, "WHO Anthro for Personal Computers (Version 3.2.2, January 2011): Software for Assessing Growth and Development of the Worlds Children." `http://www.who.int/childgrowth/software/en/`, Dec. 2013.

[145] D. Andreuccetti, R. Fossi, and C. Petrucci, "An Internet resource for the calculation of the dielectric properties of body tissues in the frequency range 10 Hz - 100 GHz." `http://niremf.ifac.cnr.it/tissprop/`, June 1996.

[146] P. Dimbylow, W. Bolch, and C. Lee, "SAR calculations from 20 MHz to 6 GHz in the University of Florida newborn voxel phantom and their implications for dosimetry," *Physics in Medicine and Biology*, vol. 55, pp. 1519–30, Mar. 2010.

[147] A. Peyman, A. A. Rezazadeh, and C. Gabriel, "Changes in the dielectric properties of rat tissue as a function of age at microwave frequencies," *Physics in Medicine and Biology*, vol. 46, no. 6, pp. 1617–1629, 2001.

[148] D. Hoult and P. C. Lauterbur, “The sensitivity of the zeugmatographic experiment involving human samples,” *Journal of Magnetic Resonance (1969)*, vol. 34, no. 2, pp. 425–433, 1979.

[149] N. Leitgeb, G. Loos, and F. Ebner, “MRI-Induced Tissue Heating at Metallic Sutures (Cerclages),” *Journal of Electromagnetic Analysis and Applications*, vol. 2013, no. September, pp. 354–358, 2013.

[150] A. Sharma, S. Ford, and J. Calvert, “Adaptation for life: A review of neonatal physiology,” *Anaesthesia and Intensive Care Medicine*, vol. 15, no. 3, pp. 89–95, 2014.

[151] R. C. Semelka, W. Chew, H. Hricak, E. Tomei, and C. B. Higgins, “Fat-saturation mr imaging of the upper abdomen.,” *American Journal of Roentgenology*, vol. 155, no. 5, pp. 1111–1116, 1990.

Appendix A

VOP Algorithm

A number of properties must be held by the VOPs for their estimation framework to be feasible [66]. If the overestimation factor ϵ in the expression in Equation 3.27 is ignored, then the condition can be restated by the existence of a matrix $\mathbf{M} = V_j - Q_v$ that itself is positive semidefinite (PSD). This ensures that a positive value is given for any complex vector $\mathbf{W} \in \mathbb{C}^n$.

If **M** is PSD and the condition in equation 3.27 is valid, then it can be said that V_j dominates Q_v [66]. Furthermore if there exist matrices in the set Ω for which $V_j - Q_v$ is not PSD, then these matrices are considered nondominated elements of Ω. The set of these elements P_Ω function as virtual observation points because the elements in this set will always dominate all the elements in Ω [66].

The VOP clustering algorithm developed by Eichfelder and Gerbhardt is written here in a condensed form. For further details please refer to their paper [66].

1. Set $\Omega = \{Q_v \mid v = 1, \ldots, M\}$ and choose upper bound u for $\|\mathbf{Z}\| \leq u$, set $c = 1$.
2. Select $\mathbf{A}^{c^*} = \operatorname{argmax}\{\|A\|_2 \mid A \in \Omega\}$.
3. Sort all matrices $\mathbf{A} \in \Omega$ w.r.t. $\lambda_{min}(\mathbf{A}^{c^*} - \mathbf{A})$ in descending order.
   Set $l := 2, \mathbf{Z}^c := 0, \epsilon^c := 0$.
   Set $S^c := \{\mathbf{A}_1, \mathbf{A}_2\}$.
4. Solve
   min $\|\mathbf{Z}\|$
   w.r.t. $\mathbf{A}^{c^*} + \mathbf{Z} - \mathbf{A}$ PSD $\forall \mathbf{A} \in S^c$
   Z PSD Hermitian
   If a minimal solution $\overline{\mathbf{Z}}$ with $\|\overline{\mathbf{Z}}\| \leq u$ is obtained, set
   $\epsilon^c := -\lambda_{min}(\mathbf{A}^{c^*} - \mathbf{A}_l)$, set $l := l + 1$ and $\mathbf{Z}^c := \overline{\mathbf{Z}}$.
   If $l \leq n_c$, set $S^c := S^c \cup \{\mathbf{A}_l\}$ and repeat step 4.

5. Set $S^c := \left\{ \mathbf{A}^{c^*} = \mathbf{A}_1, \mathbf{A}_2, \ldots, \mathbf{A}_{l-1} \right\}$ and $\Omega := \Omega \setminus \{\mathbf{A}_1, \mathbf{A}_2, \ldots, \mathbf{A}_{l-1}\}$
   If $\Omega = \emptyset$, set $N = k$ and stop.
   Else set $k := k + 1$ and go to step 2 to begin a new cluster.

The final output of the algorithm will be a set of VOPs $\mathbf{A}_1, \ldots, \mathbf{A}_2$ which represent the full set of matrices Ω with an overestimation factor ϵ for any given input to the matrices.

Appendix B

Neonatal Tissue Properties

Neonatal tissue properties of permittivity and electrical conductivity are shown below for frequencies of 64 and 128 MHz. The tissue density is also given.

Tissue	Permittivity Ratio	Neonatal Tissue Permittivity		Conductivity Ratio	Neonatal Tissue Conductivity (Sm^{-1})		Density ($kg\,m^{-3}$)
		64 MHz	128 MHz		64 MHz	128 MHz	
Adrenals	1.28	94.65	85.50	1.7	1.3231	1.3670	1050
Bone	2.18	36.36	32.12	3.9	0.2321	0.2623	1562
Bladder wall	1.28	31.48	28.01	1.5	0.4310	0.4468	1050
Bladder contents	1.00	24.60	21.88	1.0	0.2870	0.2979	987
Brain	1.45	119.81	91.61	1.7	0.6820	0.7883	987
Breast	1.28	7.43	7.23	1.5	0.0443	0.0454	1050
Connective tissue	1.28	76.15	66.43	1.5	0.7115	0.7470	987
Eyes	1.28	96.38	83.30	1.5	1.3240	1.3758	1050
Eye lens	1.28	77.48	68.00	1.5	0.8787	0.9129	1050
Gall bladder wall	1.00	87.40	74.29	1.0	0.9660	1.0409	1050
Gall bladder contents	1.00	105.44	89.09	1.0	1.4818	1.5753	1050
Heart	1.28	136.33	108.09	1.5	1.0176	1.1475	1050
Kidney	1.34	158.87	120.41	1.5	1.1120	1.2764	1050
Large intestine wall	1.28	121.22	98.18	1.5	0.9570	1.0560	1050
Large intestine contents	1.00	72.20	63.60	1.0	0.6880	0.7190	987
Liver	1.14	91.84	73.40	1.3	0.5824	0.6631	1050
Lung	1.28	96.36	81.71	1.5	0.7965	0.8627	296
Muscle	1.39	100.41	88.36	1.7	1.1699	1.2220	1050
Oesophagus	1.28	109.85	95.97	1.5	1.3167	1.3686	1050
Ovaries	1.28	136.72	101.64	1.5	1.0278	1.1836	50
Pancreas	1.28	94.65	85.56	1.5	1.1675	1.2057	50
Skin	1.89	145.01	116.63	2.1	1.0249	1.1413	1105
Small intestine wall	1.28	151.50	112.91	1.5	2.3871	2.5374	1050
Small intestine contents	1.00	72.20	63.60	1.0	0.6880	0.7190	987
Spinal cord	1.28	70.48	56.52	1.5	0.4683	0.5299	1050
Spleen	1.14	126.04	94.75	1.5	0.9671	1.0843	1050
Stomach wall	1.28	109.85	95.97	1.5	1.3167	1.3686	1050
Stomach contents	1.00	72.20	63.60	1.0	0.6880	0.7190	987
Thymus	1.28	94.65	85.56	1.5	1.1675	1.2057	1050
Thyroid	1.28	94.65	85.56	1.5	1.1675	1.2057	1050
Uterus	1.28	117.91	96.72	1.5	1.3659	1.4405	987

Table B.1: Neonatal tissue properties shown for 64 and 128 MHz along with the ratios of the dielectric properties taken from the ratio of these between newborn and adult rats – this ratio is given as newborn/adult. The neonatal permittivity and conductivity are then the human adult properties multiplied by these ratios.